Fullerene Based Nanomaterials for Biomedical Applications

Tinghui Li

Dissertation submitted to the faculty of the Virginia Polytechnic Institute and State University in partial fulfillment of the requirements for the degree of

Doctor of Philosophy
In
Chemistry

Harry C. Dorn

Leslie LaConte

Louis A. Madsen

Brian M. Tissue

September 19th 2017
Blacksburg, Virginia

Keywords: Endohedral Metallofullerene, Gadolinium, Magnetic Resonance Imaging, Contrast agents, Antioxidant agents, Diagnostic and therapeutic nanoparticles

Fullerene Based Nanomaterials for Biomedical Applications

Tinghui Li

ABSTRACT

Trimetallic nitride endohedral fullerenes (TNT-EMF) have been recognized for their multifunctional capabilities in biomedical applications. Functionalized gadolinium-loaded fullerenes attracted much attention as a potential new nanoplatform for next-generation magnetic resonance imaging (MRI) contrast agents, given their inherent higher ^{1}H relaxivity than most commercial contrast agents. The fullerene cage is an extraordinarily stable species which makes it extremely unlikely to break and release the toxic Gd metal ions into the bioenvironment. In addition, radiolabeled metals could be encapsulated in this robust carbon cage to deliver therapeutic irradiation. In this dissertation, we aim to develop a series of functionalized TNT-EMFs for MRI detection of various pathological conditions, such as brain cancer, chronic osteomyelitis, and gastrointestinal (GI) tract.

As a general introduction, Chapter 1 briefly introduces recent progress in developing metallofullerenes for next-generation biomedical applications. Of special interest are MRI contrast agents. Other potential biomedical applications, toxicity, stability and biodistribution of metallofullerenes are also discussed. Finally, the challenges and future outlook of using fullerene in biomedical and diagnosis applications are summarized at the end of this chapter.

The large carbon surface area is ideally suited for multiple exo-functionalization approaches to modify the hydrophobic fullerene cage for a more hydrophilic bio-environment. Additionally, peptides and other agents are readily covalently attached to this nanoprobe for targeting applications. Chapter 2 presents the functionalized metallofullerenes conjugated with interleukin-

13 peptide exhibits enhanced targeting of U-251 glioblastoma multiforme (GBM) cell lines and can be effectively delivered intravenously in an orthotopic GBM mouse model. Chapter 3 shows, with the specific targeting moiety, the functionalized metallofullerenes can be applied as a non-invasive imaging approach to detect and differentiate chronic post-traumatic osteomyelitis from aseptic inflammation.

Fullerene is a powerful antioxidant due to delocalization of the π-electrons over the carbon cage, which can readily react with free radicals and subsequently delivers a cascade of downstream possessions in numerous biomedical applications. Chapter 4 investigates the antioxidative and anti-inflammatory properties of functionalized $Gd_3N@C_{80}$. This nanoplatform would hold great promise as a novel class of theranostic agent in combating oxidative stress and resolving inflammation, given their inherent MRI applications.

In chapter 5, $Gd_3N@C_{80}$ is modified with polyethylene glycol (PEG) for working as MRI contrast agents for GI tract. The high molecular weight can prevent any appreciable absorption through the skin or mucosal tissue, and offer considerable advantages for localized agents in the GI tract. Besides the excellent contrast capability, the PEGylated-$Gd_3N@C_{80}$ exhibits outstanding radical scavenging ability, which can potentially eliminate the reactive oxygen species in GI tract. The biodistribution result suggests this nanoplatform can be worked as the potential contrast agent for GI tract at least for 6 hours.

A novel amphiphilic $Gd_3N@C_{80}$ derivative is discussed in Chapter 6. It has been noticed for a long time the functionalization $Gd_3N@C_{80}$ contrast agents have higher relaxivity at lower concentrations. The explanation for the concentration dependency is not fully understood. In this work, the amphiphilic $Gd_3N@C_{80}$ derivative is used as the model to investigate the relationship between the relaxivity and concentration of the Gd-based fullerenes.

Click chemistry has been extensively used in functionalization due to the high efficiency and technical simplicity of the reaction. Appendix A describes a new type of $Sc_3N@C_{80}$ derivative conducted by employing the click reaction. The structure of $Sc_3N@C_{80}$-alkynyl and $Sc_3N@C_{80}$-alkynyl-benzyl azide are characterized by NMR, MALDI-TOF, UV-Vis, and HPLC. The high yield of the click reaction can provide access to various derivatives which have great potential for application in medical and materials science.

The functionalization and characterizations of $Ho_3N@C_{80}$ derivatives are reported in Appendix B. The contrast ability of $Ho_3N@C_{80}$ is directly compared with $Gd_3N@C_{80}$. The Ho-based fullerenes can be performed as the radiotherapeutic agents; the leaching study is performed to test the stability of carbon cage after irradiation.

Appendix C briefly shows a new method to develop $Gd_3N@C_{80}$ based targeting platform, which can be used as the probe for chronic post-traumatic osteomyelitis.

Fullerene Based Nanomaterials for Biomedical Applications

Tinghui Li

General Audience Abstract

Since the discovery of fullerene in 1985, fullerenes and metallofullerene in medical and diagnostics applications is rapidly increasing. Functionalized gadolinium-loaded fullerenes attracted much attention as a potential new nanoplatform for magnetic resonance imaging (MRI) contrast agents, given their inherent better contrast ability than most commercial contrast agents. The fullerene cage is an extraordinarily stable species which makes it extremely unlikely to break and release the toxic metal ions into the bioenvironment. In this dissertation, we report the development of a series of functionalized fullerenes for MRI detection of various pathological conditions, such as brain cancer and chronic osteomyelitis, and working as the agent for gastrointestinal (GI) tract.

As a general introduction, Chapter 1 briefly introduces recent progress in developing fullerenes for next-generation biomedical applications. Of special interest are MRI contrast agents. Other potential biomedical applications, toxicity, stability and biodistribution of fullerenes are also discussed. Finally, the challenges and future outlook of using fullerene in biomedical and diagnosis applications are summarized at the end of this chapter.

The large carbon surface area is ideally suited for multiple chemical reactions approaches to make the fullerene soluble in bio-environment. Additionally, peptides and other agents are readily attached to this nanoprobe for targeting applications. Chapter 2 presents the functionalized fullerenes conjugated with interleukin-13 peptide exhibits enhanced targeting of glioblastoma multiforme (GBM) cell lines and can be delivered efficiently intravenously in a GBM mouse

model. Chapter 3 shows, with the specific targeting moiety, the functionalized fullerenes can be applied as a non-invasive imaging approach to detect and differentiate chronic post-traumatic osteomyelitis from aseptic inflammation.

The nature of fullerene aromaticity makes it a powerful antioxidant. Fullerene can readily react with free radicals and subsequently delivers a cascade of downstream possessions in numerous biomedical applications. Chapter 4 investigates the antioxidative and anti-inflammatory properties of functionalized $Gd_3N@C_{80}$. This nanoplatform would hold great promise as a novel class of theranostic agent in combating oxidative stress and resolving inflammation, given their inherent MRI applications.

In chapter 5, $Gd_3N@C_{80}$ is modified with polymer polyethylene glycol (PEG) for working as MRI contrast agents for GI tract. The high molecular weight can prevent any appreciable absorption through the skin or mucosal tissue, and offer considerable advantages for localized agents in the GI tract. Besides the excellent contrast capability, the PEGylated-$Gd_3N@C_{80}$ exhibits outstanding radical scavenging ability, which can potentially eliminate the reactive oxygen species in GI tract. The biodistribution result suggests this nanoplatform can be worked as the potential contrast agent for GI tract at least for 6 hours.

A novel amphiphilic $Gd_3N@C_{80}$ derivative is discussed in Chapter 6. It has been noticed for a long time the functionalization $Gd_3N@C_{80}$ contrast agents have better contrast ability at lower concentrations. The explanation for the concentration dependency is not fully understood. In this work, the amphiphilic $Gd_3N@C_{80}$ derivative is used as the model to investigate the relationship between the contrast ability and concentration of the Gd-based fullerenes.

Click chemistry has been extensively used in functionalization due to the high efficiency and technical simplicity of the reaction. Appendix A describes a new type of $Sc_3N@C_{80}$ derivative

conducted by employing the click reaction. The high yield of the click reaction can provide access to various derivatives. It makes this kind of fullerene has excellent potential for application in medical and materials science.

The functionalization and characterizations of $Ho_3N@C_{80}$ derivatives are reported in Appendix B. The contrast ability of $Ho_3N@C_{80}$ is directly compared with $Gd_3N@C_{80}$. The Ho-based fullerenes can be performed as the radiotherapeutic agents; the leaching study is conducted to test the stability of carbon cage after irradiation.

Appendix C briefly shows a new method to develop $Gd_3N@C_{80}$ based targeting platform, which can be used as the probe for chronic post-traumatic osteomyelitis.

Acknowledgement

I would like to express my sincere gratitude and appreciation to my advisor, Dr. Harry Dorn. To me, he is not only a research advisor, who provides me valuable guidance, inspirations, and advice on how to be a competent scientist. He is also a life mentor, who never stop supporting and encouraging me to overcome difficulties and be more self-confident. Whenever I feel unconfident, his word would give me strength and drive me to create a better version of myself. I enjoyed talking with him when we drove to VTCRI, enjoyed discussing and editing the manuscript at the local coffee shop over the weekend. Thank you Dr. Harry Dorn, without your help, I probably would not walk through this Ph.D. journey, and thank you for opening my eyes to new stages of opportunity and strength. I will forever be grateful for your guidance and kindness

I am lucky enough to have Dr. Leslie LaConte, Dr. Louis Madsen, and Dr. Brian Tissue as my committee members. Thanks Dr. LaConte for teaching and helping me in EPR measurement. Dr. Louis Madsen and Dr. Brian Tissue have given me valuable training class in analytical chemistry, NMR in Chemistry and Polymer Science, and Instrument Design, respectively. Thanks Dr. Madsen provided many insightful suggestions to my work on relaxivity and diffusion coefficient measurement. Thanks Dr. Tissue for showing me how to write better in scientific language. Again, for my committee members, I appreciate your time, patience, encouragements and suggestions.

I would also like to acknowledge the support from my research collaborators. I thank Dr. Stephen LaConte and his student Amnah Eltahir, from VTCRI, for help with magnetic resonance imaging taken and data processing, which provided key results for Chapter2, 5, 6, and Appendix B. Thanks Dr. Zhi Sheng and Dr. Susan Murphy, who also from VTCRI, for their *in vitro* and *in vivo* research collaboration, which substantially contribute to the work in Chapter 2. I sincerely thank and enjoy the work with Dr. Xiao Li, Dr. Li Jin, and Dr. Xudong Li and other colleagues from Department

of Orthopaedic Surgery, University of Virginia. Our collaborate work are presented in Chapter 3, 4 and Appendix C. Thanks Dr. John Morris and Dr. Richey Davis for their help in XPS, and DLS, respectively. I also thank Dr. Daniel Bearden from Hollings Marine Laboratory, for his NMR collaboration, which described in Appendix A. I gratefully thank other faculty members and colleagues in Virginia Tech who has been so helpful. Thanks Dr. Keith Ray for teaching me to use MALD-TOF MS. Thanks Jeffery Parks for helping me measuring the concentration of metallofullerenes. Thank Dr. Mehdi Ashraf-Khorassani for his help with HPLC.

My sincerest thanks also go to my bright and talented colleagues in the Dorn Lab and Chemistry department. I enjoy the collaborative atmosphere and thank the help from Dr. Jianyuan Zhang, Dr. Ying Chen, Dr. Yafen Zhang, Dr. Yuming Dai, Dr. Ying Wang, Dr. Libin Bai, Dr. Roberto Padilla, Youqing Ye, Dr. Boris Kiseley, Dr. Kanwarpal S. Bakshi, Dr. James Duchamp, Xiaoyang Liu, Kyle Kirkpatrick, José Rodríguez-Corrales, Guanyu Wang, Dr. Yonjae Kim, and our administrative assistant, Stephanie Hurt.

I would like to give special thanks to my family, my mother Chunxia Huang, and my father Ruizhou Li. They are always supportive and encouraging to me. I thank my husband, colleague and best friend, Jie Zhu. Thanks for coming into my life, giving me joy and always being here for me. And, thanks Potato, he is not only our cute dog but also a loved member of our family. I would like to thank all the friends I met at Blacksburg, thank you for making my life wonderful and full of happiness.

Thank you all, you are special who shapes who I am, who helps to determine the person I become.

Table of Contents

List of Figures

Chapter 1

Chapter 2

showed no or little reduction in LPS-elicited ROS generation. (e) Representative fluorescence images of intracellular ROS illustrated robust ROS-scavenging activity of carboxyl-Gd_3NC80. Image taken at ×200 magnification. Scale bar represented 100 μm. *p<0.05 vs non-LPS control, $^{\#}p$<0.05 vs LPS-treated groups.

Figure 3. Carboxyl-$Gd_3N@C_{80}$ protected Raw 264.7 cells from LPS-induced oxidative stress and upregulated pro-inflammatory cytokine via elevating Nrf2 expression. Cells were pretreated with carboxyl-$Gd_3N@C_{80}$ (3.5 μM) for 20 h before treatment of LPS (100 ng/mL) for 4 h. (a) Real-time reverse transcription polymerase chain reaction (RT-PCR) suggested LPS stimulation significantly increased mRNA expression of inducible nitric oxide synthase (iNOS) (**p<0.01 vs control), whereas carboxyl-$Gd_3N@C80$ dramatically reversed such induction ($^{\#\#\#}p$<0.001 *vs.* LPS). (b) Similarly, the upregulation of pro-inflammatory cytokine tumor necrosis factor-alpha (TNF-α) (***p<0.001 *vs.* control) upon LPS treatment was significantly alleviated by carboxyl-$Gd_3N@C_{80}$ ($^{\#\#}p$<0.01 *vs.* LPS). (c) The antioxidative enzyme hemooxygenase-1 (HO-1) was significantly enhanced by carboxyl-$Gd_3N@C_{80}$ (***p<0.001 *vs.* control, $^{\#\#\#}p$<0.001 *vs.* LPS) but it was not altered by LPS stimulation. (d), Immunofluorescence staining of Nrf2, a key antioxidative enzyme regulator, was dramatically increased upon nanoparticle treatment in the present and absence of LPS, whereas no significant intensity difference was observed in LPS treated cells. (e) Mean fluorescence intensity analysis of d suggested carboxyl-$Gd_3N@C_{80}$ effectively upregulated the protective Nrf2 protein expression (***p<0.001 *vs.* control, $^{\#\#\#}p$<0.001 *vs.* LPS). Experiments were repeated three times (n=3). Scale bar in d represented 100 μm. 102

Figure 4. Carboxyl-$Gd_3N@C_{80}$ rescued Raw 264.7 cells from LPS-induced oxidative stress via ERK and Akt pathways. (a) Representative immunoblotting analysis of phosphor-ERK, total ERK, phosphor-Akt, and total Akt of cell lysates subjected to different treatments. Cells were preincubated with carboxyl-$Gd_3N@C_{80}$ (3.5 μM) for 20 h and treated with or without LPS (100 ng/mL) for another 4 h. (b) Quantification of pERK/tERK (n=4) intensity showed carboxyl- 103

List of Schemes

List of Tables

Appendix B

Appendix C

Chapter 1 Biomedical Applications of Metal-Encapsulated Fullerene Nanoparticles

Part of this chapter is adopted from a manuscript published on Small with appropriate modifications under the permission of the Wiley. Full text of the published manuscript, entitled "*Biomedical Applications of Metal-Encapsulated Fullerene Nanoparticles"* by Tinghui Li and Harry C. Dorn, can be obtained at

http://onlinelibrary.wiley.com/doi/10.1002/smll.201603152/full.

1.1 Chapter overview

The carbonaceous nanomaterials known as *metallofullerenes* have attracted considerable attention due to their attractive properties. The robust nature of the "Trojan Horse" fullerene cage provides an important structural component which isolates the metal cluster from the bio-environment. The large carbon surface area is ideally suited for multiple exo-functionalization approaches to modify the hydrophobic cage for a more hydrophilic bio-environment. Additionally, peptides and other agents are readily covalently attached to this nanoprobe for targeting applications. In this chapter, I briefly introduce the discovery, and early biomedical application of metallofullerenes. Then I review the recent progress in developing metallofullerenes for next-generation biomedical applications. Of special interest are magnetic resonance imaging (MRI) contrast agents. Gadolinium-based metallofullerenes provide 2-3 orders of magnitude improvement in MRI relaxivity and potentially lower clinical levels of toxic Gd^{3+} ions deposited. Third, I describe by modifying the carbon cage, metallofullerene can obtain specific ability to target to certain tumors, or organs. Fourth, I discuss other potential biomedical applications of metallofullerenes, such as, working as neutron capture therapy (NCT), and radical scavenger. Since the metallofullerenes are proposed as potential applications in biomedical fields, the toxicity, stability and biodistribution is

discussed in next part. Finally, I summarize the challenges and future outlook of using fullerene in biomedical and diagnosis applications.

1.2 Brief introduction the discovery and biomedical application of metallofullerene

It is well-recognized that nanoparticles offer promising solutions to numerous biomedical applications. They present a new toolset with a size range closely matching that of cellular units (1 to 1,000 nm), a substantial multi-functional capability, and an inherently large surface-to-volume ratio. Endohedral metallofullerenes (EMFs) represent a unique nanoparticle platform and are currently being evaluated for next-generation biomedical applications. Their potential was first recognized shortly after the discovery of fullerenes, and there are now several reviews describing their structures, functionalization reactions, and physical properties.[1-16] Mono-metal EMF ($A@C_{82}$) radiopharmaceuticals were initially explored because the radioactive metal ion was isolated from the extracellular space of the bio-system by the fullerene cage. In the 1990's, Sueki and coworkers prepared mono-metallic EMFs encaging radioisotopes of Gd, Sm, and Yb.[17,18] In other works, Braun, Rausch, and colleagues described the preparation of fullerenes encapsulating radioisotopes of La, Ho, and Pr.[19] In 1999, Wilson and coworkers published an original study in which they prepared a $^{166}Ho@C_{82}$ derivative as a water-soluble radioactive metallofullerene and a corresponding biodistribution study using BALB/c mice.[20] During the same period, the importance of gadolinium EMFs was also recognized as a potential new nanoplatform for next-generation magnetic resonance imaging (MRI) contrast agents, once again exploiting the inherent property that confines the toxic Gd^{3+} ions inside the robust carbon cage of the EMF. Seminal early works by Shinohara[21,22] and Wilson[23,24] focused on mono-metal EMFs, namely, $Gd@C_{82}$ and $Gd@C_{60}$, with the metallofullerene cage surfaces consisting of negatively-charged carboxyl or hydroxyl groups. These nanoplatforms exhibit 10-40 times higher ^1H relaxivity (r_1) than most

commercial contrast agents.[25] The discovery of the trimetallic nitride template metallofullerene (TNT-EMF) family, $A_{3-x}B_xN@I_h\text{-}C_{80}$, (x = 0-3, A, B = metal), provides a nanoplatform where more than one metal can be encapsulated in the fullerene cage.[26] Another key structural feature of this family is the icosahedral I_h cage which is stabilized by transfer of six electrons from the trimetallic cluster $(A_3N)^{6+}$ to the fullerene cage $(C_{80})^{6-}$. The $Gd_3N@I_h\text{-}C_{80}$ cage is an extraordinarily stable species in which the Gd_3N cluster is non-covalently bound to the $I_h\text{-}C_{80}$ cage with a strong binding energy of 13.63 eV, making it extremely unlikely for the cluster to break and release the Gd^{3+} ions. [27-29] The higher stability of the icosahedral $I_h\text{-}C_{80}$ cage enables efficient chemical separation approaches based on the corresponding lower chemical reactivity of the $A_3N@C_{80}$ families.[30-32] On the other hand, the TNT-EMFs still exhibit sufficient chemical reactivity for a variety of different chemical reactions, including Diels-Alder,[32,33] Bingel-Hirsch,[34-36] Prato,[37-39] and free radical reactions.[40,41] As illustrated in **Figure 1**, both the mono-metallic $Gd@C_{82}$ and trimetallic $Gd_3N@I_h\text{-}C_{80}$ have hydrophobic cage surfaces (~0.8nm d) that are subsequently functionalized with hydrophilic groups (-OH, -COOH) that readily aggregated in aqueous solutions (~30-150 nm d).

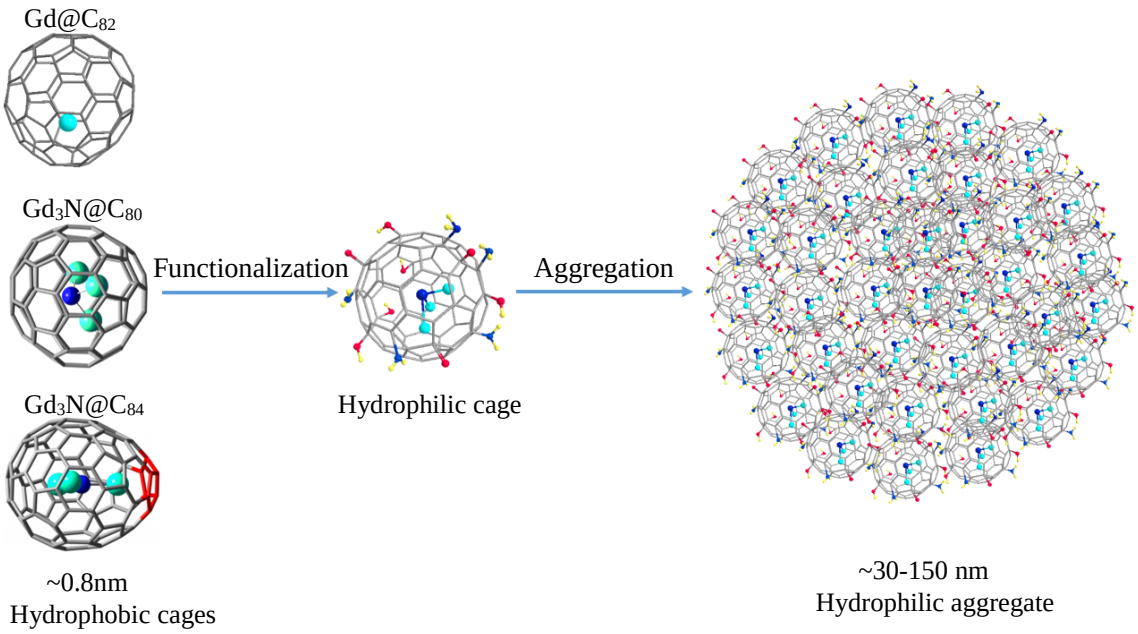

Figure 1. Gd Metallofullerene Nanoparticle Structures.

Since the early 1990's, there has been a widespread clinical application of gadolinium-based MRI contrast agents, employed in 25-50% of all MRI examinations. These clinical MRI contrast agents all have linear or macrocyclic complexation ligands for trapping the Gd^{3+} ions (**Figure 2**). Despite the broad adoption of Gd-based clinical MRI agents, commonly used commercial agents have some deficiencies such as low relaxivity, extracellular distribution, non-specificity, immediate hypersensitivity reactions, and potential release of toxic Gd^{3+} ions. To overcome the problem of low relaxivity, high clinical doses are generally required for efficient diagnosis, which results in enhanced toxicity issues especially for individuals with multiple MR imaging procedures. In 2006, the association between the use of gadolinium-containing contrast agents for MRI and the severe dermal and systemic disease, nephrogenic fibrosing dermopathy/nephrogenic systemic fibrosis (NFD/NSF) was reported for patients with impaired renal function.[34] After the guidelines to avoid the use of Gd-based agents in patients with impaired renal function were adopted, no new NSF cases have been reported.[42] More recently, McDonald and Kanda have reported intracranial gadolinium deposition found on autopsy after contrast-enhanced MR imaging brain

specimens.[43,44] In other work published by Radbruch and coworkers, signal intensity ratio increases indicated a signal-to-noise increase in the dentate nucleu s (DN) and globus pallidus (GP) on T_1-weighted images caused by serial application of gadopentetate dimeglumine.[45] All of these studies found only DN and GP hyperintensity following linear agent administration, but not caused by the macrocyclic agents.[44-46] Very recent work confirmed that even the macrocyclic agent gadoteridol was deposited in healthy brain and bone tissue in patients with normal renal function.[47] These recent studies clearly describe a potential clinical problem of Gd^{3+}

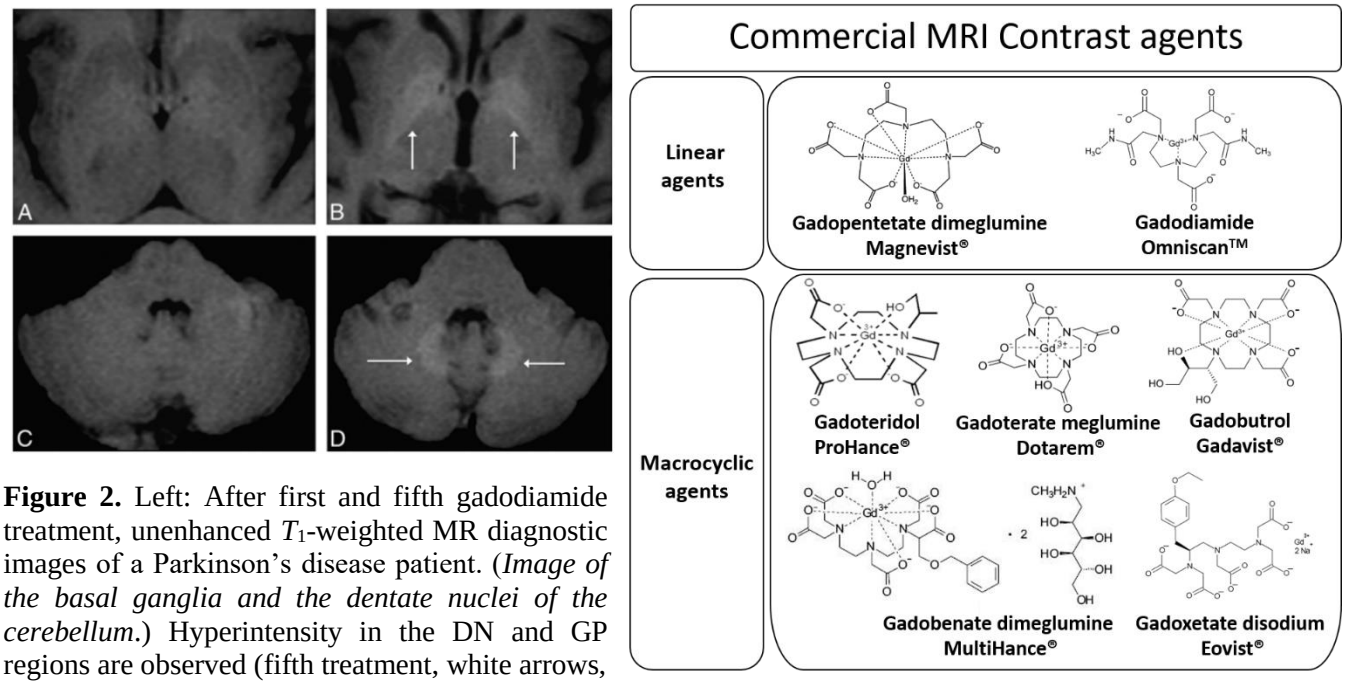

Figure 2. Left: After first and fifth gadodiamide treatment, unenhanced T_1-weighted MR diagnostic images of a Parkinson's disease patient. (*Image of the basal ganglia and the dentate nuclei of the cerebellum*.) Hyperintensity in the DN and GP regions are observed (fifth treatment, white arrows, B and D), undetectable on the first images (A and C). Right: liner and macrocyclic clinical MRI contrast agents. Reprinted with permission from ref 49. Copyright 2015 American Society of Neuroradiology.

ion retention in clinical MRI patients.[44-49] In one example, a 51-year-old female patient with Parkinsonism clearly shows hyperintensity in the DN and GP regions of the brain after multiple MRI examinations utilizing the linear agent gadodiamide (**Figure 2**).[49] Although the long-term and cumulative clinical effects of retained gadolinium are unknown, there is clearly a need for improved high-relaxivity MRI contrast agents that significantly suppress the release of the toxic Gd^{3+} ions and allow for clinical efficacy at reduced dosage levels. The endohedral

metallofullerenes would appear to be leading candidates because the encapsulated Gd^{3+} ions are more efficiently isolated from the bio-environment by the robust fullerene cage. Also, the enhanced MR relaxivity allows equivalent contrast for significantly lower levels of the administered Gd contrast agent.

1.3 Endohedral Metallofullerene Magnetic Resonance Imaging Agents

Due to the advantages of Gd-based metallofullerenes acting as MRI contrast agents, several surface modification methods have been reported, mainly focused on polyhydroxylated, carboxylated, and PEGylated-hydroxylated methods. Some of the functionalized metallofullerenes are summarized in **Figure 3**. It is important to note that the relaxivities in this figure are based on the Gd concentrations typically obtained by ICP-MS measurements, and would be three times higher for the trimetallic nitride endohedral metallofullerenes if based on a per molecule standard.

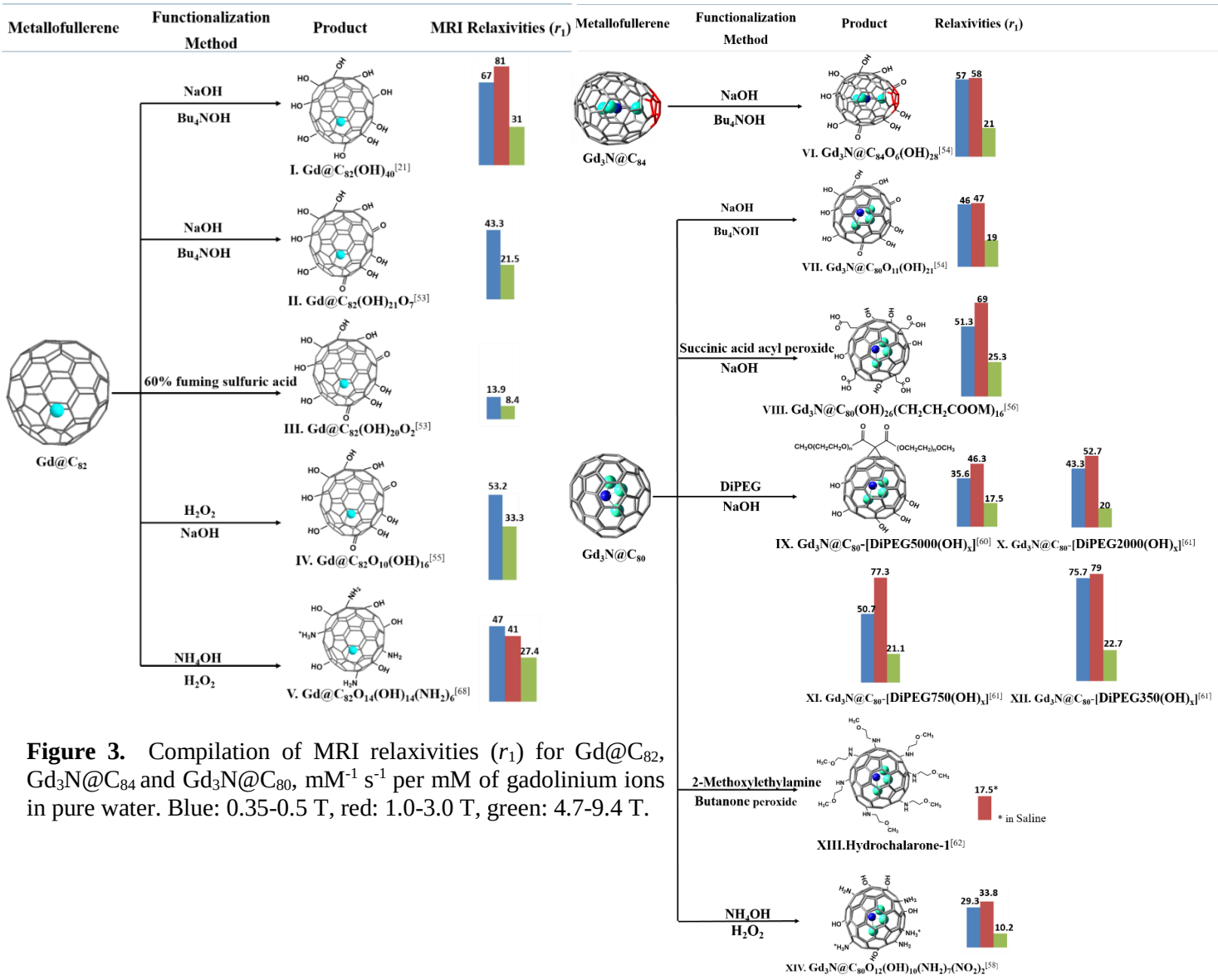

Figure 3. Compilation of MRI relaxivities (r_1) for Gd@C_{82}, Gd_3N@C_{84} and Gd_3N@C_{80}, mM^{-1} s^{-1} per mM of gadolinium ions in pure water. Blue: 0.35-0.5 T, red: 1.0-3.0 T, green: 4.7-9.4 T.

Hydroxylation procedures are the most common methods to convert both fullerene and EMF cage surfaces to a more hydrophilic environment. These functionalization reactions include alkaline reaction conditions[21,50] and the hydrolysis of polycyclosulfated precursors.[51] In an early study, Shinohara and coworkers prepared one of the first polyhydroxylated metallofullerene contrast agents by functionalizing a mono-metal Gd@C_{82} (f-Gd@C_{82}-**I**) with NaOH via a phase-transfer catalysis method.[21] In the case of hydroxylation on the EMF cage surface, differences in the number of groups per cage can lead to different relaxivities of the corresponding EMF contrast

agent by controlling the degree of aggregation, the correlation time, and the number of complexation sites.[52] Zou and coworkers studied the effect of hemiketal formation on the relaxivity of gadofullerenols.[53] Gd@$C_{82}(OH)_xO_y$ with more hemiketals (f-Gd@C_{82}-**II**) exhibited significantly higher relaxivities than those with fewer hemiketals (f-Gd@C_{82}-**III**). Hemiketal groups are readily converted to ketone analogs, with the higher relaxivities due to an increase in electronegative carbonyl groups adjacent to the hydroxyl groups. These more easily form hydrogen bonds among fullerenols. Therefore, the different number of hemiketal groups might affect the aggregation behavior of functionalized gadofullerenes.

To examine how the shape of the EMF cage influences the MR relaxivity, hydroxylated "spherical" $Gd_3N@I_h$-C_{80} and "egg-shaped" $Gd_3N@Cs$-C_{84} with a pentalene motif were investigated.[54] As expected, the ellipsoidal shape and the pentalene motif of the $Gd_3N@C_{84}$ (f-$Gd_3N@C_{84}$-**VI**) system contribute to differences in functionalization, aggregation, and MR relaxivity in comparison with the more spherical $Gd_3N@C_{80}$ system (f-$Gd_3N@C_{80}$-**VII**). Compared with the clinical MRI contrast agents, the relaxivities of both **VI** and **VII** are significantly higher, and do not significantly change in the low-to-mid-field magnetic field strength region, but do decrease at high magnetic fields. It is interesting to note that derivative **VI** exhibits higher ^{1}H MR relaxivity compared with **VII** (**Figure 3**), due to a slightly higher magnetic moment of $Gd_3N@C_{84}$ (11.5 μ_B) than $Gd_3N@C_{80}$ (10.8 μ_B). Other contributing factors to the higher relaxivity of **VI** are higher hydroxyl content, changes in molecular shape, and/or aggregation size. Recently, Gd@$C_{82}O_{10}(OH)_{16}$ (f-Gd@C_{82}-**IV**) was prepared by nucleophilic addition of H_2O_2 under alkaline conditions through a solid–liquid reaction.[55] In comparison with the clinical gadopentetate dimeglumine agent, the f-Gd@C_{82}-**IV** nanoparticles exhibited a much higher r_1 relaxivity at 0.5 T and 7.0 T both *in vitro* and *in vivo.* This mono-metallic metallofullerene derivative was found to

possess a higher effective magnetic moment (8.98 μ_B) when compared with $Gd@C_{82}$ (6.4 μ_B). The significant change in the magnetic moment was ascribed to the chemical derivatization on the carbon cage with a major revision of the highest occupied carbon π-states. These results parallel the results of $Gd_3N@C_{80}$ versus $Gd_3N@C_{84}$ derivative, described above, *vide supra*.

A more facile method to functionalize EMFs in a shorter period has been reported in which $Gd_3N@C_{80}$ reacts with succinyl peroxide to produce a highly water-soluble derivative, $Gd_3N@C_{80}(OH)_{26}(CH_2CH_2COOM)_{16}$ (M = H, Na) (f-$Gd_3N@C_{80}$-**VIII**), in high yield.[56] The carboxyl groups on the fullerenes' surface allow peptide conjugation.[12,57-59]

The first polyethylene glycol (PEG) modified Gd-based trimetallic nitride endohedral metallofullerenes with MRI contrast properties, $Gd_3N@C_{80}$[DiPEG5000$(OH)_x$] (f-$Gd_3N@C_{80}$-**IX**), were reported in 2006.[60] In later studies, different PEG lengths (2000/750/350 Da) were used for metallofullerene functionalization (f-$Gd_3N@C_{80}$-**X, XI, XII**). PEG 350 derivatives have the highest relaxivities among them for both r_1 and r_2 at a clinically relevant magnetic field: 2.4 T. This is due to the larger average aggregation size and less anisotropic rotation (**Figure 3**)[61]. As illustrated in **Figure 4**, the f-$Gd_3N@C_{80}$-**IX** contrast agent exhibits hyperintense T_1-weighted MRI

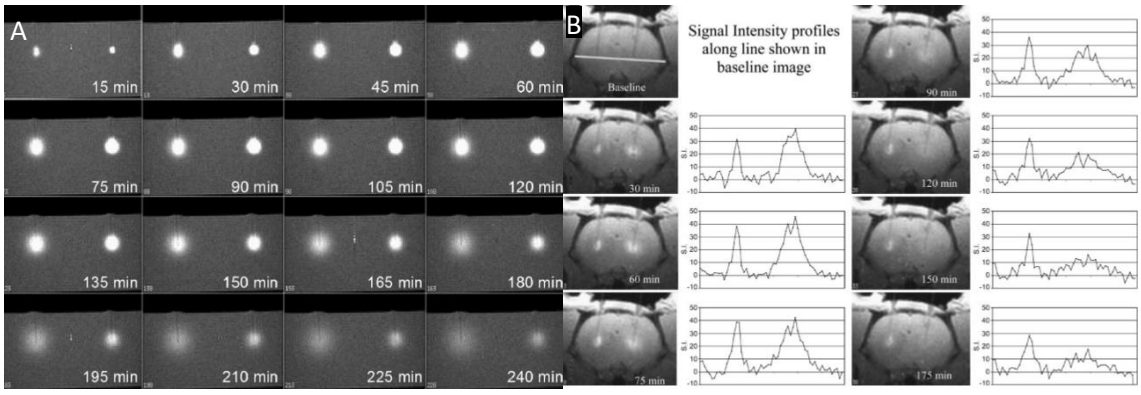

Figure 4. A: T_1-weighted MR images of bilateral infusion into agarose gel of f-$Gd_3N@C_{80}$-**IX** (right) and gadodiamide (left). B: T_1-weighted MR images of bilateral infusion into a normal rat brain of f-$Gd_3N@C_{80}$-**IX** (left) and gadodiamide (right). Reprinted with permission from ref 60. Copyright 2006 Radiological Society of North America.

images in both agarose gel and rat brains at 20-40 times lower concentrations when compared with

gadodiamide. This data also shows the greater diffusion rate and corresponding signal attenuation in both agarose gel and brain tissue of the conventional clinical gadodiamide when compared with the f-$Gd_3N@C_{80}$-**IX**. To demonstrate, the enhanced relaxivity is due nearly exclusively to the paramagnetic $(Gd_3N)^{6+}$ cluster. A slight paramagnetic contribution from the carbon cage, a diamagnetic functionalized lutetium agent, $Lu_3N@C_{80}$[DiPEG5000$(OH)_x$], was also examined and exhibited very low MR relaxivity, as expected.

A different $Gd_3N@C_{80}$ derivative functionalized with monoethyleneglycol was named as *Hydrochalarone* (water relaxer)-1, (f-$Gd_3N@C_{80}$-**XIII**).[62] Hydrochalarone-1 provided higher r_1 relaxivities without significant toxicity, as evaluated through blood immunoassays and *in vivo* acute studies, when compared with the commercial MRI contrast agent gadopentetate dimeglumine. Additionally, Hydrochalarone-1 has a prolonged blood half-life (88 minutes vs. 15 minutes of gadopentetate dimeglumine), suggesting possible application as a blood pool MRI contrast agent, as well as the potential for monitoring the vascular network of tumors.[63] This study clearly shows that nanoparticles, particularly metallofullerenes, have unique properties for biomedical applications. For example, the lack of sufficient lymphatic drainage allows nanoparticles to easily undergo extravasation from the blood pool into tumor tissues.[64,65] The selective accumulation of nano-sized particles near tumor tissues is referred to as the enhanced permeability and retention (EPR) effect.[64,65] Nanoparticles in circulation, because of their surface characteristics and size, are subjected to opsonization and clearance by the mononuclear phagocytic system (MPS).[64,66,67]

Dorn group reported a new functionalization procedure for the TNT-EMF platform by introducing positively-charged ions ($-NH_3^+$) onto the fullerene cage surface, yielding $Gd_3N@C_{80}O_{12}(OH)_{10}(NH_2)_7(NO_2)_2$ (f-$Gd_3N@C_{80}$-**XIV**).[58] It has been previously established that

positively-charged nanoparticles bind more efficiently to negatively-charged phospholipid bilayer cellular surfaces, and will subsequently more readily undergo endocytosis.[68-72] In this paper, the f-$Gd_3N@C_{80}$-**XIV** with a fullerene cage surface consisting of positively-charged amino groups was directly compared with a negatively-charged carboxyl and hydroxyl functionalized derivative. After conjugation with an IL-13 peptide targeting agent, IL-13-f-$Gd_3N@C_{80}$-**XIV** exhibits greater affinity for the brain cancer phospholipid cell membranes.

Cui and coworkers reported a novel method to make gadofullerenes water soluble, by directly noncovalently linking $Gd@C_{82}$ onto graphene oxide (GO) without any covalent fullerene cage surface modification (**Figure 5**).[73,74] This novel structure showed a high relaxation effect (368.7 $mM^{-1}\cdot s^{-1}$ 1.5 T, 439.7 $mM^{-1}\cdot s^{-1}$ 4.0 T). The T_1-weighted MR images of this GO–$Gd@C_{82}$ platform showed dramatic imaging contrast in mice. A new relaxation mechanism was proposed to explain the high relaxivity for the GO–$Gd@C_{82}$ platform. The non-covalent π–π interactions between the GO and Gd nanosheets help to transfer the electron spin density from encaged Gd^{3+} ions to GO, and then to hydrophilic groups on GO nanosheets, which interact with surrounding water protons.

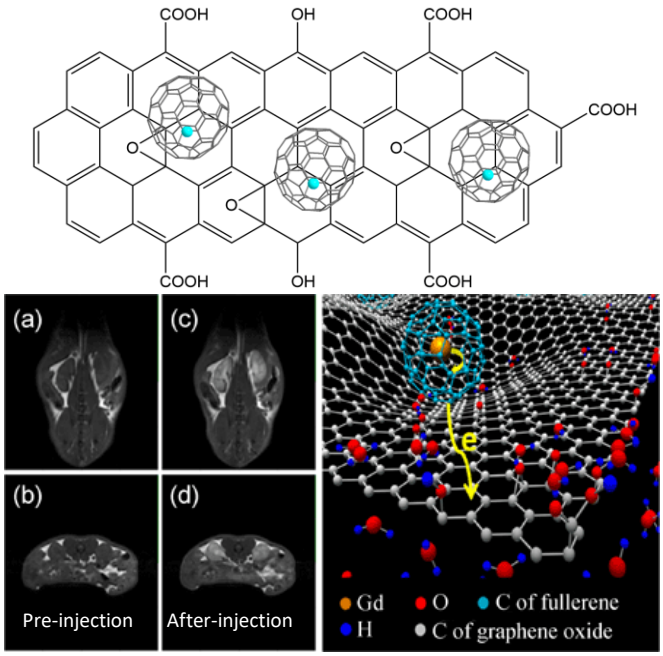

Figure 5. Top: the structure of GO–$Gd@C_{82}$ platform. Bottom: *In vivo* MR imaging demonstrated the great contrast ability of GO–$Gd@C_{82}$. A "secondary spin-electron transfer" relaxation mechanism was proposed to explain the high relaxivity for the GO–$Gd@C_{82}$ platform. Reproduced with permission from ref 74. Copyright 2015 Tsinghua University Press and Springer-Verlag Berlin Heidelberg.

One inherent advantage of the metallofullerene platform is facile functionalization as a contrast agent for dual modality diagnostic approaches. As one example, positron emission tomography

(PET) and MRI have already been merged (PET/MRI) as a dual diagnostic clinical approach. The anatomical and functional information is provided by MRI while the PET approach provides higher sensitivity with spatial location of the radiolabel. As one example, a dual PET/MRI metallofullerene agent based on ^{124}I (PET) radiolabeled $Gd_3N@C_{80}$ (MRI) nanoprobe platform has been reported. [75] In this case, the outer fullerene surface was functionalized with carboxyl and hydroxyl groups and subsequently iodinated with ^{124}I to produce a ^{124}I–f-$Gd_3N@C_{80}$ nanoprobe. Preliminary murine dual imaging results were reported for this agent. In another approach, Zheng and coworkers reported the functionalization of $Gd@C_{82}$ utilizing an ammonium hydroxide/hydrogen peroxide solution in a facile one-step reaction under mild conditions. The functionalized gadofulleride $Gd@C_{82}O_{14}(OH)_{14}(NH_2)_6$ (f-$Gd@C_{82}$-**V**) also exhibits higher MR relaxivity than commercial agents and has multi-wavelength emission features which could be important for dual-modality clinical applications. [76] Specifically, the functionalized $Gd@C_{82}$ exhibits cyan fluorescence in solution under UV irradiation at 365 nm, and could be a candidate for bimodal *in vitro* multi-wavelength imaging applications. It should be noted that the mechanism for the generation of the fluorescence phenomena for these functionalized nanoparticles needs further study.

1.4 Targeting Endohedral Metallofullerene Nanoparticles

Although most clinical MRI contrast agents employed to date are not designed for cellular targeting applications, target-selective metallofullerene MRI contrast agents functionalized with the appropriate peptides or other targeting ligands could have distinct advantages because of their high MR relaxivity by functionalizing EMFs with the relevant peptides or other ligands. Specific cancer cell peptide-targeting $Gd@C_{82}$ and $Gd_3N@C_{80}$ MRI contrast agents have been recently reported. The receptor site of cytokine interleukin-13 (IL-13) has been shown to be over-expressed

in human brain glioblastoma multiforme (GBM) cell lines, whereas it is not over-expressed in normal brain tissue. The receptor for IL-13 in glioma cells has been identified as the IL-13Rα2 receptor.[77-80] Since GBM has the worst prognosis of any central nervous system (CNS) malignancy, with a median survival rate of slightly over one year, the development of better MRI contrast agents for early GBM diagnosis is an important area of study. Fillmore and coworkers have demonstrated successful conjugation of the IL-13 peptide to $Gd_3N@C_{80}(OH)_{26}(CH_2CH_2COOM)_{16}$ (IL-13-f-$Gd_3N@C_{80}$-**VIII**) by EDC/NHS amide formation with the carboxyl groups on the EMF cage surface. This targeted EMF exhibits enhanced cellular uptake in a U-87MG cell line when compared with the control EMF, f-$Gd_3N@C_{80}$-**VIII** without the IL-13 targeting peptide. The increased uptake reflects an enhanced specificity of the targeted EMF for the human glioma cells expressing IL-13Rα2. A drawback to this study is the invasive intracranial delivery approach, which is not readily amenable to most clinical MR procedures.

More recently, Li et al.[58] reported a murine study utilizing intravenous delivery of a targeting EMF nanoparticle, $Gd_3N@C_{80}O_{12}(OH)_{10}(NH_2)_7(NO_2)_2$ (IL-13-f-$Gd_3N@C_{80}$-**XIV**), with an amino-coated metallofullerene cage surface bearing positively-charged amino groups ($-NH_3^+$). This amino-coated nanoparticle was directly compared with a similar targeting nanoparticle with cage surface negatively-coated carboxyl and hydroxyl groups (**Figure 6A**). As previously described, it is well known that nanoparticles with a positive charge will bind more efficiently to negatively-charged phospholipid bilayer cellular surfaces, thereby more readily enabling endocytosis.[68-72] In this study, a more invasive U-251 cell line was employed, as this cell line has the highest expression of IL-13Rα2 receptor sites of all GBM cell lines and is histologically similar to human GBM.[62,81] Confocal microscopy results showed both nanoparticles were internalized by the U-251 cell line with a clear preference for localization in the nucleus for both the IL-13-f-

$Gd_3N@C_{80}$-**XIV** and IL-13-f-$Gd_3N@C_{80}$-**VIII**, but with greater intensity in the former case, illustrating the importance of the surface amino groups. In direct fluorescence quantitation measurements, there was a slight preponderance of IL-13-f-$Gd_3N@C_{80}$-**XIV** in the cytoplasm and cell membrane, but a significant enhancement in the nucleus in comparison with cells treated with IL-13-f-$Gd_3N@C_{80}$-**VIII** (**Figure 6B**). Thus, the nanoparticles coated with amino groups have high cell membrane binding affinity, and readily allow translocation across the plasma membrane undergoing endocytosis. To demonstrate the potential clinical MRI feasibility of the surface-coated amino nanoparticles, a 3T MRI Siemens scanner was employed in this study. The MR images clearly showed it is possible to track the contrast agent with both T_1-weighted imaging characteristics. It shows high signal intensity with 50 ms inversion recovery times (bright tumor area), whereas T_2-weighted imaging is illustrated for 1000 ms inversion recovery times where low signal intensity is observed (dark tumor area). This is because the relaxivity ratio (r_1:r_2) is in a range that allows for T_1 enhancement while not over-shortening T_2 and quenching the signal at low inversion recovery times, but quenching the signal at high inversion recovery times.[60,82] As a control, a mouse without an implanted tumor was included for comparative purposes. The IL-13-f-$Gd_3N@C_{80}$-**XIV** nanoparticle showed the sharp definition of the tumor region in contrast with the indistinct tumor delineation of the control gadopentetate dimeglumine even at 1-2 orders of magnitude lower concentration. These results provide evidence that the nanoparticles IL-13-f-$Gd_3N@C_{80}$-**XIV** can be delivered by a less-invasive intravenous injection approach with precise targeting of GBM U-251 mice brain tumor models, and can be visualized at relatively low concentrations in a clinical MRI scanner (**Figure 6C-E**).

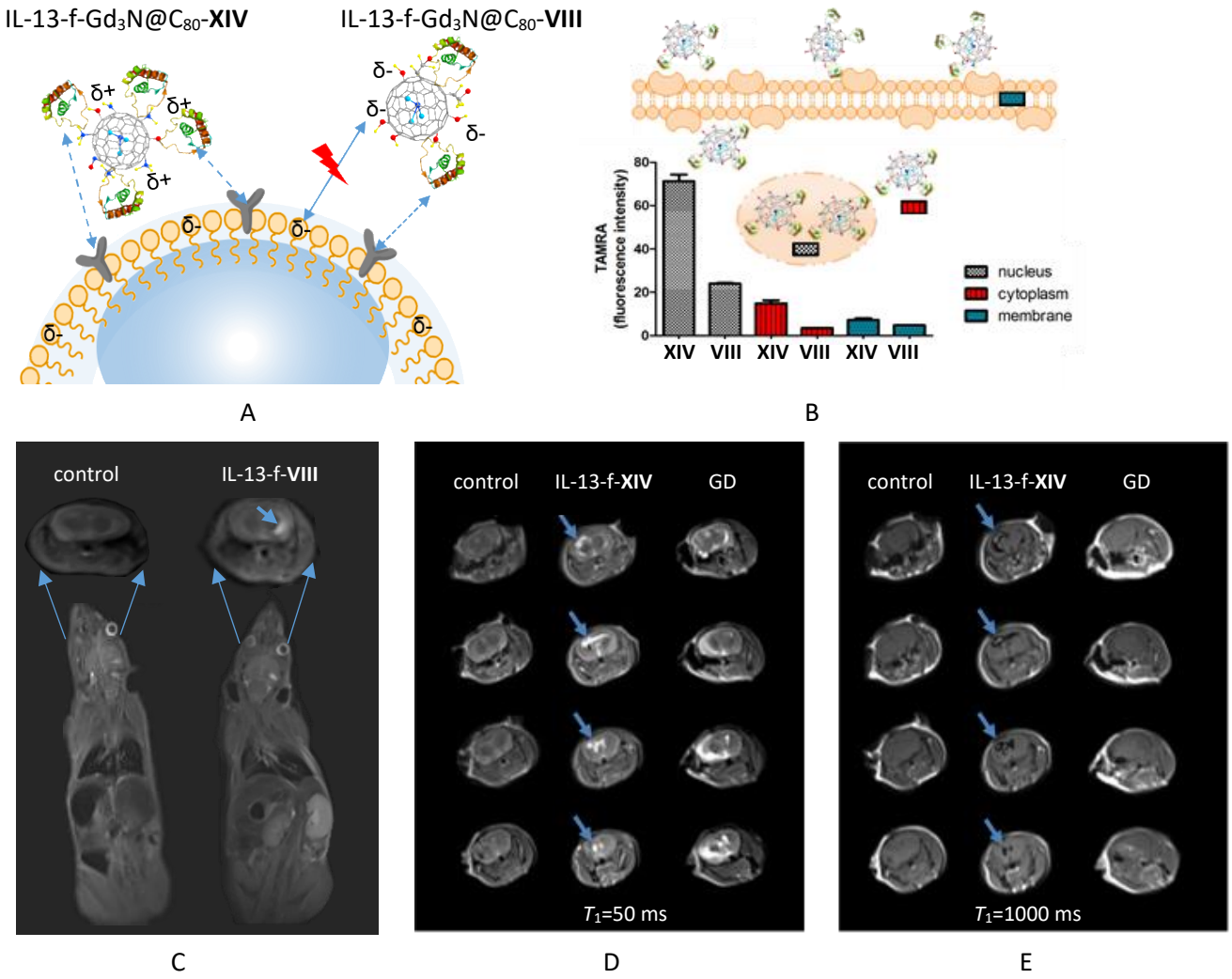

Figure 6. A: The IL-13-f-$Gd_3N@C_{80}$-**XIV** nanoparticle with positive charges illustrating facile binding to a negatively charged phospholipid bi-layer cellular surfaces. B. Translocation of IL-13-f-Gd_3N@C80-**XIV** (**XIV**) and IL-13-f-Gd_3N@C80-**VIII** (**VIII**) in U-251 cells. C: Clinical MRI 3T coronal slice and body images of orthotopic GBM murine models with intravenous delivery of IL-13-f-Gd_3N@C80-**VIII** and with no targeting contrast agent administered. D and E: *In vivo* imaging following intravenous delivery of IL-13-f-Gd_3N@C80-**XIV** left: MRI of a mouse brain without tumor as control; middle: MRI of 15 minutes after intravenous injection of IL-13-f-Gd_3N@C80-**XIV**; right: MRI of 15 minutes after intravenous injection of gadopentetate dimeglumine (GD) commercial contrast agent. Arrows indicate the location of tumor. Reproduced with permission from ref 58. Copyright 2015 American Chemical Society.

In a cardiovascular application of targeting EMFs, Dellinger and coworkers have synthesized an atherosclerotic-targeting contrast agent (ATCA) in which $Gd_3N@C_{80}$ was functionalized and formulated into liposomes with a CD36 peptide ligand intercalated into the lipid bilayer. [83] The ATCA exhibited time-dependent accumulation in atherosclerotic plaque lesions of mice, as determined using cardiovascular magnetic resonance.

In a specific cell-targeting approach, Murphy and coworkers utilized hydroxylated $Gd_3N@C_{80}$ for the non-invasive longitudinal tracking of stem cells in the lung. [84] In this study, the MRI contrast

agents were passively uptaken by the amniotic fluid stem (AFS) cells (**Figure 7A, B**). The AFS cells were infected with a lentivirus expressing luciferase genes, which co-labeled the cells with the contrast agent and performed both MR and bioluminescence imaging methods on the same cell populations. The cells were administrated into the lungs by intratracheal intubation. The *in vivo* studies demonstrate that the $Gd_3N@C_{80}(OH)_n$ MRI contrast agent-labeled stem cells can be

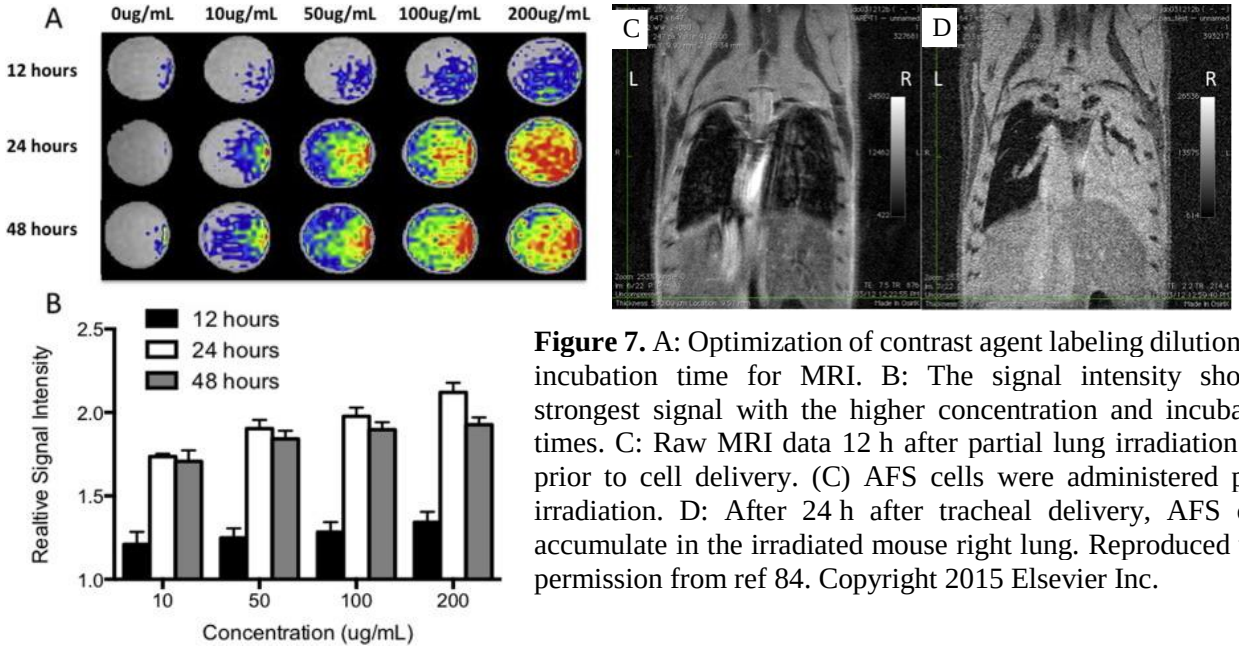

Figure 7. A: Optimization of contrast agent labeling dilution and incubation time for MRI. B: The signal intensity showed strongest signal with the higher concentration and incubation times. C: Raw MRI data 12 h after partial lung irradiation and prior to cell delivery. (C) AFS cells were administered post-irradiation. D: After 24 h after tracheal delivery, AFS cells accumulate in the irradiated mouse right lung. Reproduced with permission from ref 84. Copyright 2015 Elsevier Inc.

administered and tracked within lung tissue (**Figure 7C, D**). These findings can be performed as future pre-clinical applications of this imaging methodology to answer various questions about the optimum timing of administration, cell location, and cell viability over time.

1.5 Therapeutic Approaches for Endohedral Metallofullerenes

Since the cage of the fullerene is highly stable, the radiolabeled metals can be encapsulated in the carbon cage for therapeutic applications. Additionally, metallofullerenes can be used as anti-cancer drugs, with low toxicity by different mechanisms. A promising approach for selective irradiation of tumors is neutron capture therapy (NCT). The most common method uses boron compounds due to the reasonably high neutron capture cross-section. Boron neutron capture therapy (BNCT) is a new approach for the treatment of intractable tumors (i.e., brain tumors) and is currently in clinical trials.[85] Compared with BNCT with ^{10}B, GdNCT has the inherent advantage, ^{155}Gd and ^{157}Gd have much higher neutron capture cross-sections.[86,87] In a study by Horiguchi and coworkers, poly(ethylene glycol)-block-poly(2-(*N*,*N*-diethylamino)ethyl methacrylate) (PEG-*b*-PAMA) was utilized to solubilize Gd@C_{82}.[88] The presence of the PEG-*b*-PAMA avoids covalent derivatization forming a transparent compound. Gd@C_{82}-PEG-*b*-PAMA-complexed nanoparticles showed sufficient cytotoxicity. Neutron irradiation of colon-26 cells dosed with Gd@C_{82} induces cell death, indicating the emission of gamma rays and conversion electrons upon

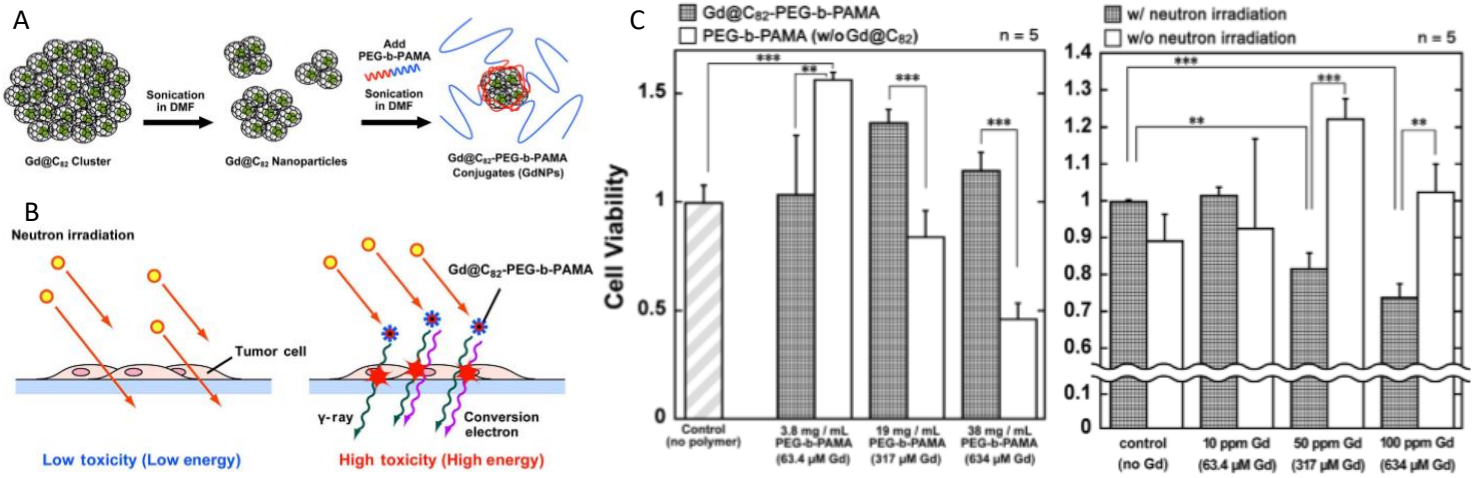

Figure 8. A: Schematic of the preparation process of GdNPs. B: Illustration of neutron irradiation of culture cells with (right) and without (left) GdNPs. C: Cell viability determined by the WST-assay. GdNPs showed extremely low toxicity *in vitro* without neutron irradiation, and remarkable difference in cell viability with after irradiation. Reproduced with permission from ref 88. Copyright 2011 IOP Publishing.

the neutron capture reactions of ^{155}Gd and ^{157}Gd. The cytotoxicity data results suggest fullerene cages remain intact after neutron irradiation (**Figure 8**). GdNCT with bioimaging could evolve as a high-performance frontier "theranostic" because MRI can monitor the spatial location and bio-distribution of the GdNCT agent.

In other studies, the ^{177}Lu radionuclide has emerged as a potential radioisotope for therapeutic applications due to its ideal nuclear characteristics: half-life of 6.61 days, beta-emitter at 497 keV, gamma-emitter at 208 keV (11%) and 113 keV (6.4%). [89] The gamma emission of this nuclide allows diagnostic single-photon emission tomography (SPECT) imaging for evaluation of localization, biokinetics, and targeting applications. The low-energy beta radiation allows soft tissue penetration of only 2-3 mm. These low energies guarantee dose-localized delivery to the immediate cellular environment, suggesting best use following molecular targeting. The Dorn laboratory and collaborators have reported two radiolabeled functionalized metallofullerenes $^{177}Lu_xLu_{(3-x)}N@C_{80}$ and ^{177}Lu-DOTA-f-$Gd_3N@C_{80}$.[59,90] $^{177}Lu_xLu_{(3-x)}N@C_{80}$ was prepared by using a modified Krätschmer-Huffman apparatus to encapsulate the $^{177}Lu^{3+}$ in the fullerene cages. In comparison to other exohedral radiolanthanide EMFs, this platform encapsulated the radionuclide atoms or clusters inside fullerene cages, protecting the radioactive metal ion and completely isolating it from the biosystem, with the encaged $^{177}Lu^{3+}$ ions demonstrated lack of release for at least one half-life. Subsequently, $^{177}Lu_xLu_{(3-x)}N@C_{80}$ was conjugated with IL-13 to target overexpressed receptor cells in GBM.[59] A multi-modal nanoplatform (^{177}Lu-DOTA-f-$Gd_3N@C_{80}$) was developed in 2011 by functionalized $Gd_3N@C_{80}$ with carboxyl groups, then radiolabeled with ^{177}Lu and tetraazacyclododecane tetraacetic acid (DOTA), to provide an anchor to deliver effective brachytherapy and enable longitudinal tumor imaging.[82] This agent showed increased murine GBM models' median survival, even up to 100 days with long-term diagnostic

MRI (**Figure 9**).[90] These two nanoparticle platforms provided the potential ability to meet a broad range of other radiotherapeutic and radiodiagnostic applications. Additionally, the co-treating agents can be selected to increase the tumor specificity of the therapy and reduce the possibility of normal tissue damage.

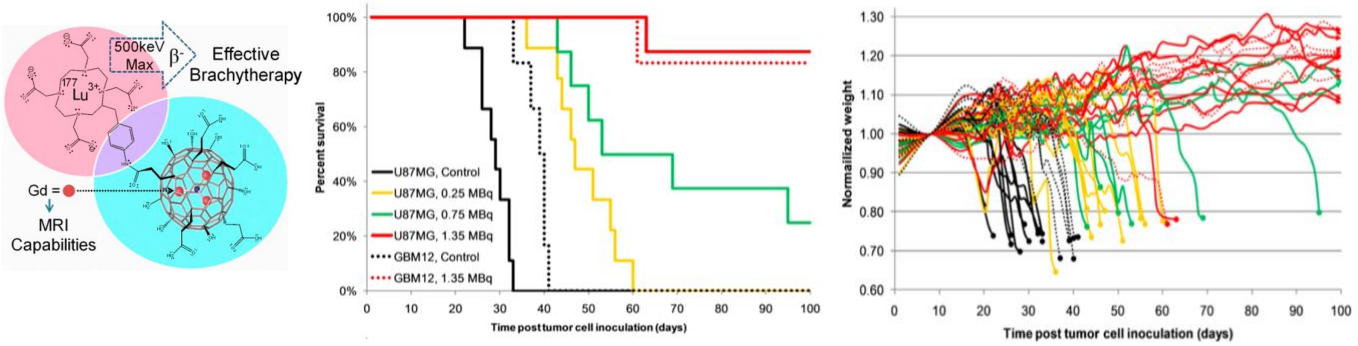

Figure 9. Left: Exohedral radiolabeling of TNT-EMF derivatives. Middle: Survival studies verify efficacy of the ^{177}Lu-DOTA-f-$Gd_3N@C_{80}$ in U87MG and GBM12. Right: Weights of the mice during the survival studies normalized to the day of treatment or control infusion. Reproduced with permission from ref 90. Copyright 2012 American Chemical Society.

Compared with the previously reported method,[59] Zhang and coworkers reported a facile method to prepare $^{177}Lu_xLu_{(3-x)}N@C_{80}$ by direct irradiation of $Lu_3N@C_{80}$ with a neutron flux.[91] The neutron-activated nanoparticle was modified with PGE-5000. The polyethylene was helpful in assisting nanoparticles to escape the endothelial system and prolonging the materials' blood circulation time. Moreover, the particle size (~144nm) might give nanomaterials the property of passive tumor targeting. Biodistribution results indicated that $^{177}Lu_xLu_{(3-x)}N@C_{80}$–PCBPEG (PCBM: 1-(3-methoxycarbonyl)propyl-1-phenyl-[6,6]-methanofullerene) has a long blood circulation time (up to 48 h postinjection) and outstanding tumor-targeting properties, which would have potential in tumor therapeutic applications.

Antineoplastic and radical scavenging properties for the metallofullerene platforms have been reported. Numerous studies have demonstrated the free radical scavenging capabilities of fullerenes, to such a degree that fullerenes have been described as "free radical sponges."[92-96] In work by Zheng and coworkers, $Gd@C_{82}O_{14}(OH)_{14}(NH_2)_6$ can efficiently scavenge •OH

radicals.[68] The active hydroxyl radical can attack the electron-deficient areas on the carbon cage surface or be stabilized by forming hydrogen bonds with the proximate hydroxyl protons of functionalized Gd@C_{82}. In other studies, researchers have shown that polyhydroxylated fullerenols, specifically Gd@$C_{82}(OH)_{22}$, have low toxicities and directly suppress the growth of several tumors. Gd@$C_{82}(OH)_{22}$ can work as non-toxic cancer stem cells (CSCs) specific inhibitors with significant therapeutic potential. Gd@$C_{82}(OH)_{22}$, while mostly non-toxic to normal mammary epithelial cells, has been shown to possess intrinsic inhibitory activity against triple-negative breast cancer cells. [97-101] In other work, Gd@$C_{82}(OH)_{22}$ was applied to block epithelial-to-mesenchymal transitions with the resultant efficient elimination of breast CSCs resulting in abrogation of tumor initiation and metastasis.[99] Moreover, Gd@$C_{82}(OH)_{22}$ can suppress pancreatic cancer metastasis by inhibiting MMP-2/9 expression and activity.[98,100,102] Adoptive immunotherapy is a highly effective approach for cancer treatment in which fullereneols can be used as drugs that regulate the immune system and eliminate cancers.[4,103] Several studies suggest that Gd@$C_{82}(OH)_{22}$ can control the production of reactive oxygen species to induce cancer cell death. The Gd@$C_{82}(OH)_{22}$ can activate the macrophages, enhance macrophage cell viability, increase phagocytosis, and significantly enhance the secretion of multi-cytokines related to cancer. Gd@$C_{82}(OH)_{22}$ was shown to have stronger ability than $C_{60}(OH)_{22}$ to improve the macrophage function due to the difference in distinct geometrical and physical properties.[101] Common activators of macrophages include LPS or INF-γ, but safety issues and durability limit their use. The fullerenols can be used in place of LPS or INF-γ to stimulate the macrophage-mediated immune response continuously.

The hydroxylated Gd@C_{82} can inhibit tumor cell growth effectively with low toxicity and high antineoplastic activity; no important observable organs are known to be impaired by

$Gd@C_{82}(OH)_{22}$. Compared with traditional anticancer drugs, the proper surface functionalization could reduce or reverse the toxic response of nanoparticles.[104]

In an unusual therapeutic application, certain crystalline gadofullerenes ($Gd@C_{82}$ polycrystals) have size-expansible phase transition under heating.[24,68] Zheng and coworkers observed that, after continuously irradiating by a 200 MHz pulsed RF, the size of the gadofullerenes was found to expand from 136±7 to 204±10 nm.[105] Thus, water-soluble $Gd@C_{82}$ can be applied as a new potent tumor vascular targeting therapeutic technique for solid cancers by cutting off the nutrient supply of tumor cells to physically destroy the abnormal tumor blood vessels (**Figure 10**).

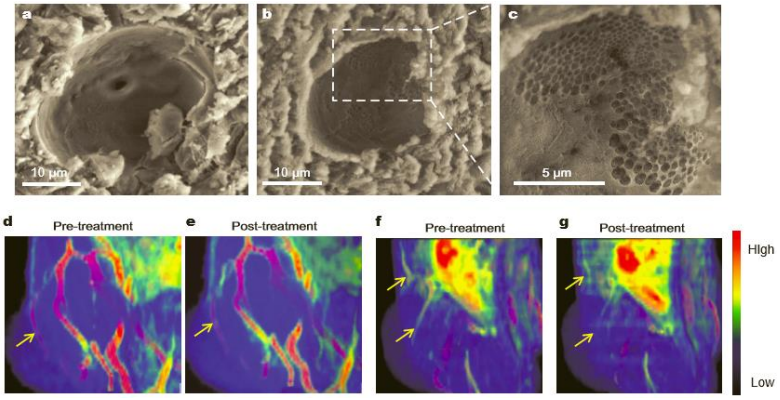

Figure 10. Top: The observation of tumor blood vessels. The endothelial cells were chipped off from the basilemma at 24 h after the treatment (c). Bottom: The MRA images of tumor vascular (yellow arrows) exhibited identifiable reduction of the arterial vessels flowing to the tumor. Reprinted with permission from ref 105. Copyright 2015 Science China Press and Springer-Verlag Berlin Heidelberg.

1.6 Toxicity, Stability, and Biodistribution of Endohedral Metallofullerenes

To date, there is a paucity of studies regarding the toxicity and pharmacological properties of EMFs. For the trimetallic nitride endohedral metallofullerene, Ehrich and coworkers have demonstrated the low cytotoxicity of the hydroxylated TNT-EMFs in a cell viability study of hen brain and human neuroblastoma SH-SY5Y cells (**Figure 11A**).[6] In a study by Murphy and coworkers, amniotic fluid stem cells were incubated with different concentrations of

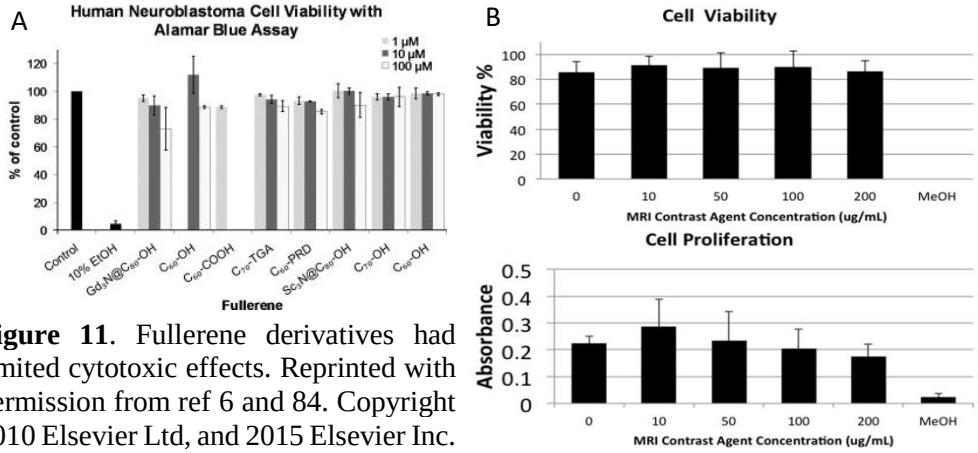

Figure 11. Fullerene derivatives had limited cytotoxic effects. Reprinted with permission from ref 6 and 84. Copyright 2010 Elsevier Ltd, and 2015 Elsevier Inc.

$Gd_3N@C_{80}(OH)_n$ for 48 hours. The results indicated that, at all concentrations evaluated, the culture and uptake of the contrast agent had no effect on cell viability, proliferation, or induction of cellular stress responses (**Figure 11B**).[84] Fillmore and coworkers performed cellular uptake studies of IL-13-$Gd_3N@C_{80}$-**VIII** and $Gd_3N@C_{80}$-**VIII** in human glioma U-87MG cells. Compared with the control, the cell viability was not affected by either agent at 3 hours and 6 hours post-incubation.[57] In Dellinger et al.'s study, the ATCA injection was well tolerated, did not demonstrate toxicity *in vitro* or *in vivo*, and no accumulation was observed in the major organs.[83]

Physicochemical properties, such as the surface functionalization, can strongly affect the interaction of nanoparticles with biological systems, thus ultimately influencing their cell uptake, translocation biodistribution, bioelimination, and biology effect. The positively-charged metallofullerenes ($-NH_3^+$) have a higher rate of cell uptake, higher nonspecific internalization rate, and shorter blood circulation half-life compared to neutral or negatively-charged metallofullerenes (-OH, -COOH). The carboxylated $Gd_3N@C_{80}$ (f-$Gd_3N@C_{80}$-**VIII**) and PEGylated-hydroxylated $Gd_3N@C_{80}$ (f-$Gd_3N@C_{80}$-**IX** and **XII**) can be detected in the rat brain glioma tumor seven days post-injection, indicating they can work as long-term diagnostic agents.[56,61] In earlier animal studies, water-soluble metallofullerenes functionalized with hydroxyl or carboxyl groups without specific targeting agents generally localize in the reticuloendothelial system (RES), such as liver

and kidney, because of these nanoparticles are recognized by reticuloendothelial cells, with continued slow but steady clearance over 5 to 7 days.[20,21,23,82] In other studies, C_{60}-COOH and C_{60}-OH showed a decrease in the accumulation level and distribution rate when compared with pristine C_{60}.[106] However, surprisingly although the functionalized fullerene C_{60} and the monometallic metallofullerene Gd@C_{82} have similar chemical structures, their biodistribution is distinctly different *in vivo*. In a study, the biodistribution and metabolism of functionalized fullerenes C_{60} and the monometallic metallofullerene Gd@C_{82} radiolabeled with a chelator for ^{64}Cu that was monitored by PET. The biodistribution and the excretion indicated that the C_{60} samples have higher blood retention and lower renal clearance than the Gd@C_{82} radiolabeled sample *in vivo* and suggested that the differences in metabolism and distribution were caused by the structural differences of the groups on the fullerene cages though there is chemical similarity.[107] Thus, surface functionality and differences in the fullerene cage structure are critical parameters in controlling the biodistribution, and can be used to improve the biocompatibility of metallofullerenes.

Additionally, particle size and conjugation with targeting ligands are other key factors in the biodistribution of long-circulating nanoparticles and the achievement of therapeutic efficacy, such as the long blood circulation time and outstanding tumor-targeting properties of $^{177}Lu_xLu_{(3-x)}N@C_{80}$–PCBPEG *vide supra*.[91]

An indirect method was reported to study the fullerene cage stability. The biodistributions of Gd@$C_{82}(OH)_{22}$ nanoparticles and $GdCl_3$ were investigated in mice. The polyhydroxylated metallofullerenes, with high biostability, were mainly delivered to lung, liver, spleen, and kidney via intravenous administration. The different organ accumulation levels suggest that the fullerene cage was not destroyed during metabolism in mice, and free Gd^{3+} was not released into the tissues

by $Gd@C_{82}(OH)_{22}$ nanoparticles.[108] However, to date, no comprehensive study has been reported that directly determines if free Gd^{3+} has escaped from the fullerene cage. Therefore, the stability of the carbon cage of functionalized EMFs *in vitro* and *in vivo* needs more exhaustive study.

1.7 Metallofullerenes Challenges and Future Outlook

In spite of the optimistic view of metallofullerenes for-next generation biomedical applications, some formidable obstacles must still be overcome. For example, the synthetic production yields of metallofullerenes are very low and typically less than 1% in the usual electric-arc batch reactor. This approach employs a Krätschmer-Huffman two-electrode in-line arc discharge reactor with packed graphite electrodes.[109] In one recent study with an improved yield, a 5% yield of $Gd@C_{82}$ was obtained by optimizing the He gas pressure in the electric-arc reactor.[47] Another significant improvement, in this regard, for the preparation of the TNT-EMFs is a continuous-feed 3-phase electric arc system by Bezmelnitsyn and coworkers that continuously cycles the reactants through the 3-phase electric arc.[109] This recent significant production improvement, coupled with the development of efficient chemical separation procedures, improves the availability of TNT-EMFs significantly, but the cost and yield still represent a major problem, limiting research exploration and future clinical utilization.[3,8,12,111]

As previously indicated, the major clinical problem with current linear and macrocyclic Gd-containing MRI contrast agents is the low relaxivity and established loss of Gd^{3+} ions (in certain cases) to surrounding tissue (e.g., brain and bone). The EMF MRI contrast agents *vide supra* clearly exhibit 2-3 orders of magnitude better relaxivity than the current clinical agents. This helps alleviate, but does not eliminate, potential concerns of the adverse effects of Gd-based toxicity. More importantly, although the pristine metallofullerene cage is very robust, functionalized metallofullerenes with sp^3 hybridized carbons on the cage surface are undoubtedly less stable.

Detailed *in vitro* and *in vivo* studies are needed to demonstrate that the encapsulated Gd^{3+} or trimetallic nitride cluster $(Gd_3N)^{6+}$ ions of Gd-EMFs stay completely encapsulated and isolated from the bio-environment. As illustrated, the spherical EMF sp^2 hybridized carbon cage is very amenable to functionalization to convert the hydrophobic cage surface to a more hydrophilic surface as well as covalently attach different targeting peptides. The endohedral encapsulated lanthanide metal can also be readily changed, for example, ^{177}Lu and ^{166}Ho for radionuclides, Gd and Er for fluorescence, and Gd for MR imaging providing a multi-modal platform for both diagnostic and therapeutic ("theranostic") applications. As previously described, numerous studies have demonstrated the free radical scavenging capabilities of not only fullerenes but also metallofullerenes. The antineoplastic and radical scavenging properties for the metallofullerene platforms are an additional biomedical application approach that needs further study before clinical use. Moreover, due to the usual presence of a different number of functional groups on the carbon cage for the metallofullerene MRI agents described in this review, a challenge is to develop "single molecule" contrast agents because of potential toxicity issues. This challenge is compounded by the clinical desire for total body clearance of Gd-based MRI contrast agents *vide supra*. Finally, specific targeting, multi-modality, and therapeutic agents are also important goals for future development of the metallofullerene platforms for clinical applications. In spite of these challenges, the metallofullerene could evolve as an important molecular platform for future clinical applications.

References

[1] L. Dunsch, S. Yang, *Small* **2007,** *3*, 1298.

[2] M. N. Chaur, F. Melin, A. L. Ortiz, L. Echegoyen, *Angew. Chem., Int. Ed.* **2009,** *48*, 7514.

[3] H. C. Dorn, P. P. Fatouros, *Nanosci. Nanotechnol. Lett.* **2010,** *2*, 65.

[4] J. Meng, D.L. Wang, P. C. Wang, L. Jia, C. Y. Chen, X. J. Liang, *J. Nanosci. Nanotechnol.* **2010,** *10*, 8610.

[5] J. W. M. Bulte, *Radiology* **2011,** *261*, 1.

[6] M. Ehrich, R. Van Tassell, Y. Li, Z. Zhou, C. L. Kepley, *Toxicol. In Vitro* **2011,** *25*, 301.

[7] A. Rodriguez-Fortea, A. L. Balch, L. M. Poblet, *Chem. Soc. Rev.* **2011,** *40*, 3551.

[8] X. Lu, L. Feng, T. Akasaka, S. Nagase, *Chem. Soc. Rev.* **2012,** *41*, 7723.

[9] P. P. Fatouros, M. D. Shultz, *Nanomedicine (London, U. K.)* **2013,** *8*, 1853.

[10] A. A. Popov, S. Yang, L. Dunsch, *Chem. Rev.* **2013,** *113*, 5989.

[11] M. Sergio, H. Behzadi, A. Otto, D. van der Spoel, *Environ. Chem. Lett.* **2013,** *11*, 105.

[12] J. Y. Zhang, S. Stevenson, H. C. Dorn, *Acc. Chem. Res.* **2013,** *46*, 1548.

[13] K. B. Ghiassi, M. M Olmstead, A.L. Balch, *Dalton Trans.* **2014,** *43*, 7346.

[14] C. Kepley, A. Dellinger, *Toxicol. Sci.* **2014,** *141*, 325.

[15] X. Lu, L. Bao, T. Akasaka, S. Nagase, *Chem. Commun. (Cambridge, U. K.)* **2014,** *50*, 14701.

[16] T. Wang, C. Wang, *Acc. Chem. Res.* **2014,** *47*, 450.

[17] K. Kikuchi, K. Kobayashi, K. Sueki, S. Suzuki, H. Nakahara, Y. Achiba, K. Tomura, M. Katada, *J. Am. Chem. Soc.* **1994,** *116*, 9775.

[18] K. Sueki, K.Akiyama, Y. L. Zhao, I. Ito, Y. Ohkubo, K. Kikuchi, M. Katada, H. Nakahara, *J. Radioanal. Nucl. Chem.* **2003,** *255*, 159.

[19] T. Braun, H. Rausch, *Chem. Phys. Lett.* **1998,** *288*, 179.

[20] D. W. Cagle, S. J. Kennel, S. Mirzadeh, J. M. Alford, L. J. Wilson, *Proc. Natl. Acad. Sci. U. S. A.* **1999,** *96*, 5182.

[21] M. Mikawa, H. Kato, M. Okumura, M. Narazaki, Y. Kanazawa, N. Miwa, H. Shinohara, *Bioconjugate Chem.* **2001,** *12*, 510.

[22] H. Kato, Y. Kanazawa, M. Okumura, A. Taninaka, T. Yokawa, H. Shinohara, *J. Am. Chem. Soc.* **2003,** *125*, 4391.

[23] R. D. Bolskar, A. F. Benedetto, L. O. Husebo, R. E. Price, E. F. Jackson, S. Wallace, L. J. Wilson, J. M. Alford, *J. Am. Chem. Soc.* **2003,** *125*, 5471.

[24] B. Sitharaman, R. D. Bolskar, I. Rusakova, L. J. Wilson, *Nano Letters* **2004,** *4*, 2373.

[25] M. Rohrer, H. Bauer, J. Mintorovitch, M. Requardt, H. J. Weinmann, *Invest. Radiol.* **2005,** *40* , 715.

[26] S. Stevenson, G. Rice, T. Glass, K. Harich, F. Cromer, M. R. Jordan, J. Craft, E. Hadju, R. Bible, M. M. Olmstead, K. Maitra, A. J. Fisher, A. L. Balch, H. C. Dorn, *Nature* **1999,** *402*, 898.

[27] M. C. Qian, S. V. Ong, S. N. Khanna, M. B. Knickelbein, *Phys. Rev. B* **2007,** *75*, 104424.

[28] J. Lu, R. F. Sabirianov, W. N. Mei, Y. Gao, C. G. Duan, X. C. Zeng, *J. Phys. Chem. B* **2006,** *110*, 23637.

[29] M. Krause, L. Dunsch, *Angew. Chem., Int. Ed.* **2005,** *44*, 1557.

[30] Z. X. Ge, J. C. Duchamp, T. Cai, H. W. Gibson, H. C. Dorn, *J. Am. Chem. Soc.* **2005,** *127* , 16292.

[31] S. Stevenson, K. Harich, H. Yu, R. R. Stephen, D. Heaps, C. Coumbe, J. P. Phillips, *J. Am. Chem. Soc.* **2006,** *128*, 8829.

[32] C. D. Angeli, T. Cai, J. C. Duchamp, J. E. Reid, E. S. Singer, H. W. Gibson, H. C. Dorn, *Chem. Mater.* **2008,** *20*, 4993.

[33] E. B. Iezzi, J. C. Duchamp, K. Harich, T. E. Glass, H. M. Lee, M. M. Olmstead, A. L. Balch, H. C. Dorn, *J. Am. Chem. Soc.* **2002,** *124*, 524.

[34] J. R. Pinzon, T. Zuo, L. Echegoyen, *Chem. - Eur. J.* **2010,** *16*, 4864.

[35] O. Lukoyanova, C. M. Cardona, J. Rivera, L. Z. Lugo-Morales, C. J. Chancellor,M. M. Olmstead, A. Rodriguez-Fortea, J. M. Poblet, A. L. Balch, L. Echegoyen, *J. Am. Chem. Soc.* **2007,** *129*, 10423.

[36] M. N. Chaur, F. Melin, A. J. Athans, B. Elliott, K. Walker, B. C. Holloway, L. Echegoyen, *Chem. Commun. (Cambridge, U. K.)* **2008,** *23*, 2665.

[37] C. M. Cardona, A. Kitaygorodskiy, L. Echegoyen, *J. Am. Chem. Soc.* **2005,** *127*, 10448.

[38] T. Cai, C. Slebodnick, L. Xu, K. Harich, T. E. Glass, C. Chancellor, J. C. Fettinger, M. M. Olmstead, A. L. Balch, H. W. Gibson, H. C. Dorn, *J. Am. Chem. Soc.* **2006,** *128*, 6486.

[39] N. Chen, E. Y. Zhang, K. Tan, C. R. Wang, X. Lu, *Org. Lett.* **2007,** *9*, 2011.

[40] C. Y. Shu, T. Cai, L. S. Xu, T. M. Zuo, J. E. Reid, K. Harich, H. C. Dorn, H. W. Gibson, *J. Am. Chem. Soc.* **2007,** *129*, 15710.

[41] C. Y. Shu, C. Slebodnick, L. S. Xu, H. Champion, T. Fuhrer, T. Cai, J. E. Reid, W. J. Fu, K. Harich, H. C. Dorn, H. W. Gibson, *J. Am. Chem. Soc.* **2008,** *130*, 17755.

[42] D. E. Sosnovik, P. Caravan, *Curr Cardiovasc Imaging Rep* **2013,** *6*, 61.

[43] T. Kanda, M. Osawa, H. Oba, K. Toyoda, J. Kotoku, T. Haruyama, K. Takeshita, S. Furui, *Radiology* **2015,** *275*, 803.

[44] R. J. McDonald, J. S. McDonald, D. F. Kallmes, M. E. Jentoft, D. L. Murray, K. R. Thielen, E. E.Williamson, L. J. Eckel, *Radiology* **2015,** *275*, 772.

[45] A. Radbruch, L. D. Weberling, P. J. Kieslich, O. Eidel, S. Burth, P. Kickingereder, S. Heiland, W. Wick, H. P. Schlemmer, M. Bendszus, *Radiology* **2015,** *275*, 783.

[46] J. Ramalho, M. Castillo, M. AlObaidy, R. H. Nunes, M. Ramalho, B. M. Dale, R. C. Semelka, *Radiology* **2015,** *276*, 836.

[47] N. Murata, L. F. Gonzalez-Cuyar, K. Murata, C. Fligner, R. Dills, D. Hippe, K. R. Maravilla, *Invest. Radiol.* **2016,** *51*, 447.

[48] C. C. Quattrocchi, C. A. Mallio, Y. Errante, B. Beomonte Zobel, *Radiology* **2015,** *276*, 616.

[49] J. Ramalho, R. C. Semelka, M. Ramalho, R. H. Nunes, M. AlObaidy, M. Castillo, *AJNR Am J Neuroradiol* **2016,** *37*, 1192.

[50] C. Chen, G. Xing, J. Wang, Y. Zhao, B. Li, J. Tang, G. Jia, T. Wang, J. Sun, L. Xing, H. Yuan, Y. Gao, H. Meng, Z. Chen, F. Zhao, Z. Chai, X. Fang, *Nano Lett.* **2005,** *5*, 2050.

[51] L. Y. Chiang, L. Y. Wang, J. W. Swirczewski, S. Soled, S. Cameron, *J. Org. Chem.* **1994,** *59*, 3960.

[52] S. Laus, B. Sitharaman, V. Toth, R. D. Bolskar, L. Helm, S. Asokan, M. S. Wong, L. J. Wilson, A. E. Merbach, *J. Am. Chem. Soc.* **2005,** *127*, 9368.

[53] T. Zou, M. Zhen, J. Li, D. Chen, Y. Feng, R. Li, M. Guan, Y. Zhang, C. Shu, C. Wang, *RSC Adv.* **2015,** *5*, 96253.

[54] J. Y. Zhang, Y. Q. Ye, Y. Chen, C. Pregot, T. H. Li, S. Balasubramaniam, D. B. Hobart, Y. F. Zhang, S. Wi, R. M. Davis, L. A. Madsen, J. R. Morris, S. M. LaConte, G. T. Yee, H. C. Dorn, *J. Am. Chem. Soc.* **2014,** *136*, 2630.

[55] J. Li, T. Wang, Y. Feng, Y. Zhang, M. Zhen, C. Shu, L. Jiang, Y. Wang, C. Wang, *Dalton Trans.* **2016**, *45*, 8696.

[56] C. Y. Shu, F. D. Corwin, J. F. Zhang, Z. J. Chen, J. E. Reid, M. H. Sun, W. Xu,J. H. Sim,C. R. Wang, P. P. Fatouros, A. R. Esker, H. W. Gibson, H. C. Dorn, *Bioconjugate Chem.* **2009,** *20*, 1186.

[57] H. L. Fillmore, M. D. Shultz, S. C. Henderson, P. Cooper, W. C. Broaddus, Z. J. Chen, C. Y. Shu, J. Zhang, J. Ge, H. C. Dorn, F. Corwin, J. I. Hirsch, J. Wilson, P. P. Fatouros, *Nanomedicine (London, U. K.)* **2011,** *6*, 449.

[58] T. Li, S. Murphy, B. Kiselev, K. S. Bakshi, J. Zhang, A. Eltahir, Y. Zhang, Y. Chen, J. Zhu, J. R. M. Davis, L. A. Madsen, J. R. Morris, D. R. Karolyi, S. M. LaConte, Z. Sheng, H. C. Dorn, *J. Am. Chem. Soc.* **2015,** *137*, 7881.

[59] M. D. Shultz, J. C. Duchamp, J. D. Wilson, C. Y. Shu, J. C. Ge, J. Y.Zhang, H. W. Gibson, H. L. Fillmore, J. I. Hirsch, H. C. Dorn, P. P. Fatouros, *J. Am. Chem. Soc.* **2010,** *132*, 4980.

[60] P. P. Fatouros, F. D. Corwin, Z. J. Chen, W. C. Broaddus, J. L. Tatum, B. Kettenmann, Z. Ge, H. W. Gibson, J. L. Russ, A. P. Leonard, J. C. Duchamp, H. C. Dorn, *Radiology* **2006,** *240*, 756.

[61] J. F. Zhang, P. P. Fatouros, C. Y. Shu, J. Reid, L. S. Owens, T. Cai, H. W. Gibson, G. L. Long, F. D. Corwin, Z. J. Chen, H. C. Dorn, *Bioconjugate Chem.* **2010,** *21*, 610.

[62] P. Adiseshaiah, A. Dellinger, D. MacFarland, S. Stern, M. Dobrovolskaia, L. Ileva, A. K. Patri, M. Bernardo, D. B. Brooks, Z. Zhou, S. McNeil, C. Kepley, *Invest. Radiol.* **2013,** *48*, 745.

[63] S. Laurent, C. Burtea, L. Vander Elst, R. N. Muller, *Contrast Media Mol. Imaging* **2011,** *6*, 229.

[64] I. Brigger, C. Dubernet, P. Couvreur, *Adv. Drug Delivery Rev.* **2002,** *54*, 631.

[65] S. S. Kelkar, T. M. Reineke, *Bioconjugate Chem.* **2011,** *22*, 1879.

[66] G. Storm, S. Q. Belliot, T. Daemen, D. D. Lasic, *Adv. Drug Delivery Rev.* **1995,** *17*, 31.

[67] D. E. Owens, N. A. Peppas, *Int. J. Pharmacol.* **2006,** *307*, 93.

[68] H. R. Kumar, X. Zhong, J. A. Sandoval, R. J. Hickey, L. H. Malkas, *Expert Rev. Neurother.* **2008,** *8*, 1497.

[69] A. Verma, F. Stellacci, F., *Small* **2010,** *6*, 12.

[70] A. Y. Kardys, D. J. Bharali, S. A. Mousa, *J. Nanotechnol.* **2013,** *2013*, 8.

[71] H. R. Zhu, L. Gao, X. L. Jiang, R. Liu, Y. T. Wei, Y. L. Wang, Y. L. Zhao, Z. F. Chai, X. Y. Gao, *Chem. Commun. (Cambridge, U. K.)* **2014,** *50*, 3695.

[72] F. Alexis, E. Pridgen, L. K. Molnar, Q. C. Farokhzad, *Mol. Pharmaceutics* **2008,** *5*, 505.

[73] R. L. Cui, J. Li, H. Huang, M. Y. Zhang, X. H. Guo, Y. A. Chang, M. Li, J. Q. Dong, B. Y. Sun, G. M. Xing, *Nano Res.* **2015,** *8*, 1259.

[74] J. Li, R. Cui, Y. Chang, X. Guo, W. Gu, H. Huang, K. Chen, G. Lin, J. Dong, G. Xing, B. Sun, *RSC Adv.* **2016,** *6*, 58028.

[75] J. Q. Luo, J. D. Wilson, J. Y. Zhang, J. I. Hirsch, H. C. Dorn, P. P. Fatouros, M. D. Shultz, *Appl. Sci.* **2012**, *2*, 465

[76] J. P. Zheng, M. M. Zhen, J. C. Ge, Q. L. Liu, F. Jiang, C. Y. Shu, H. A. Alhadlaq, C. R. Wang, *Carbon* **2013,** *65*, 175.

[77] W. Debinski, D. M. Gibo, S. W. Hulet, J. R. Connor, G. Y. Gillespie, *Clin. Cancer Res.* **1999,** *5*, 985.

[78] W. Debinski, D. M. Gibo, B. Slagle, S. K. Powers, G. Y. Gillespie, *Int. J. Oncol.* **1999,** *15*, 481.

[79] A. Mintz, D. M. Gibo, B. Slagle-Webb, N. D. Christensen, W. Debinski, *Neoplasia* **2002,** *4*, 388.

[80] P. J. Lupardus, M. E. Birnbaum, K. C. Garcia, *Structure.* **2010,** *18*, 332.

[81] C. E. Brown, C. D. Warden, R. Starr, X. Deng, B. Badie, Y. C. Yuan, S. J. Forman, M. E. Barish, *PLoS One* **2013,** *8*, e77769.

[82] M. D. Shultz, J. D. Wilson, C. E. Fuller, J. Y. Zhang, H. C. Dorn, P. P. Fatouros, *Radiology* **2011,** *261*, 136.

[83] A. Dellinger, J. Olson, K. Link, S. Vance, M. G. Sandros, J. Yang, Z. Zhou, C. L. Kepley, *J Cardiovasc Magn Reson.* **2013,** *15*, 7.

[84] S. V. Murphy, A. Hale, T. Reid, J. Olson, A. Kidiyoor, J. Tan, Z. Zhou, J. Jackson, A. Atala, *Methods.* **2016,** *99*, 99.

[85] R. F. Barth, M. G. H. Vicente, O. K. Harling, W. S. Kiger, K. J. Riley, P. J. Binns, F. M. Wagner, M. Suzuki, T. Aihara, I. Kato, S. Kawabata, *Radiat. Oncol.* **2012,** *7*, 146.

[86] A. H. Soloway, W. Tjarks, B. A. Barnum, F. G. Rong, R. F. Barth, I .M. Codogni, J. G. Wilson, *Chem. Rev.* **1998,** *98*, 1515.

[87] M. Sankari, M. V. Suryanarayana, S. Gangadharan, *J. Nucl. Mater.* **1999,** *264*, 122.

[88] Y. Horiguchi, S. Kudo, Y. Nagasaki, *Sci. Technol. Adv. Mater.* **2011,** *12*, 044607.

[89] S. Sofou, *Int. J. Nanomed.* **2008,** *3*, 181.

[90] J. D. Wilson, W. C. Broaddus, H. C. Dorn, P. P. Fatouros, C. E. Chalfant, M. D. Shultz, *Bioconjugate Chem.* **2012,** *23*, 1873.

[91] G. Q. Zhang, Z. Z. Sun, H. T. Song, M. M. Zhen, M. R. Guan, T. W. Chu, S. Z. Luo, C. R. Wang, C. Y. Shu, *J. Mater. Chem. B* **2015,** *3*, 7011.

[92] L. L. Dugan, D. M. Turetsky, C. Du, D. Lobner, M. Wheeler, C. R. Almli, C. K. F. Shen, T. Y. Luh, D. W. Choi, T. S. Lin, *Proc. Natl. Acad. Sci. U. S. A.* **1997,** *94*, 9434.

[93] M. C. Tsai, Y. H. Chen, L. Y. Chiang, *J. Pharm. Pharmacol.***1997,** *49*, 438.

[94] H. S. Lai, W. J. Chen, L. Y. Chiang, *World J. Surg.* **2000,** *24*, 450.

[95] R. Injac, M. Perse, M. Cerne, N. Potocnik, N. Radic, B. Govedarica, A. Djordjevic, A. Cerar, B. Strukelj, *Biomaterials* **2009,** *30*, 1184.

[96] J. J. Yin, F. Lao, P. P. Fu, W. G. Wamer, Y. L. Zhao, P. C. Wang, Y. Qiu, B. Y. Sun, G. M. Xing, J. Q. Dong, X. J. Liang, C. Y. Chen, *Biomaterials* **2009,** *30*, 611.

[97] D. M. McCluskey, T. N. Smith, P. K. Madasu, C. E. Coumbe, M. A. Mackey, P. A. Fulmer, J. H. Wynne, S. Stevenson, J. P. Phillips, *ACS Appl. Mater. Interfaces* **2009,** *1*, 882.

[98] S. G. Kang, R. Araya-Secchi, D. Wang, B. Wang, T. Huynh, R. Zhou, *Sci Rep.* **2014,** *4*, 4775.

[99] Y. Liu, C. Y. Chen, P. X. Qian, X. F. Lu, B. Y. Sun, X. Zhang, L. M. Wang, X. F. Gao, H. Li, Z. Y. Chen, J. L. Tang, W. J. Zhang, J. Q. Dong, R. Bai, P. E. Lobie, Q. F. Wu, S. L. Liu, H. F. Zhang, F. Zhao, M. S. Wicha, T. Zhu, Y. L. Zhao, *Nat. Commun.* **2015,** *6*.

[100] Y. Pan, L. Wang, S.G. Kang, Y. Lu, Z. Yang, T. Huynh, C. Chen, R. Zhou, M. Guo, Y. Zhao, Y, *ACS Nano* **2015,** *9*, 6826.

[101] J. Tang, Z. Chen, B. Sun, J. Dong, J. Liu, H. Zhou, L. Wang, R. Bai, Q. Miao, Y. Zhao, C. Chen, Y. Liu, *Nanomedicine* **2016,** *12*, 945.

[102] S. G. Kang, G. Zhou, P. Yang, Y. Liu, B. Sun, T. Huynh, H. Meng, L. Zhao, G. Xing, C. Chen, Y. Zhao, R. Zhou, *Proc. Natl. Acad. Sci. U. S. A.* **2012,** *109*, 15431.

[103] B. S. Zolnik, A. Gonzalez-Fernandez, N. Sadrieh, M. A. Dobrovolskaia, *Endocrinology* **2010,** *151*, 458.

[104] J. Meng, X. J.Liang, X. Y. Chen, Y. L. Zhao, *Integr. Biol.* **2013,** *5*, 43.

[105] M. Zhen, C. Shu, J. Li, G. Zhang, T. Wang, Y. Luo, T. Zou, R. Deng, F. Fang, H. Lei, C. Wang, C. Bai, *Sci. China Mater.* **2015,** *58*, 799.

[106] C. L. Wang, Y. T. Bai, H. L. Li, R. Liao, J. X. Li, H. Zhang, X. Zhang, S. J. Zhang, S. T. Yang, X. L. Chang, *Part. Fibre Toxicol.* **2016,** *13*, 14.

[107] J. Li, W. J. Yang, R. L. Cui, D.L. Wang, Y. Chang, W.H. Gu, W.Y. Yin, X. Bai, K. Chen, L. Xia, H. Geng, G.M. Xing, *Nanotechnology*, **2016**, *27*, 155101.

[108] J. X. Wang, C. Y. Chen, B. Li, H. W. Yu, Y. L. Zhao, J. Sun, Y. F. Li, G. M. Xing, H. Yuan, J. Tang, Z. Chen, H. Meng, Y. X. Gao, C. Ye, Z. F. Chai, C. F. Zhu, B. C. Ma, X. H. Fang, L. J. Wan, *Biochem. Pharmacol.* **2006,** *71*, 872.

[109] W. Kratschmer, K. Fostiropoulos, D. R. Huffman, *Chem. Phys. Lett.* **1990,** *170*, 167.

[110] T. M. Gruenberger, J. Gonzalez-Aguilar, F. Fabry, L. Fulcheri, E. Grivei, N. Probst, G. Flamant, H. Okuno, J. C. Charlier, *Fullerenes, Nanotubes, Carbon Nanostruct.* **2004,** *12*, 571.

[111] J. Wang, Z. B. Hu, J. X. Xu, Y. L. Zhao, *Npg Asia Mater.* **2014,** *6*, e84.

Chapter 2 A New Interleukin-13 Amino-Coated Gadolinium Metallofullerene Nanoparticle for Targeted MRI Detection of Glioblastoma Tumor Cells

This chapter is adopted from the manuscript published on Journal of the American Chemical Society with appropriate modifications under the permission of the American Chemical Society. Full text of the published manuscript entitled "A New Interleukin-13 Amino-Coated Gadolinium Metallofullerene Nanoparticle for Targeted MRI Detection of Glioblastoma Tumor Cells" by Tinghui Li, Susan Murphy, Boris Kiseley, Kanwarpal S. Bakshi, Jianyuan Zhang, Amnah Eltahir, Yafen Zhang, Ying Chen, Jie Zhu, Richey M. Davis, Louis A. Madsen, John R. Morris, Daniel R. Karolyi, Stephen M. LaConte, Zhi Sheng, and Harry C. Dorn, can be obtained at http://pubs.acs.org/doi/abs/10.1021/jacs.5b03991

Abstract

The development of new nanoparticles as next-generation diagnostic and therapeutic ("theranostic") drug platforms is an active area of both chemistry and cancer research. Although numerous gadolinium (Gd) containing metallofullerenes as diagnostic MRI contrast agents have been reported, the metallofullerene cage surface, in most cases, consists of negatively charged carboxyl or hydroxyl groups that limit attractive forces with the cellular surface. It has been reported that nanoparticles with a positive charge will bind more efficiently to negatively charged phospholipid bi-layer cellular surfaces, and will more readily undergo endocytosis. In this paper, we report the preparation of a new functionalized trimetallic nitride template endohedral metallofullerene (TNT EMF), $Gd_3N@C_{80}(OH)_x(NH_2)_y$, with a cage surface consisting of positively charged amino groups ($-NH_3^+$) and directly compare it with a similar carboxyl and hydroxyl functionalized derivative. This new nanoparticle was characterized by X-ray photoelectron spectroscopy (XPS), dynamic light scattering (DLS), and infrared spectroscopy. It

exhibits excellent ^{1}H MR relaxivity. Previous studies have clearly demonstrated that the cytokine interleukin-13 (IL-13) effectively targets glioblastoma multiforme (GBM) cells, which are known to overexpress IL-13Rα2. We also report that this amino-coated Gd-nanoplatform, when subsequently conjugated with interleukin-13 peptide IL-13-$Gd_3N@C_{80}(OH)_x(NH_2)_y$, exhibits enhanced targeting of U-251 GBM cell lines and can be effectively delivered intravenously in an orthotopic GBM mouse model.

2.1 Introduction

Cancer is one of the most destructive diseases known to mankind, and glioblastoma multiforme (GBM) is no exception. GBM is a stage 4/4 astrocytoma, and it is the most common primary brain tumor in adults. GBM has the worst prognosis of any central nervous system (CNS) malignancy; the median survival rate is approximately one year, and less than 5% of patients diagnosed with GBM live longer than 5 years.[1] Throughout the past few years, efforts are being made in order to develop methods that specifically target cancerous cells. Specifically, nanoparticle mediated delivery of drug and diagnostic contrast material has shown tremendous potential for crossing physiologic barriers,[2] enhancing bioavailability, and enabling precise targeting.[3,4] Endohedral metallofullerenes (EMFs) represent a unique class of nanoparticles that are highly stable and resistant to opening by most biological processes.[5-10] EMFs are also advantageous as the spheroidal carbon cage structure leads to a high surface-to-volume ratio. This allows for multiple functional groups to be attached to the surface of the sphere, enhancing the potential for nanoparticles with targeting, diagnostic, and therapeutic modalities.

It has been previously established that neutral and negatively charged nanoparticles are generally less effective in crossing cell membranes than positively charged nanoparticles.[1,11-13] Numerous gadolinium-containing EMFs as diagnostic MRI contrast agents have been reported and are very promising materials that confine the toxic Gd^{3+} ions inside an inert, robust, carbon cage. These nanoplatforms exhibit 10-40 times higher ^{1}H relaxivity than most commercial contrast agents.[14] Seminal studies by Shinohara[14,15] and Wilson[16,17] focused on mono-metal EMFs, namely, $Gd@C_{82}$ and $Gd@C_{60}$, with the metallofullerene cage surfaces consisting of negatively charged carboxyl or hydroxyl groups. In the last few years, considerable attention has focused on the trimetallic nitride template endohedral metallofullerenes (TNT EMFs)[6,18-20] and many water-soluble derivatives of

$Gd_3N@I_h$-C_{80}. Gd-containing mixed metal TNT EMFs have been synthesized and recently reviewed as MRI contrast agents.[5-8,20-22] Earlier studies by Debinski and collaborators have shown that the cytokine interleukin-13 (IL-13), together with its receptor, is over-expressed in human GBM cell lines and GBM tissue but not in normal brain tissue.[23,24] We have previously reported a TNT EMF platform of $Gd_3N@C_{80}$ functionalized with carboxyl groups, and conjugated to interleukin-13, IL-13-$Gd_3N@C_{80}(OH)_{26}(CH_2CH_2COOM)_{16}$ ((IL-13-carboxyl)-**IIa**). Unfortunately, this nanoparticle was intracranially delivered to GBM xenograft mice models (U-87) via invasive convection enhanced delivery (CED).[25] In most cases reported to date, the metallofullerene nanoparticle cage surface consists of negatively charged carboxyl or hydroxyl groups that limit attractive forces on the cellular surface (**Figure 1**). A notable exception is demonstrated by Zheng and coworkers[26] reporting the preparation of the MRI contrast agent $Gd@C_{82}O_{14}(OH)_{14}(NH_2)_6$, where, under physiological conditions, the cage surface is expected to exhibit a positive charge due to the presence of $(-NH_3)^+$ groups.

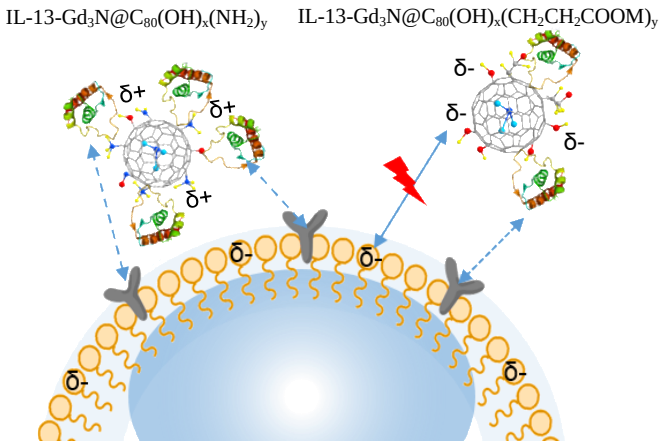

Figure 1. The IL-13-$Gd_3N@C_{80}(OH)_x(NH_2)_y$ nanoparticle with positive charges illustrating facile binding to a negatively charged phospholipid bi-layer cellular surfaces.

In this chapter, I report a new functionalization procedure for the $Gd_3N@C_{80}$ platform providing trimetallic nitride $Gd_3N@C_{80}(OH)_x(NH_2)_y$ ((amino)-**I**). This was characterized by X-ray photoelectron spectroscopy (XPS), dynamic light scattering (DLS), and infrared spectroscopy, and exhibits excellent ^1H MR relaxivity. This new Gd-nanoplatform, when conjugated with an interleukin-13 peptide, exhibits enhanced targeting of U-251 GBM cell lines. In addition, we demonstrate that the $Gd_3N@C_{80}$ platform can be successfully conjugated to an IL-13-TAMRA peptide that exhibits effective targeting of orthotopic GBM xenografts in mice by intravenous delivery. Our hypothesis is that the (amino)-**I** positively charged nanoparticle and IL-13 targeting peptide exhibit enhanced charge attraction for GBM cellular endocytosis, due to multi-receptor site binding and the presence of positively charged amino groups ($-NH_3^+$) on the metallofullerene cage surface (**Figure 1**). In addition, we show enhanced non-invasive intravenous delivery and MRI targeting of $Gd_3N@C_{80}(OH)_x(NH_2)_y$ ((amino)-**I**) to U-251 tumors implanted in a mouse model.

2. 2 Experimental procedures

2.2.1 Preparation of functionalized $Gd_3N@C_{80}$ ((amino)-I). The functionalization of the amino group onto $Gd_3N@C_{80}$, (amino)-**I**, was performed following a recently reported procedure.[26] Briefly, $Gd_3N@C_{80}$ (ca. 5 mg) was added to 246 uL of 50 wt% H_2O_2 and 180 uL of 28 wt% NH_4OH. The mixtures were vigorously stirred at 50ºC under ambient conditions for 1.5 hours. At the end of the reaction, the black suspension turned to yellow solution. The yellow solution was added to ethanol to remove the excess H_2O_2 and NH_4OH, the amount ratio between supernatant and ethanol was 1:12. The suspension was centrifuged at 10,000 rpm for 10 min, and the yellowish precipitate was collected and washed with an excess amount of ethanol, then dried under vacuum at 50ºC for 24 hours.

2.2.2 Conjugation of IL-13-TAMRA-$Gd_3N@C_{80}O_{12}(OH)_{10}(NH_2)_7(NO_2)_2$ ((IL-13-amino)-Ia). The TAMRA-VDKLLLHLKKLFREGQFNREGQFNRNFESIIICRDRT-OH is a shorter active peptide for IL-13Rα2 receptor sites, instead of the complete IL-13 sequence, was obtained from New England Peptide LLC, MA, USA (**Figure S1**).[25] This shorter peptide was dissolved in dimethyl sulfoxide (DMSO) at a concentration of 2 mg/ml. Dissolving the peptide in DMSO instead of water represented a significant change from previous work,[22,25] and led to greater solubility of the peptide. For the conjugation reaction, (amino)-**I** was diluted in 2-(*N*-morpholino)ethanesulfonic acid (MES), and filtered through a 0.45 µm syringe filter. The carboxyl groups of the IL-13-TAMRA were activated by 66 µl of 2 mM 1-Ethyl-3-[3-dimethylaminopropyl] carbodiimide hydrochloride (EDC), and the same amount of *N*-hydroxysulfosuccinimide (Sulfo-NHS). After 10 minutes, 500 µl of functionalized $Gd_3N@C_{80}$ was added and incubated at room temperature for 1.5 hours. Subsequently, 66 µl of 0.275 mM hydroxyl amine was added to quench the reaction (**Figure 2**). The resulting solution was filtered through Zeba-brand spin columns at a rate of 5000 rpm for 2 minutes. The receptacle portion of the spin column was thoroughly rinsed with solution to ensure that all the (IL-13-amino)-**Ia** product was removed from the column. Based on inductively coupled plasma mass spectroscopy (ICP-MS), the Gd^{3+} concentration of (IL-13-amino)-**Ia** was 1.98 µM.

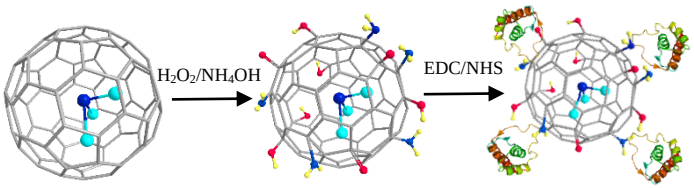

Figure 2. Functionalization and conjugation process of $Gd_3N@C_{80}$.

2.2.3 IL-13-TAMRA-$Gd_3N@C_{80}(OH)_{26}(CH_2CH_2COOM)_{16}$ (IL-13-carboxyl)-IIa). 500 µL of (carboxyl)-**II** was dissolved in MES solution and a concentration of approximately 50 µM was filtered through a 0.45 µm syringe filter. The carboxyl groups were activated via addition of 70

µL of 0.5 M EDC and 70 µL of 0.5M Sulfo-NHS to the f-$Gd_3N@C_{80}$ solution. After 10 minutes, 85 µL of the IL-13-TAMRA peptide (dissolved in DMSO) was added, and the reaction was continued for 1.5 hours. After this time, 70 µL of hydroxyl-amine solution was added to quench the reaction. The resulting solution was filtered through Zeba-brand spin columns at a rate of 5000 rpm for 2 minutes. The receptacle portion of the spin column was thoroughly rinsed to ensure that all the product was removed from the column. Based on ICP-MS, the Gd^{3+} concentration of (IL-13-carboxyl)-**IIa** was 0.47 µM.

2.2.4 Preparation of Scrambled ILs-13-TAMRA-$Gd_3N@C_{80}O_{12}(OH)_{10}(NH_2)_7(NO_2)_2$ (ILs-13-amino)-Is) and ILs-13-TAMRA-$Gd_3N@C_{80}(OH)_{26}(CH_2CH_2COOM)_{16}$ (ILs-13-carboxyl)-IIs). Both the amino functionalized nanoparticle and the carboxyl functionalized nanoparticle were conjugated with a scrambled IL-13 peptide, provided by American Peptide Company, Inc., Sunnyvale, CA, USA. The same conjugation procedure described above was used to prepare the nanoparticles, (ILs-13-amino)-**Is** and (ILs-13-carboxyl)-**IIs**, respectively.

The hydrophobic $Gd_3N@C_{80}$ reacts with H_2O_2 and NH_4OH providing aqueous colloidal stability (amino)-**I**. The second step conjugates the functionalized gadofullerene molecule to the IL-13 peptide with fluorescent tagging through amide bond formation (IL-13-amino)-**Ia** (grey: carbon; aqua: gadolinium ion; blue: nitrogen; red: oxygen; yellow: hydrogen).

2.2.5 Characterization of functionalized $Gd_3N@C_{80}$ and IL-13-TAMRA-functionalized $Gd_3N@C_{80}$. The (amino)-**I** was further characterized by XPS, DLS, and infrared spectroscopy. The (IL-13-amino)-**Ia** sample was characterized by DLS, and confocal microscopy.

2.2.6 Relaxivity Measurements for functionalized $Gd_3N@C_{80}$. The T_1 and T_2 relaxation times were measured on a Bruker Minispec mq 20 (0.47 T), mq 60 (1.41 T) analyzers, and Bruker Avance III 400 MHz (9.4 T) wide bore spectrometer equipped with an MIC 400 W1/S2 probe and

5mm ^{1}H coil. The inversion-recovery method was used to measure the spin-lattice relaxation time T_1, and the Carr-Pucell-Meiboom-Gill method was used for the spin-spin relaxation time T_2 measurement. Errors in T_1 and T_2 values were less than ±2%. Solutions with different Gd^{3+} concentrations were prepared by diluting a stock solution with deionized water. The concentration of the Gd^{3+} ions was determined by ICP-MS.

2.2.7 Confocal Microscopy Comparison Study of Nanoparticles with U-251 cell lines (increased IL-13Rα2 expression) and with HeLa Cell Lines (no overexpression of IL-13Rα2).

Cells (U-251 or HeLa $5x10^4$ cells/well) were inoculated in 4 well chamber slides, and incubated overnight. The (IL-13-amino)-**Ia**, (IL-13-carboxyl)-**IIa**, scrambled (ILs-13-amino)-**Is**, and scrambled (ILs-13-carboxyl)-**IIs** nanoparticles (0.75 μM/well) were added to each well, incubated 20 min at 37 °C, washed, stained with Hoechst (1:15,000 , 37 °C, 10 minutes), washed again and fixed with 4% buffered paraformaldehyde (37 °C, 30 min).

High-magnification optical sections were captured with a Leica spinning disk laser confocal microscope (LCM) equipped with a 63× oil-immersion objective. The micro-scope model, objective, pinhole, gain, and black level settings were held constant for each experiment. Fluorescence from Hoechst and TAMRA was generated by exciting the samples with laser lines from a blue diode (405 nm) and green HeNe (543 nm) lasers. The fluorescence emission was collected simultaneously in two separate photomultipliers with the spectrophotometer scan head detector windows set to ranges of 413–502 nm (for Hoechst) and 562–700 nm (for TAMRA). The acousto-optic tunable filter was adjusted to ensure that there was no crosstalk of signal between channels when fluorescence was collected from each channel simultaneously.

For quantitative analyses of TAMRA internalization and cellular distribution, confocal optical sections (z-stacks) were taken in at least 4 fields per slide, 1-2 μm thickness.

2.2.8 Introduction of Glioblastoma Cells to Nude Athymic Mouse model. *In vivo* orthotopic xenograft U-251 cell implantation experiments involving the use of mice were carried out in accordance with protocols approved by the Virginia Tech Institutional Animal Care and Use Committee. Female SCID/beige 7-8-week-old mice were anesthetized with isoflurane (2-4%) and placed in a stereotactic frame (World Precision Instruments). The incision site at the top of the head was disinfected with betadine and alcohol. After a midline incision, a burr hole was made in the skull 0.5 mm anterior to the bregma and 2 mm laterally either to the left or right hemisphere. A 25 μL Hamilton syringe was used to inject 2×10^5 GBM cells (U-251), suspended in 4 μL PBS, 4 mm deep from the surface of the skull. The injection was made over 5 minutes using a microinfusion pump. The needle was left in place for another 3 minutes before withdrawing. The burr hole was sealed with bone wax and the incision closed using size 4 sutures.

After the procedure animals were weighed daily and monitored carefully for signs of increased intracranial pressure from the growing tumor mass. 30 days after the introduction of the tumor cells, the IL-13-TAMRA-functionalized-$Gd_3N@C_{80}$ nanoparticle was administered to the animals using either a convection enhanced delivery (CED) approach or an intravenous approach.

2.2.9 Administration of IL-13-TAMRA-functionalized $Gd_3N@C_{80}$ to Xenografted Mice. The CED method of administration of (IL-13-carboxyl)-**IIa** nanoparticles has been reported by Fillmore and coworkers.[25] To perform this procedure, one group of animals were anesthetized via isoflurane and placed in the stereotactic frame. The burr hole from the injection of the tumors was identified, and a Hamilton syringe was inserted through it to a depth of 4 mm from the surface of the skull. 18 μL of (IL-13-carboxyl)-**IIa** nanoparticle was injected at a rate of 0.2 μL/minute (total injection time of 90 minutes). During administration of the agent, the animal was maintained under anesthesia via isoflurane 1-3% and was carefully monitored. After the full dose of agent was

administered the syringe was carefully removed and the incision closed. The animal was given buprenorphine for pain control and monitored for recovery, then returned to the vivarium.

A second group of animals received either (IL-13-amino)-**Ia** or (IL-13-carboxyl)-**IIa** nanoparticles via an intravenous tail vein delivery method. This method of administering the functionalized EMFs for the purpose of brain tumor targeting has not been previously reported and represents a major shift from the invasive intracranial CED delivery of the nanoparticles previously reported (vide supra). 250 µL of (IL-13-carboxyl)-**IIa** was injected into the left tail vein of the mouse using a tail vein illuminator (Braintree Scientific). One mouse was administered (IL-13-amino)-**Ia** (3 µM in 300µl) via the tail vein. 300 µl of 500 µM Magnevist® was intravenously delivered into another mouse. Approximately, 15 minutes after the mice were sacrificed, MRI images were obtained in a clinical 3 T MRI scanner.

2.2.10 *In vitro* and *in vivo* MRI study of the functionalized $Gd_3N@C_{80}$, IL-13-amino-Ia, and IL-13-carboxyl-IIa. The *in vitro inversion-recovery* MR images were obtained for the visual confirmation of the efficiency of the (amino)-**I** working as a contrast agent. A 3 T (123 MHz) clinical scanner was used. Various concentrations of the (IL-13-amino)-**Ia**, (IL-13-carboxyl)-**IIa**, (amino)-**I**, and the Magnevist® were used and compared. To demonstrate clinical MRI feasibility, U-251 GBM cells orthotopically implanted in mice with (IL-13-amino)-**Ia**, (IL-13-carboxyl)-**IIa** or Magnevist® were also examined with a clinical 3 T MRI Siemens scanner, utilizing a wrist hand receiver coil.

2. 3 Results and discussion

As previously indicated, transport, targeting, and cellular uptake are key considerations in the design of new "theranostic" nanoparticles for clinical cancer applications. In the present study, we have synthesized (as outlined in **Figure 2**) a new amino-functionalized nanoparticle, (amino)-**I**,

which is significantly different from previously reported hydroxyl and carboxyl TNT EMF derivatives, (carboxyl)-**II**.[5] The electronic absorption spectrum for (amino)-**I** clearly exhibits the loss of π conjugation in comparison with the precursor EMF, $Gd_3N@C_{80}$, as illustrated in **Figure 3A**. In the Reflection Absorption InfraRed Spectroscopy (RAIRS) spectrum (**Figure 3B**) for (amino)-**I**, the characteristic vibration bands of broad overlapping O-H and N-H centered at (3236 cm^{-1}), N-H (1613 cm^{-1}), C-N (1224 cm^{-1}), and C-O (1086 cm^{-1}) suggest the existence of both hydroxyl and amino groups on the carbon cage. The strong peak centered at 1436 cm^{-1} suggests overlap of the C-C stretching vibration and N-O stretching vibration, which indicates the presence of nitro groups introduced onto the carbon cage. The XPS multiplex spectra for (amino)-**I** are presented in **Figure 3C** and **3D** for the C_{1s} and N_{1s} regions, respectively. The C_{1s} peaks, centered at binding energies of 284.5, 286.4 and 290.6 eV, were assigned to the C-C, C-O (C-N), and π→π* satellite, respectively. Since there is an obvious absence of a carbonyl absorption band in the RAIRS spectrum, the peak located at the binding energy of 288.1 eV is likely due to hemiketal or hemiacetals (RO-C-OH), or cyclic ether (C-O-C) structures.[27,28] The N_{1s} peaks centered at 399.3 and 402.2 eV correspond to the free amino group ($-NH_2$) and partially protonated amino ($-NH_3^+$), indicating that amino groups have been successfully introduced to the carbon cages. Finally, the peak at the binding energy of 397.9 eV can be assigned to the metal nitride (Gd-N) group encapsulated in the carbon cage. It is worth noting that a new peak appears at around 406.5 eV that is assigned to the nitro group, which is significantly different from the previously reported $Gd@C_{82}$ case.[29,30] Based on the resulting atomic percentages of carbon and nitrogen (**Table S1**, and **Table S2**), and the peak deconvolution of the XPS profile, the average formula for (amino)-**I** can be described as $Gd_3N@C_{80}O_{12}(OH)_{10}(NH_2)_7(NO_2)_2$. **Figure 3E** shows the survey XPS spectrum of

(amino)-**I**. The peaks center at 285, 402, and 533 eV reveal the presence of C, N and O species in the compound. The residue of Na KLL peak was from water.

It is well established that water-soluble metallofullerene derivatives form aggregates in water.[31] The DLS results for (amino)-**I** (**Figure 3F**) indicate that the hydrodynamic size of an aggregate nanoparticle is ~60 nm in pure water. This is similar to the results previously reported for carboxylated and hydroxlated nanoparticles,[5] including polyethylene glycol–(PEG) functionalized derivatives as well as hydroxylated, $Gd_3N@C_{80}$.[8,9] As expected, after conjugation, the (IL-13-amino)-**Ia** exhibits a significant increase to ~1880 nm in water, somewhat larger than the (IL-13-carboxyl)-**IIa** nanoparticle (~1400 nm). The Zeta potential provides a convenient approach to assess the surface charge on nanoparticles. Kardys and coworkers recently reported an amino-functionalized silica nanoparticle (SiNPs) that exhibited preferential uptake in pancreatic cancer cells.[12] In their study, the synthetic inclusion of positively charged $–NH_2$ groups increased the zeta potential from −45 mV to −31 mV. In similar fashion, our results also exhibit an increase in the Zeta potential for the amino group nanoparticle (IL-13-amino)-**Ia** (6.46 mV) in comparison with the (IL-13-carboxyl)-**IIa** nanoparticle (−3.43 mV). It should also be noted that the unconjugated nanoparticle, (amino)-**Ia**, exhibits a Zeta potential of -31.0 mV, which is close to the Kardys value (vide supra) and also a similar amino $Gd_3N@C_{80}$ metallofullerene nanoparticle reported by Kepley and coworkers.[32]

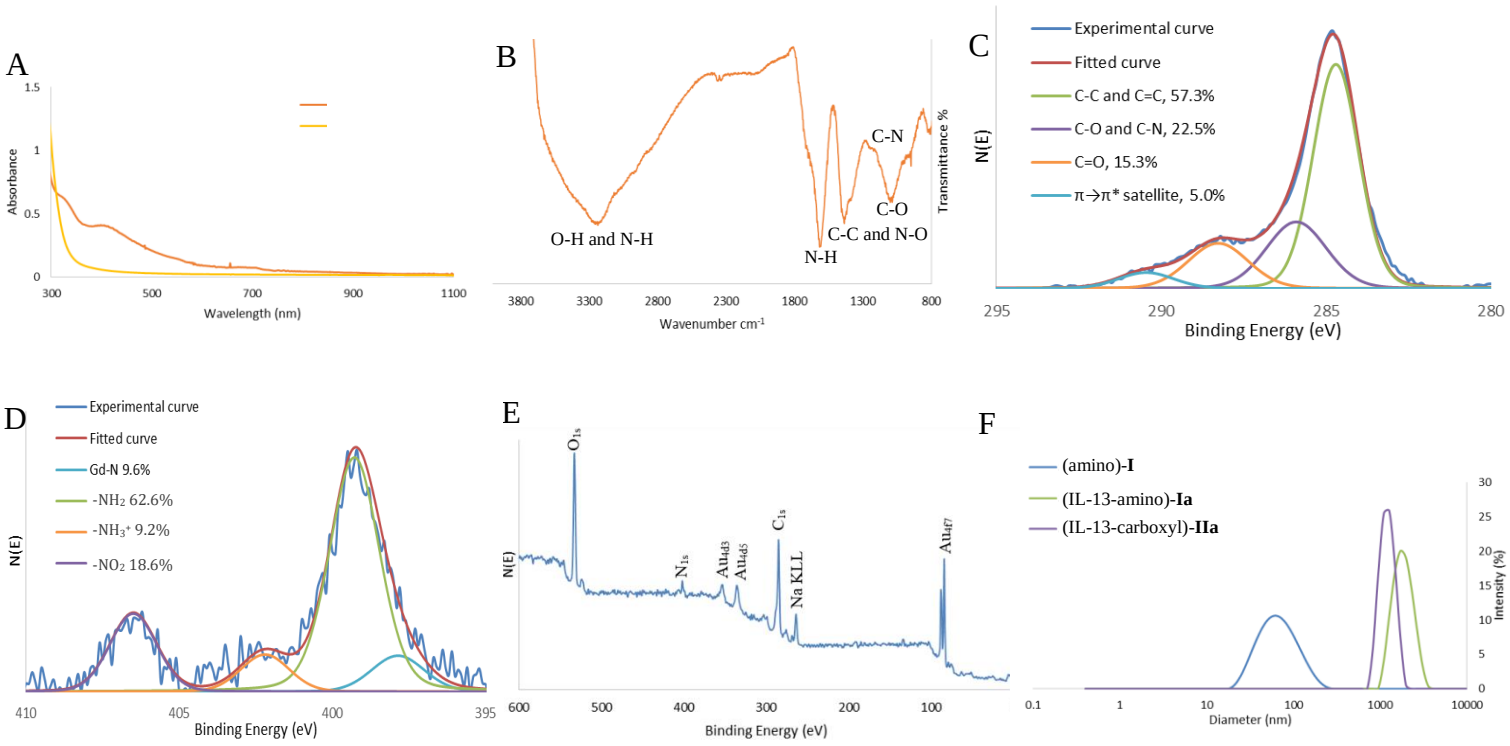

Figure 3. Characterization of the functionalized $Gd_3N@C_{80}$. A) Electronic absorption spectra of $Gd_3N@C_{80}$ before and after functionalization. B) RAIRS spectrum of (amino)-**I**. C)-D) XPS multiplex spectra of the (amino)-**I**. E) The XPS survey spectrum of (amino)-**I**. Au was used for calibration. F) Hydrodynamic size distribution of (amino)-**I**, (IL-13-amino)-**Ia** and (IL-13-carboxyl)-**IIa** in water.

In previous studies, we have reported that the (IL-13-carboxyl)-**IIa** nanoparticle targets the GBM U-87 cell line.[22,25] In the current study, we employed the U-251 cell line which have the highest expression of IL-13Rα2 receptor sites of all GBM cell lines and are histologically similar to human GBM.[33,34] In order to ensure specific targeting of the U-251 cell line, we treated HeLa cells which do not over-express the IL-13Rα2 receptor sites. The HeLa and U-251 cells were incubated with the same concentration of (IL-13-amino)-**Ia** and (IL-13-carboxyl)-**IIa**, respectively. As illustrated in **Figure 4A**, and **Figure S2**, no co-localization of TAMRA with the HeLa cells was observed.

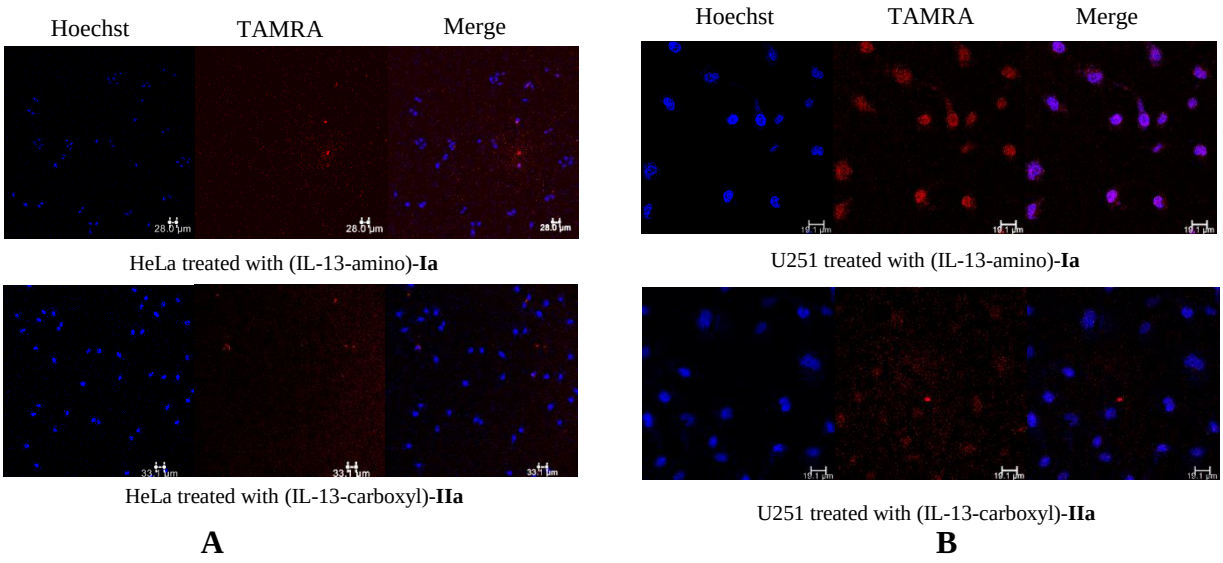

Figure 4. A) The images are projections of confocal z stacks generated from sections of 5 to 6 μm thickness comparing internalization of TAMRA in HeLa cells. Top row is HeLa treated with (IL-13-amino)-**Ia**, bottom row is HeLa treated with (IL-13-carboxyl)-**IIa**. B) The images are projections of confocal z-stacks, generated from sections of 5 to 6 μm thickness, comparing internalization of TAMRA in U-251 cells. 63× images z5, 10 images were taken 5 u apart SCALE BAR = 19.1 μm. Top row is U-251 treated with (IL-13-amino)-**Ia**, bottom row is U-251 treated with (IL-13-carboxyl)-**IIa**.

For the U-251 cells treatment, the nanoparticles are internalized by the U-251 cell line and a clear preference for localization in the nucleus is illustrated for both the (IL-13-amino)-**Ia** and (IL-13-carboxyl)-**IIa**, with a greater intensity in the former case (**Figure 4B**). In a direct fluorescence quantitation (2-way ANOVA, Graphpad), there is a slight preponderance of (IL-13-amino)-**Ia** in the cytoplasm and cell membrane that is significantly enhanced in the nucleus in comparison with cells treated with (IL-13-carboxyl)-**IIa** (**Figure 5**). Thus, the nanoparticles coated in amino groups have high cell membrane binding affinity, and readily translocate across the plasma membrane, and undergo endocytosis. This translocation process is illustrated in **Figure 5** and explains why after a significant time interval (20-30 min) the fluorescence of (IL-13-amino)-**Ia** and (IL-13-carboxyl)-**IIa** is significantly concentrated in the nucleus in comparison with the cytoplasm and cell membrane.

In order to demonstrate the cell targeting specificity is due to the IL-13 peptide and not the f-$Gd_3N@C_{80}$ platform, the U-251 cells were also treated with a scrambled peptide analog, (ILs-13-amino)-**Is** and (ILs-13-carboxyl)-**IIs**. **Figure S3** shows that the scrambled peptide analog (ILs-13-

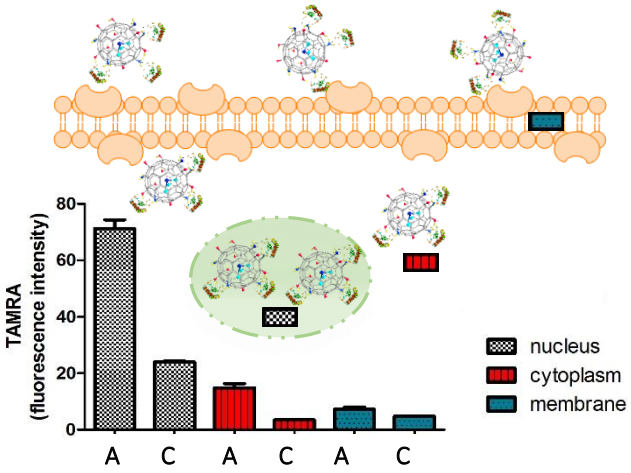

Figure 5. Translocation of (IL-13-amino)-**Ia** (A) and (IL-13-carboxyl)-**IIa** (C) in U-251 cells, quantitation of TAMRA fluorescence by 2-way ANOVA (Graphpad).

f-$Gd_3N@C_{80}$)-**Is** is not internalized by the U-251 cell line, therefore the specific IL-13 peptide is necessary to specifically bind to cells that express the interleukin receptor site, IL-13Rα2. These results support our hypothesis that although both nanoparticles (**Ia** and **IIa**) display targeting to the U-251 cell line, the (IL-13-amino)-**Ia** positively charged nanoparticle exhibits enhanced targeting for GBM cells in comparison with the (IL-13-carboxyl)-**IIa** (**Figure 1** and **Figure 5**).

Although the confocal microscopic studies (vide supra) illustrate effective targeting of U-251 GBM cell lines by both the (IL-13-amino)-**Ia** and (IL-13-carboxyl)-**IIa** nanoparticles, demonstration of effective transport of a targeting nanoparticle across the blood brain barrier (BBB) by non-invasive intravenous delivery is critically important in the development of a new clinical GBM MRI contrast agent. Thus, GBM U-251 cells were orthotopically implanted in mice and, 30 days following the implantation of the xenograft tumor the (IL-13-carboxyl)-**IIa** nanoparticle was administered to the mice using two approaches. In one approach, the nanoparticle

agent (**IIa**) was administered intracranially to the implanted tumor site by CED, as described in earlier studies.[25] In a second approach, the nanoparticle (**IIa**) was delivered by systemic intravenous delivery via the tail vein. In a very limited biodistribution study for only the (IL-13-carboxyl)-**IIa** nanoparticle, we have measured the gadolinium concentration (ICP-MS) found for these nanoparticles after intravenous delivery in other organs beside the brain including the liver, spleen, kidney, and other internal organs. However, an important feature of this limited data is the significantly higher concentration of nanoparticles in the brain hemisphere containing the implanted tumor in comparison with the contralateral brain hemisphere. This is confirmed by the confocal microscopy and MRI as illustrated below. There is significant evidence of the (IL-13-carboxyl)-**IIa** nanoparticle at the implanted tumor site by confocal microscopy of tissue slices after the animals were sacrificed. For the (IL-13-carboxyl)-**IIa** nanoparticle (**Figure S4**), the TAMRA label is specifically observed at the brain tumor (T) site. For the case of systemic delivery (**Figure S5**), the nanoparticle can be observed at the edge of the tumor, but not in the necrotic center of the tumor. There is also evidence of increased fluorescence at distances removed from the primary tumor site and may suggest evidence for detection of micrometastatic tumors. A more comprehensive study will be necessary to quantify the biodistribution of these targeting nanoparticles. These results complement the compelling (IL-13-amino)-**Ia** MRI results (vide infra) and provide evidence that both of these nanoparticles can be delivered by the less invasive intravenous tail vein injection with specific targeting to GBM U-251 mice brain tumor models.

The ^{1}H MR r_1 relaxivity results for (amino)-**I** and (carboxyl)-**II** are summarized in **Table 1** and the r_2 relaxivity results are summarized in the Supporting Information (**Table S3**). The nuclear magnetic resonance relaxivity (R_i) of both compounds were evaluated by the general equation:

$$R_i = \frac{1}{T_{i\ \ obs}} = \frac{1}{T_{i\ \ H_2O}} + \frac{1}{T_{i\ \ para}} = \frac{1}{T_{i\ \ H_2O}} + r_i[M]$$

where T_1 and T_2 are longitudinal and transverse relaxation time, respectively. The relaxation rate (reciprocal of relaxation time) is determined by both diamagnetic (pure water) and paramagnetic (contrast agent) species, and the ratio of paramagnetic relaxation rate to the concentration is the relaxivity of the paramagnetic compound, which can be experimentally obtained by the slope of ($1/T_i$) vs. concentration of the paramagnetic contrast agents.[35] These results can be compared with the relaxivity of the commercial contrast agents Magnevist® and Omniscan®, which exhibit much lower relaxivity at all magnetic field strengths (4-6 $mM^{-1}s^{-1}$) (**Table 1**).[36] The hydrodynamic size distribution is a contributing factor for the relaxivities of the nanoparticle derivatives. The aggregation of MRI contrast agents leads to bigger and slower tumbling complexes and increased rotational correlation times (τ_c); this subsequently results in enhanced relaxivities relative to smaller aggregation or nonaggregated agents. The number of hydroxyl groups is also a key factor for the relaxivity, facilitating the gadofullerenes to trap water molecules in their aggregates. The relaxivity values for the (amino)-**I** are significantly higher at all magnetic field strengths than the commercial agents, but are lower than (carboxyl)-**II**, especially at the clinical magnetic field strength. This could be due in part to the slightly larger aggregate size of the (carboxyl)-**II** nanoparticle; there is also a much larger number of hydroxyl groups (10 vs. 26) directly attached to the fullerene cage surface, which could more efficiently undergo (OH-H_2O) hydrogen exchange reactions for the (carboxyl)-**II** nanoparticle. The nanoparticle $Gd_3N@C_{80}O_{11}(OH)_{21}$, recently reported by Zhang and coworkers, also exhibits high relaxivity at all magnetic field strengths and contains a large number of hydroxyl groups (21) on the fullerene cage surface.[9] As indicated in **Table 1**, the amino functionalized nanoparticle reported by Zheng and coworkers ($Gd@C_{82}O_{14}(OH)_{14}(NH_2)_6$) ostensibly exhibits much lower relaxivity at all magnetic field

strengths. This is misleading because the data in **Table 1** is on a molar basis and not gadolinium atoms per molecule (1 vs. 3).[26]

Table 1. Comparison of r_1 Relaxivities Gadolinium Metallofullerenes (units of $mM^{-1}s^{-1}$ per mM in pure water at 298 K, [a] 300 K, [b] 310 K).

Compound	r_1 relaxivity $mM^{-1}s^{-1}$			Hydrodynamic size (nm)
	0.35-0.5 T	1.0-3.0 T	7.1-9.4 T	
$Gd_3N@C_{80}O_{12}(OH)_{10}(NH_2)_7(NO_2)_2$ (amino)-**I**	88±1 (0.47 T)	101±0.5 (1.4 T)	30.5 (9.4 T)	60
$Gd@C_{82}O_{14}(OH)_{14}(NH_2)_6$ [a] [26]	47.0 (0.5 T)	41.0 (1.5 T) 39.5 (3 T)	27.4 (7.1 T)	16
$Gd_3N@C_{80}(OH)_{26}(CH_2CH_2COOM)_{16}$ (carboxyl)-**II** [5]	154 ± 7 (0.35 T)	207 ± 9 (2.4 T)	76 ± 3 (9.4 T)	78
$Gd_3N@C_{80}O_{11}(OH)_{21}$ [9]	137 (0.47 T)	140 (1.4 T)[b]	58 (9.4 T)	125
Magnevist® or Omniscan®	4-6	4-6	4-6	-

Although the (carboxyl)-**II** exhibits somewhat higher relaxivity than the unconjugated (amino)-**I** as illustrated in **Table 1**, it is important to demonstrate that both nanoparticles exhibit similar relaxivities once they are conjugated to the IL-13 peptide. In **Figure 6A**, the inversion-recovery images obtained using a clinical MR scanner (3 T, 123 MHz) of 5 mm tubes containing various concentrations of the (amino)-**I** and commercial MR contrast agent, Magnevist®. The 1.67 μM (amino)-**I** and 50 μM Magnevist® in water share similar contrast. (IL-13-amino)-**Ia** at different concentrations (1.48 μM and 2.26 μM) are compared with the (IL-13-carboxyl)-**IIa** (1.48 μM and 2.26 μM) in **Figure 6B**. Even though the ^1H MR relaxivity of (amino)-**I** are less than (carboxyl)-**IIa**, after conjugated with IL-13, both of them appear to give similar contrast at equal concentrations in the clinical 3 T MR image. Moreover, both the (IL-13-amino)-**Ia** and (IL-13-carboxyl)-**IIa** nanoparticles exhibit similar contrast at concentrations 20-50 times lower than commercial Magnevist®.

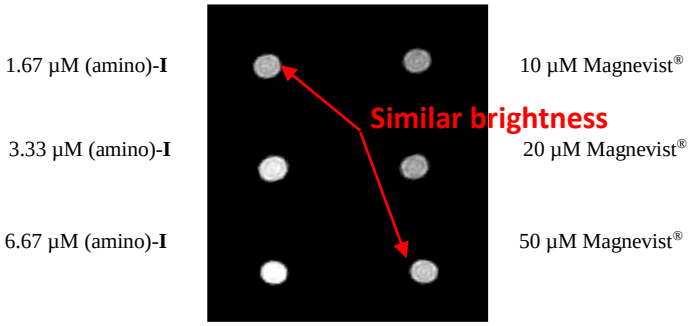

A

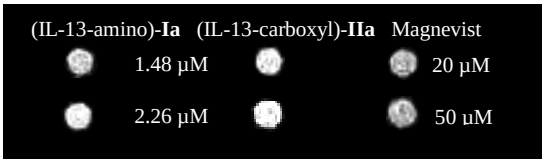

B

Figure 6. A) Inversion-recovery MR images (T_1=1000 ms, T_R=5000 ms, T_E=30 ms) with (amino)-**I** and Magnevist® as contrast agent. Left column from top to bottom: 1.67, 3.33 and 6.67 µM (amino)-**I** in water. Right column from top to bottom: 10, 20, 50 µM commercial agent Magnevist® in water. The 1.67 µM (amino)-**I** and 50 µM Magnevist® in water exhibit comparable contrast. B) Inversion-recovery MR images (T_1=1000 ms, T_R=5000 ms, T_E=30 ms) with (IL-13-amino)-**Ia** and (IL-13-carboxyl)-**IIa** and Magnevist® as contrast agent. The conjugated nanoparticles exhibit similar contrast with the commercial contrast agent.

The confocal microscopy studies (vide supra) of GBM U-251 cell tissue from orthotopically implanted U-251 GBM cell lines of both the (IL-13-amino)-**Ia** and (IL-13-carboxyl)-**IIa** nanoparticles demonstrate effective delivery of a targeting nanoparticle by non-invasive intravenous delivery. A 3 T MRI Siemens scanner was employed to demonstrate the potential clinical MRI feasibility of (IL-13-amino)-**Ia** and (IL-13-carboxyl)-**IIa** nanoparticles. In previous studies, we have shown that the (IL-13-carboxyl)-**IIa** nanoparticle provides excellent MRI contrast in animal GBM studies when administered by the invasive intracranial delivery approach CED.[25] In the current study, we find that both the (IL-13-amino)-**Ia** and (IL-13-carboxyl)-**IIa** provide targeting of an orthotopically implanted U-251 tumor model via intravenous tail delivery. The MRI results for the (IL-13-carboxyl)-**IIa** nanoparticle clearly exhibit targeting to the mouse brain tumor model as illustrated in **Figure S6A**. In an MR study with different inversion recovery times (50, 100, and 1000 ms), we have obtained 3 T MRI coronal images for the intravenously delivered (IL-13-amino)-**Ia** nanoparticle for a mouse model with U-251 tumor cells orthotopically implanted. In **Figure 7** (middle) are illustrated the coronal slices for the shortest and longest

inversion recovery times 50 and 1000 ms, respectively (100 ms MR data in **Figure S6B**). These inversion recovery times illustrate a characteristic unique to the MR contrast characteristics of the

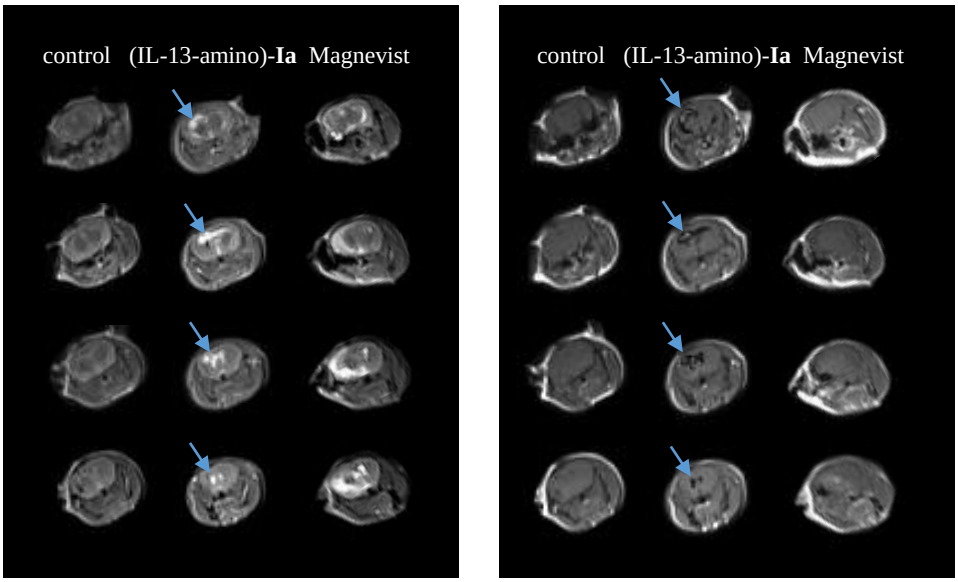

Figure 7. *In vivo* imaging following intravenous delivery of (IL-13-amino)-**Ia**; left: MRI of a mouse brain without tumor as control; middle: MRI of 15 minutes after intravenous injection of 300 µl (~0.9 nmol) of (IL-13-amino)-**Ia**. The bright contrast is due to the presence of (IL-13-amino)-**Ia**; right: MRI of 15 minutes after intravenous injection of 100 µl (50 nmol) of Magnevist® commercial contrast agent. Arrows indicate the location of tumor. A) T_1=50 ms, T_R=5000 ms, T_E=32 ms. B) T_1=1000 ms T_R=5000 ms, T_E=32 ms.

f-$Gd_3N@C_{80}$ nanoparticle platform that is different from most other contrast agents. Specifically, **Figure 7** shows that it is possible to track the material contrast with both T_1-weighted imaging characteristics where it shows high signal intensity with 50 ms inversion recovery times, (bright tumor area). Whereas, T_2-weighted imaging is illustrated for 1000 ms inversion recovery times where low signal intensity is observed, (dark tumor area). This is because the relaxivity ratio (r_1:r_2) is in a range that allows for T_1 enhancement while not overshortening T_2 and quenching the signal at low inversion recovery times, but quenching the signal at high inversion recovery times.[21] As a control, an animal without an implanted tumor is also shown (left, **Figure 7**). The (IL-13-amino)-**Ia** nanoparticle shows sharp definition of the tumor region in contrast with the indistinct tumor delineation of the control Magnevist® (right, **Figure 7**) even at 1-2 orders of magnitude lower

concentration. These results provide evidence that the nanoparticles (IL-13-amino)-**Ia** can be delivered by a less invasive intravenous injection approach with specific targeting of GBM U-251 mice brain tumor models and can be visualized at relatively low concentrations in a clinical MRI scanner.

2. 4 Conclusions

In this paper, we report preparation of a new amino-surface functionalized $Gd_3N@C_{80}$ platform, characterized as, $Gd_3N@C_{80}O_{12}(OH)_{10}(NH_2)_7(NO_2)_2$ ((amino)-**I**), which was compared with a previously described hydrophilic, carboxyl-surface functionalized $Gd_3N@C_{80}(OH)_{26}(CH_2CH_2COOM)_{16}$ ((carboxyl)-**II**). We have found that this hydrophilic nanoparticle, when conjugated with an interleukin-13 peptide, IL-13-$Gd_3N@C_{80}O_{12}(OH)_{10}(NH_2)_7(NO_2)_2$ ((IL-13-amino)-**Ia**), exhibits enhanced targeting of U-251 GBM cell lines. Our results support the notion that the (amino)-**I** positively charged nanoparticle exhibits enhanced charge attraction for GBM cellular endocytosis on the metallofullerene cage surface when directly compared with a carboxyl-surface functionalized nanoparticle, (IL-13-carboxyl)-**IIa**. Confocal microscopy results show that the (IL-13-amino)-**Ia** and (IL-13-carboxyl)-**IIa** both exhibit effective targeting of orthotopic GBM brain xenografts in mice by intravenous delivery. In similar fashion to the confocal microscopy results, we also demonstrate clinical MRI detection at low concentrations of this nanoparticle in U-251 GBM cells orthotopically implanted in mice. Although additional bio-distribution and cytotoxicity studies are needed, the feasibility of these nanoparticles as potential new agents for diagnostic clinical MRI applications can be clearly envisioned.

2. 5 Supplementary Figures

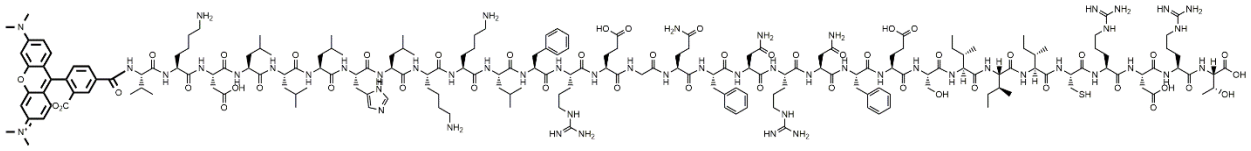

Figure S1. The structure of TAMRA-VDKLLLHLKKLFREGQFNREGQFNRNFESIIICRDRT-OH peptide.

Table S1. Curve fit results of C_{1s} binding energy.

Bond (C_{1s})	Binding Energy (eV)	Area	FWHM (eV)
C-C,C=C	284.70	6923	1.63
C-O,C-N	285.90	2714	2.15
C=O	288.27	1844	2.15
$\pi \rightarrow \pi^*$ satellite	290.46	598	1.98

Table S2. Curve fit results of N_{1s} binding energy.

Bond (N_{1s})	Binding Energy (eV)	Area	FWHM (eV)
Gd-N	397.86	135	2.02
$-NH_2$	399.28	877	1.93
$-NH_3^+$	402.2	129	1.86
$-NO_2$	406.50	261	2.02

Setting Gd-N as 1, since the total area of $–NH_2$ and $–NH_3^+$ is 7.45 times as Gd-N, there are total 7 $-NH_2$ and $–NH_3^+$ groups on the carbon cage. Base on the same rule, 2 $–NO_2$ groups have been introduced to the carbon cage. The percentage of C-O and C-N groups is 22.5%, which means there are total 19 (–OH, NH_2 and NO_2) functional groups on the cage. Therefore, the number of –OH groups is 10. According to the same rule, 12 C=O groups are on the carbon cage. Combined with C_{1s}/N_{1s} integration area and their sensitive factor (C_{1s} = 0.30, N_{1s} = 0.48), the average molecular formula can be designed as $Gd_3N@C_{80}O_{12}(OH)_{10}(NH_2)_7(NO_2)_2$.

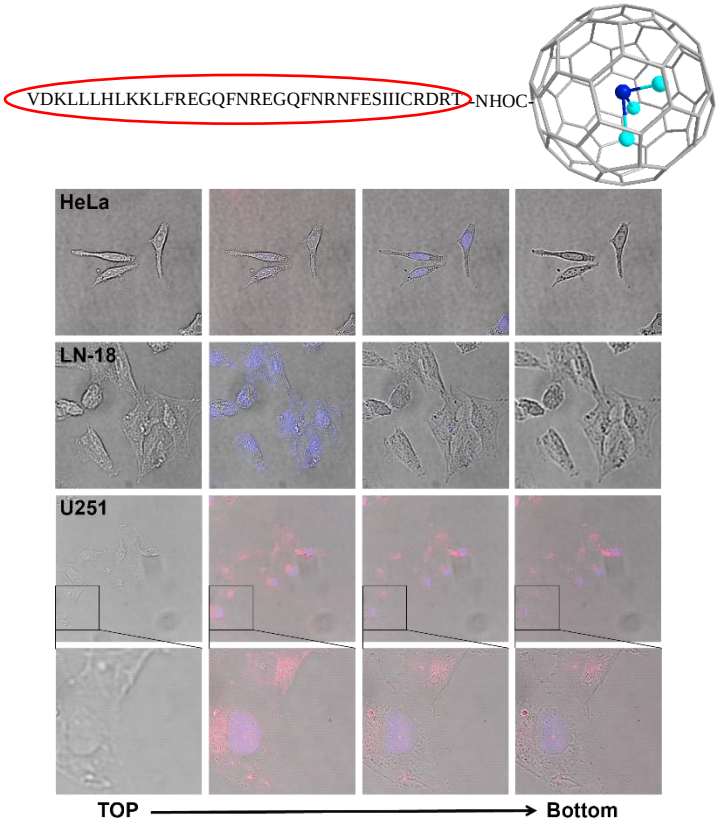

Figure S2. IL-13 peptide specifically delivered nanoparticles to IL-13Rα2 in U-251 but not IL-13Rα1 in LN18 and HeLa cells.

(IL-13-carboxyl)-**IIa** were added to U-251, LN18 and HeLa cells. We found that the TAMRA red fluorescence was only present inside of U251 cells but not LN18 or HeLa cells using confocal microscopy. Since LN18 and HeLa express IL-13Rα1, the absence of TAMRA fluorescence in these cells indicates that IL-13 peptide only binds to IL-13Rα2 but not IL-13Rα1. Therefore, this approach allows us to target IL-13Rα2 positive GBM tumors.

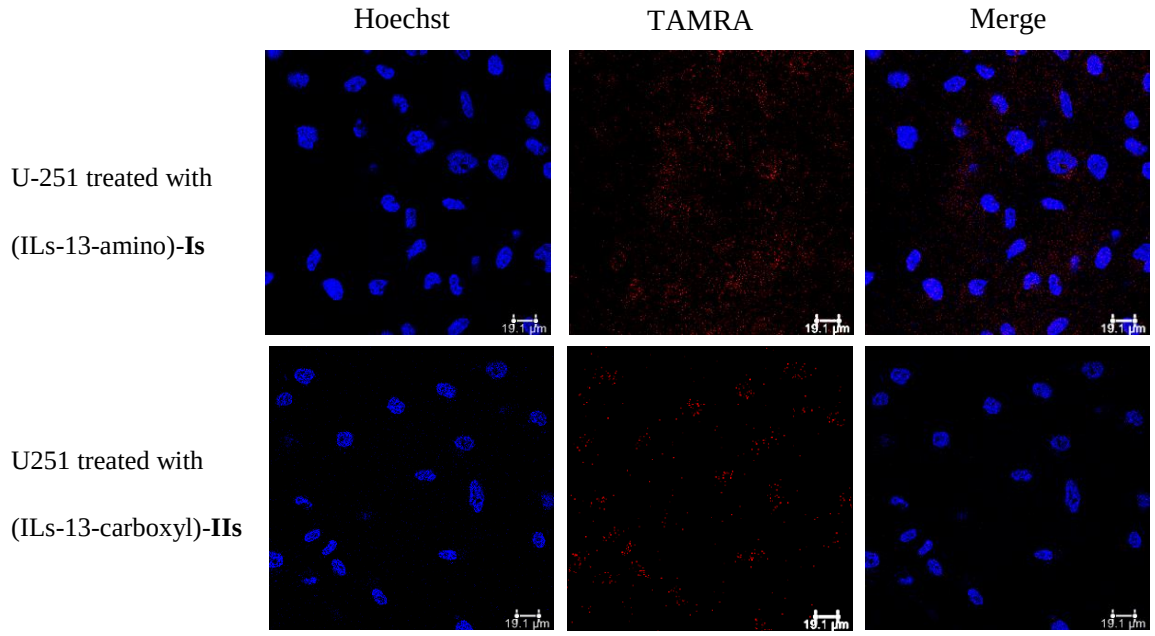

Figure S3. The images are projections of confocal z-stacks generated from sections of 5 to 6 µm thickness comparing internalization of TAMRA in U-251 cells. 63× images z5, 10 images were taken 5 u apart SCALE BAR = 19.1 µm. Top row is U-251 treated with (ILs-13-amino)-**Is**, bottom row is U-251 treated with (ILs-13-carboxyl)-**IIs**.

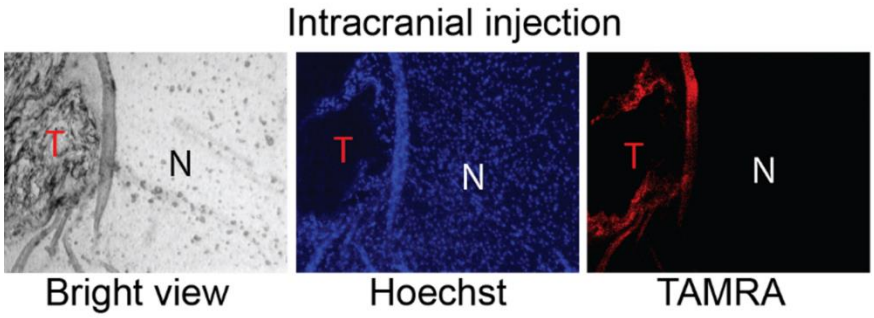

Figure S4. Fluorescent imaging of glioblastoma tumor after intracranial convection enhanced delivery of (IL-13-carboxyl)-**IIa**. Left - Bright Field, Center - Blue Fluorescence / Hoechst Stain, Right - Red Fluorescence / TAMRA.

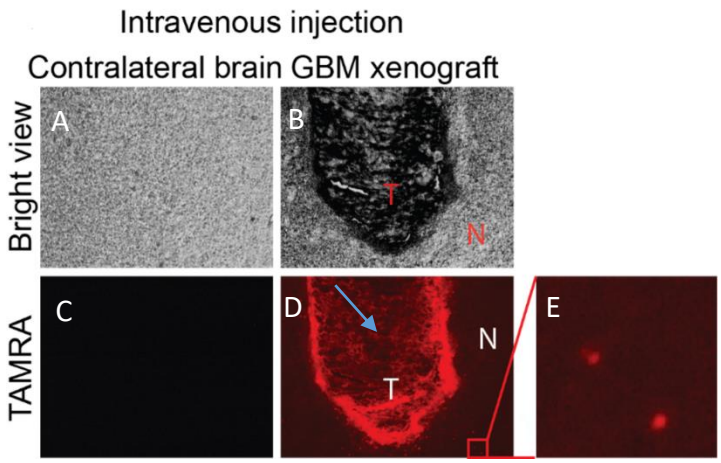

Figure S5. Fluorescent imaging of glioblastoma tumor after intravenous delivery of the (IL-13-carboxyl)-**IIa** nanoparticle. A) Bright field of contralateral brain without tumor tissue; B) Bright field of tumor tissue; C) No red signal at the contralateral brain; D) Red fluorescent imaging of tumor tissue (note signal from TAMRA around edges of tumor), the arrow points out the location of the necrotic center of the tumor; E) Areas of increased red signal on fluorescent microscopy at a distance from main tumor, possibly displaying areas of micrometastasis. (T=Tumor, N=Normal tissue).

Table S3. Comparison of relaxivities (in units of $mM^{-1}s^{-1}$ per mM of Gadofullerene Molecules) in pure water at 25ºC.

Compound	***r*$_2$ relaxivity $mM^{-1}s^{-1}$**		
	0.35-0.5 T	1.0-3.0 T	7.1-9.4 T
$Gd_3N@C_{80}O_{12}(OH)_{10}(NH_2)_7(NO_2)_2$	102 (0.47 T)	131. 1 (1.4 T)	96.1 (9.4 T)
$Gd_3N@C_{80}(OH)_{26}(CH_2CH_2COOM)_{16}$[1]	204 (0.35 T)	282 (2.4 T)	231 (9.4 T)
$Gd_3N@C_{80}O_{11}(OH)_{21}$[2]	146 (0.47 T)	180 (1.4 T)	215 (9.4 T)

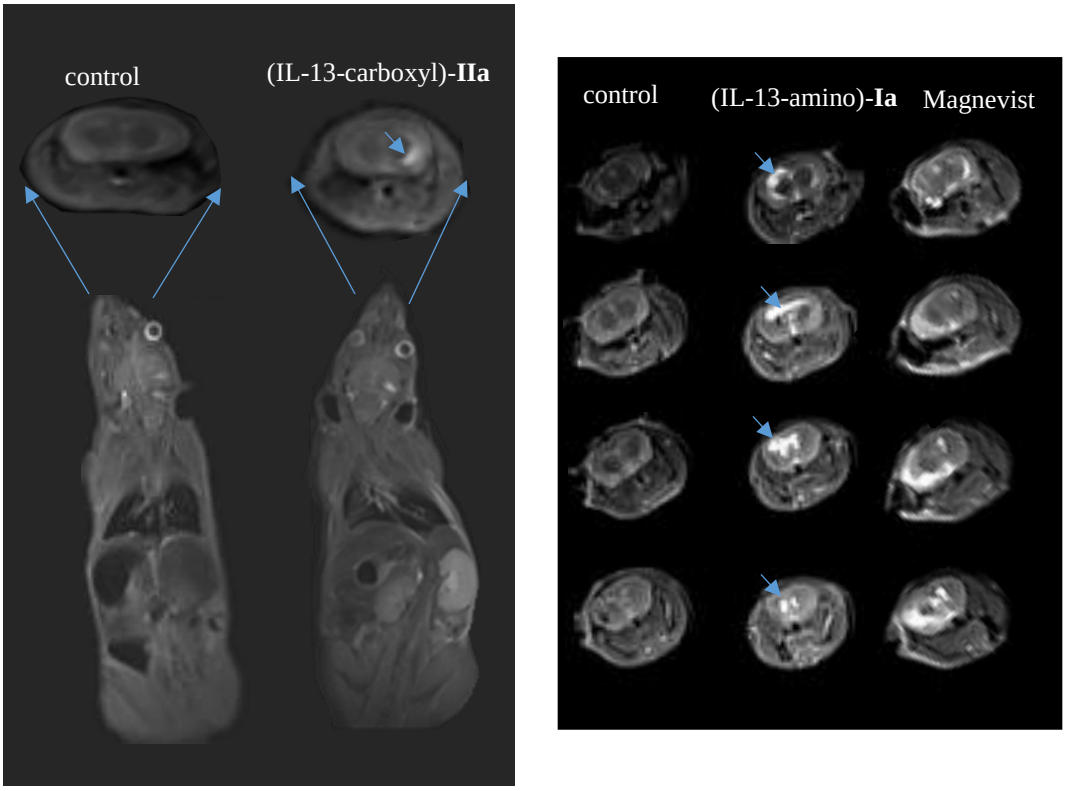

Figure S6. A) Clinical MRI 3T coronal slice and body images of orthotopic GBM murine models with intravenous delivery of 250 µl (~0.25 nmol) of (IL-13-carboxyl)-**IIa** (right) and with no targeting contrast agent administered (left). T_1=100 ms, T_R=5000 ms, T_E=30 ms. B) *In vivo* imaging following intravenous delivery of (IL-13-amino)-**Ia**; left: MRI of a mouse brain without tumor as control; middle: MRI of 15 minutes after intravenous injection of 300 µl (~0.9 nmol) of (IL-13-amino)-**Ia**. The bright contrast is due to the presence of (IL-13-amino)-**Ia**; right: MRI of 15 minutes after intravenous injection of 100 µl (50 nmol) of Magnevist® commercial contrast agent. Arrows indicate the location of tumor. T_1=100 ms, T_R=5000 ms, T_E=30 ms.

References

(1) Kumar, H. R.; Zhong, X.; Sandoval, J. A.; Hickey, R. J.; Malkas, L. H. *Expert Rev Neurother.* **2008**, *8*, 1497.

(2) Karathanasis, E.; Park, J.; Agarwal, A.; Patel, V.; Zhao, F.; Annapragada, A. V.; Hu, X.; Bellamkonda, R. V. *Nanotechnology* **2008**, *19*, 315101.

(3) Dubin, C. *Mech Eng. Nanotechnol* **2004**, *126(S)*, 10.

(4) Kelkar, S. S.; Reineke, T. M. *Bioconjugate Chem.* **2011**, *22*, 1879.

(5) Shu, C. Y.; Corwin, F. D.; Zhang, J. F.; Chen, Z. J.; Reid, J. E.; Sun, M. H.; Xu, W.; Sim, J. H.; Wang, C. R.; Fatouros, P. P.; Esker, A. R.; Gibson, H. W.; Dorn, H. C. *Bioconjugate Chem.* **2009**, *20*, 1186.

(6) Fatouros, P. P.; Corwin, F. D.; Chen, Z. J.; Broaddus, W. C.; Tatum, J. L.; Kettenmann, B.; Ge, Z.; Gibson, H. W.; Russ, J. L.; Leonard, A. P.; Duchamp, J. C.; Dorn, H. C. *Radiology* **2006**, *240*, 756.

(7) Zhang, E. Y.; Shu, C. Y.; Feng, L.; Wang, C. R. *J. Phys. Chem. B* **2007**, *111*, 14223.

(8) Zhang, J. F.; Fatouros, P. P.; Shu, C. Y.; Reid, J.; Owens, L. S.; Cai, T.; Gibson, H. W.; Long, G. L.; Corwin, F. D.; Chen, Z. J.; Dorn, H. C. *Bioconjugate Chem.* **2010**, *21*, 610.

(9) Zhang, J. Y.; Ye, Y. Q.; Chen, Y.; Pregot, C.; Li, T. H.; Balasubramaniam, S.; Hobart, D. B.; Zhang, Y. F.; Wi, S.; Davis, R. M.; Madsen, L. A.; Morris, J. R.; LaConte, S. M.; Yee, G. T.; Dorn, H. C. *J. Am. Chem. Soc.* **2014**, *136*, 2630.

(10) MacFarland, D. K.; Walker, K. L.; Lenk, R. P.; Wilson, S. R.; Kumar, K.; Kepley, C. L.; Garbow, J. R. *J. Med. Chem.* **2008**, *51*, 3681.

(11) Verma, A.; Stellacci, F. *Small* **2010**, *6*, 12.

(12) Kardys, A. Y.; Bharali, D. J.; Mousa, S. A. *J. Nanotechnol.* **2013**, *2013*, 8.

(13) Zhu, H. R.; Gao, L.; Jiang, X. L.; Liu, R.; Wei, Y. T.; Wang, Y. L.; Zhao, Y. L.; Chai, Z. F.; Gao, X. Y. *Chem. Commun.* **2014**, *50*, 3695.

(14) Mikawa, M.; Kato, H.; Okumura, M.; Narazaki, M.; Kanazawa, Y.; Miwa, N.; Shinohara, H. *Bioconjugate Chem.* **2001**, *12*, 510.

(15) Kato, H.; Kanazawa, Y.; Okumura, M.; Taninaka, A.; Yokawa, T.; Shinohara, H. *J. Am. Chem. Soc.* **2003**, *125*, 4391.

(16) Bolskar, R. D.; Benedetto, A. F.; Husebo, L. O.; Price, R. E.; Jackson, E. F.; Wallace, S.; Wilson, L. J.; Alford, J. M. *J. Am. Chem. Soc.* **2003**, *125*, 5471.

(17) Sitharaman, B.; Bolskar, R. D.; Rusakova, I.; Wilson, L. J. *Nano Lett.* **2004**, *4*, 2373.

(18) Stevenson, S.; Rice, G.; Glass, T.; Harich, K.; Cromer, F.; Jordan, M. R.; Craft, J.; Hadju, E.; Bible, R.; Olmstead, M. M.; Maitra, K.; Fisher, A. J.; Balch, A. L.; Dorn, H. C. *Nature* **1999**, *402*, 898.

(19) Zhang, J. Y.; Stevenson, S.; Dorn, H. C. *Acc. Chem. Res.* **2013**, *46*, 1548.

(20) Fatouros, P. P.; Shultz, M. D. *Nanomedicine* **2013**, *8*, 1853.

(21) Shultz, M. D.; Wilson, J. D.; Fuller, C. E.; Zhang, J. Y.; Dorn, H. C.; Fatouros, P. P. *Radiology* **2011**, *261*, 136.

(22) Shultz, M. D.; Duchamp, J. C.; Wilson, J. D.; Shu, C. Y.; Ge, J. C.; Zhang, J. Y.; Gibson, H. W.; Fillmore, H. L.; Hirsch, J. I.; Dorn, H. C.; Fatouros, P. P. *J. Am. Chem. Soc.* **2010**, *132*, 4980.

(23) Debinski, W.; Gibo, D. M.; Slagle, B.; Powers, S. K.; Gillespie, G. Y. *Int J Oncol* **1999**, *15*, 481.

(24) Debinski, W.; Gibo, D. M.; Hulet, S. W.; Connor, J. R.; Gillespie, G. Y. *Clin Cancer Res* **1999**, *5*, 985.

(25) Fillmore, H. L.; Shultz, M. D.; Henderson, S. C.; Cooper, P.; Broaddus, W. C.; Chen, Z. J.; Shu, C. Y.; Zhang, J.; Ge, J.; Dorn, H. C.; Corwin, F.; Hirsch, J. I.; Wilson, J.; Fatouros, P. P. *Nanomedicine (Lond)* **2011**, *6*, 449.
(26) Zheng, J. P.; Zhen, M. M.; Ge, J. C.; Liu, Q. L.; Jiang, F.; Shu, C. Y.; Alhadlaq, H. A.; Wang, C. R. *Carbon* **2013**, *65*, 175.
(27) Lu, X.; Li, H.; Sun, B.; Shi, Z.; Gu, Z. *Carbon* **2005**, *43*, 1546.
(28) Sun, D. Y.; Huang, H. J.; Yang, S. H.; Liu, Z. Y.; Liu, S. Y. *Chem. Mater.* **1999**, *11*, 1003.
(29) Matsubayashi, K.; Kokubo, K.; Tategaki, H.; Kawahama, S.; Oshima, T. *Fuller. Nanotub. Car. N.* **2009**, *17*, 440.
(30) Yang, G.; Hu, H.; Zhou, Y.; Hu, Y.; Huang, H.; Nie, F.; Shi, W. *Sci Rep* **2012**, *2*, 698.
(31) Laus, S.; Sitharaman, B.; Toth, V.; Bolskar, R. D.; Helm, L.; Asokan, S.; Wong, M. S.; Wilson, L. J.; Merbach, A. E. *J. Am. Chem. Soc.* **2005**, *127*, 9368.
(32) Adiseshaiah, P.; Dellinger, A.; MacFarland, D.; Stern, S.; Dobrovolskaia, M.; Ileva, L.; Patri, A. K.; Bernardo, M.; Brooks, D. B.; Zhou, Z.; McNeil, S.; Kepley, C. *Invest Radiol* **2013**, *48*, 745.
(33) Brown, C. E.; Warden, C. D.; Starr, R.; Deng, X.; Badie, B.; Yuan, Y. C.; Forman, S. J.; Barish, M. E. *PLoS One* **2013**, *8*, e77769.
(34) Jacobs, V. L.; Valdes, P. A.; Hickey, W. F.; De Leo, J. A. *Asn Neuro* **2011**, *3*.
(35) Caravan, P.; Ellison, J. J.; McMurry, T. J.; Lauffer, R. B. *Chem. Rev.* **1999**, *99*, 2293.
(36) Chang, C. A. *Invest Radiol* **1993**, *28*, S21.

Chapter 3 Detecting chronic post-traumatic osteomyelitis of mouse tibia via an IL-13Rα2 targeted metallofullerene magnetic resonance imaging probe

This chapter is adopted from the manuscript published on Bioconjugate Chemistry with appropriate modifications under the permission of the American Chemical Society. Full text of the published manuscript entitled "Detecting chronic post-traumatic osteomyelitis of mouse tibia via an IL-13Rα2 targeted metallofullerene magnetic resonance imaging probe" by Li Xiao[§], Tinghui Li[§], Mengmeng Ding, Jiezuan Yang, José Rodríguez-Corrales, Nicholas Nacey, David B. Weiss, Li Jin, Harry C. Dorn, and Xudong Li.[§] These authors contributed equally to the current work. This work can be obtained at http://pubs.acs.org/doi/abs/10.1021/acs.bioconjchem.6b00

Abstract

Differential diagnosis of chronic post-traumatic osteomyelitis (CPO) from aseptic inflammation remains challenging, since both pathological processes share similar clinical symptoms. Here we utilized a novel targeted metallofullerene nanoparticle based magnetic resonance imaging (MRI) probe IL-13-TAMRA-$Gd_3N@C_{80}(OH)_{30}(CH_2CH_2COOH)_{20}$ to detect CPO in mouse tibia via over-expressed IL-13Rα2 receptors. The functionalized metallofullerene was characterized by X-ray photoelectron spectroscopy. Upon lipopolysaccharides (LPS) stimulation, macrophage Raw 264.7 cells showed elevated IL-13Rα2 expression via immunofluorescence staining and increased MRI probe binding via built-in TAMRA fluorescence imaging. Trauma was induced in both tibia of mice and bacteria soaked suture was inserted into the right tibia to initiate infection. During the acute phase (1.5 weeks), luminol-bioluminescence imaging revealed much higher myeloperoxidase activity in the infected tibia compared to the sham. In the chronic phase (4 weeks), X-ray radiography illustrated bone deformation in the infected tibia compared to the sham. With T_1 weighted sequences, the probe clearly exhibited hyperintensity in the infection foci at both

acute and chronic phases, which was not observed in the sham tibia. Histological analysis revealed severe bone structural destruction and massive inflammatory cell infiltration in the infected tibia. Immunohistochemistry confirmed abundant expression of IL-13Rα2 in the infection site. In summary, we developed a non-invasive imaging approach to detect and differentiate CPO from aseptic inflammation using a new IL-13Rα2 targeted metallofullerene MRI probe. In addition, for the first time, IL-13Rα2 was investigated as a unique biomarker in the context of osteomyelitis. Our data established a foundation for the translational application of this MRI probe in the clinical differentiation of CPO.

3.1 Introduction

Osteomyelitis is an infection of the bone marrow and adjacent bone typically caused by Staphylococcus aureus (*S. aureus*), which associates with high levels of inflammation and bone tissue destruction[1]. Chronic post-traumatic osteomyelitis (CPO) can develop through contiguous spread from a local or circulating infective pathogens after trauma, bone surgery, or joint replacement[2]. The average rate of post traumatic infection in open tibia fractures is approximately 10%[3]. In addition, the dramatically risen number of joint replacement procedures has associated with increased incidents of infection, and projected to increase over the next 15 years[4]. Chronic osteomyelitis is painful and debilitating and is associated with considerable morbidity and may be limb-threatening[5]. Consequently, the rate of clinical failures in osteomyelitis treatment is high, and frequently results in loss of function and/or amputation[6]. Therefore, prompt and accurate diagnosis are extremely critical to early intervention and positive clinical outcome.

Unfortunately, clinical differential diagnosis of CPO from aseptic inflammation remains challenging, since many early signs of infection are similar to sterile (asepsis) inflammatory reactions following trauma or surgery. Bone culture remains as the gold standard of diagnosis, however, high false-negative rates of ~40% has been reported[7-9]. Although computed tomography (CT) can delineate lesions in the medullary canal and inflammation in the soft tissues, the presence of other pathological processes, such as stress fractures, osteoid osteomas, and benign tumor, may confound the diagnosis[10]. Nuclear medicine such as 99mTc-methylene diphosphonate (^{99m}Tc-MDP), ^{18}F-fluorodeoxyglucose (FDG), or radiolabeled white blood cells (WBC) has showed high sensitivity to track inflammatory activities associated with infection, nevertheless, these methods are still suffered from aforementioned issues[10-12].

In recently years, research efforts have shifted to develop targeted imaging probes for various modalities. Peptide, proteins or nanoparticles have been chemically synthesized to be optical, nuclear and MRI imaging probes. In general, optical imaging is preferable in research setting with limited clinical potential[13-14]. Nuclear imaging has high sensitivity and specificity[15-17], however, their clinical application might be impeded by laborious synthetic procedures, limited shelf-life of radio-isotopes, and narrow detection window following probe administration. Targeted MRI appears as a favored choice as it not only provides an excellent imaging contrast and resolution, but also allows detection of biological response at functional or even molecular level without employing ionizing radiation[18]. Recently, superparamagnetic iron oxide nanoparticles (SPIONs) have been utilized as contrast agents for *in vivo* MRI detection of infiltrated macrophages to identify infection in patients with septic arthritis and osteomyelitis, given to the phagocytosis by macrophages after probe administration [19-20]. This is because the persistence of the pathogenic agents during the chronic stage of osteomyelitis leads to constant recruitment of macrophages to the site of infection, resulting in macrophages as the most abundant immune cells in the infection foci, unlike aseptic inflammation[21-22]. Although macrophage phagocytosis contributes to the detection of most nanoparticle based imaging probes, this mechanism still relies on a passive uptake. And thus receptor-mediated targeted MRI imaging using functionalized nanoparticles would be more appealing for enhanced imaging contrast and minimized dosage.

Interleukin-13 (IL-13), a type 2 cytokine, plays a key role in the host defense such as allergic inflammation via binding to receptors on surfaces of immune and structural cells[23,24]. IL-13 mediates its effects via a complex receptor system that includes IL-4Rα, IL-13Rα1, and IL-13Rα2[13-18]. IL-13Rα1 and IL-4Rα form a heterodimeric complex that signals through the JAK-STAT pathway. In contrast, IL-13Rα2 has been postulated to be a decoy receptor, not responsible

for the signal transduction[19,20]. Increased expression of IL-13Rα2 has been reported to promote tumor progression in glioma and other tumor models[23-25] and showed a protective role in a mouse model of cutaneous inflammation[26]. However, the expression of IL-13Rα2 has not been investigated in the infection diseases. Considering its important role in several inflammatory models and the immune system, we hypothesize that this receptor may also be involved in the infection condition and thus can serve as an *in vivo* biomarker for diagnosis.

In the current study, we aim to utilize a novel class of gadolinium cluster encapsulated metallofullerene ($Gd_3N@C_{80}$) as a MRI contrast agent to detect CPO in mouse tibia via binding to over-expressed IL-13Rα2 receptors in the infection foci. The metallofullerene was functionalized and conjugated to a fragment of IL-13 with optimized coupling conditions to deliver a more homogenous and bioavailable nanoparticle product, IL-13-TAMRA-$Gd_3N@C_{80}(OH)_{30}(CH_2CH_2COOH)_{20}$. This targeted metallofullerene MRI probe specifically bound to lipopolysaccharides (LPS) stimulated macrophages and significantly delineate the hyper-intense MRI signal in the infection foci of tibia CPO model. Correspondingly, over-expression of IL-13Rα2 receptors were discovered in both LPS-elicited macrophages *in vitro* and infected tibia. The success of mouse CPO model was also validated.

3.2 Experimental Section

3.2.1 Chemical materials

$Gd_3N@C_{80}$ was purchased from LUNA Innovations (Danville, VA). The TAMRA-VDKLLLHLKKLFREGQFNREGQFNRNFESIIICRDRT-OH (IL-13-TAMRA peptide), a shorter active peptide for IL-13Rα2 receptor sites, was purchased from New England Peptide LLC (Gardner, MA). Gibco Dulbecco's Modified Eagle Medium (high glucose 4.5 g/L) (DMEM), fetal bovine serum (FBS), and Prolong Gold antifade mountant with DAPI were purchased from Life Technologies (Grand Island, NY). Dulbecco's phosphate-buffered saline (DPBS), and penicillin-streptomycin were purchased from Gibco Invitrogen (Carlsbad, CA). Other chemicals, such as 2-(N-morpholino)ethanesulfonic acid (MES), *1-Ethyl-3-(3-dimethylaminopropyl) carbodiimide* (EDC), and N-hydroxysulfosuccinimide (Sulfo-NHS) were obtained from Sigma-Aldrich (St. Louis, MO) unless mentioned.

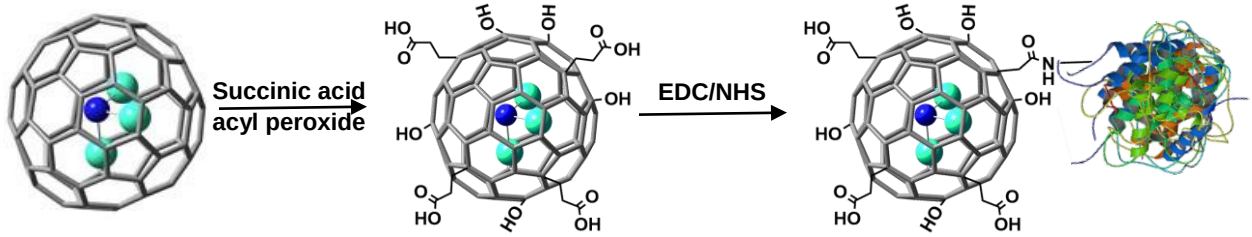

Scheme 1. Functionalization and conjugation process of IL-13-TAMRA-$Gd_3N@C_{80}(OH)_{30}(CH_2CH_2COOH)_{20}$ (gray, carbon; aqua, gadolinium ion; blue, nitrogen).

3.2.2 Conjugation of IL-13-TAMRA-$Gd_3N@C_{80}(OH)_{30}(CH_2CH_2COOH)_{20}$

The elaboration of the carboxyl group onto the cage surface of $Gd_3N@C_{80}$ was performed using an improved procedure from our earlier studies[26]. Briefly, 10 mg of the metallofullerene, $Gd_3N@C_{80}$ and 8 mg succinic acid acyl peroxide (5 Equiv) were dissolved in 10 mL of 1,2-dichlorobenzene (**Scheme 1**). The resultant solution was deoxygenated with flowing argon and heated at 84 °C for five days. Additional succinic acid acyl peroxide (5 equiv) was added every 12 hours. After the reaction, 8 mL of 0.2 M NaOH was added to extract the water-soluble product.

The top layer was concentrated, and the residue was purified by a Sephadex G-25 size-exclusion gel column[27].

A volume of 500 μL of fullerene surface carboxylated $Gd_3N@C_{80}$ was dissolved in MES (pH=5.3) solution, then filtered through a 0.45 μm syringe filter. The carboxyl groups were activated by 70 μL of 0.5 M EDC and the same amount of Sulfo-NHS. After 10 min, 85 μL of the IL-13-TAMRA peptide (dissolved in DMSO, 2mg/ml) was added, vortexed and incubated at room temperature for 1.5 h. Then 70 μL of 0.5 M hydroxylamine solution was introduced to quench the reaction. The resulting solution was filtered through Zeba-brand spin columns at a rate of 5000 rpm for 2 min. The receptacle portion of the spin column was thoroughly rinsed to ensure that all the product was removed from the column[28-29].

3.2.3 Characterization of functionalized $Gd_3N@C_{80}$ with IL-13 peptide loading per fullerene

The functionalized metallofullerene was characterized by XPS to measure the elemental composition and empirical formula. To determine the loading of IL-13 peptide per fullerene cage, a calibration curve was constructed by diluting a stock solution of IL-13-TAMRA in DMSO/water. Stock solutions of functionalized metallofullerene conjugated with IL-13-TAMRA were prepared in the same co-solvent. The concentration of functionalized $Gd_3N@C_{80}$ was measured by ICP-MS. IL-13-TAMRA standards and IL-13-TAMRA-functionalized $Gd_3N@C_{80}$ samples were transferred into a black Costar 96-well plate, after which fluorescence was measured in Cytation3 Cell Imaging Multi-Mode Reader (excitation 550 nm, emission 585 nm, gain 120, optics on the bottom, xenon flash light source, 100 ms delay).

3.2.4 Relaxivity Measurements of the functionalized $Gd_3N@C_{80}$

The T_1 and T_2 relaxation times were measured on Bruker Minispec mq 20 (0.47 T), mq 60 (1.41 T) analyzers. The *inversion−recovery* method was used to measure the spin−lattice relaxation time

T_1, and the *Carr−Pucell−Meiboom−Gill* (CPMG) method was used for the spin−spin relaxation time T_2 measurement. Errors in T_1 and T_2 values were less than ±2%.

3.2.5 *In vitro* MRI study of the functionalized $Gd_3N@C_{80}$

The *in vitro inversion-recovery* MR images were obtained under a 3T clinical scanner for the visual confirmation of the efficiency of the functionalized fullerene working as a contrast agent. Various concentrations of the Gd based fullerenes, and the commercial contrast agent Omniscan® were used and compared.

3.2.6 Raw 264.7 cell culture, immunofluorescence staining and probe binding

Raw 264.7 cells were cultured in complete growth medium (DMEM +10% FBS+1% Penicillin/Streptomycin) at 37 °C with 5% CO_2. One day before the experiment, cells were seeded onto sterile coverslips in a 6-well plate at a density of 4×10^5 cells/mL and incubated overnight. Then cells were treated with or without LPS (100 ng/mL) for 24 hrs in serum free media.

For immunofluorescence staining[38], cells on coverslips were fixed with 4% paraformaldehyde for 30 min. Goat anti-mouse IL-13Rα2 antibody (1:5000) was used to detect IL-13Ra2, and followed by incubation with Alexa Fluo 594 chicken anti-goat secondary antibody, (1:5000, Invitrogen, Waltham, MA) for 30 min. IgG control was performed excluding the primary antibody incubation. Cell nuclei were countered stained with DAPI.

For probe binding experiments, cells treated with or without LPS were fixed with 4% paraformaldehyde for 30 min and incubated with 1 μM IL-13-funcationalized $Gd_3N@C_{80}$ MRI probe labeled with TAMRA, washed with PBS twice. Cell nuclei were countered stained with DAPI. Fluorescence images were taken with a fluorescence microscope (LSM 510-UV, Carl Zeiss, Germany) and processed by NIS Element Basic Research software (Nikon Instruments Melville,

NY) with the exact same setting for infected and sham tibia samples following our published protocols[38].

3.2.7 CPO mouse model

Animal protocol was approved by the Institutional Animal Care and Use Committee at the University of Virginia. *S. aureus* ATCC 25923 (ATCC, VA) cultivated overnight in terrific broth medium at room temperature. Balb/C mice (8-10 weeks old, female, 20-25g, Envigo) were maintained in a 12-hour light cycle vivarium facility. 5 mm long Vicryl suture (#2-0) were soaked in 1×10^7 CFU/mL (150 μL) or saline (150 μL) for 30 min. a hole was developed by a 27G needle in the proximal end of tibia, followed by inserting bacteria (right) or PBS (left) soaked suture intramedullary (n=5). Body weights were continuously during the experimental period.

3.2.8 Luminol-bioluminescence imaging of myeloperoxidase

At 1.5 weeks post infection, bioluminescence imaging was performed at 20 min after intraperitoneal injection of luminol solution (200 μL, 5 mg/100 μL in DMSO) on Xenogen IVIS Spectrum (Perkin Elmer, CA) and processed on *Live Image* software (Perkin Elmer) with open filter and exposure time of 60 s[16].

3.2.9 *In vivo* MRI study of IL-13-TAMRA-$Gd_3N@C_{80}$ probe.

In vivo MRI was acquired at a 7 T ClinScan Bruker/Siemens MR scanner (Bruker, Billerica, MA) at 1.5 and 4 weeks after bacterial inoculation. Immediately before the scan, probe IL-13-funcationalized $Gd_3N@C_{80}$ (4.4 nmol per 20 g body weights) or commercial available contrast agent Dotarem (50 nmol per 20 g body weights) (Guerbet, Bloomington, IN) was administered intravenously into mice. Animals were anesthetized with 1.5% isoflurane during the procedure. Tibiae were imaged by T_1 weighted images with following settings: T_1 (Spin Echo)-Voxel size 0.102 x 0.102 x 0.7 mm, T_R 600 ms, T_E 11 ms, Averages 3, Slice Thickness of 0.7mm, matrix-

256x256; MR images were segmented using Siemens Syngo FastView (Siemens Medical Solutions, Malvern, PA)[15].

3.2.10 X-Ray radiography

Immediately after the last MRI scan at 4 weeks post infection, mice were euthanized by CO_2 asphyxiation. X-ray radiograph was captured using a low energy X-ray (Faxitron, Model 43805N, OR) with an exposure time of 30 s (30 kV). X-ray films were then processed in Konica Minolta SRX-101A Tabletop Processor (Konica Minolta Business Solutions, Ramsey, NJ)[38].

3.2.11 Histological and immunohistochemical staining

Mouse tibiae were dissected and fixed in 10% formalin for 3 days, decalcified in 0.25 M EDTA for 2 weeks, embedded in paraffin and sectioned into 5 μm thickness. Hematoxylin and eosin (H/E) staining was performed following standard protocols[39-40]. To confirm expression of IL-13Rα2 after infection and traumatic surgery, immunohistochemical staining was performed following our previously published protocols[41]. Briefly, tibia sections were deparaffinized, rehydrated and treated with 3% hydrogen peroxide in methanol for 30 min for blockade of endogenous peroxidase and followed by antigen retrieval in 10 mM citrate buffer (pH 6.0) for 30 min in 85 °C water bath. Sections were then incubated with goat anti-mouse IL-13Rα2 antibody (1:5000, R&D Systems, Minneapolis, MN) overnight at 4 °C, and followed by secondary biotinylated horse anti-goat IgG antibody (1: 200, Vector Laboratories, Burlingame, CA).

3.2.12 Statistical analysis

All *in vitro* experiments were performed at least in triplicate and data were presented as mean ± STDEV. Data comparing two groups were analyzed with a Student's t-Test. A p-value of less than 0.05 was considered statistically significant.

3.3 Results and Discussion

3.3.1 Characterization of MRI probe

The XPS survey and multiplex spectra for functionalized fullerene are presented in **Figure 1**. In the survey XPS spectrum, the peaks centered at 284, and 532 eV are characteristics of the presence of carbon and oxygen species, respectively. In the multiplex spectrum, the C_{1s} peaks, centered at binding energy values of 284.3, 285.6, and 287.4 eV, were assigned to the C−C and C=C, C−O, and C=O, respectively. Based on the peak deconvolution of the XPS profile, the average formula for functionalized fullerene can be described as $Gd_3N@C_{80}(OH)_{30}(CH_2CH_2COOH)_{20}$. In order to enhance the bioavailability and hydrophilicity of the functionalized metallofullerene, we adopted a much longer reaction time (5 days) here allowing a higher derivatization level of hydroxyl and carboxylic groups onto the nanoparticle surface compared to our previous study (2 days) [27].

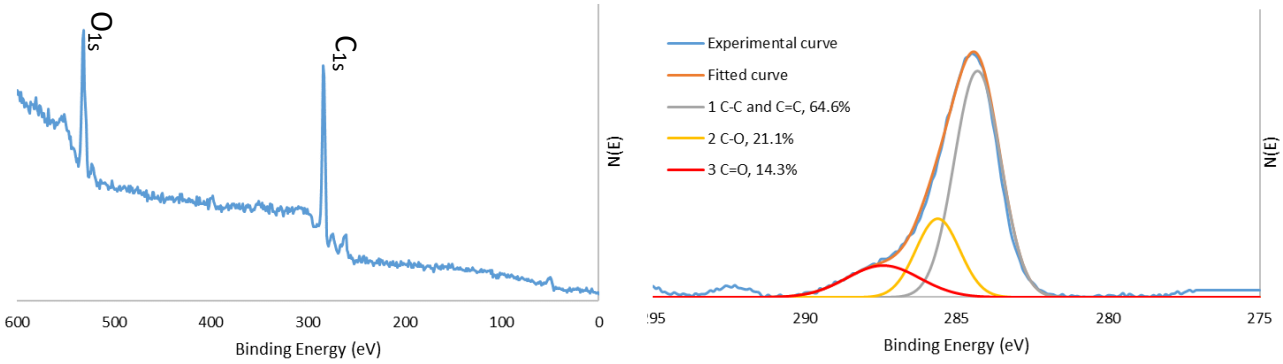

Figure 1. XPS survey (left) and multiplex (right) spectral regions of $Gd_3N@C_{80}(OH)_{30}(CH_2CH_2COOH)_{20}$.

3.3.2 Determination of the Conjugation Level of IL-13 Peptide per $Gd_3N@C_{80}$.

The concentrations of the IL-13 peptide based on the amount of TAMRA dye were determined as followed. Calibration curves of IL-13-TAMRA were constructed using five serial diluted standard solutions and one co-solvent blank at maximum fluorescence emission at 585 nm. Three sample solutions of IL-13-TAMRA-$Gd_3N@C_{80}(OH)_{30}(CH_2CH_2COOH)_{20}$ were fitted in the calibration curve to obtain IL13-TAMRA concentrations (**Supplemental Figure 1**). Based on triplicated measurements, the average peptide loading (IL-13-TAMRA per $Gd_3N@C_{80}$) was calculated based

on molar amounts of IL-13-TAMRA and $[Gd_3N@C_{80}(OH)_{30}(CH_2CH_2COOH)_{20}]_n$. As shown in **Table 1**, approximately 1~2 IL-13 peptide units were conjugated per $Gd_3N@C_{80}(OH)_{30}(CH_2CH_2COOH)_{20}$ cage. Comparing to the value estimated in our earlier study[28], the number of IL-13 peptide units per metallofullerene cage in the current study was significantly lower, since we employed a shorter time period (1.5 hr versus 12 hr) in the conjugation procedure. Our result suggested an improved homogeneity of these nanoparticle samples, which would ultimately reduce the experimental variability in biological tests.

Table 1. Concentration of the IL-13-TAMRA, and functionalized $Gd_3N@C_{80}$ (per cage).

	Intensity of IL-13-TAMRA-f-$Gd_3N@C_{80}$	Conc of IL-13-TAMRA (μM)	Conc of f-$Gd_3N@C_{80}$ (μM)	Peptide loading of per f-$Gd_3N@C_{80}$
Sample 1	10157	1.58	1.08	1.40
Sample 2	17145	2.66	1.62	1.64
Sample 3	24405	3.79	2.70	1.46

3.3.3 Relaxivity Measurements of the functionalized $Gd_3N@C_{80}$

The r_1 and r_2 relaxivity results of $[Gd_3N@C_{80}(OH)_{30}(CH_2CH_2COOH)_{20}]n$ are summarized in **Table 2**. The nuclear magnetic resonance relaxivity were calculated by the general equation:

$$\frac{1}{T_{i\ obs}} = \frac{1}{T_{i\ H_2O}} + \frac{1}{T_{i\ para}} = \frac{1}{T_{i\ H_2O}} + r_i[M]$$

The relaxation rate is determined by both diamagnetic (pure water) and paramagnetic (contrast agent) components. The ratio of paramagnetic relaxation rate to the concentration (M) is the relaxivity (r_i) of the paramagnetic compound, which can be experimentally obtained by the slope of $1/T_i$ versus concentrations of the paramagnetic contrast agents[29]. These results can be compared with the relaxivity of the commercial contrast agents, Omniscan®, which exhibit much lower relaxivity at all magnetic field strengths.

Table 2. Relaxivities of functionalized Gadolinium Metallofullerenes (Units of $mM^{-1}\ s^{-1}$ per mM in pure water at 25 °C).

Contrast agents	r_1 relaxivity ($mM^{-1}s^{-1}$)		r_2 relaxivity ($mM^{-1}s^{-1}$)	
	0.47 T	1.41 T	0.47 T	1.41 T
f-$Gd_3N@C_{80}$ (2-100 µM)	91	118	110	145
Omniscan®	~4	~4	~4	~4

3.3.4 In vitro MR contrast ability of the functionalized $Gd_3N@C_{80}$ and IL-13-TAMRA-$Gd_3N@C_{80}(OH)_{30}(CH_2CH_2COOH)_{20}$

In **Figure 2**, the *inversion-recovery* images obtained using a clinical 3T MR scanner with 5 mm NMR tubes containing various concentrations of the $[Gd_3N@C_{80}(OH)_{30}(CH_2CH_2COOH)_{20}]n$ and commercial MR contrast agent, Omniscan®. The 0.33 µM functionalized metallofullerene and 20 µM Omniscan® in water share similar contrast. The contrast ability of IL-13 conjugated MRI probe was demonstrated in earlier publication[29]. These results show that the functionalized $Gd_3N@C_{80}$ has outstanding contrast relatively to commercial agents.

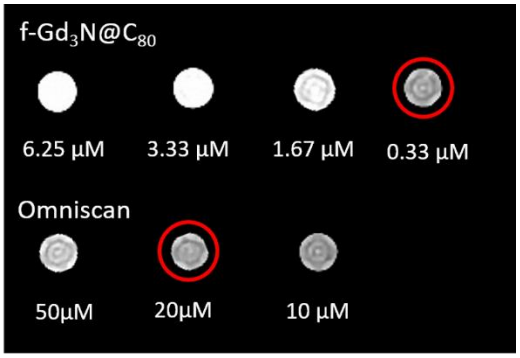

Figure 2. *Inversion-recovery* MR images (T_1=1000 ms, T_R=5000 ms, T_E=30 ms) with f-$Gd_3N@C_{80}$ and Omniscan® as contrast agent. Top row from right to left: 0.33, 1.67, 3.33 and 6.25 µM f-$Gd_3N@C_{80}$ in water. Bottom row from right to left: 10, 20, 50 µM commercial agent in water. The 0.33 µM f-$Gd_3N@C_{80}$ and 20 µM Omniscan® in water exhibit comparable contrast.

3.3.5 Increased expression of IL-13Rα2 receptors in macrophages upon LPS stimulation

IL-13Rα2 has been discovered as a decoy (no signaling) receptor in pathological context involving in type 2 helper T (Th2) cell-driven inflammation, such as asthma[30-32]. It is also the most extensively studied targets in combating glioblastoma multiforme due to its selective expression[33].

However, there has been no report on the expression of IL-13Rα2 in the infectious condition. Monocytes and macrophages are key players in the innate immune system, representing the first line of defense against microorganism[33]. In this study we employed Raw 264.7 macrophage cell line to detect the expression of IL-13Rα2 upon stimulation with LPS to mimic the inflammatory response during bacterial infection in vitro. Contrary to the low expression in unstimulated macrophages, our immunofluorescence staining results in **Figure 3A** showed abundant IL-13Rα2 expression after LPS treatment (red fluorescence signal). IgG was used as a negative control. This result indicated a potential role of IL-13Rα2 receptor in the macrophage-associated inflammatory response induced by the infection.

3.3.6 Preferential probe binding with Raw 264.7 cells upon LPS stimulation

With the built-in feature of TAMRA fluorescence dye on the MRI probe, we further assessed whether escalation of receptor expression on LPS stimulated Raw 264.7 cells could result in higher

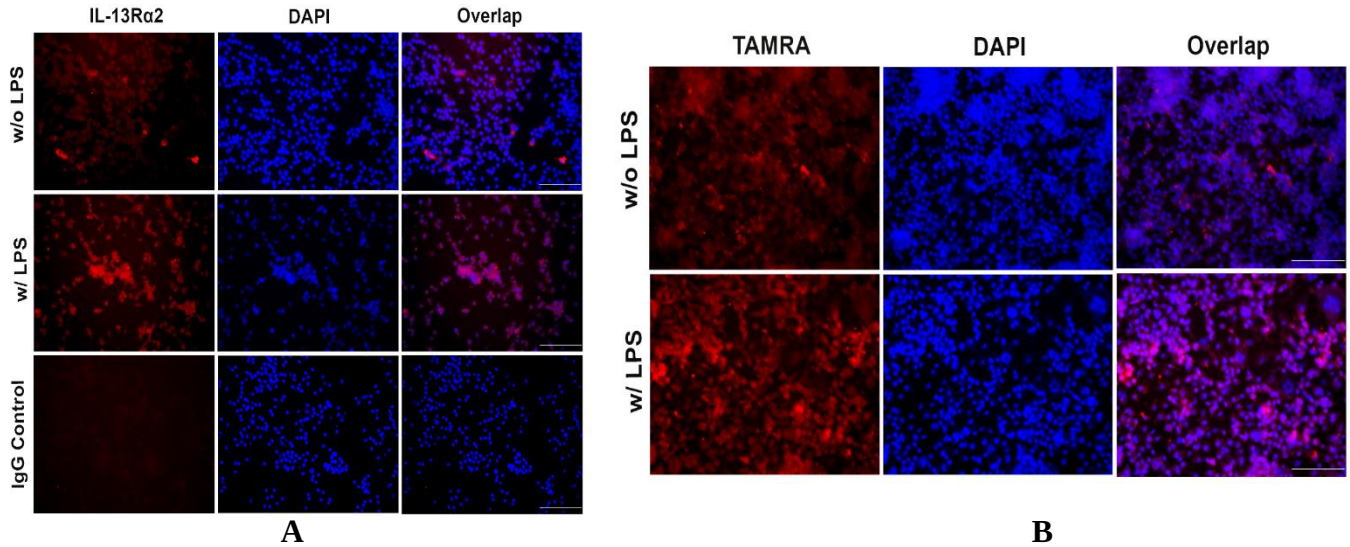

Figure 3. A) Immunofluorescence staining of IL-13Ra2 in Raw 264.7 cells with or without LPS (100 ng/mL) treatment for 1 day. Increased expression of IL-13Ra2 (red fluorescence) was observed in the cytosol upon LPS stimulation (middle row) compared to non-treated (upper row) and IgG controls (lower row). Scale bar represented 100 µM. B) *In vitro* probe binding with Raw 264.7 cells with or without LPS (100 ng/mL) treatment for 1 day. TAMRA-tagged MRI probe (1 µM) was incubated with cells for 30 min at room temperature. Much higher cell-bound TAMRA (red) fluorescence signal was observed in LPS-treated cells (lower row) compared to non-treated cells (upper row), suggesting more probe binding with Raw 264.7 cells upon LPS stimulation. Scale bar represented 100 µM.

probe binding. As expected, much stronger TAMRA signal (red fluorescence) was observed in LPS (100 ng/mL, 24 hr) stimulated cells compared to unstimulated control cells (**Figure 3B**), predominantly contributed by increased receptor-mediated probe binding after LPS activation. In addition, cell binding studies with a scrambled peptide conjugated $Gd_3N@C_{80}$ suggested Raw 264.7 cells showed little binding in presence or absence of LPS stimulation (Supplemental Figure 2). The fluorescence signal intensity was quantified and shown in Supplemental Figure 3. Such distinct probe binding data provided us a foundation to proceed into *in vivo* MRI imaging for differentiation of CPO.

3.3.7 Chronic post-traumatic tibia osteomyelitis mouse model

Given the difficulty in studying *S. aureus* infections in human subjects, animal models serve an integral role in exploring the pathogenesis of osteomyelitis. Mouse has served as the animal of choice to establish disease models, given the superior knowledge into the function and regulation of their immune system, and their small size, ease of handling, and overall lower cost. However, it is noteworthy that the smaller size makes two-stage revisions and multiple procedures in a single mouse more challenging [35]. To validate our tibia CPO mouse model, longitudinal luminol-bioluminescence imaging and X-ray radiography were employed. Luminol is a redox-sensitive compound that emits blue luminescence when exposed to myeloperoxidase (MPO) generated by

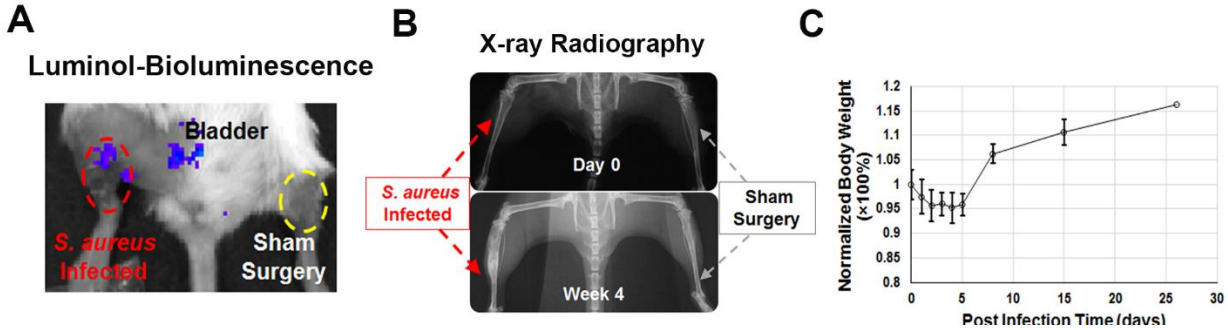

Figure 4. Infection parameters during the course of chronic post-traumatic tibia osteomyelitis. (A) Luminol-bioluminescence imaging showed higher myeloperoxidase activity in infect compared to sham; (B) X-ray radiograph demonstrated severe bone deformation and inflammatory lesion in infected tibia compared to sham; (C) Local infection was confirmed via continuous monitoring of body weight up to 4 weeks post infection.

recruited neutrophils due to infection. Luminol-bioluminescence imaging at 1.5 weeks showed a higher MPO activity in infected tibia compared to the sham (**Figure 4A**) suggesting a more numerous neutrophil infiltration and activation in the acute phase of infection compared to the sham tibia (also see Supplemental Figure 4). Representative X-ray radiographs in **Figure 4B** showed that all animals experienced evident bone destruction (osteolysis, deformation) and severe inflammatory lesions in those infected tibia after 4 weeks (chronic stage). In addition, clinical signs of illness were apparent during the acute phase of the infection (the 1st week), such as weight loss (**Figure 4C**) and decreased mobility of animals due to the initial injury. The gradual recovering in body weight and activity after the 1st week suggested improving physiological condition of animals during the chronic stage of infection and the infection was only restricted locally in the bacteria inoculated tibia. These data suggested that our surgery was successful and confirmed the progression of CPO and aseptic inflammation developed in separate tibia of the same mouse after trauma.

3.3.8 Histology confirmed bone deformation and cell infiltration of infected tibia

Histological examination was conducted to visualize the inflammatory response and structural destruction in affected tibiae. After 4 weeks of bacteria inoculation, the infected bones underwent tremendous structural changes during the destruction and remodeling processes. The infected tibia demonstrated massive influx of inflammatory cells accompanied with severe bone tissue destruction such as woven bone, dead bone, destroyed bone marrow structures (**Figure 5**, left column). While much less cell infiltration and structural change was detected in the sham tibia (**Figure 5**, right column). Consistent with the imaging data, bone structural changes in histology confirmed the success of CPO model in mouse tibia and abundant macrophages/monocytes infiltration the chronic osteomyelitis.

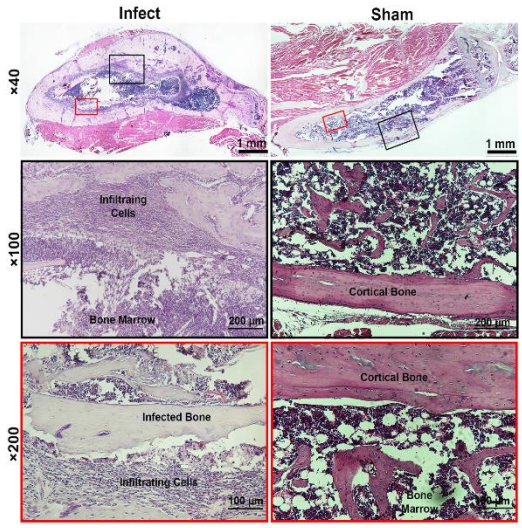

Figure 5. Hematoxylin and eosin staining of infected (left column) and sham tibia (right column) after 4 weeks post infection. Low magnification images (upper row) depicted overall structural change in the infected tibia was much more severe than the sham. High magnification images in mid- (x100) and lower-rows (x200) showed massive infiltration of inflammatory cells and formation of dead bones inside the medullary cavity of infected tibia while almost few infiltrated cells and much milder bone deformation was observed in the sham tibia.

3.3.9 Immunohistochemistry confirmed over-expression of IL-13Ra2 in infected tibia

To corroborate the in vitro findings and MRI results, we employed immunohistochemistry to evaluate IL-13Rα2 expression in both infection and aseptic inflammatory tibia sections. As shown

in **Figure 6A-C**, massive immuno-positive cells (brown signal) were detected in chronic stage of tibia infection. In infected sections, these IL-13Rα2 positive cells were primarily observed in regions of infiltrating inflammatory cells in the medullary cavity (**Figure 6A**, **6B**) and activated osteoblast (**Figure 6C**). However, only a few immuno-positive cells could be located in the medullary cavity of sham tibia (**Figure 6D, 6E**), suggesting a low level of IL-13Rα2 expression under aseptic post-traumatic injury. Together with the in vitro cell study and in vivo MRI imaging, these results indicated that IL-13Rα2 would serve as a novel and unique biomarker for detection of differentiation of CPO. In addition, our data would open up a new era of future therapeutic strategy of osteomyelitis, such as IL-13Rα2 targeted therapy and IL-13Rα2-mediated drug retention.

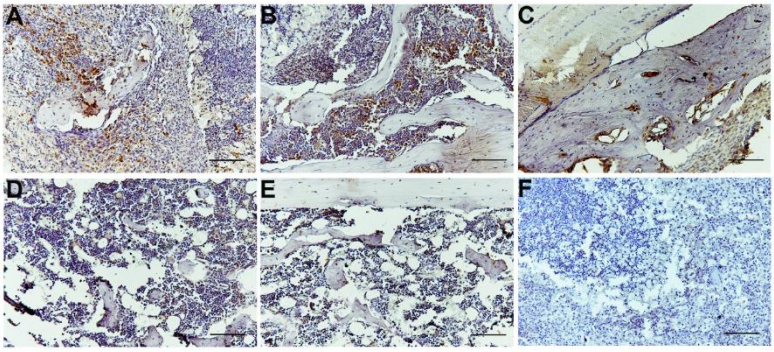

Figure 6. Immunohistochemical staining of IL-13Rα2 expression in mouse tibia after 4 weeks of *S.aureus* induced infection. In the infected tibia, significant amount of IL-13Rα2 immuno-positive signal (brown cells) was primarily detected in the medullary cavity where massive infiltrating cells (A) and infected bone marrow (B) located. Some immuno-positive signal was also observed in activated osteoclasts in the cortical bone of infected tibia (C). In comparison, few positively stained cells could be detected in either bone marrow (D) or cortical bone (E) of sham tibia. IgG control staining of infected sample (F) resulted in no positive signal suggesting the specificity of the procedure. All images were taken at x200 magnification. Scale bar represented 100 μm.

3.3.10 IL-13Rα2 targeted hyperintense MRI in the infection foci

During both acute and chronic phases of infection, MRI imaging showed hyperintensity on T_1 weighted sequences with the novel IL-13Rα2 targeted probe. As shown in **Figure 7A**, a single foci was detected in infected tibia during acute phase (1.5 weeks). Repeated MRI during chronic phase

(4 weeks post infection) showed a bright signal depicting continuous spreading and expansion of multiple foci of inflammation in the infected tibia (**Figure 7B**). Interestingly, the longitudinal MRI scan of the same animal revealed a significant change of size and location of the inflammatory foci, suggesting the progression of infectious process in the infected tibia. While no such enhanced signal was observed in sham tibia at both time points. Unlike our targeted probe, a commercial available Gd-based contrast agent Dotarem did not show any hyperintense signal enhancement between pre- and post-contrast images in our model (Supplemental Figure 5). Quantitative analysis of MRI intensity (signal-to-noise ratio, SNR) of this targeted probe was consistent with the visual observation (Supplemental Figure 6). Although future work may be needed to correlate the severity of infection with MRI signal intensity, this proof-of-concept work suggested this novel targeted MRI probe was capable to detect and differentiate CPO from aseptic inflammation in the current mouse tibia model. In addition, presumably, Gd_3N cluster is stably and securely encapsulated inside the endohedral metallofullerene cage. This unique feature of our probe greatly minimized toxicity concern associated from free unchelated Gd(III) ions in commonly used MRI contrast agents. Contradictions have been largely reported in patients with impaired renal function because of the risk of nephrogenic systemic fibrosis, as free Gd(III) ions tend to accumulate in the liver, spleen, kidney and bones and block calcium channels[2, 35]. Moreover, our unique metallofullerene nanoparticle structure has been empowered with 25-50 folds more detection sensitivity compared to conventional Gd based contrast agents[36]. Therefore, combined assets of target specificity, minimized toxicity and improved sensitivity warrants the translational potential of our MRI probe in the clinical differentiation of CPO.

Figure 7. Representative T_1-weighted (Spin-Echo, T_R 600 ms, T_E 11ms) MRI images of infected and sham tibia after intravenous injection of probe IL-13-$Gd_3N@C_{80}(OH)_{30}(CH2CH2COOH)_{20}$ (4 nmol per 20 g mice) at 1.5 (A) and 4 weeks (B) post infection. Yellow arrows indicated hyperintensity of MRI signal in infected foci while white arrowheads suggested the contra-lateral sham tibia subjected to traumatic procedure. Interestingly, longitudinal MRI scan of the same animal revealed a significant change of size and location of the inflammatory foci in the infected tibia, suggesting the progression of osteomyelitis (yellow arrows).

3.4 On-going research

To address this clinical challenge, we developed another novel macrophage mediated, formyl peptide receptor-1 (FPR-1) specific MRI nano-platform to differentiate CPO from aseptic inflammation. The cFLFLF peptide, a FPR-1 targeting peptide moiety specifically recognizing abundantly activated macrophages in the infection foci, was used as targeting moiety. Compared with conventional Gd contrast agents, this proposed approach will shift the diagnostic paradigm of chronic osteomyelitis, via delivering macrophages and FPR-1 double selective hyper-intense T_1 weighted MRI readouts, to a confusion-free manner.

A volume of 500 µL of 0.37 µmol carboxylated $Gd_3N@C_{80}$ was dissolved in DMSO, then the carboxyl groups were activated by 7.5 µmol of diisopropylcarbodiimide (DIC) and 1-hydroxybenzotriazole (HOBt) in DMF. After 4 hours, 150 µL of 0.2 µmol cy5-FLFLFK peptides (MW 1451.7) was added, vortexed and incubated at room temperature for 12 hours (**Figure 8A**). The resulting solution was filtered through polyacrylamide desalting columns. The final product was further purified *via* LC-MS, using a gradient of H_2O 0.1% TFA: MeCN 0.1% TFA on a C_{18} reverse phase column. The formation has been confirmed by both MALDI-TOF mass spectrometry

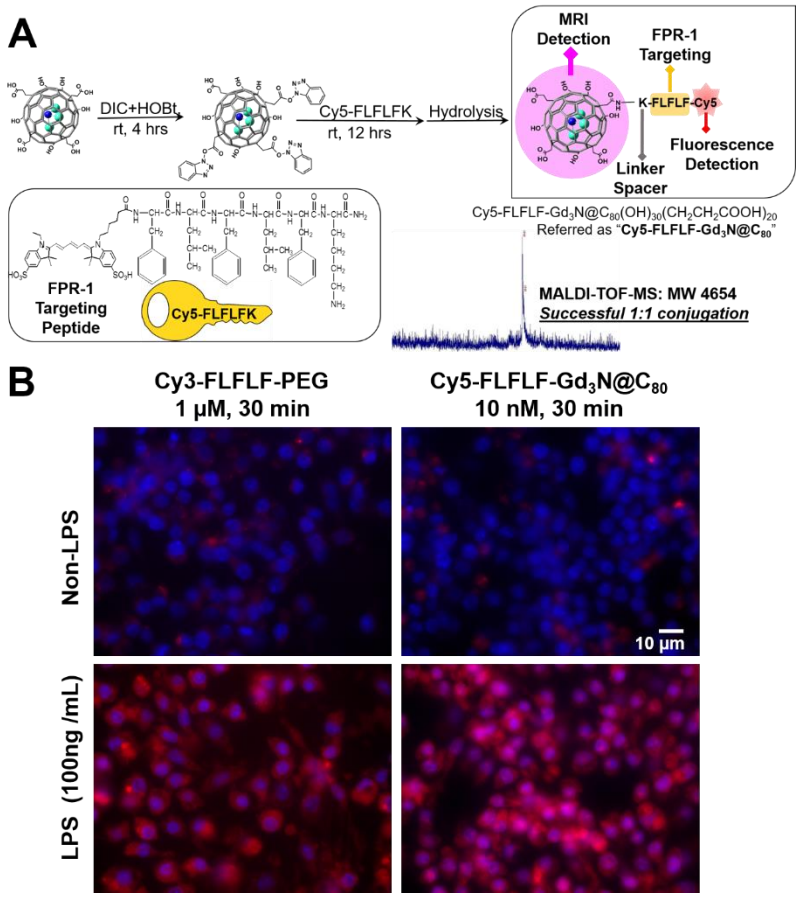

Figure 9. Conjugated Cy5-FLFLF-$Gd_3N@C_{80}$ (A) with observed molecular weight 4654, exhibited similar preferential binding and possibly uptake towards LPS-stimulated macrophage Raw 264.7 cells after 30 min incubation (B).

(**Figure 8A**) and LC-MS. The molecular weight of cy5-FLFLFK-$Gd_3N@C_{80}(OH)_{30}(CH_2CH_2COOH)_{20}$ is 4654, which suggests each fullerene cage only attached

with one peptide. The novle nanoplatform exhibited much stronger binding and preferential uptake in LPS-activated macrophages, compared to Cy3-FLFLF-$PEG_{3.4k}$ peptide only (**Figure 8B**). This probe, however, exhibited rapid blood clearance and predominant liver accumulation shortly after intravenous injection in mice. In future, incorporation of low molecular weight (<5kDa) PEG can extend blood half-life of nanoparticles, decrease structural rigidity, and therefore improve the biocompatibility and bioavailability for desired *in vivo* performance.

3.5 Conclusion

In summary, we developed a novel non-invasive imaging approach to detect and differentiate CPO from post-traumatic aseptic inflammation using a novel IL-13Rα2 targeted metallofullerene MRI probe in a mouse tibia model. To the best of our knowledge, we are the first to identify IL-13Rα2 as a unique biomarker for diagnostic imaging of CPO, given to its dramatically increased and distinct expression during bacterial infection. Such a translational imaging approach would eventually aid clinical differentiation of CPO from aseptic post-traumatic or surgical inflammation, hence providing critical and timely information for decision making of therapeutic strategy.

References

1. Horst, S. A.; Hoerr, V.; Beineke, A.; Kreis, C.; Tuchscherr, L.; Kalinka, J.; Lehne, S.; Schleicher, I.; Köhler, G.; Fuchs, T. et al. (2012) A Novel Mouse Model of Staphylococcus aureus Chronic Osteomyelitis That Closely Mimics the Human Infection. *Am. J. Pathol. 181*, 1206-1214.

2. Lew , D. P.; Waldvogel , F. A. (1997) Osteomyelitis. *N. Engl. J. Med. 336*, 999-1007.

3. Kamat, A. S. (2011) Infection Rates in Open Fractures of the Tibia: Is the 6-Hour Rule Fact or Fiction? *Ad. Orthop. 2011*, 4.

4. Kurtz, S.; Ong, K.; Lau, E.; Mowat, F.; Halpern, M. (2007) Projections of Primary and Revision Hip and Knee Arthroplasty in the United States from 2005 to 2030. *J. Bone Joint Surg. 89*, 780-785.

5. Lew, D. P.; Waldvogel, F. A. (2004) Osteomyelitis. *Lancet 364*, 369-379.

6. Mader, J. T.; Norden, C.; Nelson, J. D.; Calandra, G. B. (1992) Evaluation of new anti-infective drugs for the treatment of osteomyelitis in adults. *Clin. Infect. Dis. 15 Suppl 1*.

7. Zuluaga, A. F.; Galvis, W.; Jaimes, F.; Vesga, O. (2002) Lack of microbiological concordance between bone and non-bone specimens in chronic osteomyelitis: an observational study. *BMC Infect. Dis. 2*, 8.

8. Perry, C. R.; Pearson, R. L.; Miller, G. A. (1991) Accuracy of cultures of material from swabbing of the superficial aspect of the wound and needle biopsy in the preoperative assessment of osteomyelitis. *J. Bone Joint Surg. Am. 73*, 745-9

9. Khatri, G.; Wagner, D. K.; Sohnle, P. G. (2001) Effect of bone biopsy in guiding antimicrobial therapy for osteomyelitis complicating open wounds. *Am. J. Med. Sci. 321*, 367-71

10. Lee, Y. J.; Sadigh, S.; Mankad, K.; Kapse, N.; Rajeswaran, G. (2016) The imaging of osteomyelitis. *Quant. Imaging Med. Surg. 6*, 184-198.

11. Palestro, C. J. (2016) Radionuclide Imaging of Musculoskeletal Infection: A Review. *J. Nucl. Med. 57*, 1406-1412.

12. Govaert, G. A. M.; Glaudemans, A. W. J. M. (2016) Nuclear medicine imaging of posttraumatic osteomyelitis. *Eur. J. Trauma Emerg. Surg. 42*, 397-410.

13. Xiao, L.; Zhang, Y.; Berr, S. S.; Chordia, M. D.; Pramoonjago, P.; Pu, L.; Pan, D. (2012) A novel near-infrared fluorescence imaging probe for in vivo neutrophil tracking. *Mol. Imaging 11*, 372-82.

14. Xiao, L.; Zhang, Y.; Liu, Z.; Yang, M.; Pu, L.; Pan, D. (2010) Synthesis of the Cyanine 7 labeled neutrophil-specific agents for noninvasive near infrared fluorescence imaging. *Bioorg. Med. Chem. Lett. 20*, 3515-7.

15. Xiao, L.; Zhang, Y.; Yang, Z.; Xu, Y.; Kundu, B.; Chordia, M. D.; Pan, D. (2012) Synthesis of PECAM-1-specific 64Cu PET imaging agent: Evaluation of myocardial infarction caused by ischemia-reperfusion injury in mouse. *Bioorg. Med. Chem. Lett. 22*, 4144-4147.

16. Zhang, Y.; Xiao, L.; Chordia, M. D.; Locke, L. W.; Williams, M. B.; Berr, S. S.; Pan, D. (2010) Neutrophil Targeting Heterobivalent SPECT Imaging Probe: cFLFLF-PEG-TKPPR-99mTc. *Bioconjugate Chem. 21*, 1788-1793.

17. Locke, L. W.; Chordia, M. D.; Zhang, Y.; Kundu, B.; Kennedy, D.; Landseadel, J.; Xiao, L.; Fairchild, K. D.; Berr, S. S.; Linden, J.; Pan, D. (2009) A novel neutrophil-specific PET imaging agent: cFLFLFK-PEG-64Cu. *J. Nucl. Med.50*, 790-7.

18. Pugmire, B. S.; Shailam, R.; Gee, M. S. (2014) Role of MRI in the diagnosis and treatment of osteomyelitis in pediatric patients. *World J. Radiol. 6*, 530-537.

19. Neuwelt, A.; Sidhu, N.; Hu, C.-A. A.; Mlady, G.; Eberhardt, S. C.; Sillerud, L. O. (2015) Iron-Based Superparamagnetic Nanoparticle Contrast Agents for MRI of Infection and Inflammation. *AJR. Am. J. Roentgenol. 204*, W302-W313.

20. Bierry, G.; Jehl, F.; Boehm, N.; Robert, P.; Dietemann, J.-L.; Kremer, S. (2009) Macrophage imaging by USPIO-enhanced MR for the differentiation of infectious osteomyelitis and aseptic vertebral inflammation. *Eur. Radiol. 19*, 1604-1611.

21. Faz-López, B.; Morales-Montor, J.; Terrazas, L. I. (2016) Role of Macrophages in the Repair Process during the Tissue Migrating and Resident Helminth Infections. *BioMed Res. Int.2016*, 8634603.

22. Resnick, M.; Fibach, E.; Lebastard, M.; Levy, L.; Bercovier, H. (1988) Response of the murine hematopoietic system to chronic infection with Mycobacterium lepraemurium. *Infect.Immun. 56*, 3145-3151.

23. Wills-Karp, M.; Luyimbazi, J.; Xu, X.; Schofield, B.; Neben, T. Y.; Karp, C. L.; Donaldson, D. D. (1998) Interleukin-13: Central Mediator of Allergic Asthma. *Science 282*, 2258-2261.

24. Li, T.; Dorn, H. C., Biomedical Applications of Metal-Encapsulated Fullerene Nanoparticles. *Small* **2016**.

25. Sengupta, S.; Thaci, B.; Crawford, A. C.; Sampath, P. (2014) Interleukin-13 Receptor Alpha 2-Targeted Glioblastoma Immunotherapy. *BioMed Res. Int. 2014*, 952128.

26. Sivaprasad, U.; Warrier, M. R.; Gibson, A. M.; Chen, W.; Tabata, Y.; Bass, S. A.; Rothenberg, M. E.; Khurana Hershey, G. K. (2010) IL-13Rα2 Has a Protective Role in a Mouse Model of Cutaneous Inflammation. *J. Immunol. 185*, 6802-6808.

27. Shu, C. Y.; Corwin, F. D.; Zhang, J. F.; Chen, Z. J.; Reid, J. E.; Sun, M. H.; Xu, W.; Sim, J. H.; Wang, C. R.; Fatouros, P. P. et al. (2009) Facile Preparation of a New Gadofullerene-Based Magnetic Resonance Imaging Contrast Agent with High H-1 Relaxivity. *Bioconjugate Chem. 20*, 1186-1193.

28. Fillmore, H. L.; Shultz, M. D.; Henderson, S. C.; Cooper, P.; Broaddus, W. C.; Chen, Z. J.; Shu, C. Y.; Zhang, J. F.; Ge, J. C.; Dorn, H. C. et al. (2011) Conjugation of functionalized gadolinium metallofullerenes with IL-13 peptides for targeting and imaging glial tumors. *Nanomedicine-Uk 6*, 449-458.

29. Li, T. H.; Murphy, S.; Kiselev, B.; Bakshi, K. S.; Zhang, J. Y.; Eltahir, A.; Zhang, Y. F.; Chen, Y.; Zhu, J.; Davis, R. M. (2015) A New Interleukin-13 Amino-Coated Gadolinium Metallofullerene Nanoparticle for Targeted MRI Detection of Glioblastoma Tumor Cells. *J. Am. Chem. Soc. 137*, 7881-7888.

30. Alizadeh-Navaei, R.; Rafiei, A.; Hedayatizadeh-Omran, A.; Mohammadzadeh, I.; Arabi, M., Gene (2014) Susceptibility in Iranian Asthmatic Patients: A Narrative Review. *Ann. Med.Health Sci. Res. 4*, 837-840.

31. Vatrella, A.; Fabozzi, I.; Calabrese, C.; Maselli, R.; Pelaia, G. (2014) Dupilumab: a novel treatment for asthma. *J Asthma Allergy 7*, 123-130.

32. Bice, J. B.; Leechawengwongs, E.; Montanaro, A. (2014) Biologic targeted therapy in allergic asthma. *Ann. Allergy Asthma Immunol. 112*, 108-115.

33. Feuerstein, R.; Kolter, J.; Henneke, P. (2016) Dynamic interactions between dermal macrophages and Staphylococcus aureus. *J. Leukoc. Biol.* doi:10.1189/jlb.3MR0316-097RR

34. Reizner, W.; Hunter, J. G.; O'Malley, N. T.; Southgate, R. D.; Schwarz, E. M.; Kates, S. L. (2014) A systematic review of animal models for Staphylococcus aureus osteomyelitis. *Eur. Cell Mat. 27*, 196-212.

35. Khawaja, A. Z.; Cassidy, D. B.; Al Shakarchi, J.; McGrogan, D. G.; Inston, N. G.; Jones, R. G. (2015) Revisiting the risks of MRI with Gadolinium based contrast agents—review of literature and guidelines. *Insight Imaging 6*, 553-558.

36. Murphy, S. V.; Hale, A.; Reid, T.; Olson, J.; Kidiyoor, A.; Tan, J.; Zhou, Z.; Jackson, J.; Atala, A. (2016) Use of trimetasphere metallofullerene MRI contrast agent for the non-invasive longitudinal tracking of stem cells in the lung. *Methods 99*, 99-111.

37. Xiao, L.; Ding, M.; Saadoon, O.; Vess, E.; Fernandez, A.; Zhao, P.; Jin, L.; Li, X. (2016) A novel culture platform for fast proliferation of human annulus fibrosus cells. *Cell Tissue Res.* doi:10.1007/s00441-016-2497-4.

38. Liang, H.; Wang, K.; Shimer, A. L.; Li, X.; Balian, G.; Shen, F. H. (2010) Use of a bioactive scaffold for the repair of bone defects in a novel reproducible vertebral body defect model. *Bone 47*, 197-204.

39. Jin, L.; Wan, Y.; Shimer, A. L.; Shen, F. H.; Li, X. J. (2012) Intervertebral disk-like biphasic scaffold—demineralized bone matrix cylinder and poly(polycaprolactone triol malate)—for interbody spine fusion. *J. Tissue Eng. 3*, 2041731412454420.

40. Jin, L.; Feng, G.; Reames, D. L.; Shimer, A. L.; Shen, F. H.; Li, X. (2013) The Effects of Simulated Microgravity on Intervertebral Disc Degeneration. *Spine J. 13*, 235-242.

41. Jin, L.; Liu, Q.; Scott, P.; Zhang, D.; Shen, F.; Balian, G.; Li, X. (2014) Annulus Fibrosus Cell Characteristics Are a Potential Source of Intervertebral Disc Pathogenesis. *PLoS ONE 9*, e96519.

Chapter 4 Trimetallic Nitride Endohedral Fullerenes Carboxyl-$Gd_3N@C_{80}$: A New Theranostic Agent for Combating Oxidative Stress and Resolving Inflammation

This chapter is adopted from the manuscript published on ACS Applied Materials & Interfaces with appropriate modifications under the permission of the American Chemical Society. Full text of the published manuscript entitled "Trimetallic Nitride Endohedral Fullerenes Carboxyl-$Gd_3N@C_{80}$: A New Theranostic Agent for Combating Oxidative Stress and Resolving Inflammation" by Tinghui Li[§], Li Xiao[§], Jiezuan Yang, Mengmeng Ding, Zhiguo Zhou, Leslie LaConte, Li Jin, Harry C. Dorn, Xudong Li. [§]These authors contributed equally to the current work. This work can be obtained at http://pubs.acs.org/doi/abs/10.1021/acsami.7b04718

Abstract

Anti-oxidative and anti-inflammatory effects of trimetallic nitride endohedral fullerenes Carboxyl-$Gd_3N@C_{80}$, a newly developed magnetic resonance imaging (MRI) contrast agent, was investigated. All hydrochalarone and carboxyl- functionalized fullerenes showed effective radical (hydroxyl and superoxide anion) scavenging, while the Carboxyl-$Gd_3N@C_{80}$ more efficiently attenuated lipopolysaccharide (LPS) induced oxidative stress in macrophages. Carboxyl-$Gd_3N@C_{80}$ also suppressed LPS-elicited mRNA expression of pro-inflammatory inducible nitric oxide synthase and tumor necrosis factor-alpha, and upregulated anti-oxidative enzyme axis Nrf2 and hemooxygenase-1, possibly via ERK but not AKT signaling pathways. Therefore, Carboxyl-$Gd_3N@C_{80}$ held a great promise in becoming a novel theranostic nano-platform for simultaneously deliver MRI contrast and therapeutic functions to inflammation-related diseases.

4.1 Introduction

Oxidative stress is characterized by increased level of reactive oxygen species (ROS) and/or reactive nitrogen species (RNS). This may be caused by impaired antioxidant enzyme activity, low concentrations of antioxidant, and excessive ROS production. Under the normal physiological condition, ROS play essential roles in maintaining redox signaling balance and controlling cell survival. However, high levels of ROS may induce alteration or damage to DNA, proteins, and lipids, which has been implied in the pathogenesis of a number of diseases,[1-3] including cancer, diabetic mellitus, cardiovascular, neurodegeneration, skeletal muscle degeneration, osteoarthritis, and intervertebral disc degeneration. Antioxidative supplements, enzymes, nanoparticles, and inhibitors for ROS-generating nicotinamide adenine dinucleotide phosphate-oxidase (NADPH) oxidases have become potential therapeutic interventions to combat oxidative stress via scavenging/neutralizing ROS directly and/or inhibiting downstream deleterious effects of ROS. Among them, nanoparticles with intrinsic ROS scavenging and antioxidant properties exhibit superior pharmacological profiles to other antioxidants via enhanced absorption, bioavailability, and readily functionalization for targeted delivery. These nanoparticles include mesoporous silica, cerium oxide, and fullerene.

Fullerene is a molecule of carbon in the form of a hollow sphere with diversified applications, such as photovoltaic and electronic devices, surface coating material, and antioxidant.[4] Shortly after the discovery of fullerenes in the 1990s, endohedral metallofullerenes (EMF) and trimetallic nitride endohedral fullerenes (TNT-EMF) were recognized for their multifunctional capabilities in biomedical applications. Functionalized gadolinium-loaded fullerenes, $Gd@C_{82}$ and $Gd_3N@C_{80}$, attracted much attention as a potential new nanoplatform for next-generation magnetic resonance imaging (MRI) contrast agents, given their inherent higher ^1H relaxivity than most commercial

contrast agents.[5-13] The fullerene cage is an extraordinarily stable species which makes it extremely unlikely to break and release the toxic Gd metal ions into the bioenvironment. In addition, radiolabeled metals could be encapsulated in this robust carbon cage to deliver therapeutic irradiation.[14-16] In the past decade, we has endeavored to discover a series of functionalized $Gd_3N@C_{80}$ for MRI detection of various pathological conditions, such as chronic osteomyelitis and brain cancer.[13, 17-18]

Fullerene is a powerful antioxidant due to delocalization of the π-electrons over the carbon cage, which can readily react with free radicals and subsequently delivers a cascade of downstream possessions in numerous biomedical applications.[19] Numerous studies have demonstrated the free radical scavenging capabilities, to such a degree that fullerenes have been described as "free radical sponges".[20] Functionalized C_{60} and $Gd@C_{82}$ have been reported to quench radicals efficiently.[8, 12, 21] However, the therapeutic potential of functionalized $Gd_3N@C_{80}$ has not been investigated. If these TNT-EMF exhibit antioxidative and anti-inflammatory properties, similar as their nonmetal or monometal counterparts, they would hold great promise as a novel class of theranostic agent in combating oxidative stress and resolving inflammation, given their inherent MRI applications.

In the current study, we performed chemical and biological screening on three $Gd_3N@C_{80}$-based derivatives, including $Gd_3N@C_{80}(OH)_{30}(CH_2CH_2COOH)_{20}$ (carboxyl-$Gd_3N@C_{80}$)[17] (**Figure 1a**) and Hydrochalarone-1 (HyC-1-$Gd_3N@C_{80}$), Hydrochalarone-3 (HyC-3-$Gd_3N@C_{80}$), ($Gd_3N@C_{80}$-Rx, where $R=[N(OH)(CH_2CH_2O)_nCH_3]_x$, n=1,3,6 and x=10-22)[10] (**Figure 1b**) to assess their radical scavenging, antioxidative and anti-inflammatory properties. The related characterization of these three compounds were reported in the earlier papers.[10,17] We demonstrated intriguing results on structure-activity relationship, and investigated molecular and

cellular mechanisms regarding the biological/therapeutic performance of the most promising fullerene carboxyl-$Gd_3N@C_{80}$ using an *in vitro* macrophage model.

4.2 Experimental procedures

4.2.1 Material

$Gd_3N@C_{80}$ were purchased from LUNA Innovations (Danville, VA). HyC-1-$Gd_3N@C_{80}$ and HyC-3-$Gd_3N@C_{80}$ were generous gifts from Luna Innovations. Carboxyl-$Gd_3N@C_{80}$ was prepared according to the work from Xiao et al.[1] Hydrogen peroxide (H_2O_2), ferrous sulfate heptahydrate ($FeSO_4$), xanthine, xanthine oxidase from bovine milk (XOD), diethylenetriaminepentaacetic acid (DTPA), and lipopolysaccharide (LPS) were purchased from Sigma Aldrich. Spin traps, 5-diethoxyphosphoryl-5-methyl-I-pyrroline N-oxide (DEPMPO) was purchased from Focus Biomolecules, 5-tert-Butoxycarbonyl-5-methyl-1-pyrroline-N-oxide (BMPO) was supplied by Cayman Chemical. The clear EPR quartz capillary tubes (ID 1.0mm, OD 1.2mm) were obtained from Wilmad-LabGlass.

4.2.2 Electron paramagnetic resonance (EPR) spectroscopic measurements

All EPR measurements were carried out at 20 °C using a Bruker ELEXSYS-II EPR spectrometer. To analyze the free radical-scavenging capability of $Gd_3N@C_{80}$ derivatives, cell-free radical producing systems were used for measurement of hydroxyl radical and superoxide radical anion. The concentration of $Gd_3N@C_{80}$ derivatives were determined by ICP-MS. Each experiment was repeated at least three times.

4.2.3 Hydroxyl radical (HO) scavenging activity

Interception of hydroxyl radicals by each metallofullerene derivative was determined by the EPR spin-trapping technique. The EPR assay was based on the competition between the trapping agent, DEPMPO, and the fullerene derivative nanoparticles for HO. Hydroxyl radicals were generated

by the classical Fenton reaction with the reaction mixture containing freshly prepared 500 μM DEPMPO, 20 μM $FeSO_4$ and 200 μM H_2O_2 with or without 56 μM of $Gd_3N@C_{80}$ derivatives. The clear quartz capillary tubes (ID 1.0mm, OD 1.2mm) were used as the sample container. The EPR data were collected at ambient temperature, 2 min after initiating the formation of HO by the addition of $FeSO_4$. The following instrument settings were used for collecting EPR spectra: microwave power of 10 mW, field modulation frequency of 100 kHz, and modulation amplitude of 1 G.

4.2.4 Superoxide radical anion ($O_2^{\bullet-}$) scavenging activity

BMPO was used to trap and detect $O_2^{\bullet-}$ by EPR spectroscopy. Superoxide radical anion was generated using the xanthine/ xanthine oxidase system. The radical scavenger reaction was initiated by the addition of xanthine oxidase solution (XOD). The reaction contained 100 μM xanthine (1M NaOH in PBS), 20 mM BMPO, 50 μM DTPA, 0.1 U/ml XOD, in the presence or absence of 42 μM of $Gd_3N@C_{80}$ derivatives. The EPR spectra were recorded at 1.5 min after initiating the generation of $O_2^{\bullet-}$ by the addition of XOD. The instrument settings were used as the same as hydroxyl radicals.

4.2.5 *In vitro* culture of Raw 264.7 macrophages

Raw 264.7 cells were purchased from American Type Culture Collection (ATCC) (Manassas, VA). Cells were cultured with Dulbecco's modified Eagle's medium (DMEM, high glucose, Gibco, Grand Island, NY) supplied with 10% fetal bovine serum (Gibco, Grand Island, NY), 1% penicillin (100 μg/mL), and 1% streptomycin (100 μg/mL) (Gibco, Grand Island, NY) and maintained in 5% CO_2 at 37 °C.

4.2.6 Nanoparticle screening assay against LPS-induced intracellular reactive oxygen species (ROS)

To evaluate the protective effect of three metallofullerene nanoparticles against oxidative stress, Raw 264.7 cells were seeded onto 96-well plate (Black/Clear, tissue culture treated, BD Falcon, Bedford, MA) at a density of 5×10^5 cells/mL, and incubated overnight until 90-95% confluency. On the day of experiment, cells were incubated with aqueous nanoparticle samples (Carboxyl-$Gd_3N@C_{80}$, HyC-1- $Gd_3N@C_{80}$, HyC-3- $Gd_3N@C_{80}$, CoPP) at different concentrations (0, 0.1, 1, and 10 μM) in serum free media (DMEM with 1% penicillin and streptomycin) for 20 h. After incubation with lipopolysaccharide (LPS) (100 ng/mL) for 4 h at 37 °C, culture media was replaced with serum free DMEM containing 5 μM 2',7' dichlorodihydrofluorescein diacetate (H_2DCFDA) (Life Technologies, Carlsbad, CA) and incubated for 30 min at 37 °C in dark. Cells were washed twice with 150 μL of warm phosphate buffered saline (PBS, Invitrogen, Carlsbad, CA), and left 50 μL of PBS/well with the last wash. Fluorescence intensity was measured using a fluorescence plate reader (Molecular Devices SPECTRAmax Gemini EM, Sunnyvale, CA) with E_x/E_m=495/525 nm. The hemooxygenase-1 inducer protoporphyrin IX cobalt chloride (CoPP) (Sigma Aldrich) here was used as a positive control. For each treatment group, triplicated wells were analyzed. Background reading from blank wells were subtracted. Mean fluorescence intensities were normalized to that of non-LPS control groups (without nanoparticle).

4.2.7 Cell viability assay

To further assess the effect of selected Carboxyl-$Gd_3N@C_{80}$ nanoparticle on cell viability, an MTS assay was performed following our published protocols.[2] In brief, Raw 264.7 cells were cultured in 96-well plates (tissue culture treated, Corning Incorporated) at 37 °C for 24 h. The cells were incubated with or without the Carboxyl-$Gd_3N@C_{80}$ nanoparticle at a final concentration of 3.5 μM for 24 h and 48 h. Then cell viability assay was carried out using CellTiter Aqueous Non-Radioactive Cell Proliferation Assay Kit (Promega, Madison, WI) following manufacture's

instruction. OD_{490} was measured using VERSA max microplate reader (Molecular Devices, Sunnyvale, CA) and normalized to the value of control group at both time points.

4.2.8 Fluorescence imaging of intracellular ROS

To visualize the intracellular fluorescence change of ROS, one day before the experiment, cells were cultured onto sterilized glass coverslips in a 6-well plate at a density of 4×10^5 cells/mL overnight. Cells were treated with or without nanoparticle (3.5 μM) for 20 h, and further stimulated with LPS (100 ng/mL) for 4 h in serum free media. Cells were then incubated with 5 μM 2',7' dichlorodihydrofluorescein diacetate (H_2DCFDA) as above, washed twice, and mounted with Prolong Gold antifade reagent with DAPI (Life Technologies) on slides. Fluorescence images were captured with a fluorescence microscope (LSM 510-UV, Carl Zeiss, Germany) and processed using NIS Element. Basic Research software (Nikon Instruments Melville, NY) with the exact same setting (green and blue channel) throughout the experiment.[3]

4.2.9 Griess assay

Nitric oxide (NO) is a molecular mediation of many physiological processes. Under oxidative stress, the formation of NO in Raw 264.7 cells is usually up-regulated due to activation of inducible nitric oxide synthase (iNOS), contributing to the accumulation of reactive nitrogen species (RNS). Raw 264.7 cells were treated with carboxyl-$Gd_3N@C_{80}$ (3.5 μM) for 6 h and stimulated with LPS (100 ng/mL) for another 20 h. Culture media were collected and subjected to Griess Assay (Promega, Madison, WI) following the manufacture instruction. Since NO is induced after the activation of iNOS during LPS-induced inflammatory response in macrophages, time points for nanoparticle incubation and LPS stimulation were designed differently for Griess assay and iNOS mRNA measurements.

4.2. 10 Real-time reverse transcription polymerase chain reaction

Raw 264.7 cells were seeded onto 24-well plates at a density of 5×10^5 cells/mL and cultured for 1-2 days until confluency of 90%. Cells were treated with carboxyl-$Gd_3N@C_{80}$ (3.5 μM) in serum-free DMEM for 20 h and then stimulated with LPS (100 ng/mL) for 4 h. Total RNA was isolated with Trizol Reagent (Invitrogen) and quantified with NanoDrop™ 1000 Spectrophotometer (ThermoFisher Scientific, Waltham, MA). cDNA was subsequently synthesized with iScript cDNA synthesis kit (Bio-Rad Laboratories, Hercules, CA) following the manufacture's instruction. Real-time reverse transcription polymerase chain reaction (RT-PCR) was performed with RT^2 SYBR Green Fluo FAST Mastermix (Qiagen Sciences, Germantown, MA) and an iQ5 multicolor real-time PCR Detection System (Bio-Rad Laboratories, Hercules, California). Each qPCR reaction solutions were prepared by 10 ng of cDNA, 5 μM of desired primer, SYBR®Premix Ex Taq™ (1×) in a total volume of 12.5 μL with 35 cycles of 10 s at 95 °C, 10 s at 55 °C, and 30 s at 72 °C. The mRNA expression of target genes (*iNOS*, *HO-1, TNF-α*) were analyzed and normalized to the reference gene β-tubulin III.

4.2.11 Immunofluorescence staining of nuclear factor erythroid 2-related factor 2 (Nrf2) and fluorescence image analysis

For immunofluorescence staining, Raw 264.7 cells were seeded onto Nunc Lab-Tek 8-well chamber slide (Sigma Aldrich) at a 5×10^5 cells/mL (0.2 mL per well) and incubated the plate at 37°C for additional 1-2 days until 80-90% confluency. Cells were fixed with 4% PFA for 30 min, permeablized with 0.3% Triton X-100 for 5 min, and blocked with 3% BSA for 1 h at room temperature. Cells were incubated with mouse anti-Nrf2 monoclonal IgG_1 (1:300, Santa Crutz Biotechnology) at 4°C overnight, visualized with Alexa Fluo488 goat-anti-mouse IgG_1 (1:1000) (Molecular Probes, Eugene, OR). Following incubation, cells were mounted with glass coverslips with Prolong Gold antifade reagent with DAPI (Life Technologies). IgG was used as a negative

control. Fluorescence images were taken with Olympus FV300 confocal laser scanning microscope (Olympus Corporation, Center Valley, NJ), and processed using NIS Element at a magnification of 200. Basic Research software (Nikon Instruments Melville, NY) with the exact same setting (green and blue channel) was used.[3] Using the software's built-in function, mean green fluorescence intensity were measured within fixed area of region-of-interest (ROI) in a square of 100 × 100 μm. The mean value of mean fluorescence intensity in each treatment group were obtained via averaging values from three randomly chosen ROI per image (×200) and analyzing three fluorescence images per condition.

4.2.12 Western blotting

Western blot assay was employed for the investigation of related protein levels as the method described in our previous publication.[2] After pre-incubation with carboxyl-$Gd_3N@C_{80}$ (3.5 μM) for 20 h and LPS (100 ng/mL) stimulation for 4 h in serum-free DMEM, cells were washed with 1×PBS and lysed with RIPA buffer containing 1 × protease inhibitor cocktail and PMSF (Sigmal-Aldrich). Equal amounts of protein (~20 μg per sample) were subjected to sodium dodecyl sulfate polyacrylamide gel electrophoresis (SDS-PAGE) and transferred to a nitrocellulose membrane. After incubation with Odyssey Blocking Buffer (LI-COR, Lincoln, NE) for 1 h at room temperature, the membranes were incubated with mouse phospho-ERK1/2 (1:1000) (cell signaling, Danvers, Massachusetts), rabbit total ERK 1/2 (1:1000) (cell signaling), rabbit phosphor-Akt1/2/3 (1:1000) (Santa Cruz Biotechnology, Dallas, TX), rabbit total Akt1/2/3 (1:1000) (Santa Crutz Biotechnology), or mouse phosphor-p65 monoclonal IgG (1:1000) (Santa Crutz Biotechnology) antibodies overnight at 4 °C, followed by incubation with a goat-anti-mouse Alexa Fluo 680 (1:5000) or goat-anti-rabbit Alexa Fluo 800 (1:5000) (ThermoFisher Scientific) for 1 h at room temperature. Membranes were washed, scanned and analyzed with Odyssey

Infrared Imaging System (LI-COR Biosciences). Experiment were performed in duplicated samples each time. Results from three independent experiments were analyzed.

4.2.13 Statistical analysis

All *in vitro* cellular experiments were replicated for at least three times with duplicated or triplicated biological samples each time. Quantitative data were presented as mean ± SEM. Data comparing two groups were analyzed with a Student's t-Test. A *p*-value of less than 0.05 was considered statistically significant.

4.3 Results and discussion

Electron paramagnetic resonance (EPR) techniques were utilized to evaluate the capability of carboxyl-$Gd_3N@C_{80}$ (**Figure 1A**), HyC-1-$Gd_3N@C_{80}$ and HyC-3-$Gd_3N@C_{80}$ (**Figure 1B**) to eliminate ROS in a cell free system, which provided direct evidence in their radical scavenging capabilities. As hydroxyl radical (•OH) and superoxide radical anion ($O_2^{\bullet-}$), are the most common ROS in the body, they were chosen as model in this experiment. Due to the relatively low sensitivity of EPR detection and short-lived biological free radicals, exogenous spin traps were used. The EPR assay was based on the competition between the trapping agents, and functionalized fullerenes for radicals. Hydroxyl radicals were generated by the classical Fenton reaction, which involves the reaction of $FeSO_4$ and H_2O_2. The concentration of H_2O_2 was 200 μM, DEPMPO was 500 μM, which was 9 times higher than the metallofullerene derivatives (56 μM). The superoxide radical anion was generated by using the xanthine/ xanthine oxidase system. The concentration of trapping agent, BMPO, was about 500 times concentrated than metallofullerenes. As shown in **Figure 1C**, **D**, a portion of radicals were quenched by the functionalized metallofullerenes, and the residues were captured by the trapping agents to yield adducts of DEPMPO-OH and BMPO-OOH, respectively. After treatment with $Gd_3N@C_{80}$-based nanoparticles, EPR profiles of both

DEPMPO-OH and BMPO-OOH were significantly declined compared with the control. The inhibitory effects of three $Gd_3N@C_{80}$ derivatives were further summarized in **Figure 1E**. Although carboxyl-$Gd_3N@C_{80}$ exhibited the highest scavenging capability toward hydroxyl radicals among all three fullerenes, there was no difference between HyC-1-$Gd_3N@C_{80}$ and HyC-3-$Gd_3N@C_{80}$ in hydroxyl radical elimination. These three $Gd_3N@C_{80}$-based derivatives exhibited similar quenching ability for superoxide radical anions. Such desired but slightly varied radical scavenging properties of these functionalized $Gd_3N@C_{80}$ could be attributed to their different surface functionalization. After chemical modification, some of the π-system of fullerene framework is altered by replacing a cage carbon with another unit. The active hydroxyl radical could attack the electron-deficient areas on the carbon cage surface or be stabilized by forming hydrogen bonds with the proximate hydroxyl protons of functionalized $Gd_3N@C_{80}$. There were more hydroxyl groups on the cage of carboxyl-$Gd_3N@C_{80}$ as compared to HyC-1-$Gd_3N@C_{80}$ and HyC-3-$Gd_3N@C_{80}$ (30 *vs*. 10-22), making the carboxyl-$Gd_3N@C_{80}$ a more efficient nanoparticle on quenching hydroxyl radicals. Our observation is also consistent with previous reports that modification the fullerene cage with *tris*-malonic acid leads to electron deficient areas on the surface which facilitate binding of superoxide radical anions.[22] In addition, binding of a second superoxide radical anions to an adjacent electron deficient area might result in the destruction of this type of radicals to produce H_2O_2, and regeneration of the functionalized metallofullerene in a reaction similar to that catalyzed by superoxide dismutase. The number of -C-O- groups on this three $Gd_3N@C_{80}$ based derivatives were similar (20 *vs*. 10-22), hence leading to a similar scavenging effect of superoxide radical anions for all three fullerenes.

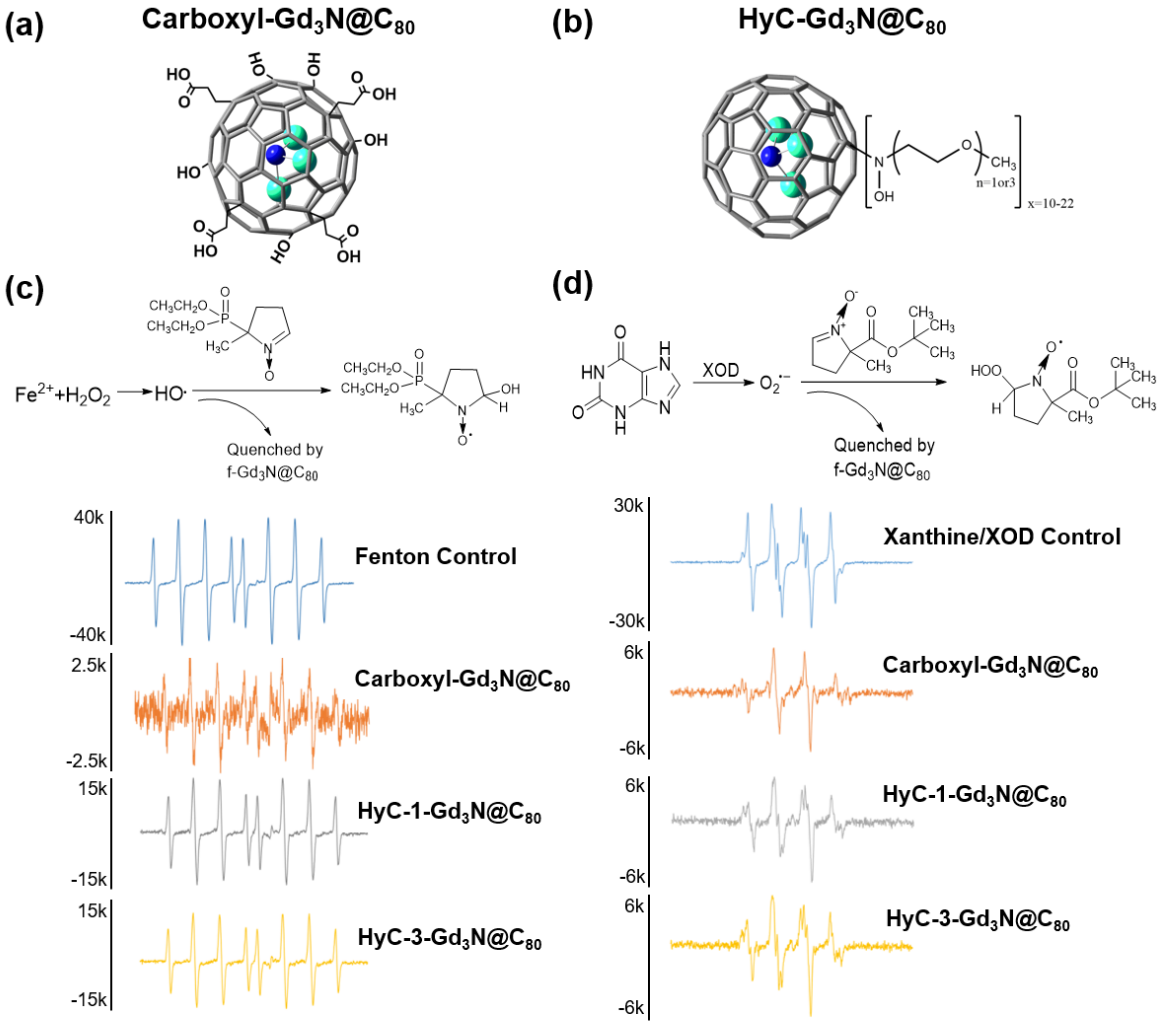

(e)

Percentage of signal reduction (%)	•OH	$O_2^{\bullet-}$
Carboxyl-$Gd_3N@C_{80}$	94.4	83.8
HyC-1-$Gd_3N@C_{80}$	70.0	83.9
HyC-3-$Gd_3N@C_{80}$	72.4	81.8

Figure 1. Radical scavenging properties of three trimetallic nitride endohedral fullerenes. Structures of (a) carboxyl-$Gd_3N@C_{80}$, (b) HyC-1-$Gd_3N@C_{80}$ and HyC-3-$Gd_3N@C_{80}$. (c) Mechanism of the hydroxyl radical production by Fenton reaction and capture by DEPMPO. EPR spectra of the hydroxyl radicals captured by DEPMPO with and without $Gd_3N@C_{80}$ derivatives. Ultrapure water was used as a control. (d) Mechanism of superoxide radical production by xanthine/ xanthine oxidase (XOD) system and capture by BMPO. EPR spectra of superoxide radicals captured by BMPO with and without $Gd_3N@C_{80}$ derivatives. PBS was used as a control. (e) Table summary of scavenging capabilities of hydroxyl radical and superoxide radical anion by three $Gd_3N@C_{80}$ derivatives, carboxyl-$Gd_3N@C_{80}$, HyC-1-$Gd_3N@C_{80}$, and HyC-3-$Gd_3N@C_{80}$.

Although ROS signaling is a complicated, cell- and tissue-specific, physiological and pathophysiological context, restoring ROS hemostasis has been a well-respected therapeutic strategy to combat oxidative stress and a cascade of pro-inflammatory events.[23] To confirm our cell free EPR assays on radical scavenging, an *in vitro* macrophage cell model (Raw 264.7 cells with or without LPS stimulation) was adopted for biological characterization. First of all, we observed little cytotoxicity of all three nanoparticles at 0.1, 1 and 10 μM concentration for up to 24 h with or without LPS treatment (**Figure S1, S2**). Subsequently, a fluorescence assay was developed by incorporating an intracellular ROS sensitive dye 2',7' dichlorodihydrofluorescein diacetate (H_2DCFDA) in a 96-well plate. A well-known antioxidative enzyme hemooxygenase-1 (HO-1) inducer protoporphyrin IX cobalt chloride (CoPP) was used as a positive control. Briefly, cells were preincubated with various concentration of nanoparticles (0.1, 1 and 10 μM) for 20 h and treated with or without LPS (100 ng/mL) for additional 4 h. The green fluorescence emitted from intracellular space indicated the abundance of ROS. As shown in **Figure 2**, LPS dramatically stimulated intracellular ROS production by ~4-fold compared to non-LPS control (*p<0.05 *vs.* control). The positive control CoPP pretreated cells showed a significant inhibitory effect on ROS production in Raw 264.7 cells (**Figure 2D**) via its known effect in promoting antioxidative enzyme HO-1 activity.[24] Carboxyl-$Gd_3N@C_{80}$ demonstrated a similar inhibitory trend in alleviating LPS-induced ROS (**Figure 2A**) in a dose-dependent manner. In contrast, the ROS inhibitory effect of hydrochalarone functionalized HyC-1 (**Figure 2B**) and HyC-3 (**Figure 2C**) was not as efficient as carboxyl-$Gd_3N@C_{80}$ even at 10 μM. This data corroborated with EPR hydroxyl radical scavenging data, which suggested that carboxyl-$Gd_3N@C_{80}$ would be an optimal candidate warranting further investigation. Therefore, we chose carboxyl-$Gd_3N@C_{80}$ for further biological evaluation.

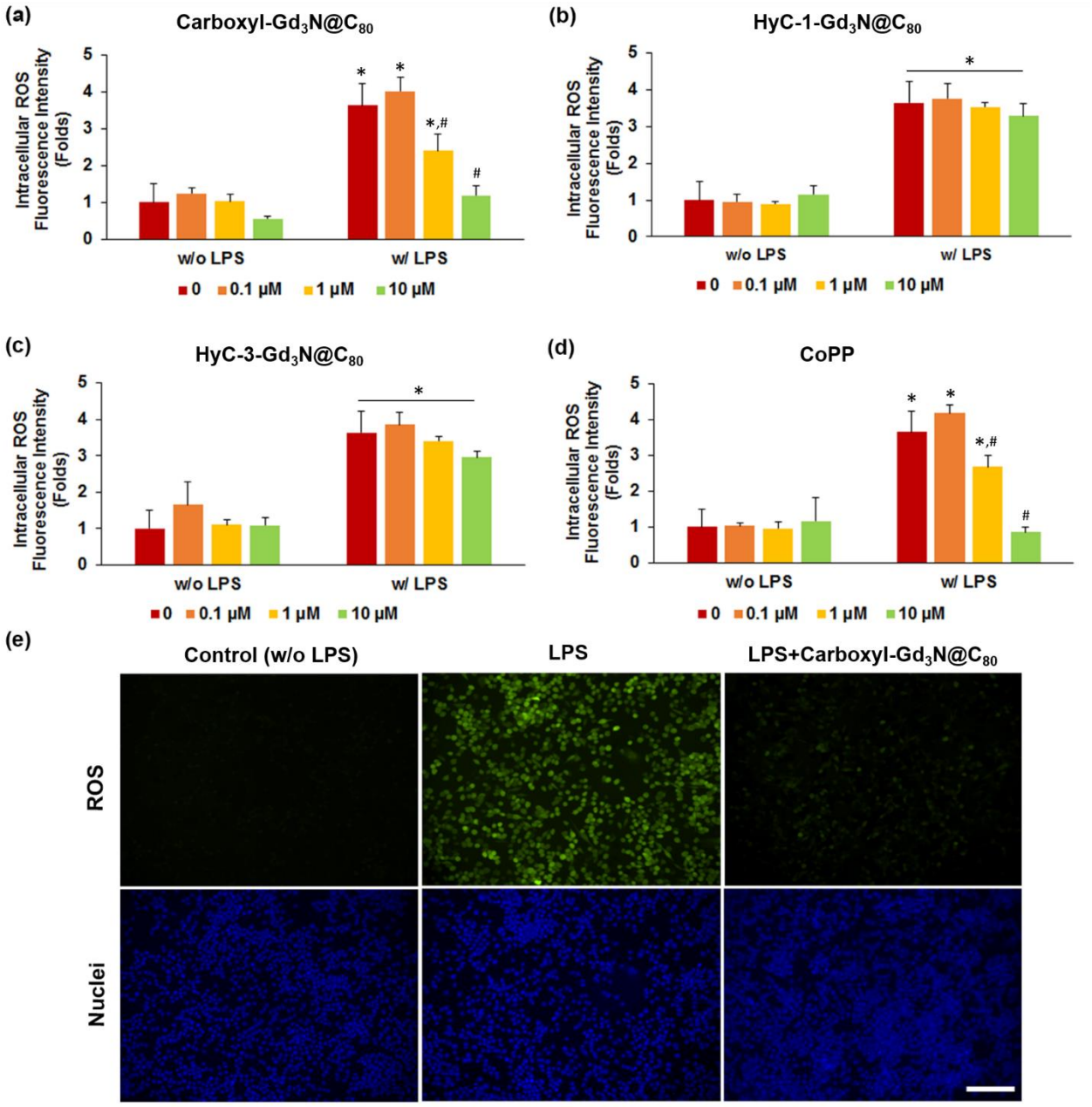

Figure 2. Biological screening of trimetallic nitride endohedral fullerenes for quenching LPS-induced reactive oxygen species (ROS). Raw 264.7 cells were treated with nanoparticles at various concentration (0, 0.1, 1, and 10 μM) in serum-free medium for 20 h, stimulated with or without LPS (100 ng/mL) for another 4 h, followed by intracellular ROS staining with 5 μM 2',7' dichlorodihydrofluorescein diacetate (H_2DCFDA) and fluorescence plate reading at E_x/E_m of 495/525 nm. (a) Carboxyl-$Gd_3N@C_{80}$ exhibited dose-dependent efficacy in attenuating LPS-induced excessive ROS, in a similar fashion as (d) the positive control protoporphyrin IX cobalt chloride (CoPP) a well-known hemooxygenase-1 inducer. In contrast, (b) HyC-1 and (c) HyC-3 showed no or little reduction in LPS-elicited ROS generation. (e) Representative fluorescence images of intracellular ROS illustrated robust ROS-scavenging activity of carboxyl-Gd_3NC80. Image taken at ×200 magnification. Scale bar represented 100 μm. $^*p<0.05$ vs non-LPS control, $^{\#}p<0.05$ vs LPS-treated groups.

Both inducible nitrite oxide synthase (iNOS) and tumor necrotic factor-alpha (TNF-α) are pro-inflammatory mediators, which are dramatically up-regulated during LPS-induced inflammatory responses in macrophages, therefore down-regulation of iNOS and TNF-α have been considered as a therapeutic maker for anti-inflammatory agents. HO-1 is an endogenous anti-oxidative microsomal enzyme whose upregulation showed a protective role (such as immune-modulation) in combating oxidative stress and resolving inflammation.[25] Nrf2 is a basic leucine zipper (bZIP) protein that regulates the expression of antioxidative proteins, such as HO-1.[26] To examine the antioxidative and anti-inflammatory effect of carboxyl-$Gd_3N@C_{80}$, we pretreated Raw 264.7 cells with nanoparticle at 3.5 μM for 20 h and LPS for another 4 h. Total RNA were isolated, reverse-transcribed to cDNA, and analyzed with real-time PCR. As shown in **Figure 3**, LPS significantly promoted the mRNA expression of iNOS (**p<0.01) and TNF-α compared to the control (***p<0.001). Carboxyl-$Gd_3N@C_{80}$ treatment markedly suppressed the upregulated iNOS and TNF-α mRNA. In contrast to LPS that possesses no impact on the gene expression of HO-1 ($p>0.05$. *vs.* control), carboxyl-$Gd_3N@C_{80}$ significantly elevated mRNA level of HO-1 (***p<0.0001 *vs.* control; $^{\#\#\#}p$<0.0001 vs LPS). In addition, Griess assay to assess nitrite (stable end-product of released NO) in cell media at a later time point illustrated carboxyl-$Gd_3N@C_{80}$ inhibited LPS-elicited nitric oxide release significantly (**Figure S3**), consistent with iNOS mRNA expression and prior intracellular ROS screening (**Figure 2A**). Our immunofluorescence staining data of Nrf2 expression in various treatment groups suggested carboxyl-$Gd_3N@C_{80}$ effectively elevated the global Nrf2 expression in presence or absence of LPS (***p<0.001 *vs.* Control, $^{\#\#\#}p$<0.001 vs LPS) linking its protective function for antioxidative and anti-inflammatory uses (**Figure 3D, E**). Primer sequences are listed in Table S1.

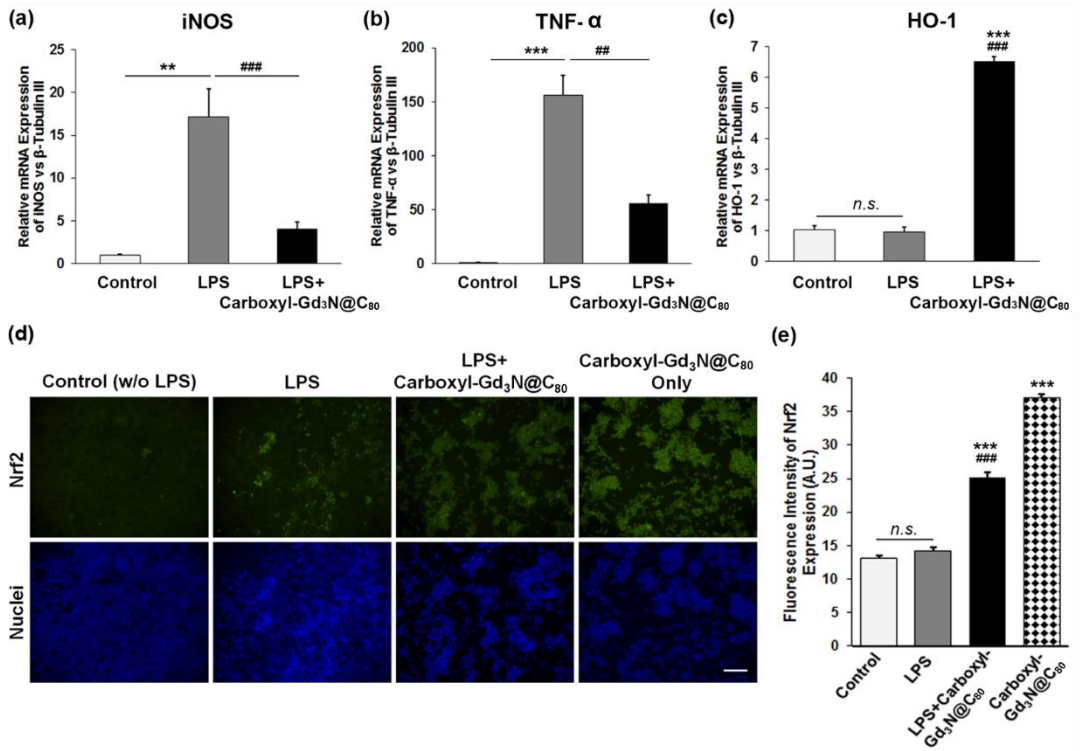

Figure 3. Carboxyl-$Gd_3N@C_{80}$ protected Raw 264.7 cells from LPS-induced oxidative stress and upregulated pro-inflammatory cytokine via elevating Nrf2 expression. Cells were pretreated with carboxyl-$Gd_3N@C_{80}$ (3.5 μM) for 20 h before treatment of LPS (100 ng/mL) for 4 h. (a) Real-time reverse transcription polymerase chain reaction (RT-PCR) suggested LPS stimulation significantly increased mRNA expression of inducible nitric oxide synthase (iNOS) (**p<0.01 vs control), whereas carboxyl-Gd_3N@C80 dramatically reversed such induction ($^{###}p$<0.001 *vs.* LPS). (b) Similarly, the upregulation of pro-inflammatory cytokine tumor necrosis factor-alpha (TNF-α) (***p<0.001 *vs.* control) upon LPS treatment was significantly alleviated by carboxyl-$Gd_3N@C_{80}$ ($^{##}p$<0.01 *vs.* LPS). (c) The antioxidative enzyme hemooxygenase-1 (HO-1) was significantly enhanced by carboxyl-$Gd_3N@C_{80}$ (***p<0.001 *vs.* control, $^{###}p$<0.001 *vs.* LPS) but it was not altered by LPS stimulation. (d), Immunofluorescence staining of Nrf2, a key antioxidative enzyme regulator, was dramatically increased upon nanoparticle treatment in the present and absence of LPS, whereas no significant intensity difference was observed in LPS treated cells. (e) Mean fluorescence intensity analysis of d suggested carboxyl-$Gd_3N@C_{80}$ effectively upregulated the protective Nrf2 protein expression (***p<0.001 *vs.* control, $^{###}p$<0.001 *vs.* LPS). Experiments were repeated three times (n=3). Scale bar in d represented 100 μm.

Mitogen-activated protein kinase MAPK (p38, ERK1/2, JNK) signaling play crucial roles in regulating pro-inflammatory cytokines and mediators such as TNF-α and iNOS during the course of inflammatory response. In particular, activation of ERK1/2 has been reported to stimulate TNF-α transcription and control the transport of TNF-α mRNA from the nucleus to the cytoplasm.[27] To further elucidate the molecular and cellular pathways regarding how carboxyl-$Gd_3N@C_{80}$ regulated oxidative stress and inflammation in macrophages, phosphorylation of ERK, and Akt

proteins were studied using Western blotting. As shown in **Figure 4**, LPS significantly elevated the phosphorylation of both ERK (***p<0.001) and Akt (*p<0.05) compared to control groups, whereas carboxyl-$Gd_3N@C_{80}$ (3.5 μM) markedly reduced phospho-ERK ($^{###}p$<0.001) with no significant effect on the change of phospho-Akt (p>0.05) compared to LPS groups. These results suggested that carboxyl-$Gd_3N@C_{80}$ protected macrophages from oxidative stress and inflammatory response primarily via downregulating LPS-induced phosphorylation of ERK but not AKT. Since activation of ERK is an early event in ROS signaling of macrophages activation, predominant regulation of this pathway by carboxyl-$Gd_3N@C_{80}$ would benefit substantial downstream intracellular targets to lessen oxidative stress and resolve inflammation.

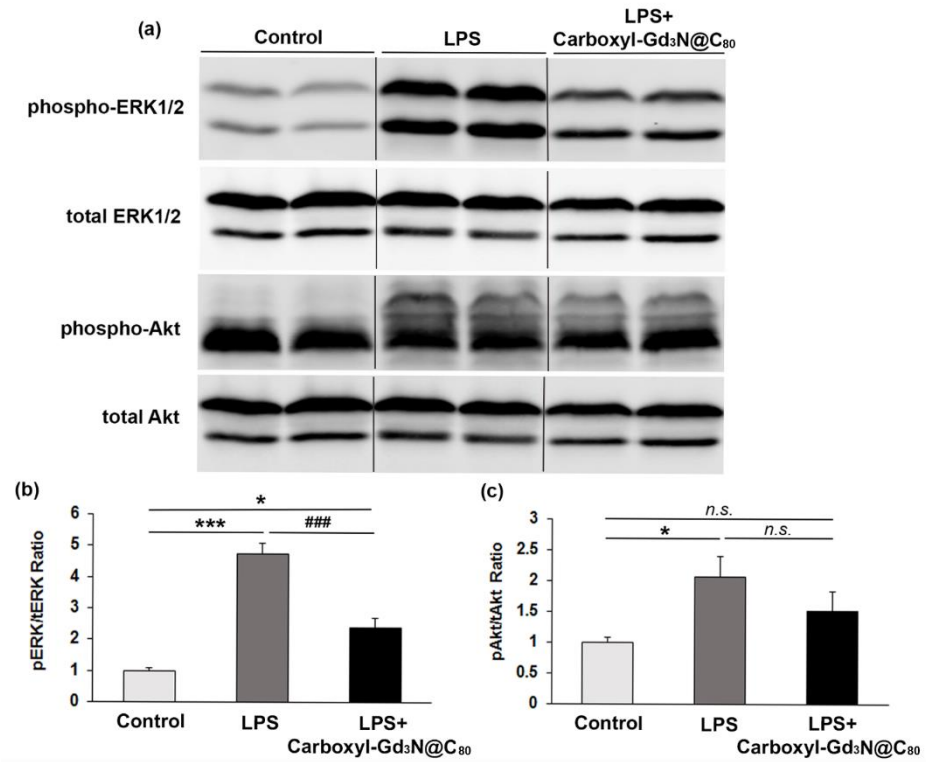

Figure 4. Carboxyl-$Gd_3N@C_{80}$ rescued Raw 264.7 cells from LPS-induced oxidative stress via ERK and Akt pathways. (a) Representative immunoblotting analysis of phosphor-ERK, total ERK, phosphor-Akt, and total Akt of cell lysates subjected to different treatments. Cells were preincubated with carboxyl-$Gd_3N@C_{80}$ (3.5 μM) for 20 h and treated with or without LPS (100 ng/mL) for another 4 h. (b) Quantification of pERK/tERK (n=4) intensity showed carboxyl-$Gd_3N@C_{80}$ significantly reversed LPS-induced ERK phosphorylation. (c) Quantitation analysis of pAkt/tAkt (n=4) exhibited some increase in p-Akt upon LPS stimulation, which was not significantly reduced by carboxyl-$Gd_3N@C_{80}$ pretreatment. Note, $*p<0.05$, $***p<0.001$ *vs.* control; $^{###}p<0.001$ *vs.* LPS group.

4.4 Conclusion

In this paper, we report the first discovery here that functionalized $Gd_3N@C_{80}$ possessed robust radical scavenging properties in solution and suppressed LPS-induced ROS in macrophage cell model, which was predominantly correlated to varied surface functionalization of metallofullerene. Carboxyl-$Gd_3N@C_{80}$ significantly attenuated LPS-induced iNOS and TNF-α mRNA expression, and correspondingly increased expression antioxidative enzyme HO-1 mRNA and its regulatory protein Nrf2. Such antioxidative and anti-inflammatory effects might be regulated via ERK but not Akt signaling pathways. In summary, we prove the concept that trimetallic nitride endohedral fullerenes, especially carboxyl-$Gd_3N@C_{80}$ hold great promise in becoming a novel class of theranostic agent against the oxidative stress and inflammation, in combination with their inherited MRI applications.

4.5 Supplementary Figures

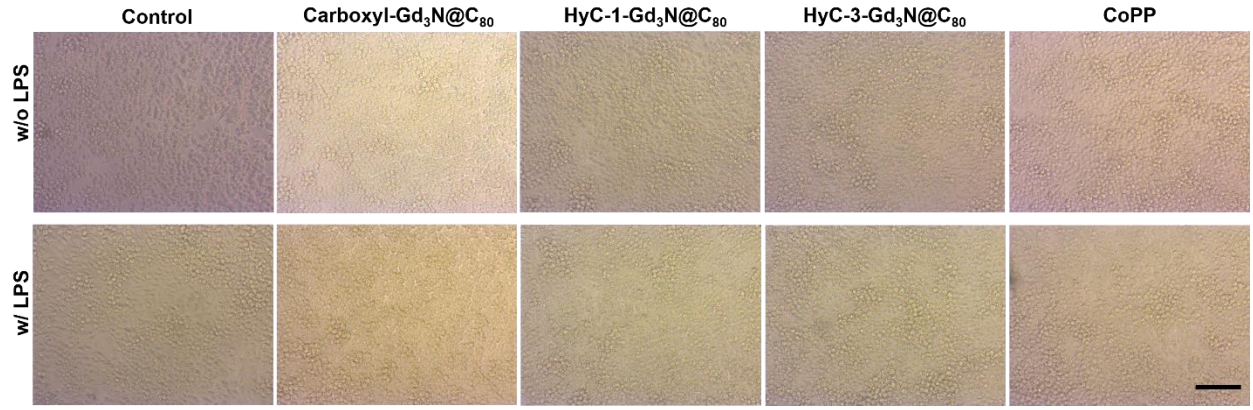

Figure S1. Representative phase contrast images of Raw 264.7 cells subjected to various pre-treatment with no nanoparticle, carboxyl-$Gd_3N@C_{80}$, HyC-1-$Gd_3N@C_{80}$, HyC-3-$Gd_3N@C_{80}$ and CoPP, and with or without LPS (100 ng/mL) stimulation for another 4 h. Scale bar represented 50 µm. Images were captured at ×200 magnification with a Zeiss bright-field microscope, an Axiocam camera and Zen software. Note, nanoparticles and CoPP were added at 10 µM as final concentration. No significant cytotoxicity was visualized in all groups.

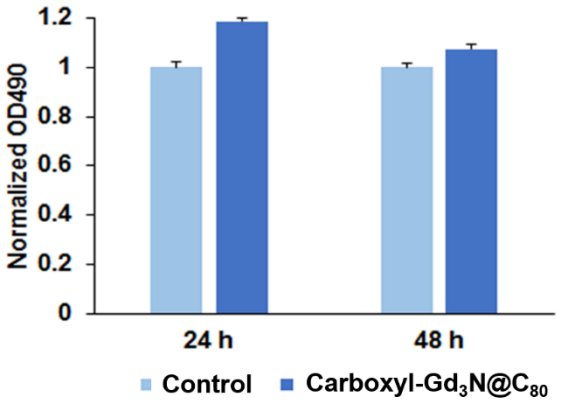

Figure S2. MTS assay of Raw 264.7 cells suggested Carboxyl-$Gd_3N@C_{80}$ (3.5 µM) did not significantly impact the viability and metabolic status of cells in vitro.

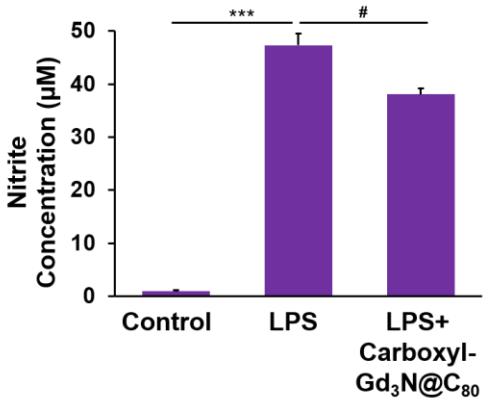

Figure S3. Griess assay showed carboxyl-$Gd_3N@C_{80}$ effectively decreased LPS induced nitric oxide release in Raw 264.7 cells media. ***p<0.001 *vs.* control, $^{\#}p$<0.05 *vs.* LPS.

Table S1. Primer sequences for real-time RT-PCR.

Gene Names	Forward (5'-3')	Reverse (5'-3')
Mouse β-tubulin III	AGGTGCGTGAGGAGTACCC	AGGGCTTCATTGTCGATGCAG
Mouse iNOS	GTTCTCAGCCCAACAATACAAGA	GTGGACGGGTCGATGTCAC
Mouse TNF-α	CGGGGTGATCGGTCCCCAAAG	GGAGGGCGTTGGCGCGCTGG
Mouse HO-1	CAGGTGTCCAGAGAAGGCTTT	TCTTCCAGGGCCGTGTAGAT

References

1. Liu, H.; Yang, X.; Zhang, Y.; Dighe, A.; Li, X.; Cui, Q., Fullerol antagonizes dexamethasone-induced oxidative stress and adipogenesis while enhancing osteogenesis in a cloned bone marrow mesenchymal stem cell. *J. Orthop. Res.* **2012,** *30* (7), 1051-1057.
2. Akhtar, M. J.; Ahamed, M.; Alhadlaq, H. A.; Alshamsan, A., Mechanism of ROS scavenging and antioxidant signalling by redox metallic and fullerene nanomaterials: Potential implications in ROS associated degenerative disorders. *Biochim. Biophys. Acta* **2017,** *1861* (4), 802-813.
3. Markovic, Z.; Trajkovic, V., Biomedical potential of the reactive oxygen species generation and quenching by fullerenes (C_{60}). *Biomaterials* **2008,** *29* (26), 3561-3573.
4. Morry, J.; Ngamcherdtrakul, W.; Yantasee, W., Oxidative stress in cancer and fibrosis: Opportunity for therapeutic intervention with antioxidant compounds, enzymes, and nanoparticles. *Redox Biol.* **2017,** *11*, 240-253.
5. Mikawa, M.; Kato, H.; Okumura, M.; Narazaki, M.; Kanazawa, Y.; Miwa, N.; Shinohara, H., Paramagnetic water-soluble metallofullerenes having the highest relaxivity for MRI contrast agents. *Bioconjugate Chem.* **2001,** *12* (4), 510-514.
6. Fatouros, P. P.; Corwin, F. D.; Chen, Z. J.; Broaddus, W. C.; Tatum, J. L.; Kettenmann, B.; Ge, Z.; Gibson, H. W.; Russ, J. L.; Leonard, A. P.; Duchamp, J. C.; Dorn, H. C., In vitro and in vivo imaging studies of a new endohedral metallofullerene nanoparticle. *Radiology* **2006,** *240* (3), 756-764.
7. Shu, C. Y.; Corwin, F. D.; Zhang, J. F.; Chen, Z. J.; Reid, J. E.; Sun, M. H.; Xu, W.; Sim, J. H.; Wang, C. R.; Fatouros, P. P.; Esker, A. R.; Gibson, H. W.; Dorn, H. C., Facile Preparation of a New Gadofullerene-Based Magnetic Resonance Imaging Contrast Agent with High H^1 Relaxivity. *Bioconjugate Chem.* **2009,** *20* (6), 1186-1193.
8. Yin, J. J.; Lao, F.; Fu, P. P.; Wamer, W. G.; Zhao, Y.; Wang, P. C.; Qiu, Y.; Sun, B.; Xing, G.; Dong, J.; Liang, X. J.; Chen, C., The scavenging of reactive oxygen species and the potential for cell protection by functionalized fullerene materials. *Biomaterials* **2009,** *30* (4), 611-21.
9. Zhang, J. F.; Fatouros, P. P.; Shu, C. Y.; Reid, J.; Owens, L. S.; Cai, T.; Gibson, H. W.; Long, G. L.; Corwin, F. D.; Chen, Z. J.; Dorn, H. C., High Relaxivity Trimetallic Nitride (Gd_3N)

Metallofullerene MRI Contrast Agents with Optimized Functionality. *Bioconjugate Chem.* **2010,** *21* (4), 610-615.

10. Adiseshaiah, P.; Dellinger, A.; MacFarland, D.; Stern, S.; Dobrovolskaia, M.; Ileva, L.; Patri, A. K.; Bernardo, M.; Brooks, D. B.; Zhou, Z. G.; McNeil, S.; Kepley, C., A Novel Gadolinium-Based Trimetasphere Metallofullerene for Application as a Magnetic Resonance Imaging Contrast Agent. *Invest. Radiol.* **2013,** *48* (11), 745-754.

11. Zhang, J. Y.; Ye, Y. Q.; Chen, Y.; Pregot, C.; Li, T. H.; Balasubramaniam, S.; Hobart, D. B.; Zhang, Y. F.; Wi, S.; Davis, R. M.; Madsen, L. A.; Morris, J. R.; LaConte, S. M.; Yee, G. T.; Dorn, H. C., $Gd_3N@C_{84}(OH)_x$: A New Egg-Shaped Metallofullerene Magnetic Resonance Imaging Contrast Agent. *J. Am. Chem. Soc.* **2014,** *136* (6), 2630-2636.

12. Li, J.; Guan, M.; Wang, T.; Zhen, M.; Zhao, F.; Shu, C.; Wang, C., $Gd@C_{82}$-$(ethylenediamine)_8$ Nanoparticle: A New High-Efficiency Water-Soluble ROS Scavenger. *ACS Appl. Mater. Interfaces* **2016,** *8* (39), 25770-25776.

13. Li, T. H.; Murphy, S.; Kiselev, B.; Bakshi, K. S.; Zhang, J. Y.; Eltahir, A.; Zhang, Y. F.; Chen, Y.; Zhu, J.; Davis, R. M.; Madsen, L. A.; Morris, J. R.; Karolyi, D. R.; LaConte, S. M.; Sheng, Z.; Dorn, H. C., A New Interleukin-13 Amino-Coated Gadolinium Metallofullerene Nanoparticle for Targeted MRI Detection of Glioblastoma Tumor Cells. *J. Am. Chem. Soc.* **2015,** *137* (24), 7881-7888.

14. Shultz, M. D.; Duchamp, J. C.; Wilson, J. D.; Shu, C. Y.; Ge, J. C.; Zhang, J. Y.; Gibson, H. W.; Fillmore, H. L.; Hirsch, J. I.; Dorn, H. C.; Fatouros, P. P., Encapsulation of a Radiolabeled Cluster Inside a Fullerene Cage, $^{177}Lu_xLu_{(3-x)}N@C_{80}$: An Interleukin-13-Conjugated Radiolabeled Metallofullerene Platform. *J. Am. Chem. Soc.* **2010,** *132* (14), 4980.

15. Wilson, J. D.; Broaddus, W. C.; Dorn, H. C.; Fatouros, P. P.; Chalfant, C. E.; Shultz, M. D., Metallofullerene-Nanoplatform-Delivered Interstitial Brachytherapy Improved Survival in a Murine Model of Glioblastoma Multiforme. *Bioconjugate Chem.* **2012,** *23* (9), 1873-1880.

16. Horiguchi, Y.; Kudo, S.; Nagasaki, Y., $Gd@C_{82}$ Metallofullerenes for Neutron Capture Therapy-Fullerene Solubilization by Poly(ethylene glycol)-block-poly(2-(N, N-diethylamino)ethyl methacrylate) and Resultant Efficacy in vitro. *Sci. Technol. Adv. Mater.* **2011,** *12* (4).

17. Xiao, L.; Li, T.; Ding, M.; Yang, J.; Rodriguez-Corrales, J.; LaConte, S. M.; Nacey, N.; Weiss, D. B.; Jin, L.; Dorn, H. C.; Li, X., Detecting Chronic Post-Traumatic Osteomyelitis of

Mouse Tibia via an IL-13Ralpha2 Targeted Metallofullerene Magnetic Resonance Imaging Probe. *Bioconjugate Chem.* **2017,** *28* (2), 649-658.

18. Shultz, M. D.; Wilson, J. D.; Fuller, C. E.; Zhang, J. Y.; Dorn, H. C.; Fatouros, P. P., Metallofullerene-based Nanoplatform for Brain Tumor Brachytherapy and Longitudinal Imaging in a Murine Orthotopic Xenograft Model. *Radiology* **2011,** *261* (1), 136-143.

19. Morry, J.; Ngamcherdtrakul, W.; Yantasee, W., Oxidative Stress in Cancer and Fibrosis: Opportunity for Therapeutic Intervention with Antioxidant Compounds, Enzymes, and Nanoparticles. *Redox Biol.* **2017,** *11*, 240-253.

20. Li, T.; Dorn, H. C., Biomedical Applications of Metal-Encapsulated Fullerene Nanoparticles. *Small* **2017,** *13* (8).

21. Wang, J.; Chen, C.; Li, B.; Yu, H.; Zhao, Y.; Sun, J.; Li, Y.; Xing, G.; Yuan, H.; Tang, J.; Chen, Z.; Meng, H.; Gao, Y.; Ye, C.; Chai, Z.; Zhu, C.; Ma, B.; Fang, X.; Wan, L., Antioxidative Function and Biodistribution of $[Gd@C_{82}(OH)_{22}]_n$ Nanoparticles in Tumor-bearing Mice. *Biochem. Pharmacol.* **2006,** *71* (6), 872-881.

22. Ali, S. S.; Hardt, J. I.; Quick, K. L.; Kim-Han, J. S.; Erlanger, B. F.; Huang, T. T.; Epstein, C. J.; Dugan, L. L., A Biologically Effective Fullerene (C_{60}) Derivative with Superoxide Dismutase Mimetic Properties.
Free Radical Biol. Med. **2004,** *37* (8), 1191-202.

23. Xu, J.; Chen, L.; Li, L., Pannexin Hemichannels: A Novel Promising Therapy Target for Oxidative Stress Related Diseases. *J. Cell. Physiol.* **2017**.

24. Cai, C.; Teng, L.; Vu, D.; He, J.-Q.; Guo, Y.; Li, Q.; Tang, X.-L.; Rokosh, G.; Bhatnagar, A.; Bolli, R., The Heme Oxygenase 1 Inducer (CoPP) Protects Human Cardiac Stem Cells against Apoptosis through Activation of the Extracellular Signal-regulated Kinase (ERK)/NRF2 Signaling Pathway and Cytokine Release.
J. Biol. Chem. **2012,** *287* (40), 33720-33732.

25. Maamoun, H.; Zachariah, M.; McVey, J. H.; Green, F. R.; Agouni, A., Heme Oxygenase (HO)-1 Induction Prevents Endoplasmic Reticulum Stress-mediated Endothelial Cell Death and Impaired Angiogenic Capacity. *Biochem. Pharmacol.* **2017,** *127*, 46-59.

26. Montana, G.; Lampiasi, N., Substance P Induces HO-1 Expression in RAW 264.7 Cells Promoting Switch towards M2-Like Macrophages. *PLoS One* **2016,** *11* (12), e0167420.

27. Xagorari, A.; Roussos, C.; Papapetropoulos, A., Inhibition of LPS-stimulated Pathways in Macrophages by the Flavonoid Luteolin. *Br. J. Pharmacol.* **2002,** *136* (7), 1058-1064.

Chapter 5 Designed the peglayted-$Gd_3N@C_{80}$ as magnetic resonance imaging contrast agent of the gastrointestinal tract

Tinghui Li[†], Yonjae J. Kim[‡, ǁ], Stephen LaConteǁ, Dixon Smileyǁ, Harry C. Dorn[†, ǁ,*]

[†] Department of Chemistry, Virginia Polytechnic Institute and State University, Blacksburg, VA

[‡] Virginia Tech Carilion School of Medicine, Roanoke, VA

ǁ Virginia Tech Carilion Research Institute, Roanoke, VA

5.1 Introduction

Since the early 1990's, there has been a widespread clinical application of gadolinium-based magnetic resonance imaging (MRI) contrast agents, employed in 25-50% of all MRI examinations. Despite the broad adoption of Gd-based clinical MRI agents, commonly used commercial agents have some deficiencies such as low relaxivity, extracellular distribution, non-specificity, immediate hypersensitivity reactions, and potential release of toxic Gd^{3+} ions.[1] In 2006, the association between the use of gadolinium-containing contrast agents for MRI and the severe dermal and systemic disease, nephrogenic fibrosing dermopathy/nephrogenic systemic fibrosis (NFD/NSF) was reported for patients with impaired renal function. More recently, several works confirmed that the Gd^{3+} ions were deposited in the healthy brain and bone tissue in patients with normal renal function after serial application of commercial contrast agents.[2-5] Although the long-term and cumulative clinical effects of retained gadolinium are unknown, there is a need for improved high-relaxivity MRI contrast agents that significantly suppress the release of the toxic Gd^{3+} ions and allow for clinical efficacy at reduced dosage levels. The endohedral metallofullerenes would appear to be leading candidates because the encapsulated Gd^{3+} ions are more effectively isolated from the bio-environment by the robust fullerene cage. Also, the enhanced MR relaxivity allows equivalent contrast for significantly lower levels of the administered Gd contrast agent.

Functionalized Gd-loaded fullerenes, $Gd@C_{82}$ and $Gd_3N@C_{80}$, have attracted much attention as a potential new nanoplatform for next-generation MRI contrast agents, given to their inherent higher ^1H relaxivity than most commercial contrast agents.[6-9] The fullerene cage is an extraordinarily stable species which makes it extremely unlikely to break and release the toxic Gd metal ions into the bio-environment. In the last decade, our group has endeavored to discover a series of functionalized $Gd_3N@C_{80}$ for MRI detection of various pathological conditions, such as chronic osteomyelitis and brain cancer.[9-11] These studies reported the Gd-based metallofullerene could be administered intravenously then excreted from the body within 7 days. However, the possibility of Gd-based metallofullerene working as MRI contrast agents for gastrointestinal (GI) tract has never been investigated.

In addition, oxidative stress is characterized by increased level of reactive oxygen species (ROS) and/or reactive nitrogen species (RNS). High level of ROS may induce alternation or damage to DNA, proteins, and lipids, which has been implied in the pathogenesis of a number of diseases. The pathogenesis of various GI diseases including peptic ulcers, gastrointestinal cancers, and inflammatory bowel disease is in part due to oxidative stress.[12,13] Our group demonstrated functionalized $Gd_3N@C_{80}$ possessed robust radical scavenging properties in solution and suppressed LPS-induced ROS in macrophage cell model. With excellent antioxidative and anti-inflammatory properties, functionalized $Gd_3N@C_{80}$ hold great promise in becoming a novel class of theranostic agent against the oxidative stress and inflammation, in combination with their inherited MRI applications.[14-16]

In this work, $Gd_3N@C_{80}$ was modified with polyethylene glycol ($Gd_3N@C_{80}$-$DiPEG_{2000}(OH)x$) for working as MRI contrast agents for GI tract. The high molecular weight can prevent any appreciable absorption through the skin or mucosal tissue, and offer considerable advantages for

localized agents in the GI tract.[17,18] Besides the excellent contrast capability, the PEGylated-$Gd_3N@C_{80}$ exhibited outstanding radical scavenging ability, which can potentially eliminate the ROS in GI tract. The biodistribution result suggests this nanoplatform can be worked as the potential contrast agent for GI tract at least for 6 hours.

5.2 Experimental

5.2.1 Materials

$Gd_3N@C_{80}$ was purchased from LUNA Innovations (Danville, VA). 98% 1,8-Diazabicyclo(5.4.0)undec-7-ene (DBU), 99% trimethylamine (TEA), polyethylene glycol 2000 (PEG_{2000}), 99% CBr_4, 99% 18crown-6, 50% sodium hydroxide solution, and 50 % hydrogen peroxide were used as obtained from Sigma-Aldrich. Hydrogen peroxide (H_2O_2), ferrous sulfate heptahydrate ($FeSO_4$), xanthine, xanthine oxidase from bovine milk (XOD), diethylenetriaminepentaacetic acid (DTPA), and lipopolysaccharide (LPS) were purchased from Sigma Aldrich. Spin traps, 5-diethoxyphosphoryl-5-methyl-I-pyrroline N-oxide (DEPMPO) was purchased from Focus Biomolecules, 5-tert-Butoxycarbonyl-5-methyl-1-pyrroline-N-oxide (BMPO) was supplied by Cayman Chemical. The clear EPR quartz capillary tubes (ID 1.0mm, OD 1.2mm) were obtained from Wilmad-LabGlass.

5.2.2 Synthesis of Di{ω-methyl-poly(ethylene glycol)} malonate ($DiPEG_{2000}$)

To a solution with 5g PEG_{2000}, 0.7 ml triethylamine in 7 ml CH_2Cl_2, was added dropwise a solution of 0.25 ml malonyl dichloride. The solution was stirred at room temperature under N_2 protection for 4 hours. The final mixture was concentrated and the residue was dissolves in chloroform and then poured into a large amount of toluene, filtrated and the filtrate was concentrated under vacuum to give a yellow viscous liquid (**Scheme 1A**)[19].

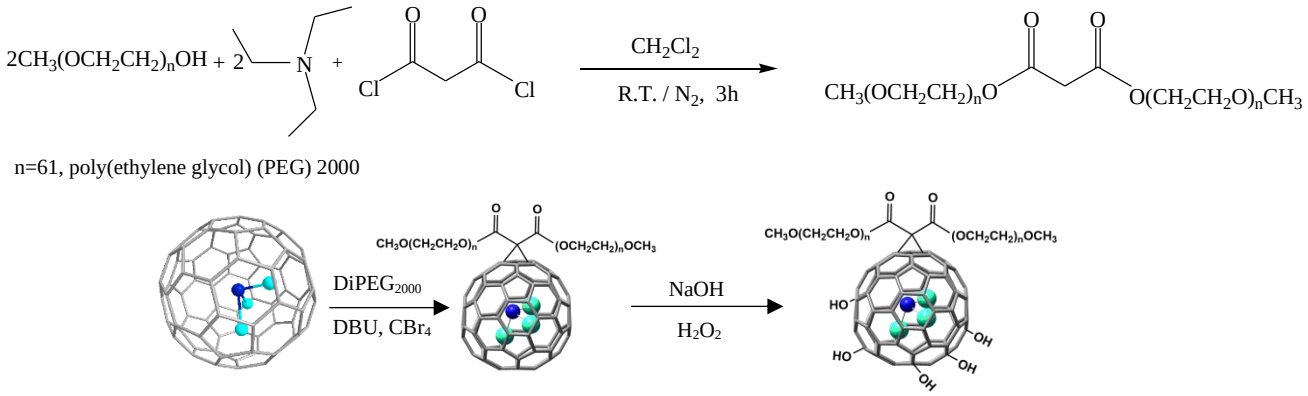

Scheme 1. A) Synthesis of Di{ω-methyl-poly(ethylene glycol)} malonate and B) Functionalization and Conjugation Process of $Gd_3N@C_{80}$-$DiPEG_{2000}(OH)x$ (Gray, Carbon; Aqua, Gadolinium Ion; Blue, Nitrogen).

5.2.3 Synthesis of $Gd_3N@C_{80}$-$DiPEG_{2000}(OH)x$

The mixture of $Gd_3N@C_{80}$, $DiPEG_{2000}$, DBU and CBr_4 (molar ratio 1:20:20:67) was dissolved in 10 mL chlorobenzene with degassed by argon for 30 min. The solution was stirred at room temperature for 12 hours. The resultant mixture was evaporated to remove solvent and then redissolved in toluene. 5 ml of NaOH and 2mg 18-crown-6 were added and the resultant solution was stirred for another 3 hours. Then 3ml water and 15 drops of H_2O_2 were added and the mixture was stirred at ambient temperature overnight (**Scheme 1B**). The resultant solution was concentrated and separated by Sephadex G25.

5.2.4 Relaxivity Measurements for $Gd_3N@C_{80}$-$DiPEG_{2000}(OH)x$

Solutions with different Gd^{3+} concentrations were prepared by diluting a stock solution with deionized water. The concentration of the Gd^{3+} ions was determined by Varian 820-MS ICP Mass

Spectrometer. The T_1 and T_2 relaxation times were measured at three different magnetic field strength, Bruker Minispec mq 20 (0.47 T), mq 60 (1.41 T) analyzers, and Bruker Avance III 400 MHz (9.4 T) wide bore spectrometer equipped with an MIC 400 W1/S2 probe and 5mm ^{1}H coil. The inversion-recovery method was used to measure the spin-lattice relaxation time T_1, and the Carr-Pucell-Meiboom-Gill method was used for the spin-spin relaxation time T_2 measurement. Errors in T_1 and T_2 values were less than ±2%.

5.2.5 MRI Acquisition

The relaxivity data of the samples were obtained at 3T on a Siemens MAGNETOM Prisma scanner using a four element surface coil. An inversion recovery spin echo sequence was implemented, acquiring images at different inversion times (T_I=24, 50, 100, 200, 500, 1000, 2000 and 2500 ms) while keeping all other parameters fixed (20 slices, T_E=36 ms, T_R=4000 ms, flip angle=150^o). $Gd_3N@C_{80}$-$DiPEG_{2000}$(OH)x were placed in 5mm NMR tubes with various concentrations of 2 μM, 5 μM, 10 μM, 20 μM and 100 μM.

5.2.6 *In vitro* MRI study of the functionalized $Gd_3N@C_{80}$

The *in vitro inversion-recovery* MR images were obtained under the same 3T clinical scanner for the visual confirmation of the efficiency of the functionalized fullerene working as a contrast agent. Various concentrations of the Gd based fullerenes, and the commercial contrast agent Omniscan® were used and compared.

5.2.7 Hydroxyl radical (HO) scavenging activity

Interception of hydroxyl radicals by each fullerene derivative was determined by the EPR spin-trapping technique. The EPR assay was based on the competition between the trapping agent, DEPMPO, and the fullerene derivative nanoparticles for HO. Hydroxyl radicals were generated by the classical Fenton reaction with the reaction mixture containing freshly prepared 500 µM

DEPMPO, 20 μM $FeSO_4$ and 200 μM H_2O_2 with or without 14 μM of a $Gd_3N@C_{80}$-$DiPEG_{2000}$(OH)x. The clear quartz capillary tubes (ID 1.0mm, OD 1.2mm) were used as the sample container. The EPR data were collected at ambient temperature, 2 min after initiating the formation of HO by addition of $FeSO_4$. The following instrument settings were used for collecting EPR spectra: microwave power of 10 mW, field modulation frequency of 100 kHz, and modulation amplitude of 1 G.

5.2.8 Superoxide radical anion ($O_2^{\bullet-}$) scavenging activity

BMPO was used to trap and detect $O_2^{\bullet-}$ by EPR spectroscopy. Superoxide radical anion was generated using the xanthine/ xanthine oxidase system. The scavenger radical reaction was initiated by addition of xanthine oxidase solution (XOD). The reaction contained 100 μM xanthine (1M NaOH in PBS), 20 mM BMPO, 50 μM DTPA, 0.1 U/ml XOD, in the presence or absence of 11 μM of a $Gd_3N@C_{80}$-$DiPEG_{2000}$(OH)x. The EPR spectra were recorded at 1.5 min after initiating the generation of $O_2^{\bullet-}$ by addition of XOD. The instrument settings were used as the same as hydroxyl radicals.

5.2.9 Mice breed and housing

For the biodistribution studies, 8-10 week old ICR CD-1 outbred mice (Envigo Inc., Indianapolis, IN) weighing 25-30 g were used. The CD-1 mice are an albino strain bred without any specific disease models that are often used to study physiology and general safety, making them ideal for this study. In order to minimize conflicts between mice within the same cage, only female mice were used and they were housed with maximum of four animals per cage. They were fed standard rodent chow and water via *ad libitum* feeding, and they were exposed to standard 12 h on, 12 h off lighting conditions. The mice were housed in facility for 3 to 5 days before administration of $Gd_3N@C_{80}$-$DiPEG_{2000}$(OH)x.

5.2.10 Oral biodistribution groups

The mice were divided into 4 groups of 5 animals (total 20 animals), and each group was euthanized at a different time after oral administration: 15 minutes, 3 hours, 6 hours, and 7 days. The group size was based on those utilized by previous literature that performed similar biodistribution studies involving metallofullerenes, which ranged from 3-4 mice per group.

5.2.11 Feeding and Euthanization

Each animal was fed a single 200 µL bolus of 43.7 µM solution of $Gd_3N@C_{80}$-$DiPEG_{2000}$(OH)x using a 1 mL insulin syringe through a curved, 20 gauge, 3.8 cm long stainless steel gavage needle with a 2.4mm tip (GloMed Inc., Sherman Oaks, CA). Food was removed from cages 3 hours before administartion of the bolus and was returned a hour after administration if the mouse was still alive. The mice in the 7 days group were placed into metabolism cages for 24 hours after administration, and the fecal samples were collected at 6 hours and 24 hours after administration. After 24 hours, the mice were returned to their standard housing cages for the rest of the 7 days. The mice were euthanized using 5L/min of CO_2 for 10 minutes, followed by mechanical separation of the spine. After euthanization, the mice's liver, kidneys, spleen, and the GI tract from mid-esophagus to rectum were dissected and placed into 50 mL centrifuge tubes. The lungs were also collected in order to check for experimental errors in cases where the bolus may have been administered into the lungs rather than the stomach.

5.2.12 Organ processing and measurement

The spleens and kidneys were digested in 70% HNO_3 solution for 2 hours at ~100°C. Livers and GI tracts required more prolonged digestive periods, requiring 4 h and 8 h, respectively. The digested samples were then cooled to room temperature before being filtered using a hydrophilic PTFE 0.45 µm pore syringe filter (Millex KGaA, Darmstadt, Germay). The empty digestion tubes

were washed three times with 1 mL of 70% HNO_3 solution, and the wash fluid was added to the samples after being filtered through the same syringe filters. The filtered samples were diluted to 1:10 ratio with deionized water in order to reduce its acidity to be compatible with the mass spectrometer. The gadolinium concentration in the samples was measured by ICP-MS.

5.3Results and Discussion

5.3.1 Relaxivity Measurements of the functionalized $Gd_3N@C_{80}$

The r_1 and r_2 relaxivity results of $Gd_3N@C_{80}$-$DiPEG_{2000}$(OH)x are summarized in **Table 1**. The nuclear magnetic resonance relaxivity were calculated by the general equation (Eq 1.)[9]

$$\frac{1}{T_{i\,obs}} = \frac{1}{T_{i\,H_2O}} + \frac{1}{T_{i\,para}} = \frac{1}{T_{i\,H_2O}} + r_i[M] \quad \text{Eq. 1}$$

The relaxation rate is determined by both diamagnetic (pure water) and paramagnetic (contrast agent) components. The ratio of paramagnetic relaxation rate to the concentration (M) is the relaxivity (r_i) of the paramagnetic compound, which can be experimentally obtained by the slope of $1/T_i$ versus concentrations of the paramagnetic contrast agents. These results can be compared with the relaxivity of the commercial contrast agents, Omniscan®, which exhibit much lower relaxivity at all magnetic field strengths.

Table 1. Relaxivities of functionalized Gadolinium Metallofullerenes (Units of $mM^{-1}\ s^{-1}$ per mM in pure water at 25 °C).

Contrast agents	0.47 T			1.41 T			9.4 T		
	r_1	r_2	r_2/r_1	r_1	r_2	r_2/r_1	r_1	r_2	r_2/r_1
f-$Gd_3N@C_{80}$ (2-100 µM)	100.6	115.7	1.2	128.8	167.7	1.3	42.3	186.5	4.4
Omniscan®	~4	~4	~1	~4	~4	~1	~4	~4	~1

5.3.2 MRI Acquisition and Processing

The *inversion recovery* (IR) sequence is an NMR method of estimating the T_1 relaxation time. The method uses a 180° pulse, followed by the variable inversion time T_I, and then a 90° pulse to produce the free induction decay (FID) signal in the x-y plane. **Equation 2** describes the relaxation of magnetization toward maximumM_z. This function, modeled in **Figure 1**, was used to fit the signal of each sample over the range of inversion times to estimate their T_1 relaxation times.

$$M_z = M_0(1 - 2e^{-\frac{TI}{T_1}}) \qquad \text{Eq. 2}$$

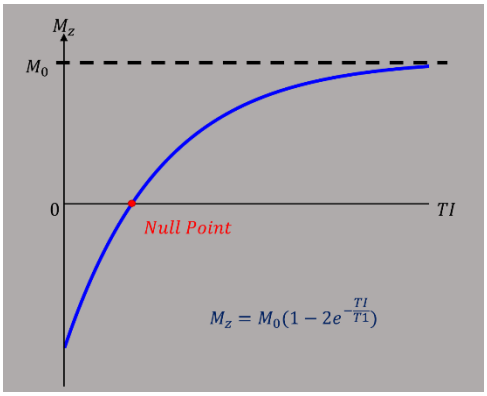

Figure 1. Model of *inversion recovery* function. As T_I increases, the magnetization along z returns to its maximum value. Labeled in red is the null point.

The IR curve used for estimating T_1 ranges from negative to positive values. However, images acquired by the MR scanner only provide the magnitude intensities, which are all positive (**Figure 2A**). The sign of intensities at inversion time (T_{IS}) on the left of "null point" (the signal intensity is approximately zero) need to be flipped over as shown in **Figure1**. After fit an exponential to extract the T_1 time of each sample by using the inversion recovery equation. Multiple fits based on the location of the minimum signal relative to the null point were tested, best T_1 time were selected based on the R^2_{adj} value (**Figure 2B**). According to the fitting, the r_1 of $Gd_3N@C_{80}$-$DiPEG_{2000}(OH)x$ under 3T is 61.08 mM^{-1} s^{-1}.

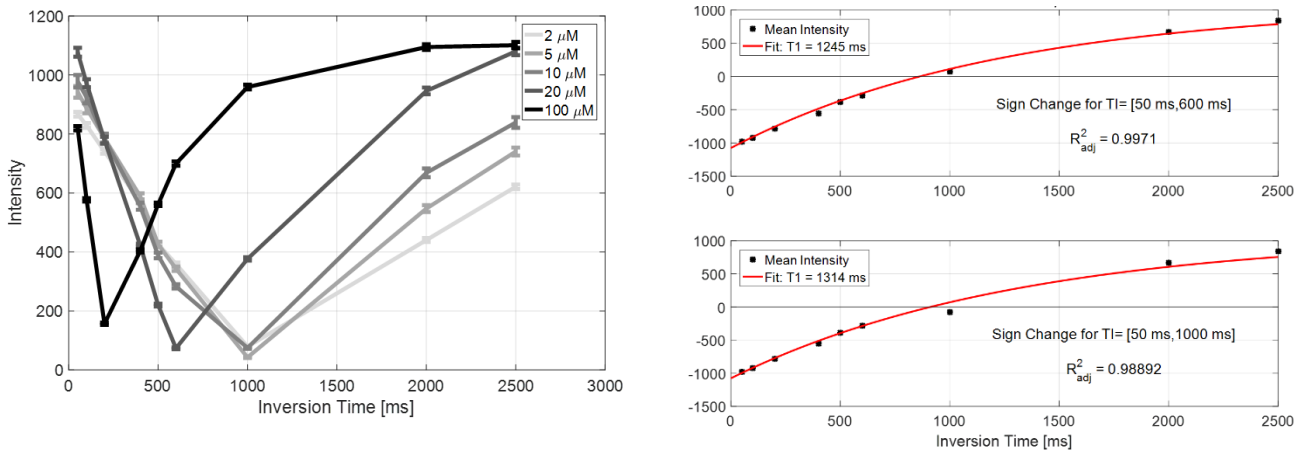

A B

Figure 2. A) Plots of mean intensity values of $Gd_3N@C_{80}$-$DiPEG_{2000}$(OH)x for the inversion recovery sequence. B) Example of testing multiple T_1 fits for $Gd_3N@C_{80}$-$DiPEG_{2000}$(OH)x at 10 ***μM***. The change in sign was applied to data between 50 ms and 600 ms (top) and then between 50 ms and 1000 ms (bottom). The first case produces the better fit, as reflected in the $\boldsymbol{R^2_{adj}}$ metric.

5.3.3 *In vitro* MR contrast ability of the functionalized $Gd_3N@C_{80}$

In **Figure 3**, the *inversion-recovery* images obtained using a clinical 3T MR scanner with 5 mm NMR tubes containing various concentrations of $Gd_3N@C_{80}$-$DiPEG_{2000}$(OH)x and commercial MR contrast agent, Omniscan®. The 2 μM functionalized metallofullerene and 20 μM Omniscan® in water share similar contrast. These results show that the functionalized $Gd_3N@C_{80}$ has outstanding contrast relatively to commercial agents.

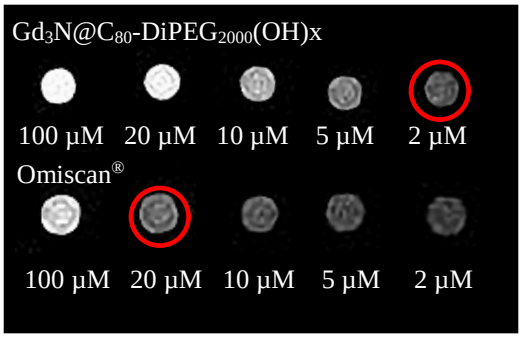

Figure 3. *Inversion-recovery* MR images (T_1=2000 ms, T_R=4000 ms, T_E=32 ms) with f-$Gd_3N@C_{80}$ and Omniscan® as contrast agent. From right to left: 2, 5, 10, 20 and 100 μM f-$Gd_3N@C_{80}$. The 2 μM f-$Gd_3N@C_{80}$ and 20 μM Omniscan® in water exhibit comparable contrast.

5.3.4 Scavenging of ROS

In this work, hydroxyl radical (•OH) and superoxide radical anion ($O_2^{\bullet-}$), the most common ROS in the body, were chosen as the models to evaluate the capability of $Gd_3N@C_{80}$-$DiPEG_{2000}$(OH)x to eliminate ROS by using EPR methods. Due to the relatively low sensitivity of EPR detection and the biological free radicals are short-lived, the exogenous spin traps were used. The EPR assay was based on the competition between the trapping agents, and pegylated-hydroxylated fullerenes for radicals.

Hydroxyl radicals were generated by the classical Fenton reaction, which involves the reaction of $FeSO_4$ and H_2O_2. The concentration of H_2O_2 was 200 μM, DEPMPO was 500 μM, which was 36 times higher than the fullerene derivatives (14 μM). The superoxide radical anion was generated by using the xanthine/ xanthine oxidase system. The concentration of trapping agent, BMPO, was 1200 times concentrated than the fullerene. A portion of radicals were quenched by the functionalized fullerenes, and the residues were captured by the trapping agents to give the adduct of DEPMPO-OH and BMPO-OOH, respectively.

After treatment with $Gd_3N@C_{80}$-$DiPEG_{2000}$(OH)x, EPR profiles of both DEPMPO-OH and BMPO-OOH were significantly declined compared with the control. The reductions in signal intensities were approximate 100% and 83% (**Figure 4**).

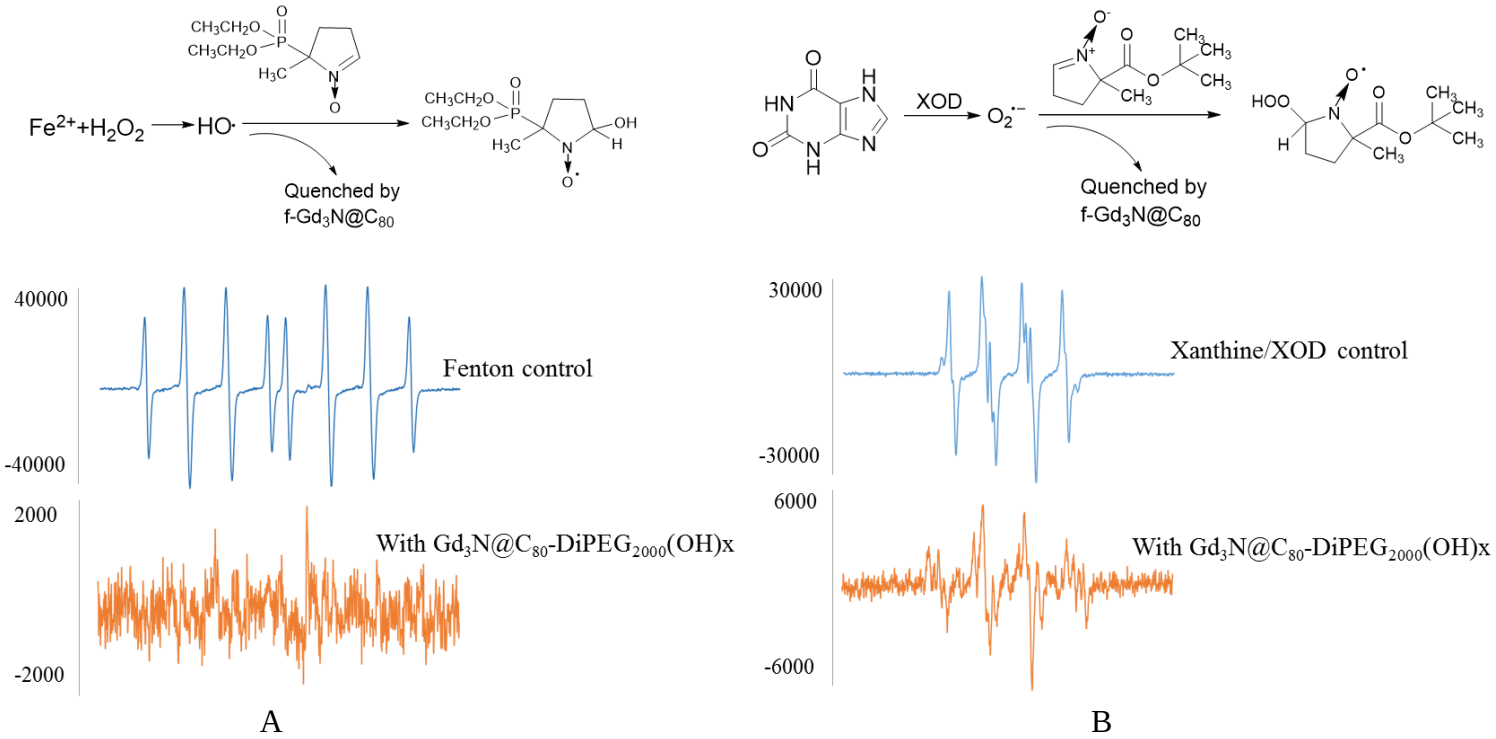

Figure 4. A) Mechanism of the production of hydroxyl radicals by Fenton reaction and the capture of them by DEPMPO. EPR spectra of the hydroxyl radicals captured by DEPMPO with and without $Gd_3N@C_{80}$-$DiPEG_{2000}$(OH)x. Ultrapure water was used as a control. B) Mechanism of the production of superoxide radicals by xanthine/ xanthine oxidase system and the capture of them by BMPO. EPR spectra of the hydroxyl radicals captured by BMPO with and without $Gd_3N@C_{80}$-$DiPEG_{2000}$(OH)x. PBS water was used as a control.

Numerous studies have demonstrated the free radical scavenging capabilities of fullerenes, to such a degree that fullerenes have been described as "free radical sponges." $Gd_3N@C_{80}$-$DiPEG_{2000}$(OH)x obtains greater scavenging ability than hollow cage fullerene or mono-metal endohedral fullerene. The excellent ROS quenching capability of $Gd_3N@C_{80}$-$DiPEG_{2000}$(OH)x is attributed to its molecular properties, such as the functional groups on the fullerene surface.[20] After chemical modification, some of the π-system of fullerene framework by replacing a cage carbon with another unit. The active hydroxyl radical can attack the electron-deficient areas on the carbon cage surface or be stabilized by forming hydrogen bonds with the proximate hydroxyl protons of functionalized $Gd_3N@C_{80}$.

Additionally, PEG has been reported to increase the residence time of nanoparticles and proteins inside cells and provide biocompatibility. PEGylated counterparts of the Superoxide Dismutase

(SOD) enzymes have shown improved performance over non-PEGylated enzymes.[21] With the PEG modification, this type of $Gd_3N@C_{80}$ can work as promising ROS scavenging particles in GI tract.

5.3.5 Biodistribution result

The percentage biodistribution of gadolinium ions of each mouse in the certain time points (15 min, 3 hours, 6hours and 7 days) are shown in **Figure 5**. The average biodistribution of gadolinium content in each organ at each time point is summarized in **Table S1**.

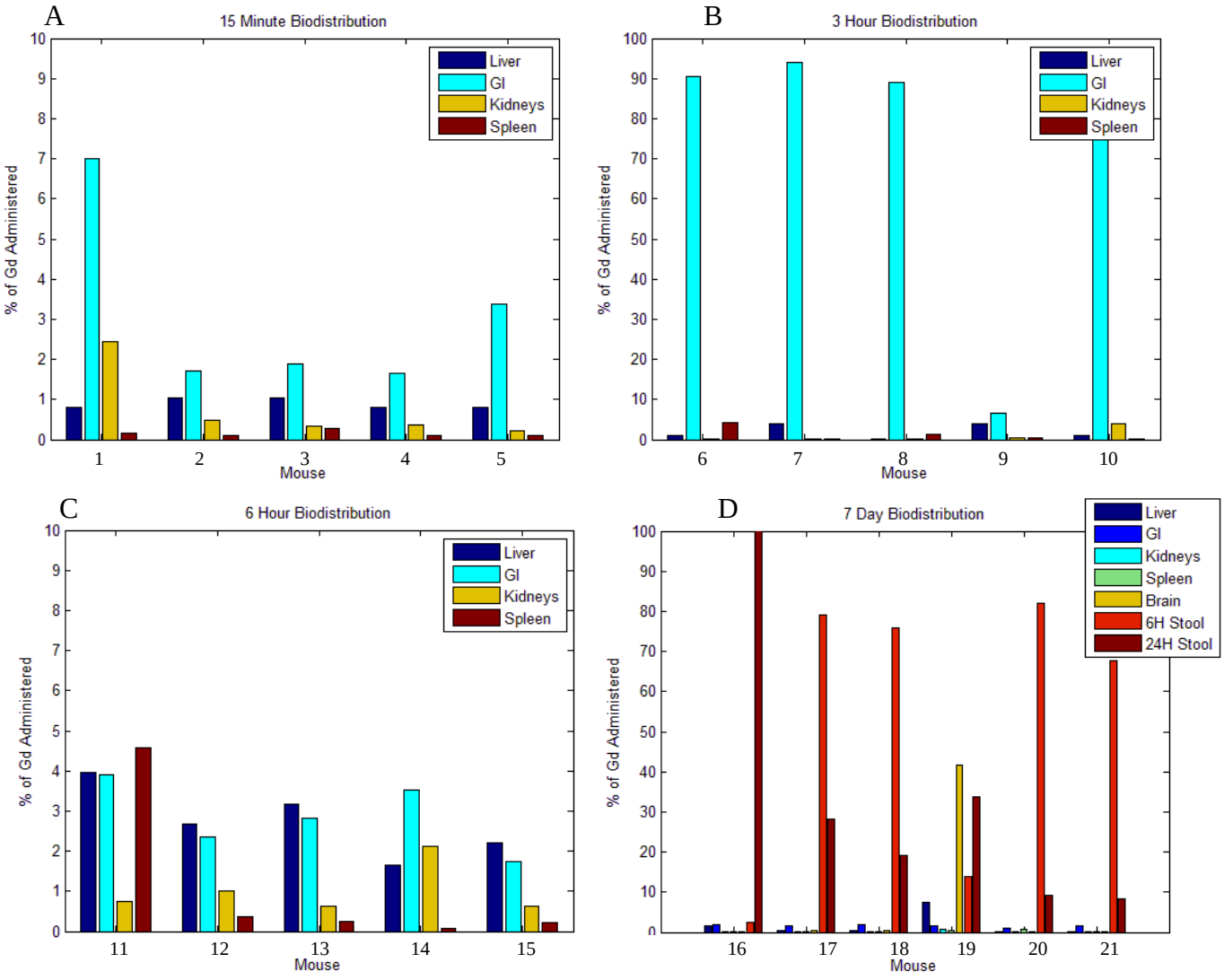

Figure 5. Biodistribution of Gd^{3+} in mice at A) 15 minutes, B) 3hours, C) 6hours, and D) 7 days.

The group A (1~5) mice had larger amount of the nanoparticles in GI tracts compared with other three organs. However, the total averaging less than 5%, the loss of samples might be caused by the mis-adminstrated either into the lungs or esophagus. The group B (6~10) mice had most of Gd-based nanoparticles within the GI tract, after three hours' administration. The 9th mouse in the 3 hours group had 6.70% of particles in GI tract, which was much lower than the other group B mice but significantly greater than the group C mice. This drastic difference from other mice of both groups makes it more likely that number 9 mouse simply had quicker peristalsis compared to the other mice and was actively excreting the nanoparticles when it was euthanized, rather than that it managed to absorb approximately 93% of the nanoparticles when the other mice in its group absorbed between 3 to 11%.

According to group C and D data, low percentage of the Gd ions measured within the organs. The result suggests large amount of the particles started to be excreted after 6 hours (except in mouse number 16), and the most of them were fecally excreted by 24 hours. In group C, the remained particles inside the mice bodies were mainly accumulated in the livers (2.74%) and GI tracts (2.87%). The kidneys and spleens also had measurable Gd^{3+}, but the levels were not as significant or as consistent between the mice as the liver Gd^{3+} levels were. This demonstrates that a small but certainly percentage of $Gd_3N@C_{80}$-DiPEG$_{2000}$(OH)x was absorbed from the GI tract and deposits in the liver. Since the long flexible PEG chains conjugated to the surface can help the nanoparticles penetrate through the mucus barrier and entanglement in the mucus network.[17,18]

Multiple studies have evaluated the effect of pegylation on the oral bioavailability of various agents, with mixed results. The study by Zabaleta et al.[22] showed that loading paclitaxel onto pegylated poly(anhydride) nanoparticles enhanced its oral bioavailability compared to loading it onto non-pegylated nanoparticles. However, as the size of the pegylation was increased from

PEG_{2000} to PEG_{10000}, the bioavailability gains significantly decreased. Li et al. found that while the oral bioavailability of all trans-retinoic acid (ATRA) was enhanced by functionalization with PEG_{1000}, the membrane permeability, and oral bioavailability was significantly decreased for longer polymer chains such as PEG_{2000} or PEG_{5000}.[23] These contrasting findings seem to suggest that pegylation can significantly increase the oral bioavailability of molecules that would otherwise be degraded in the GI lumen, but at sufficient molecular size can begin to hinder its absorption. In the case of PEGylated-$Gd_3N@C_{80}$, our data suggests that the molecule has a very low bioavailability, but a measurable quantity is absorbed nonetheless.

The major amount of the nanoparticles can be excreted out of the body after 7 days administration. It is possible that PEGylated-$Gd_3N@C_{80}$ will be excreted through the biliary system, as it may be too large molecularly to be renally cleared. Alternatively, Li et al.[23] suggest that the nanoparticles lose its pegylation on its first pass through the liver. The histopathological effect of these nanoparticles on the liver and kidneys may be worth studying. As there are still gadolinium-based particles measured in the organs at 7 days, it may be beneficial to perform a longer trial to test if PEGylated-$Gd_3N@C_{80}$ is cleared if given more time or if the deposition is more permanent.

5.4 Conclusion and Future work

In this paper, the PEGylated-$Gd_3N@C_{80}$ exhibited both outstanding MRI contrast and radical scavenging ability, which can be worked as both contrast agent and antioxidative agent in GI tract at least for 6 hours, then will be cleared from body within 7 days. It is our very first time to extract the relaxivity values under 3T scanner from images, which provides a new method to obtain the relaxivity. For the future work, the in vivo MRI and biodistribution studies need to be performed for fully understand the mechanism of this agent as working for the GI tract. The pH in the GI tract

can vary from 1 in the stomach to 9 in parts of the intestine, it is critical to evaluate the stability of the carbon cage under this bio-environment.

5.5 Supplementary Materials

Table S1: Biodistribution of Orally Administered $Gd_3N@C_{80}$-$DiPEG_{2000}(OH)x$ in Mice (μ ± SD, % of administered Gd) *Mouse number 9 and 16 were not included in the calculations due to outlier data.

n = 5	15 Minutes	3 Hours*	6 Hours	7 Days*
Liver	0.90 ± 0.13	1.55 ± 1.62	2.74 ± 0.89	0.58 ± 0.60
GI	3.12 ± 2.28	92.57 ± 3.30	2.87 ± 0.88	1.62 ± 0.34
Kidney	0.77 ± 0.94	1.06 ± 1.84	1.03 ± 0.63	0.13 ± 0.06
Spleen	0.15 ± 0.08	1.41 ± 1.91	1.10 ± 1.95	0.27 ± 0.22
Brain	-	-	-	0.23 ± 0.12
6h Stool	-	-	-	61.74 ± 33.61
24h Stool	-	-	-	34.78 ± 42.02
Total	4.94 ± 3.12	96.60 ± 4.47	7.74 ± 3.21	100.30 ± 14.31

References

(1) Dunsch, L.; Yang, S. *Small* **2007**, *3*, 1298.

(2) Kanda, T.; Fukusato, T.; Matsuda, M.; Toyoda, K.; Oba, H.; Kotoku, J.; Haruyama, T.; Kitajima, K.; Furui, S. *Radiology* **2015**, *276*, 228.

(3) Kanda, T.; Matsuda, M.; Oba, H.; Toyoda, K.; Furui, S. *Radiology* **2015**, *276*, 617.

(4) Kanda, T.; Matsuda, M.; Oba, H.; Toyoda, K.; Furui, S. *Radiology* **2015**, *277*, 924.

(5) Kanda, T.; Osawa, M.; Oba, H.; Toyoda, K.; Kotoku, J.; Haruyama, T.; Takeshita, K.; Furui, S. *Radiology* **2015**, *275*, 803.

(6) Shu, C. Y.; Corwin, F. D.; Zhang, J. F.; Chen, Z. J.; Reid, J. E.; Sun, M. H.; Xu, W.; Sim, J. H.; Wang, C. R.; Fatouros, P. P.; Esker, A. R.; Gibson, H. W.; Dorn, H. C. *Bioconjugate Chem* **2009**, *20*, 1186.

(7) Fillmore, H. L.; Shultz, M. D.; Henderson, S. C.; Cooper, P.; Broaddus, W. C.; Chen, Z. J.; Shu, C. Y.; Zhang, J. F.; Ge, J. C.; Dorn, H. C.; Corwin, F.; Hirsch, J. I.; Wilson, J.; Fatouros, P. P. *Nanomedicine-Uk* **2011**, *6*, 449.

(8) Shultz, M. D.; Wilson, J. D.; Fuller, C. E.; Zhang, J. Y.; Dorn, H. C.; Fatouros, P. P. *Radiology* **2011**, *261*, 136.

(9) Li, T. H.; Murphy, S.; Kiselev, B.; Bakshi, K. S.; Zhang, J. Y.; Eltahir, A.; Zhang, Y. F.; Chen, Y.; Zhu, J.; Davis, R. M.; Madsen, L. A.; Morris, J. R.; Karolyi, D. R.; LaConte, S. M.; Sheng, Z.; Dorn, H. C. *Journal of the American Chemical Society* **2015**, *137*, 7881.

(10) Li, T.; Dorn, H. C. *Small* **2017**, *13*.

(11) Xiao, L.; Li, T.; Ding, M.; Yang, J.; Rodriguez-Corrales, J.; LaConte, S. M.; Nacey, N.; Weiss, D. B.; Jin, L.; Dorn, H. C.; Li, X. *Bioconjug Chem* **2017**, *28*, 649.

(12) Liu, H. J.; Yang, X. L.; Zhang, Y.; Dighe, A.; Li, X. D.; Cui, Q. J. *J Orthop Res* **2012**, *30*, 1051.

(13) Akhtar, M. J.; Ahamed, M.; Alhadlaq, H. A.; Alshamsan, A. *Bba-Gen Subjects* **2017**, *1861*, 802.

(14) Li, T.; Xiao, L.; Yang, J.; Ding, M.; Zhou, Z.; LaConte, L.; Jin, L.; Dorn, H. C.; Li, X. *ACS Appl Mater Interfaces* **2017**, *9*, 17681.

(15) Yin, J. J.; Lao, F.; Fu, P. P.; Wamer, W. G.; Zhao, Y. L.; Wang, P. C.; Qiu, Y.; Sun, B. Y.; Xing, G. M.; Dong, J. Q.; Liang, X. J.; Chen, C. Y. *Biomaterials* **2009**, *30*, 611.

(16) Li, J.; Guan, M. R.; Wang, T. S.; Zhen, M. M.; Zhao, F. W.; Shu, C. Y.; Wang, C. R. *Acs Appl Mater Inter* **2016**, *8*, 25770.

(17) Ensign, L. M.; Cone, R.; Hanes, J. *Adv Drug Deliver Rev* **2012**, *64*, 557.

(18) Pridgen, E. M.; Alexis, F.; Farokhzad, O. C. *Expert Opin Drug Del* **2015**, *12*, 1459.

(19) Zhang, J.; Fatouros, P. P.; Shu, C.; Reid, J.; Owens, L. S.; Cai, T.; Gibson, H. W.; Long, G. L.; Corwin, F. D.; Chen, Z. J.; Dorn, H. C. *Bioconjug Chem* **2010**, *21*, 610.

(20) Ali, S. S.; Hardt, J. I.; Quick, K. L.; Kim-Han, J. S.; Erlanger, B. F.; Huang, T. T.; Epstein, C. J.; Dugan, L. L. *Free Radical Bio Med* **2004**, *37*, 1191.

(21) Karakoti, A. S.; Singh, S.; Kumar, A.; Malinska, M.; Kuchibhatla, S. V. N. T.; Wozniak, K.; Self, W. T.; Seal, S. *Journal of the American Chemical Society* **2009**, *131*, 14144.

(22) Zabaleta, V.; Ponchel, G.; Salman, H.; Agueros, M.; Vauthier, C.; Irache, J. M. *Eur J Pharm Biopharm* **2012**, *81*, 514.

(23) Li, Z. B.; Han, X. P.; Zhai, Y. L.; Lian, H.; Zhang, D.; Zhang, W. J.; Wang, Y. J.; He, Z. G.; Liu, Z.; Sun, J. *Colloid Surface B* **2015**, *130*, 133.

Chapter 6 MRI Relaxivity Studies of the Amphiphilic Nanoparticle $Gd_3N@C_{80}$-DiPEG$_{2000}$

Tinghui Li[†], Stephen LaConte[‖], Harry C. Dorn[†, ⁄⁄,*]

[†] Department of Chemistry, Virginia Polytechnic Institute and State University, Blacksburg, VA

[‡] Virginia Tech Carilion School of Medicine, Roanoke, VA

[‖] Virginia Tech Carilion Research Institute, Roanoke, VA

6.1 Introduction

The fullerene molecular allotrope of carbon is a hollow sphere which potentially has numerous diversified applications, such as, photovoltaic and electronic devices, surface coating material, and antioxidants.[1] Shortly after the discovery of fullerenes in the 1990s, endohedral metallofullerenes (EMF) and trimetallic nitride endohedral fullerenes (TNT-EMF) were recognized for their multi-functional capabilities in biomedical applications. Functionalized gadolinium-loaded fullerenes, $Gd@C_{82}$ and $Gd_3N@C_{80}$ have attracted much attention as a potential new nanoplatform for next-generation magnetic resonance imaging (MRI) contrast agents, given to their inherent higher ^1H relaxivity than most commercial contrast agents.[2-10] In the last decade, we have explored a series of functionalized $Gd_3N@C_{80}$ TNT-EMFs for MRI detection of various pathological conditions,

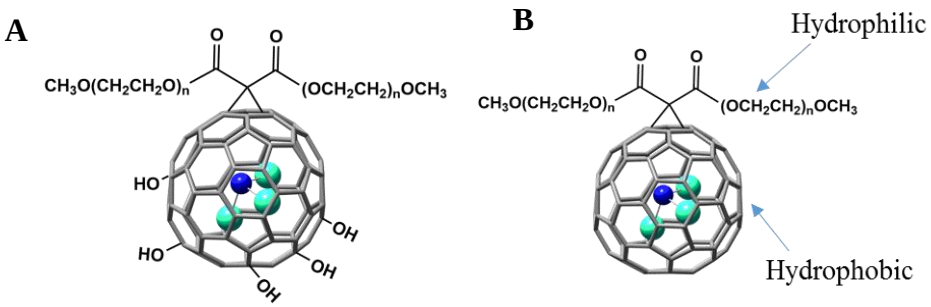

Figure 1. $Gd_3N@C_{80}$-DiPEG$_{2000}$ (OH)x and $Gd_3N@C_{80}$-DiPEG$_{2000}$.

such as chronic osteomyelitis and brain cancer.[10-12] So far, most metallofullerene contrast agents studied to date have focused on the hydroxylated fullerenes, which have good solubility in water. The hydroxylated and polyethylene glycol (PEGylated) $Gd_3N@C_{80}$ has been designed and

developed with excellent MRI contrast ability (**Figure 1A**).[13] However, its counterpart PEGylated $Gd_3N@C_{80}$ (**Figure 1B**), is an amphiphilic compound and can also be dissolved into water due to the hydrophilic high molecular weight of PEG on to the cage, but doesn't have exceptional MRI contrast ability compared with the hydroxylated metallofullerene (**Figure 1A**). The absence of hydroxyl functional groups on the carbon cage results in lower MR relaxivity. It has been known for a long time that this type of contrast agent has higher relaxivity at lower concentrations. The explanation for the concentration dependency is not fully understood. In this work, $Gd_3N@C_{80}$-$DiPEG_{2000}$ was used as the model to investigate the relationship between the relaxivity and concentration of the Gd-based metallofullerenes.

6.2 Experimental

6.2.1 Materials

$Gd_3N@C_{80}$ was purchased from LUNA Innovations (Danville, VA). 98% 1, 8-Diazabicyclo(5.4.0)undec-7-ene (DBU), 99% trimethylamine (TEA), polyethylene glycol 2000 (PEG_{2000}), 99% CBr_4, 99% 18 crown-6, 50% sodium hydroxide solution, and 50 % hydrogen peroxide were used as obtained from Sigma-Aldrich. Hydrogen peroxide (H_2O_2), ferrous sulfate heptahydrate ($FeSO_4$), xanthine, xanthine oxidase from bovine milk (XOD), diethylenetriaminepentaacetic acid (DTPA), and lipopolysaccharide (LPS) were purchased from Sigma Aldrich. Spin traps, 5-diethoxyphosphoryl-5-methyl-I-pyrroline N-oxide (DEPMPO) was purchased from Focus Biomolecules, 5-tert-Butoxycarbonyl-5-methyl-1-pyrroline-N-oxide (BMPO) was supplied by Cayman Chemical. The clear EPR quartz capillary tubes (ID 1.0 mm, OD 1.2 mm) were obtained from Wilmad-LabGlass.

6.2.2 Synthesis of Di{ω-methyl-poly(ethylene glycol)} malonate ($DiPEG_{2000}$)

To a solution with 5g PEG_{2000}, 0.7 ml triethylamine in 7 ml CH_2Cl_2, was added dropwise a solution of 0.25 ml malonyl dichloride. The solution was stirred at room temperature under N_2 protection for 4 hours. The final mixture was concentrated and the residue was dissolved in chloroform and then poured into a large amount of toluene, filtered and the filtrate was concentrated under vacuum to give a yellow viscous liquid (**Scheme 1A**).[13]

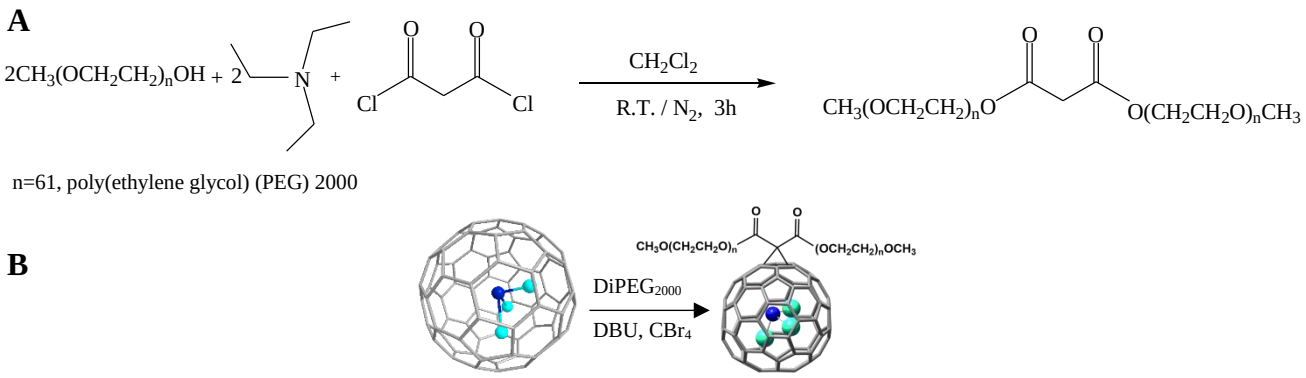

Scheme 1. A) Synthesis of Di{ω-methyl-poly(ethylene glycol)} malonate and B) Functionalization and Conjugation Process of $Gd_3N@C_{80}$-$DiPEG_{2000}$ (Gray, Carbon; Aqua, Gadolinium Ion; Blue, Nitrogen).

Synthesis of $Gd_3N@C_{80}$-$DiPEG_{2000}$

The mixture of $Gd_3N@C_{80}$, $DiPEG_{2000}$, DBU and CBr_4 (molar ratio 1:20:20:67) was dissolved in 10 mL chlorobenzene and degassed with argon for 30 min. The solution was stirred at room temperature for 12 hours. The resultant mixture was evaporated to remove solvent, redissolved in water and then separated by Sephadex G25. (**Scheme 1B**).

6.2.3 Relaxivity Measurements for $Gd_3N@C_{80}$-$DiPEG_{2000}$

Solutions with different Gd^{3+} concentrations were prepared by diluting a stock solution with deionized water. The concentration of the Gd^{3+} ions was determined by Varian 820-MS ICP Mass Spectrometer. The T_1 and T_2 relaxation times were measured at three different magnetic field strength, Bruker Minispec mq 20 (0.47 T), mq 60 (1.41 T) analyzers, and Bruker Avance III 400 MHz (9.4 T) wide bore spectrometer equipped with an MIC 400 W1/S2 probe and 5mm ^1H coil.

The inversion-recovery method was used to measure the spin-lattice relaxation time T_1, and the Carr-Pucell-Meiboom-Gill method was used for the spin-spin relaxation time T_2 measurement. Errors in T_1 and T_2 values were less than ±2%.

6.2.4 Dynamic light scattering (DLS) and Zeta potential measurement

The hydrodynamic size distribution and surface charge of $Gd_3N@C_{80}$-$DiPEG_{2000}$ in water was measured by DLS at the concentrations 2, 5, 10, 20, 50, 100 μM.

6.2.5 *In vitro* MRI study of the functionalized $Gd_3N@C_{80}$

The *in vitro inversion-recovery* MR images were obtained under the same 3T clinical scanner for the visual confirmation of the efficiency of the functionalized fullerene working as a contrast agent. Various concentrations of the Gd based fullerenes, and the commercial contrast agent Omniscan® were used and compared.

6.2.6 Hydroxyl radical (HO) scavenging activity

The trapping of hydroxyl radicals by each metallofullerene derivative was determined by the EPR spin-trapping technique. The EPR assay was based on the competition between the trapping agent, DEPMPO, and the fullerene derivative nanoparticles for HO. Hydroxyl radicals were generated by the classical Fenton reaction with the reaction mixture containing freshly prepared 500 μM DEPMPO, 20 μM $FeSO_4$ and 200 μM H_2O_2 with or without 14 μM of a $Gd_3N@C_{80}$-$DiPEG_{2000}$. The clear quartz capillary tubes (ID 1.0mm, OD 1.2mm) were used as the sample container. The EPR data were collected at ambient temperature, 2 min after initiating the formation of HO by addition of $FeSO_4$. The following instrument settings were used for collecting EPR spectra: microwave power of 10 mW, field modulation frequency of 100 kHz, and modulation amplitude of 1 G.

6.2.7 Superoxide radical anion ($O_2^{\bullet-}$) scavenging activity

BMPO was used to trap and detect $O_2^{\bullet-}$ by EPR spectroscopy. Superoxide radical anion was generated using the xanthine/ xanthine oxidase system. The scavenger radical reaction was initiated by addition of xanthine oxidase solution (XOD). The reaction contained 100 µM xanthine (1M NaOH in PBS), 20 mM BMPO, 50 µM DTPA, 0.1 U/ml XOD, in the presence or absence of 11 µM of a $Gd_3N@C_{80}$-$DiPEG_{2000}$. The EPR spectra were recorded at 1.5 min after initiating the generation of $O_2^{\bullet-}$ by addition of XOD. The instrument settings were used as the same as hydroxyl radicals.

6.3 Results and Discussion

6.3.1 DLS and Zeta potential measurements of $Gd_3N@C_{80}$-$DiPEG_{2000}$

The hydrodynamic size distributions of $Gd_3N@C_{80}$-$DiPEG_{2000}$ were measured with six different concentrations. As shown (**Figure 2**) the hydrodynamic size of the compound is concentration dependent. At low concentration 2µM, the nanoparticles are dispersed in water as small aggregates "monomers"with hydrodynamic size of ~10 nm. The nanoparticles initiate aggregation as the concentration increases, and reach the largest aggregation size of about 100 nm at the highest concentration. The surface charge results parallel the DLS measurements and progress from -57 to -15 at high concentrations.

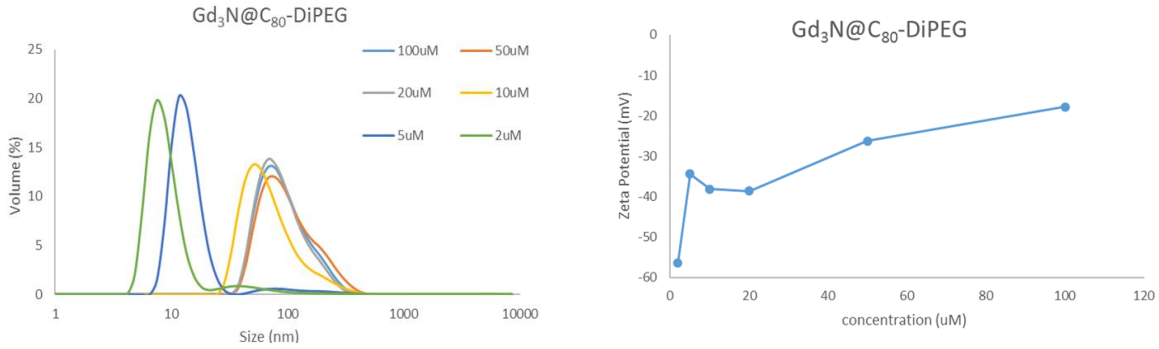

Figure 2. Hydrodynamic size distribution and surface charge of Gd_3N @C_{80}-DiPEG$_{2000}$ with different concentrations.

6.3.2 Relaxivity Measurements of the functionalized $Gd_3N@C_{80}$

The r_1 and r_2 relaxivity results of $Gd_3N@C_{80}$-DiPEG$_{2000}$ are summarized in **Table 1**. The nuclear magnetic resonance relaxivity were calculated by the general equation (Eq 1.)

$$\frac{1}{T_{i\,obs}} = \frac{1}{T_{i\,H_2O}} + \frac{1}{T_{i\,para}} = \frac{1}{T_{i\,H_2O}} + r_i[M] \quad \text{Eq. 1}$$

The relaxation rate is determined by both diamagnetic (pure water) and paramagnetic (contrast agent) components. The ratio of paramagnetic relaxation rate to the concentration (M) is the relaxivity (r_i) of the paramagnetic compound, which can be experimentally obtained by the slope of $1/T_i$ versus concentrations of the paramagnetic contrast agents. These results can be compared with the relaxivity of the commercial contrast agents, Omniscan®.

Table 1. Relaxivities of functionalized Gadolinium Metallofullerenes (Units of mM^{-1} s^{-1} per mM in pure water at 25 °C)

Table A Contrast agents	0.47 T			1.41 T			9.4 T		
	r_1	r_2	r_2/r_1	r_1	r_2	r_2/r_1	r_1	r_2	r_2/r_1
f-$Gd_3N@C_{80}$(OH)x (2-100 µM)	100.6	115.7	1.2	128.8	167.7	1.3	42.3	186.5	4.4
f-$Gd_3N@C_{80}$ (80-240 µM)	2.8	4.0	1.4	3.8	9.4	2.5	6.3	19.7	3.1
Omniscan®	~4	~4	~1	~4	~4	~1	~4	~4	~1

Table B f-$Gd_3N@C_{80}$	9.4 T	
	r_1	r_2
20-300 µM	5.17	62.15
80-240 µM	6.3	19.7
30-90 µM	7.4	32.7
2-10 µM	26.08	61.94

The comparison of relaxivities between $Gd_3N@C_{80}$-$DiPEG_{2000}$(OH)x and $Gd_3N@C_{80}$-$DiPEG_{2000}$ confirms that the hydroxyl groups attached to the cage is the key factor (**Table 1A**) for enhanced relaxivity. One hypothesis is that the hydroxyl functional groups facilitate hydrogen bonding and exchange interactions with water molecules more efficiently at low metallofullerene concentrations and smaller aggregation sizes, (**Table 1B**). Whereas, it is reasonable that the water soluble amphiphilic metallofullerenes form micelles at higher concentrations, thereby excluding more water (and exchange) and lowering relaxivity.

6.3.3 *In vitro* MR contrast ability of the functionalized $Gd_3N@C_{80}$

In **Figure 3**, the *inversion-recovery* images obtained using a clinical 3T MR scanner with 1 mm capillary tubes containing various concentrations of f-$Gd_3N@C_{80}$, f-$Ho_3N@C_{80}$ and commercial

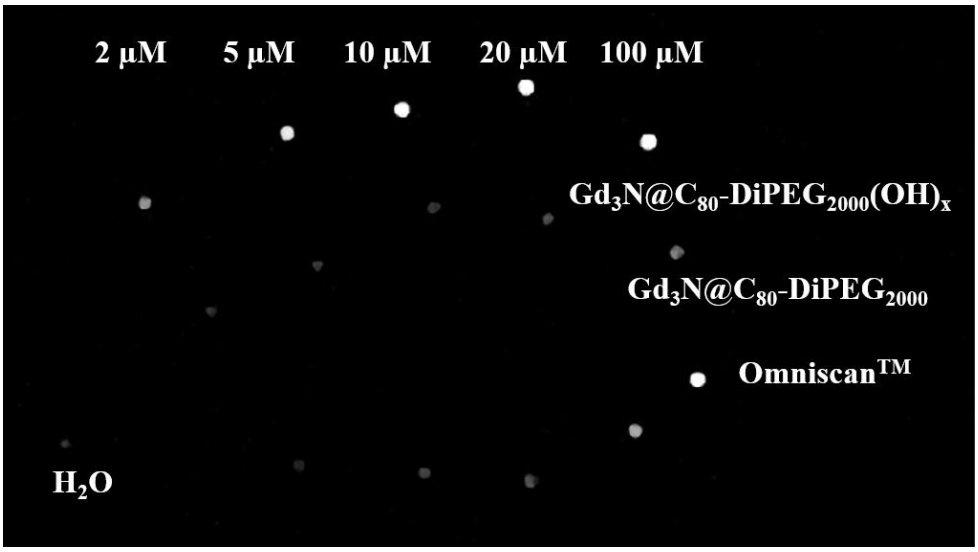

Figure 3. *Inversion-recovery* MR images (T_1=1500 ms, T_R=4000 ms, T_E=32 ms) with f-$Gd_3N@C_{80}$, f-$Ho_3N@C_{80}$, and Omniscan® as contrast agent.

contrast agent, Omniscan®. With the highest concentration, the $Gd_3N@C_{80}$-$DiPEG_{2000}$(OH)x, $Ho_3N@C_{80}$-$DiPEG_{2000}$(OH)x and Omniscan® shared the similar brightness. This suggests three contrast agents reached their plateau. At lower concentrations, the $Gd_3N@C_{80}$-$DiPEG_{2000}$(OH)x are brighter than other agents, and there is no difference between $Gd_3N@C_{80}$-$DiPEG_{2000}$ with other agents, which corresponds to the previous relaxivity results.

6.3.4 Scavenging of Reactive oxygen species

In this work, hydroxyl radical (•OH) and superoxide radical anion ($O_2^{\bullet-}$), the most common reactive oxygen species (ROS) in the body, were chosen as the models to evaluate the capability of $Gd_3N@C_{80}$-$DiPEG_{2000}$(OH)x and $Gd_3N@C_{80}$-$DiPEG_{2000}$ to eliminate ROS by using EPR methods. Due to the relatively low sensitivity of EPR detection and the biological free radicals are short-lived, the exogenous spin traps were used. The EPR assay was based on the competition between the trapping agents, and pegylated-hydroxylated fullerenes for radicals.

Hydroxyl radicals were generated by the classical Fenton reaction, which involves the reaction of $FeSO_4$ and H_2O_2. The superoxide radical anion was generated by using the xanthine/ xanthine oxidase system. A portion of radicals were quenched by the functionalized fullerenes, and the residues were captured by the trapping agents to give the adduct of DEPMPO-OH and BMPO-OOH, respectively.

After treatment with $Gd_3N@C_{80}$ derivatives, EPR profiles of both DEPMPO-OH and BMPO-OOH were significantly declined compared with the control. The reductions in signal intensities were summarized in **Figure 4C**. Both derivatives can quench nearly 100% hydroxyl radical, and hydroxylated $Gd_3N@C_{80}$ acquires better scavenging ability than non-hydroxylated fullerene. The excellent ROS quenching capability of $Gd_3N@C_{80}$ derivatives is attributed to its molecular properties, such as the functional groups on the fullerene surface. After chemical modification,

some of the π-system of fullerene framework by replacing a cage carbon with another unit. The active hydroxyl radical can attack the electron-deficient areas on the carbon cage surface or be stabilized by forming hydrogen bonds with the proximate hydroxyl protons of functionalized $Gd_3N@C_{80}$.[14,15]

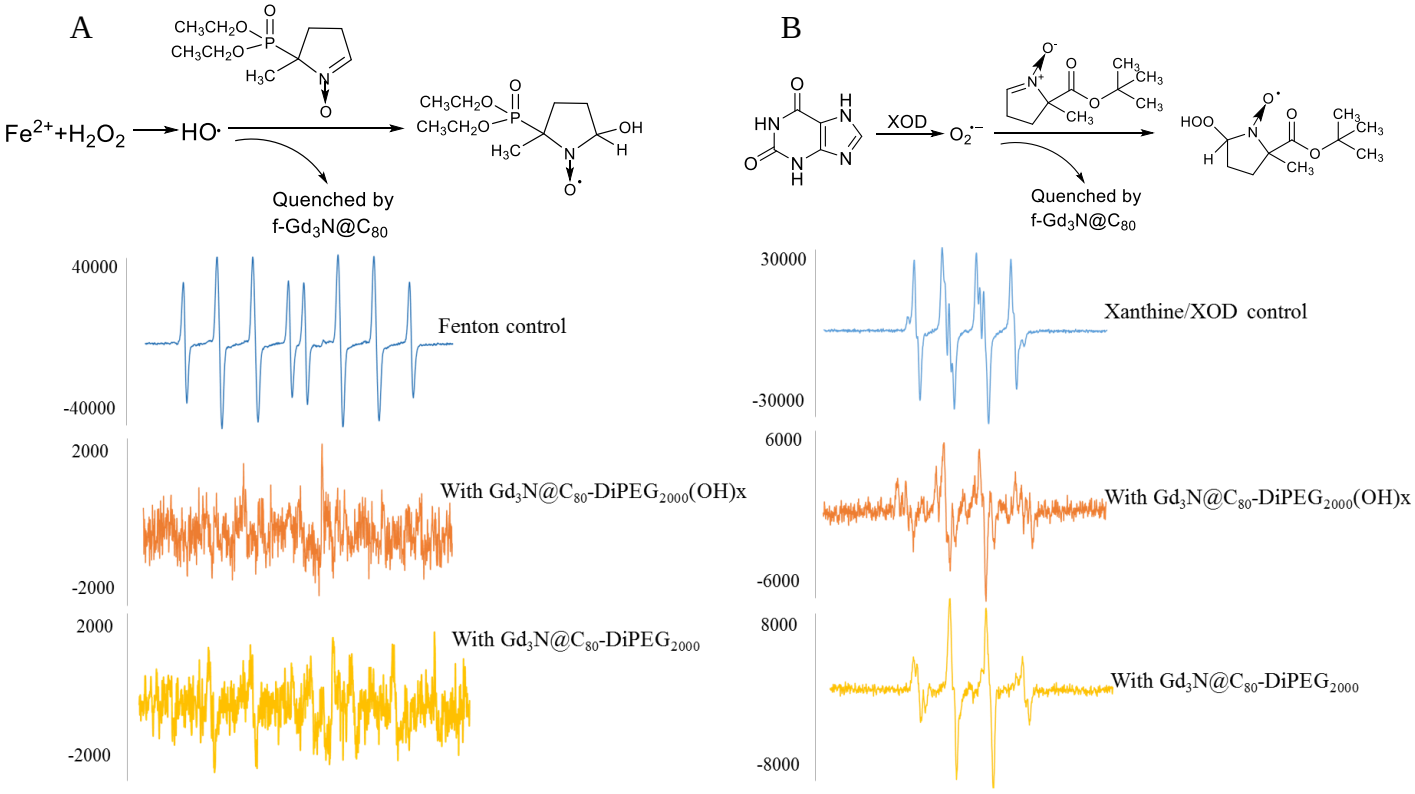

C

Percentage of signal reduction (%)	OH•	$O_2^{\bullet-}$
$Gd_3N@C_{80}$-DiPEG$_{2000}$(OH)x	~100	82.8
$Gd_3N@C_{80}$-DiPEG$_{2000}$	~100	67.6

Figure 4. Radical scavenging properties of three trimetallic nitride endohedral fullerenes. A) Mechanism of the hydroxyl radical production by Fenton reaction and capture by DEPMPO. EPR spectra of the hydroxyl radicals captured by DEPMPO with and without $Gd_3N@C_{80}$ derivatives. Ultrapure water was used as a control. B) Mechanism of superoxide radical production by xanthine/ xanthine oxidase (XOD) system and capture by BMPO. EPR spectra of superoxide radicals captured by BMPO with and without $Gd_3N@C_{80}$ derivatives. PBS was used as a control. C) Table summary of scavenging capabilities of hydroxyl radical and superoxide radical anion by two $Gd_3N@C_{80}$ derivatives.

6.4 Conclusion and Future work

In summary, a novel amphiphilic compound $Gd_3N@C_{80}$-$DiPEG_{2000}$ was developed and preliminary characterized. To the best of our knowledge, it is the first time to study the chemical and psychical properties of Gd-based amphiphilic fullerene. It might also explain why this type of contrast agent has higher relaxivity at lower concentrations. In future, the NMR experiments of diffusion coefficients of Gd3N@C80-DiPEG2000 need to be performed to further understand this particle.

References

(1) Morry, J.; Ngamcherdtrakul, W.; Yantasee, W. *Redox Biology* **2017**, *11*, 240.

(2) Mikawa, M.; Kato, H.; Okumura, M.; Narazaki, M.; Kanazawa, Y.; Miwa, N.; Shinohara, H. *Bioconjugate Chem* **2001**, *12*, 510.

(3) Fatouros, P. P.; Corwin, F. D.; Chen, Z. J.; Broaddus, W. C.; Tatum, J. L.; Kettenmann, B.; Ge, Z.; Gibson, H. W.; Russ, J. L.; Leonard, A. P.; Duchamp, J. C.; Dorn, H. C. *Radiology* **2006**, *240*, 756.

(4) Shu, C. Y.; Corwin, F. D.; Zhang, J. F.; Chen, Z. J.; Reid, J. E.; Sun, M. H.; Xu, W.; Sim, J. H.; Wang, C. R.; Fatouros, P. P.; Esker, A. R.; Gibson, H. W.; Dorn, H. C. *Bioconjugate Chem* **2009**, *20*, 1186.

(5) Yin, J. J.; Lao, F.; Fu, P. P.; Wamer, W. G.; Zhao, Y.; Wang, P. C.; Qiu, Y.; Sun, B.; Xing, G.; Dong, J.; Liang, X. J.; Chen, C. *Biomaterials* **2009**, *30*, 611.

(6) Zhang, J. F.; Fatouros, P. P.; Shu, C. Y.; Reid, J.; Owens, L. S.; Cai, T.; Gibson, H. W.; Long, G. L.; Corwin, F. D.; Chen, Z. J.; Dorn, H. C. *Bioconjugate Chem* **2010**, *21*, 610.

(7) Adiseshaiah, P.; Dellinger, A.; MacFarland, D.; Stern, S.; Dobrovolskaia, M.; Ileva, L.; Patri, A. K.; Bernardo, M.; Brooks, D. B.; Zhou, Z. G.; McNeil, S.; Kepley, C. *Invest Radiol* **2013**, *48*, 745.

(8) Zhang, J. Y.; Ye, Y. Q.; Chen, Y.; Pregot, C.; Li, T. H.; Balasubramaniam, S.; Hobart, D. B.; Zhang, Y. F.; Wi, S.; Davis, R. M.; Madsen, L. A.; Morris, J. R.; LaConte, S. M.; Yee, G. T.; Dorn, H. C. *J Am Chem Soc* **2014**, *136*, 2630.

(9) Li, J.; Guan, M.; Wang, T.; Zhen, M.; Zhao, F.; Shu, C.; Wang, C. *ACS Appl Mater Interfaces* **2016**, *8*, 25770.

(10) Li, T. H.; Murphy, S.; Kiselev, B.; Bakshi, K. S.; Zhang, J. Y.; Eltahir, A.; Zhang, Y. F.; Chen, Y.; Zhu, J.; Davis, R. M.; Madsen, L. A.; Morris, J. R.; Karolyi, D. R.; LaConte, S. M.; Sheng, Z.; Dorn, H. C. *Journal of the American Chemical Society* **2015**, *137*, 7881.

(11) Xiao, L.; Li, T.; Ding, M.; Yang, J.; Rodriguez-Corrales, J.; LaConte, S. M.; Nacey, N.; Weiss, D. B.; Jin, L.; Dorn, H. C.; Li, X. *Bioconjug Chem* **2017**, *28*, 649.

(12) Shultz, M. D.; Wilson, J. D.; Fuller, C. E.; Zhang, J. Y.; Dorn, H. C.; Fatouros, P. P. *Radiology* **2011**, *261*, 136.

(13) Zhang, J.; Fatouros, P. P.; Shu, C.; Reid, J.; Owens, L. S.; Cai, T.; Gibson, H. W.; Long, G. L.; Corwin, F. D.; Chen, Z. J.; Dorn, H. C. *Bioconjug Chem* **2010**, *21*, 610.

(14) Xu, J.; Chen, L.; Li, L. *J Cell Physiol* **2017**.

(15) Li, T.; Xiao, L.; Yang, J.; Ding, M.; Zhou, Z.; LaConte, L.; Jin, L.; Dorn, H. C.; Li, X. *ACS Appl Mater Interfaces* **2017**, *9*, 17681.

Chapter 7 Overall Conclusions

Fullerenes have been recognized for their multifunctional capabilities in biomedical applications. This dissertation has focused on functionalized gadolinium-loaded fullerenes which have attracted attention as a new nanoplatform for next-generation magnetic resonance imaging (MRI) contrast agents. A gadolinium ion is paramagnetic and has seven unpaired electrons. The long electron relaxation time makes Gd^{3+} ions influence the relaxation times of water protons.[1] The ionic radius of gadolinium is very similar to that of calcium, which causes Gd^{3+} ions to compete with Ca^{2+} ions in biological systems that require Ca^{2+} ions for proper function. The trivalent Gd^{3+} ions bind with much higher affinity than the Ca^{2+} ions.[2] Due to the toxicity of free gadolinium ions, they cannot be administered directly to the body. The fullerene cage is an extraordinarily stable species which makes it extremely unlikely to break and release the toxic Gd^{3+} ions into the bioenvironment. In this dissertation, we report the development of a series of functionalized TNT-EMFs for MRI detection of various pathological conditions, such as brain cancer and chronic osteomyelitis, and working as agent for gastrointestinal (GI) tract.[3]

A new amino-surface functionalized $Gd_3N@C_{80}$ platform is reported in Chapter 2. This platform is compared with a previously described hydrophilic, carboxyl-surface functionalized $Gd_3N@C_{80}$. We have found that this hydrophilic nanoparticle, when conjugated with an interleukin-13 peptide, exhibited increased targeting of U-251 GBM cell lines. Our results support the notion that the positively charged nanoparticle has enhanced charge attraction for GBM cellular endocytosis on the metallofullerene cage surface when directly compared with a carboxyl-surface functionalized nanoparticle. Confocal microscopy results show the agent can effectively target orthotopic GBM brain xenografts in mice. In a similar fashion to the confocal microscopy results, we also

demonstrate clinical MRI detection at low concentrations of this nanoparticle in U-251 GBM cells orthotopically implanted in mice.[4]

In Chapter 3, we develop a novel non-invasive imaging approach to detect and differentiate chronic post-traumatic osteomyelitis (CPO) from post-traumatic aseptic inflammation using the IL-13Rα2 targeted metallofullerene MRI probe in a mouse tibia model. To the best of our knowledge, we are the first to identify IL-13Rα2 receptor as a unique biomarker for diagnostic imaging of CPO, given to this type of receptor dramatically increased and distinct expression during bacterial infection. Such a translational imaging approach would aid clinical differentiation of CPO from aseptic post-traumatic or surgical inflammation, hence providing critical and timely information for developing a therapeutic strategy.[5]

The discovery that functionalized $Gd_3N@C_{80}$ possess robust radical scavenging properties in solution and suppressed LPS-induced ROS in macrophage cell model is presented in Chapter 4. Carboxyl-$Gd_3N@C_{80}$ significantly attenuate LPS-induced iNOS and TNF-α mRNA expression. We provide evidence that TNT-EMFs, especially carboxyl-$Gd_3N@C_{80,}$ hold great promise in becoming a novel class of theranostic agent against the oxidative stress and inflammation, in combination with their inherited MRI applications.[6]

The molecular weight of 5-10kDa macromolecules is considered high enough to prevent any appreciable absorption through skin or mucosal tissue. Such systems can offer considerable advantages for localized treatments of the GI tract. Therefore, poly(ethylene glycol) is used to functionalize the fullerene as the contrast agent for GI tract. The PEGylated-$Gd_3N@C_{80}$ exhibits both outstanding MRI contrast and radical scavenging ability. PEGylated-$Gd_3N@C_{80}$ works as both contrast agent and antioxidative agent in GI tract at least for 6 hours, then is cleared from body within 7 days. For future work, *in vivo* MRI and biodistribution studies need to be performed

to fully understand the mechanism of this agent in the GI tract. The pH in the GI tract can vary from 1 in the stomach to 9 in parts of the intestine. Evaluation of the stability of the carbon cage under this bio-environment will be critical.

Although additional bio-distribution and cytotoxicity studies are needed, the feasibility of these nanoparticles as potential new agents for diagnostic MRI applications can be clearly envisioned.

A novel amphiphilic $Gd_3N@C_{80}$ derivative is discussed in Chapter 6. It has been observed for a long time that the functionalization $Gd_3N@C_{80}$ contrast agents have higher relaxivity at lower concentrations. The explanation for the concentration dependence is not fully understood. In this work, the amphiphilic $Gd_3N@C_{80}$ derivative is used as the model to investigate the relationship between the relaxivity and concentration of the metallofullerenes.

In spite of the optimistic view of metallofullerenes for-next generation biomedical applications, some formidable obstacles must still be overcome. For example, the synthetic production yields of metallofullerenes are very low and typically less than 1% in the usual electric-arc batch reactor. As previously indicated, the major clinical problem with current linear and macrocyclic Gd-containing MRI contrast agents is the low relaxivity and established loss of Gd^{3+} ions to surrounding tissue. The EMF MRI contrast agents exhibit 2-3 orders of magnitude better relaxivity than current clinical agents. This helps alleviate, but does not eliminate, potential concerns related to the adverse effects of Gd-based toxicity. More importantly, although the pristine metallofullerene cage is very robust, functionalized metallofullerenes with sp^3 hybridized carbons on the cage surface are less stable. Detailed *in vitro* and *in vivo* studies are needed to demonstrate that the encapsulated Gd^{3+} or trimetallic nitride cluster $(Gd_3N)^{6+}$ ions of Gd-EMFs stay completely encapsulated and isolated from the bio-environment. Moreover, due to the presence of a different number of functional groups on the carbon cage for the metallofullerene MRI agents, a challenge

is to develop “single molecule” contrast agents. This challenge is compounded by the clinical desire for total body clearance of Gd-based MRI contrast agents. Finally, specific targeting, multi-modality, and therapeutic agents are also important goals for future development of the metallofullerene platforms for clinical applications. In spite of these challenges, the metallofullerene will likely evolve as an important molecular platform for future clinical applications.

References

(1) Bloembergen, N.; Morgan, L. O. *J Chem Phys* **1961**, *34*, 842.

(2) Sherry, A. D.; Caravan, P.; Lenkinski, R. E. *J Magn Reson Imaging* **2009**, *30*, 1240.

(3) Li, T.; Dorn, H. C. *Small* **2017**, *13*.

(4) Li, T.; Murphy, S.; Kiselev, B.; Bakshi, K. S.; Zhang, J.; Eltahir, A.; Zhang, Y.; Chen, Y.; Zhu, J.; Davis, R. M.; Madsen, L. A.; Morris, J. R.; Karolyi, D. R.; LaConte, S. M.; Sheng, Z.; Dorn, H. C. *J Am Chem Soc* **2015**, *137*, 7881.

(5) Xiao, L.; Li, T.; Ding, M.; Yang, J.; Rodriguez-Corrales, J.; LaConte, S. M.; Nacey, N.; Weiss, D. B.; Jin, L.; Dorn, H. C.; Li, X. *Bioconjug Chem* **2017**, *28*, 649.

(6) Li, T.; Xiao, L.; Yang, J.; Ding, M.; Zhou, Z.; LaConte, L.; Jin, L.; Dorn, H. C.; Li, X. *ACS Appl Mater Interfaces* **2017**, *9*, 17681.

Appendix A

New Synthetic Click Reactions of Endohedral Metallofullerenes for Biomedical Applications

Libin Bai[†,‡], Tinghui Li[†], Daniel W Bearden [^], Xinwu Ba[†,‡], Haijun Wang[†,‡] and Harry C. Dorn[†,ǁ*]

[†] Department of Chemistry, Virginia Polytechnic Institute and State University, Blacksburg, VA

[‡] College of Chemistry and Environmental Science, Hebei University, Baoding, China

[^]National Institute of Standards and Technology, Chemical Science Division, Hollings Marine Laboratory, Charleston, South Carolina

[ǁ] Virginia Tech Carilion Research Institute, Roanoke, VA

Abstract

In this paper, we synthesized a new type of $Sc_3N@C_{80}$ derivative bearing alkynyl group by using Prato reaction. The post-functionalized reaction was successfully conducted by employing the click reaction with the benzyl azide as a model compound. The structure of $Sc_3N@C_{80}$-alkynyl ($Sc_3N@C_{80}$-Alk) and $Sc_3N@C_{80}$- Alk-benzyl azide ($Sc_3N@C_{80}$-Alk-BA) were determined by NMR spectrum, MS, UV-vis and HPLC. The high yield of the $Sc_3N@C_{80}$-Alk-BA can provide access to various derivatives which have great potential for application in medical and materials science.

Since the initial discovery of Endohedral metallofullerenes (EMFs) in 1991[1], EMFs have attracted increasing attention as promising spherical molecules for material and biomedical applications because of the unique properties of EMFs[2,3]. Recently, Trimetallic nitride endohedral fullerenes (TNT-EMFs), possessing a metal-nitride cluster (M_3N) encapsulated within the fullerene cage, has been demonstrated to alter the electronic and magnetic properties due to the charge transfer from the metal to the carbon shell[4,5]. Allowing for the unique feature of TNT-EMFs, they are functionalized and expected to show promising performance in the diverse application areas of

electronics, optical and biological[6-9]. Using Bingel reaction, Guldi et al synthesized $Lu_3N@C_{80}$-perylenebisimide conjugate which show unique oxidative role because of the construction of novel optoelectronic device[10]. For functionalized EMFs, expect for the Bingel reaction, there are other various types of chemical transformation such as Diels-Alder reactions, [2+2] cycloadditions, [2+1] cycloadditions, Prato reactions, Azide addition, and free-radical reactions[6-9,11]. Usually, most of these functionalization reactions were conducted with one-step strategy to improve the yield of MNFs derivatives. The second strategy is step by step method. According to this strategy, Shiladitya synthesized fullerenol-doxorubicin conjugate which suppressed the proliferation of cancer cell-lines in vitro through a G2-M cell cycle block, resulting in apoptosis[12]. Fréchet prepared fullerene-bound dendrimers which dramatically improved the solubility of the fullerenes[13]. Eiichi also obtained fullerene-glycoconjugates by employing the step by step method[14]. Indeed, the yield for the functionalization of fullerenes will dramatically decrease with more steps being utilized. However, subsequent functionalization will introduce more diverse performance to EMFs and more flexible synthetic strategy.

Click chemistry has been extensively used in functionalization due to the high efficiency and technical simplicity of the reaction. Furthermore, this procedure can be conducted in aqueous or organic media and no unwanted side reactions in a wide temperature range[15,16]. The Cu(I)-catalyzed azide-alkyne Huisgen cycloaddition is an important kinds of click chemistry[17-19]. Nakamura used the click reaction to prepare a new type of fullerene-oligosaccharides with 98% high yielding[14]. Jiang synthesized a new type of fullerene-based donor-acceptor systems by using click reaction with high yield[20]. Cheng applied click chemistry to the synthesis of fullerene-polymer hybrids[21]. Undoubtedly, the click reaction is a good choice for the post-functionalization of EMFs derivative.

Here in, we first synthesized a new type of $Sc_3N@C_{80}$ derivatives bearing alkynyl group by using Prato reaction. For the further modification of the EMFs, click reaction was utilized with benzyl azide as a model molecular. The structure of $Sc_3N@C_{80}$-alkynyl ($Sc_3N@C_{80}$-Alk) and $Sc_3N@C_{80}$-Alk-benzyl azide ($Sc_3N@C_{80}$-Alk-BA) were characterized by NMR spectrum, MS, UV-vis, and HPLC.

Scheme 1-1 shows the synthetic procedures of $Sc_3N@C_{80}$-ALK. Accounting for the high yield and operational simplicity of Prato reaction which was used for chemical functionalization of C_{60}, the

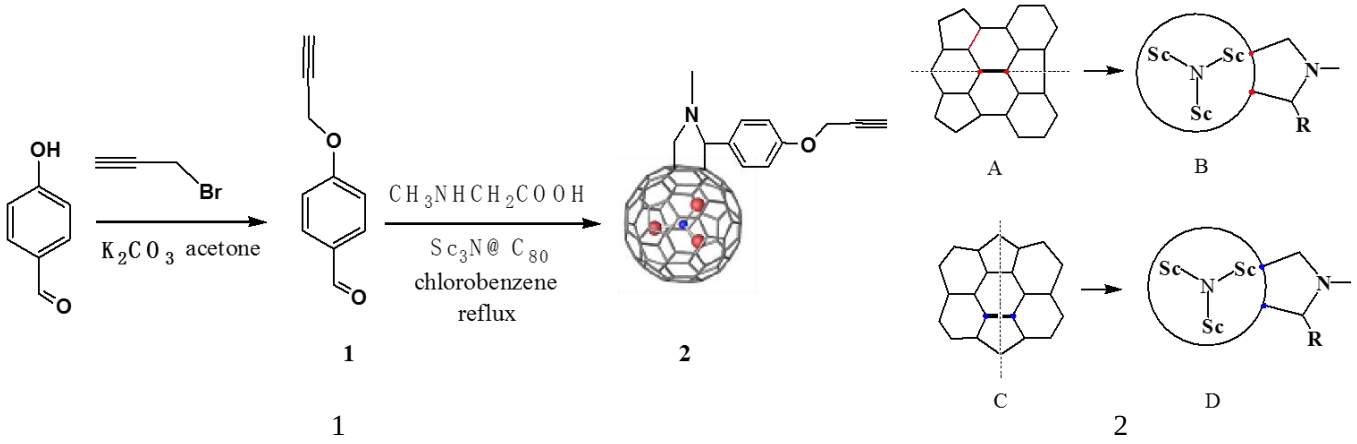

Scheme 1. A) Synthetic steps of $Sc_3N@C_{80}$-ALK. B) Prato reaction at the 6,6-ring junction (A→B) and at the 5,6 ring junction (C→D).

Prato reaction was chosen to prepare the $Sc_3N@C_{80}$-ALK derivative. The synthesis of $Sc_3N@C_{80}$-ALK (**2**) was carried out by heating chlorobenzene solution containing $Sc_3N@C_{80}$ (1 equiv), sarcosine (10 equiv) and compound **1** (20 equiv) at reflux temperature for 10 h. The progress of the reaction was monitored by high pressure liquid chromatography (HPLC) as shown in **Figure 1A**. After 40 minutes, two new peaks appeared at 21 min (1a) and 24 min (1b), respectively, which are assigned as the monoadducts of I_h $Sc_3N@C_{80}$. Base on the our previous works[22], the sarcosine and compound **1** can only react with a localized double bond at one of the two types of ring juncture available on the I_h symmetric C_{80} cage. The 6, 6-ring juncture abutted by one five- and one six-membered ring (**Scheme 1-2A**) and the 5, 6-ring juncture is abutted by tow six membered rings

(**Scheme 1-2C**). Usually, the isomer of [5, 6] monoadduct was eluted earlier than the isomer of [6, 6] monoadduct which was also proved by Yoko Yamakoshi using the $M_3N@C_{80}$ (M=Sc, Lu, Y, Gd) to conduct the Prato reaction[23]. H1a and H1b were eluted earlier than $Sc_3N@C_{80}$ because of significant differences in the polarizability and solubility caused by the 4-propargylbenzaldehyde groups. The yield of H1a and H1b were increased from 7%, 0.47% to 2 3% and 2.08%, respectively, after 10 h.

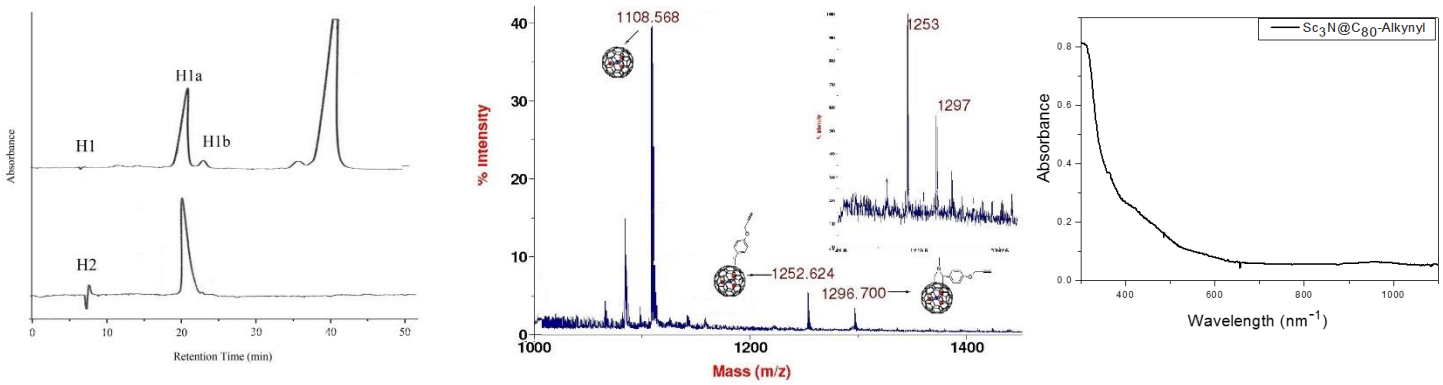

A B C

Figure 1. A) Generation of Prato monoadducts H1a and H1b of $Sc_3N@C_{80}$ monitored by HPLC (Buckyprep, 4.6 mm i.d × 250 mm, toluene, 2 mL/min, 390 nm). B) MALDI-TOF spectra (9-nitroanthracene as matrix and negative ionization) of pure monoadducts H1a. C) UV-vis spectra of $Sc_3N@C_{80}$-Alkynyl (solvent: toluene).

Monoadducts H1a was isolated in 30% yield with further purification. The HPLC traces of monoadducts H1a on PBB columns consist of single symmetric peaks centered at retention time of 21.2 min, revealing pure isomer. The matrix assisted laser desorption ionization time-of-flight (MALDI-TOF) mass spectrum was shown in **Figure 1B**. The mass spectra exhibit a molecular ion peak from 2a+ at m/z 1296. The peak at m/z 1109 is attributed to $Sc_3N@C_{80}$ formed by loss of the exohedral functional groups as usually observed under laser desorption conditions. The peak at m/z 1252 is attributed to $Sc_3N@C_{80}$-ALK derivative which loss the groups of CH_2NCH_3. UV-vis absorption spectra of monoadduct H1a is shown in **Figure 1C**. The spectra of monoadduct H1a is similar to the $Sc_3N@C_{80}$, indicating that the $Sc_3N@C_{80}$ derivatives retain the main aromatic cage features of the parent metallofullerenes.

To demonstrate the structure of compound **2**, the 800MHz ^{1}H NMR, ^{13}C NMR, HSQC, and HMBC were applied (**Figure 2**). Functionalized metallofullerene was dissolved into CS_2 with 10% methylene Chloride-d_2. According to the NMR spectrum, the end of alkyne (a) is (2.6, 76 ppm), the chemical shift of b is 79 ppm, and the methylene group nearby the ether oxygen (c) is assigned by (4.8, 56 ppm). The proton chemical shift of methyl group (d) connected with nitrogen was coincidently overlapped with alkyne group (a), based on HMBC and HSQC, the carbon chemical shift of this functional group is 39.5 ppm. The chemical shift of methane group (e) is (3.7, 85 ppm). From the spectrum of HMBC and HSQC, the carbon shifts of methylene group (f) is 72 ppm, and the shift of two protons are 4.4 ppm (d, J = 9.2 Hz, 1H) and 3.1 ppm (d, J = 9.2 Hz, 1H) because of the molecular geometry. Two quaternary carbons k and l on the aromatic ring are 136.6 and 158.6 ppm, respectively. The carbon chemical shift of other two peaks on the aromatic ring m, n is 143.9 and 140.5 ppm, and the proton shifts are 7.3 ppm.

Since the aromatic ring on the carbon cage was destroyed by the modification, the NMR peaks of two carbons (g and h) on the carbon cage were shifted to high filed to 64 and 56 ppm. According to HMBC result, the chemical shift of two adjacent carbons (i and j) are 113 and 115.5 ppm. The peaks for other 74 carbons on the cage are between 160 and 128 ppm (**Table 1**).

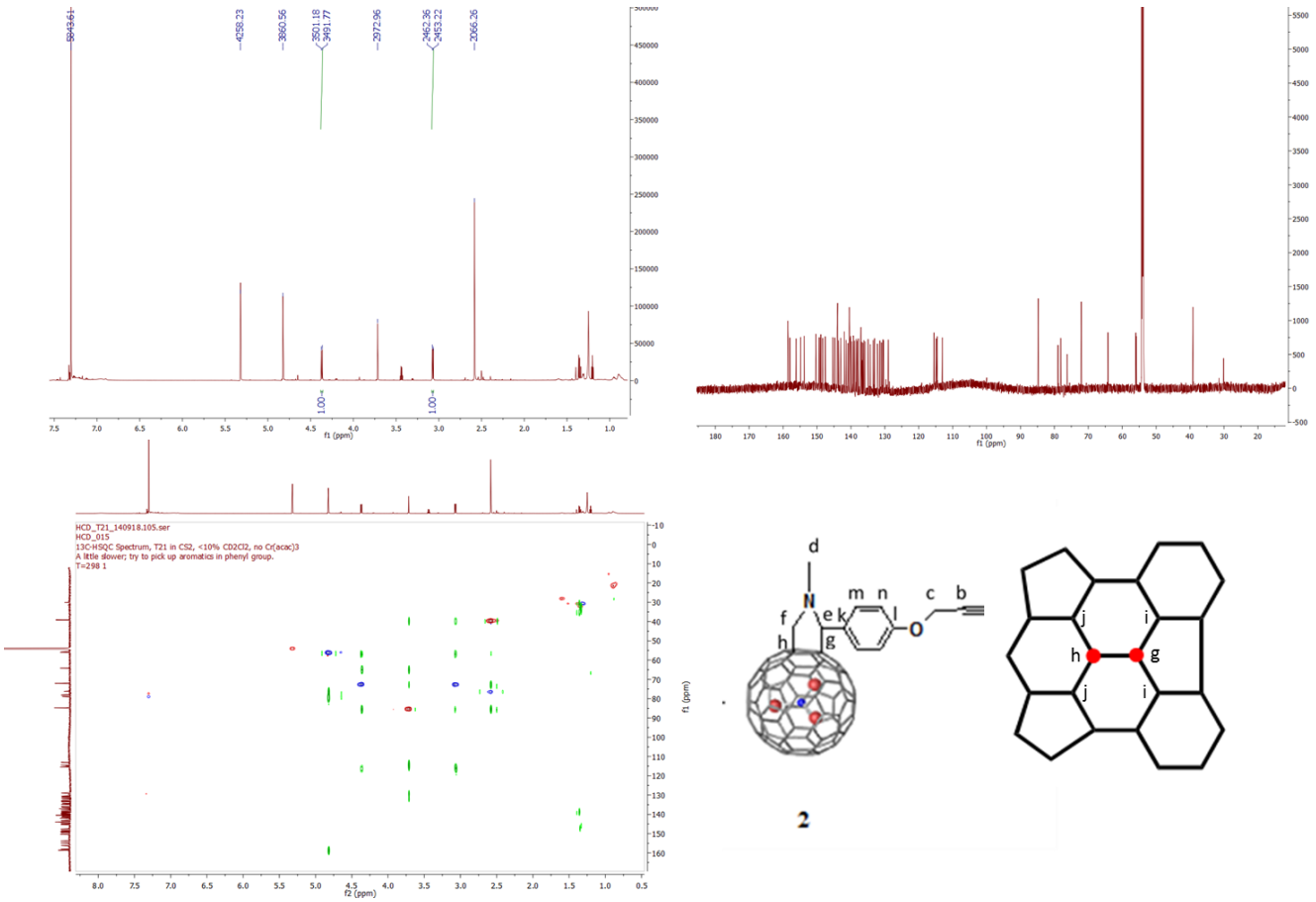

Figure 2. 800MHz ^{1}H NMR, ^{13}C NMR and HSQC spectra of compound **2**.

peak	1H chemical shift ppm	13C chemical shift ppm
a	2.6	76
b	-	79
c	4.8	56
d	2.6	39.5
e	3.7	85
f	4.4 (d, J = 9.2 Hz, 1H) 3.1 (d, J = 9.2 Hz, 1H)	72
g	-	64
h	-	56
i	-	113
j	-	115.5
k	-	136.6
l	-	158.6
m	7.3	143.9
n	7.3	140.5
There are 82 peaks from 110-160 ppm		

Table 1. Summarized NMR data of compound **2**.

To evaluate the utility of these $Sc_3N@C_{80}$-Alkynyls as scaffolds for further functionalization, click reaction was carried out with the benzyl azide as a model chemical (**Scheme 2**). The click reaction was carried out by heating toluene solution containing $Sc_3N@C_{80}$-Alkynyl (1 equiv), benzyl azide (100 equiv), CuI (5 equiv) at 60 ^oC after the solution was degassed with argon for thirty minutes. After 10 hours, the reaction was monitored by HPLC as shown in **Figure 3A** (C1). The peaks H1a (21 min) and H1b (24 min) (1b) were the two isomer of unreacted $Sc_3N@C_{80}$-ALK and the peak of H1a significantly decrease means that most of $Sc_3N@C_{80}$-ALK reacted with benzyl azide under the CuI as the catalysator. A new peak appeared at 29 min is assigned as $Sc_3N@C_{80}$-Alkynyl-benzyl azide ($Sc_3N@C_{80}$-Alk-BA). The product of click reaction was isolated in 75% yield by using HPLC as shown in **Figure 3A** C2. The single symmetric peaks centered at retention time of 29 min, revealing a pure isomer.

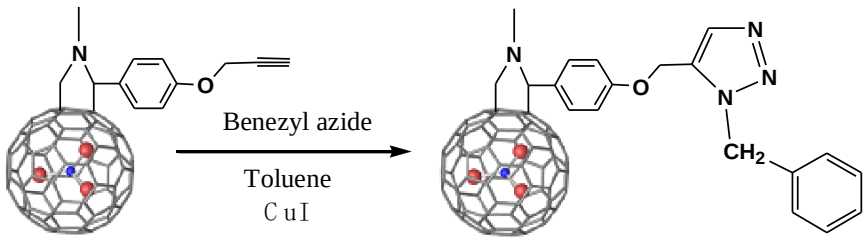

3

Scheme 2 Synthetic scheme of $Sc_3N@C_{80}$-ALK-BA.

The MALDI-TOF mass spectrum was shown in **Figure 3B**. The mass spectrum exhibits a molecular ion peak from 2a+ at m/z 1562. Furthermore, the structure of pure $Sc_3N@C_{80}$-ALK-BA was confirmed by ^1H NMR spectroscopy (**Figure 3C**). The ^1H NMR spectrum of $Sc_3N@C_{80}$-ALK-BA contains resonances at 7.3-6.9 (CH-$C_6\underline{H}_4$-O), (-CH_2-($C_6\underline{H}_5$)) and (-C=C$\underline{H}$-N), 5.6 (O-

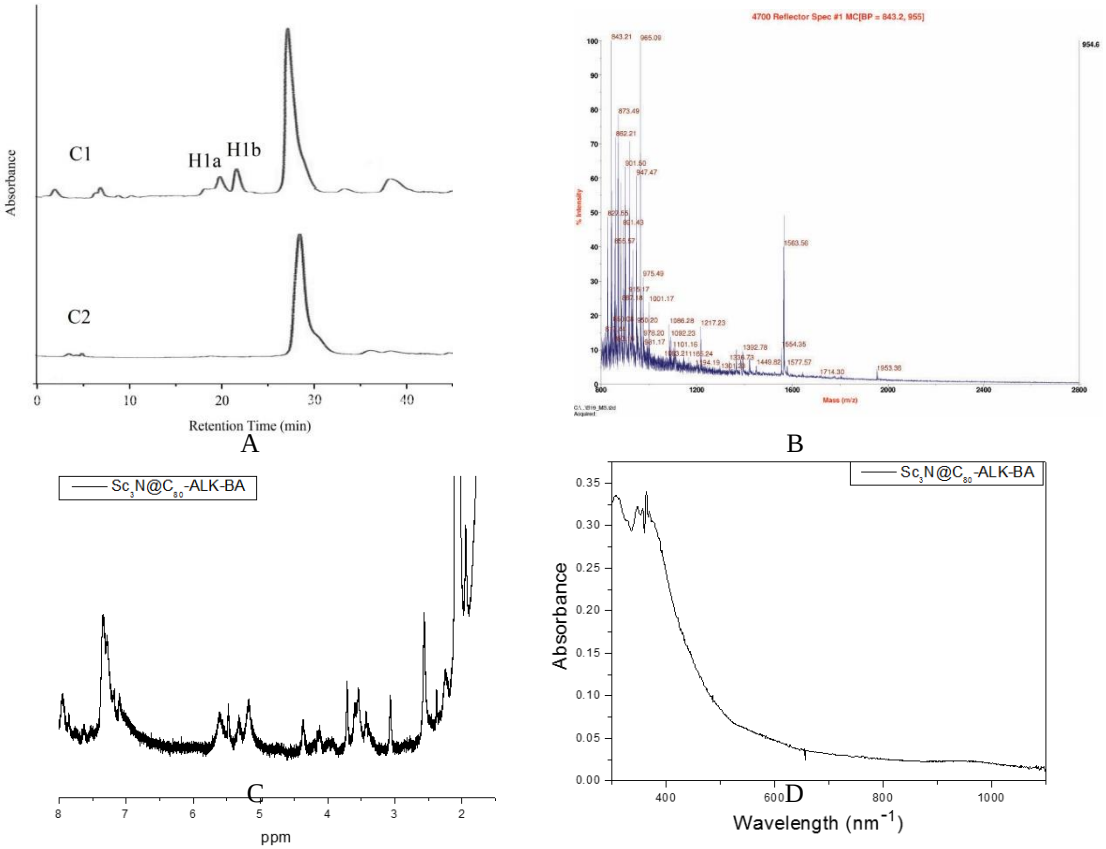

Figure 3. A) Click reaction monitored by HPLC, C1: the reaction solvent, C2: the product of click reaction after purifying by HPLC. (Buckyprep, 4.6 mm i.d × 250 mm, toluene, 2 mL/min, 390 nm). B) MALDI-TOF spectrum of pure $Sc_3N@C_{80}$-ALK-BA. C) ^1H NMR spectrum of $Sc_3N@C_{80}$-ALK-BA (800 MHz, D-acetone/CS_2 =10/90 v/v, doped with chromuium acetylacetonate). D) UV-vis spectra of $Sc_3N@C_{80}$-Alkynyl (solvent: toluene).

$C\underline{H}_2$), 5.1(N-$C\underline{H}_2$-(C_6H_5)), 3.7 ($Sc_3N@C_{80}$-$C(C_6H_4)\underline{H}$-N), 3.0, 4.3 ($Sc_3N@C_{80}$-$\underline{CH}_2$-N), 2.1 ($C\underline{H}_3$-N) ppm. The UV-vis absorption spectrum of $Sc_3N@C_{80}$-ALK-BA shows the similar pattern as $Sc_3N@C_{80}$ and $Sc_3N@C_{80}$-Alkynyl, indicating that the $Sc_3N@C_{80}$ derivatives retain the main aromatic cage features of the parent metallofullerenes.

In summary, we have successfully synthesized and characterized the $Sc_3N@C_{80}$-alkynyl by using the Prato reaction. The high yield of the $Sc_3N@C_{80}$-Alk-BA can provide access to various derivatives which have great potential for application in medical and materials science. In future work, the signal crystal of compound 1 and 2 need to be obtained for the further structure illustration.

Experimental Section

Materials and methods.

All chemicals were used as received. Toluene was purchased from Spectrum chemical MFG. CORP. Silica gel (200-400 mesh), chlorobenzene (anhydrous, 99%), carbon disulfide, acetone, dichloromethane, sarcosine (98%), copper(I) iodide, were purchased from Sigma-Aldrich (St. Louis, USA). Benzyl azide (94%) was purchased from Alfa Aesar. 4-hydroxybenzaldehyde, potassium carbonate, propargyl bromide, $Sc_3N@C_{80}$.

Synthesis of the 4-propargylbenzaldehyde (compound 1)

4-hydroxybenzaldehyde (1.50 g, 12.3 mmol), potassium carbonate (6.79 g, 49.2 mmol), propargyl bromide (5.85 g, 49.2 mmol), and acetone (200 mL) were mixed in a 500 mL round bottom flask equipped with a magnetic stir bar. The mixture was heated to reflux. After 4h, the reaction was stopped when the system was cooled to room temperature, then 200 mL water was added and the mixture was extracted twice with dichloromethane. The organic layers were dried overnight and removed under reduced pressure to afford 1.90 g (97%) of the compound 1 as pale yellow solid.

^{1}H NMR (CDCl3): 9.91 (s, 1H), 7.86 (d, J = 8.4 Hz, 2H), 7.09 (d, J = 8.9 Hz, 2H), 4.79 (d, J = 2.3 Hz, 2H), 2.58 (t, J = 2.4 Hz, 1H).

Synthesis of the $Sc_3N@C_{80}$-alkynyl (compound 2, $Sc_3N@C_{80}$-ALK)

A 50 mL three-necked flask equipped with a magnetic stir bar and Ar_2 inlet was charged with sarcosine (8 mg, 0.1 mmol), compound 1(40 mg, 2.5 mmol) and $Sc_3N@C_{80}$ (18.6 mg, 0.016 mmol), and chlorobenzene (5 mL). The mixture was heated to reflux for 12h in an Ar_2 atmosphere. After cooling, the solvent was evaporated by using air blowing. The crude solid was dissolved in CS_2 (1 ~ 2 mL) and poured on silica gel column, eluted with CS_2. After the first fraction, containing unreacted $Sc_3N@C_{80}$, was collected, the toluene was used as the eluent, obtaining the second fraction (compound 2, 5.4 mg, 30%).

Synthesis of the $Sc_3N@C_{80}$-alkynyl –benzyl azide (compound 3, $Sc_3N@C_{80}$-ALK-BA)

To a 10 mL round-bottomed flask charged with compound 2 (3.3 mg, 0.00578 mmol, 1 equiv.) and benzyl azide (30 mg) in toluene (3 mL) was added CuI (7 mg, 0.0116 mmol, equiv.). The solution was degassed with argon for thirty minutes and then heated to 60 ^{o}C while flushing with argon. The solution was stirred at 60 ^{o}C under argon for 12 h. The mixture was then cooled to room temperature and purified via HPLC to afford $Sc_3N@C_{80}$-ALK-BA compound 3 (0.0184 g, 0.0326 mmol, 56% yield).

References:

(1) Chai, Y.; Guo, T.; Jin, C.; Haufler, R. E.; Chibante, L. P. F.; Fure, J.; Wang, L.; Alford, J. M.; Smalley, R. E. *The Journal of Physical Chemistry* **1991**, *95*, 7564.

(2) Feng, L.; Radhakrishnan, S. G.; Mizorogi, N.; Slanina, Z.; Nikawa, H.; Tsuchiya, T.; Akasaka, T.; Nagase, S.; Martin, N.; Guldi, D. M. *J Am Chem Soc* **2011**, *133*, 7608.

(3) Zhang, J.; Fatouros, P. P.; Shu, C.; Reid, J.; Owens, L. S.; Cai, T.; Gibson, H. W.; Long, G. L.; Corwin, F. D.; Chen, Z. J.; Dorn, H. C. *Bioconjug Chem* **2010**, *21*, 610.

(4) Jones, M. A. G.; Taylor, R. A.; Ardavan, A.; Porfyrakis, K.; Briggs, G. A. D. *Chemical Physics Letters* **2006**, *428*, 303.

(5) MacFarland, D. K.; Walker, K. L.; Lenk, R. P.; Wilson, S. R.; Kumar, K.; Kepley, C. L.; Garbow, J. R. *J Med Chem* **2008**, *51*, 3681.

(6) Chaur, M. N.; Melin, F.; Ortiz, A. L.; Echegoyen, L. *Angew Chem Int Ed Engl* **2009**, *48*, 7514.

(7) Yamada, M.; Akasaka, T.; Nagase, S. *Acc Chem Res* **2010**, *43*, 92.

(8) Lu, X.; Akasaka, T.; Nagase, S. *Chem Commun (Camb)* **2011**, *47*, 5942.

(9) Yang, S.; Liu, F.; Chen, C.; Jiao, M.; Wei, T. *Chem Commun (Camb)* **2011**, *47*, 11822.

(10) Feng, L.; Rudolf, M.; Wolfrum, S.; Troeger, A.; Slanina, Z.; Akasaka, T.; Nagase, S.; Martin, N.; Ameri, T.; Brabec, C. J.; Guldi, D. M. *J Am Chem Soc* **2012**, *134*, 12190.

(11) Liu, T. X.; Wei, T.; Zhu, S. E.; Wang, G. W.; Jiao, M.; Yang, S.; Bowles, F. L.; Olmstead, M. M.; Balch, A. L. *J Am Chem Soc* **2012**, *134*, 11956.

(12) Chaudhuri, P.; Paraskar, A.; Soni, S.; Mashelkar, R. A.; Sengupta, S. *ACS Nano* **2009**, *3*, 2505.

(13) Wooley, K. L.; Hawker, C. J.; Frechet, J. M. J.; Wudl, F.; Srdanov, G.; Shi, S.; Li, C.; Kao, M. *Journal of the American Chemical Society* **1993**, *115*, 9836.

(14) Isobe, H.; Cho, K.; Solin, N.; Werz, D. B.; Seeberger, P. H.; Nakamura, E. *Org Lett* **2007**, *9*, 4611.

(15) Hawker, C. J.; Frechet, J. M. J. *Journal of the American Chemical Society* **1990**, *112*, 7638.

(16) Kolb, H. C.; Finn, M. G.; Sharpless, K. B. *Angewandte Chemie* **2001**, *113*, 2056.

(17) Moses, J. E.; Moorhouse, A. D. *Chem Soc Rev* **2007**, *36*, 1249.

(18) Tron, G. C.; Pirali, T.; Billington, R. A.; Canonico, P. L.; Sorba, G.; Genazzani, A. A. *Med Res Rev* **2008**, *28*, 278.

(19) Sletten, E. M.; Bertozzi, C. R. *Angew Chem Int Ed Engl* **2009**, *48*, 6974.

(20) Chen, L.; Furukawa, K.; Gao, J.; Nagai, A.; Nakamura, T.; Dong, Y.; Jiang, D. *Journal of the American Chemical Society* **2014**, *136*, 9806.

(21) Zhang, W.-B.; Tu, Y.; Ranjan, R.; Van Horn, R. M.; Leng, S.; Wang, J.; Polce, M. J.; Wesdemiotis, C.; Quirk, R. P.; Newkome, G. R.; Cheng, S. Z. D. *Macromolecules* **2008**, *41*, 515.

(22) Cai, T.; Ge, Z.; Iezzi, E. B.; Glass, T. E.; Harich, K.; Gibson, H. W.; Dorn, H. C. *Chem Commun (Camb)* **2005**, 3594.

(23) Aroua, S.; Yamakoshi, Y. *J Am Chem Soc* **2012**, *134*, 20242.

Appendix B

Characterization of PEGylated $Ho_3N@C_{80}$

Materials

$Ho_3N@C_{80}$ was purchased from LUNA Innovations (Danville, VA). 98% 1,8-Diazabicyclo(5.4.0)undec-7-ene (DBU), 99% trimethylamine (TEA), polyethylene glycol 2000 (PEG_{2000}), 99% CBr_4, 99% 18crown-6, 50% sodium hydroxide solution, and 50 % hydrogen peroxide were used as obtained from Sigma-Aldrich.

Synthesis of Di{ω-methyl-poly(ethylene glycol)} malonate ($DiPEG_{2000}$)

To a solution with 5g PEG_{2000}, 0.7 ml triethylamine in 7 ml CH_2Cl_2, was added dropwise a solution of 0.25 ml malonyl dichloride. The solution was stirred at room temperature under N_2 protection for 4 hours. The final mixture was concentrated and the residue was dissolves in chloroform and then poured into a large amount of toluene, filtrated and the filtrate was concentrated under vacuum to give a yellow viscous liquid.

Synthesis of $Ho_3N@C_{80}$-$DiPEG_{2000}$ and $Ho_3N@C_{80}$-$DiPEG_{2000}$(OH)x

The mixture of $Ho_3N@C_{80}$, $DiPEG_{2000}$, DBU and CBr_4 (molar ratio 1:20:20:67) was dissolved in 10 mL chlorobenzene with degassed by argon for 30 min. The solution was stirred at room temperature for 12 hours. The resultant mixture was evaporated to remove solvent and then redissolved in toluene. Half of the resultant solution was concentrated and separated by Sephadex G25 to obtain $Ho_3N@C_{80}$-$DiPEG_{2000}$. 5 ml of NaOH and 2mg 18-crown-6 were added and the resultant solution was stirred for another 3 hours. Then 3ml water and 15 drops of H_2O_2 were added and the mixture was stirred at ambient temperature overnight. The $Ho_3N@C_{80}$-$DiPEG_{2000}$(OH)x was concentrated and separated by Sephadex G25.[1]

Relaxivity Measurements for $Ho_3N@C_{80}$-$DiPEG_{2000}$ and $Ho_3N@C_{80}$-$DiPEG_{2000}$(OH)x

Solutions with different Ho^{3+} concentrations were prepared by diluting a stock solution with deionized water. The concentration of the Ho^{3+} ions was determined by Varian 820-MS ICP Mass Spectrometer. The T_1 and T_2 relaxation times were measured at three different magnetic field strength, Bruker Minispec mq 20 (0.47 T), mq 60 (1.41 T) analyzers, and Bruker Avance III 400 MHz (9.4 T) wide bore spectrometer equipped with an MIC 400 W1/S2 probe and 5mm ^1H coil. The inversion-recovery method was used to measure the spin-lattice relaxation time T_1, and the Carr-Pucell-Meiboom-Gill method was used for the spin-spin relaxation time T_2 measurement. Errors in T_1 and T_2 values were less than ±2%.

Table 1. The relaxivity results of $Ho_3N@C_{80}$-$DiPEG_{2000}$ and $Ho_3N@C_{80}$-$DiPEG_{2000}$(OH)x under three magnetic fields. (units of $mM^{-1}s^{-1}$ per mM in pure water at 298 K).

Fullerene Derivatives	0.47 T		2.4T		9.4 T	
	r_1	r_2	r_1	r_2	r_1	r_2
$Ho_3N@C_{80}$-$DiPEG_{2000}OH_x$ (300-3000 µM)	0.62	0.75	0.92	1.17	0.34	1.12
$Ho_3N@C_{80}$-$DiPEG_{2000}OH_x$ (3-60 µM)	42.65	44.17	49.87	44.35	-	-
$Ho_3N@C_{80}$-$DiPEG_{2000}OH_x$ (2-36 µM)	68.57	70.79	79.23	62.17	-	-
$Ho_3N@C_{80}$-$DiPEG_{2000}$ (63-255 µM)	2.37	5.10	2.56	10.05	-	-

The data summarized in **Table 1** indicates the Ho-based hydroxylated metallofullerenes also require the T_1 contrast ability, due to the unpaired electrons in its 4f subshell, but are less effective compared with Gd-based fullerenes. The hydroxyl groups attached onto the cage is also a key factor for the relaxivity, facilitating the Ho-based fullerenes to trap water molecules in their aggregates, which could more efficiently undergo (OH-H_2O) hydrogen exchange reactions for the nanoparticle. What's more, the contrast agents have higher relaxivity at lower concentrations. The explanation for the concentration dependency is not fully understand. It is possible that the water

soluble metallofullerenes act like amphiphilic compounds, forming micelles at higher concentrations, which might hinder the proton exchange.

MRI Acquisition

The relaxivity data of the samples were obtained at 3T on a Siemens MAGNETOM Prisma scanner using a four element surface coil. An inversion recovery spin echo sequence was implemented, acquiring images at different inversion times (T_I=24, 50, 100, 200, 500, 1000, 1500, 2500 and 3500 ms) while keeping all other parameters fixed (20 slices, T_E=36 ms, T_R=4000 ms, flip angle=150º). $Ho_3N@C_{80}$-$DiPEG_{2000}$ and $Ho_3N@C_{80}$-$DiPEG_{2000}$(OH)x were placed in 5mm NMR tubes with various concentrations of 2 μM, 5 μM, 10 μM, 20 μM and 100 μM.

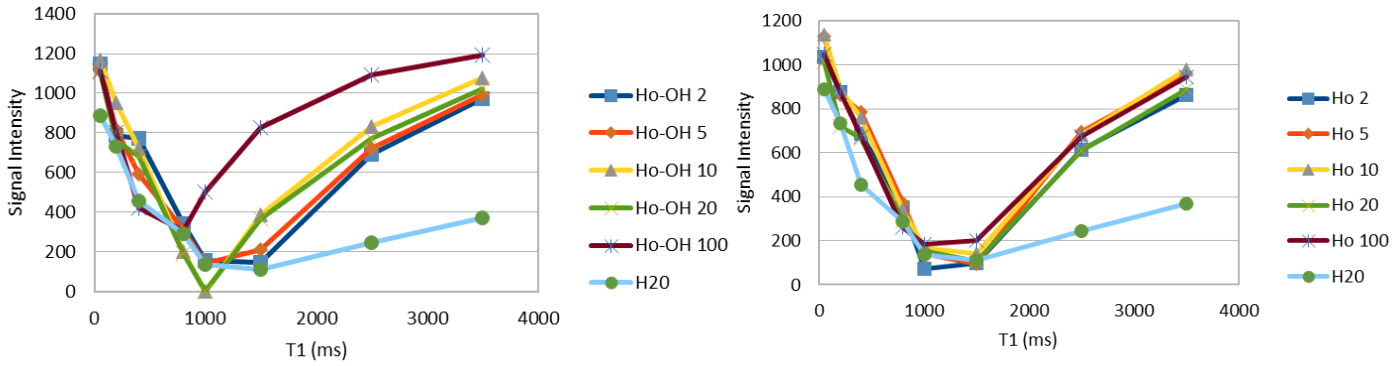

Figure 1. Plots of mean intensity values of $Ho_3N@C_{80}$-$DiPEG_{2000}$(OH)x and $Ho_3N@C_{80}$-$DiPEG_{2000}$ for the inversion recovery sequence.

***In vitro* MRI study of the functionalized $Ho_3N@C_{80}$**

The *in vitro inversion-recovery* MR images were obtained under the same 3T clinical scanner for the visual confirmation of the efficiency of the functionalized fullerene working as a contrast agent. Various concentrations of the Ho based fullerenes, and the commercial contrast agent Omniscan® were used and compared.

With the highest concentration, the $Gd_3N@C_{80}$-DiPEG$_{2000}$(OH)x, $Ho_3N@C_{80}$-DiPEG$_{2000}$(OH)x and Omniscan shared the similar brightness. This suggests three contrast agents reached their plateau. At lower concentrations, the Gd-based fullerenes are brighter than other agents, which corresponds to the previous relaxivity results.

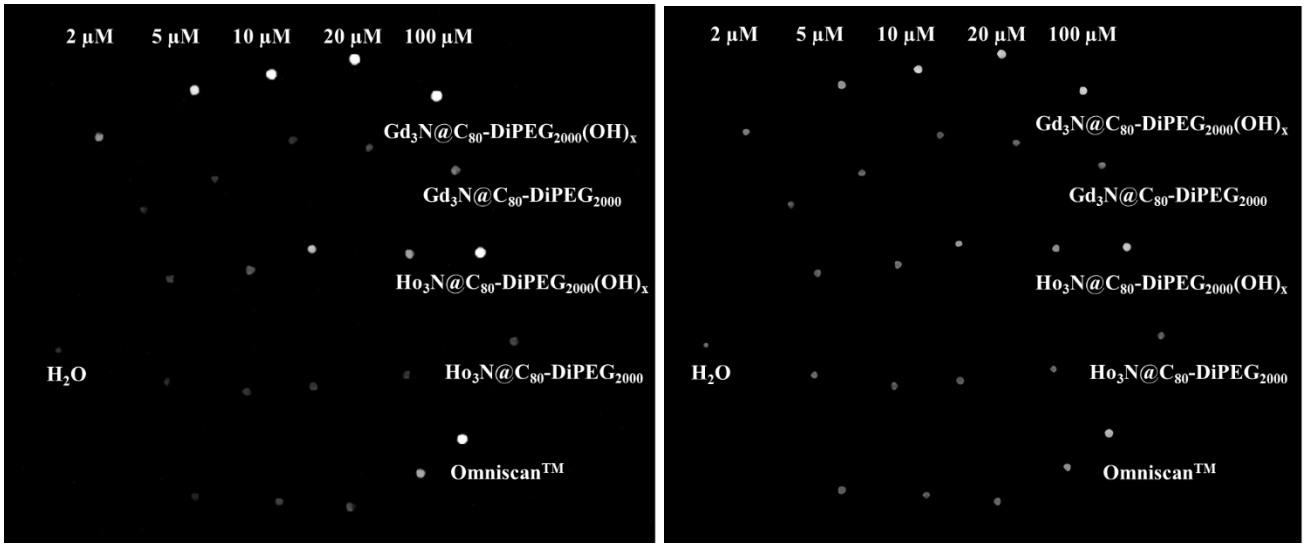

Figure 2. *Inversion-recovery* MR images (T_1=1500 ms and 2500 ms, T_R=4000 ms, T_E=32 ms) with f-$Gd_3N@C_{80}$, f-$Ho_3N@C_{80}$, and Omniscan® as contrast agent.

Dynamic light scattering (DLS) measurement

The hydrodynamic size distribution of $Ho_3N@C_{80}$-DiPEG$_{2000}$ in water and PBS were measured by DLS at time 0, 15 and 30min. The concentration of $Ho_3N@C_{80}$-DiPEG$_{2000}$ is 36 µM per Ho^{3+} ions. The DLS results (**Figure 3**) indicate that the hydrodynamic size of an aggregate nanoparticle is ~100 nm in both PBS and water. The aggregations are stable in both media at least for 30 min.

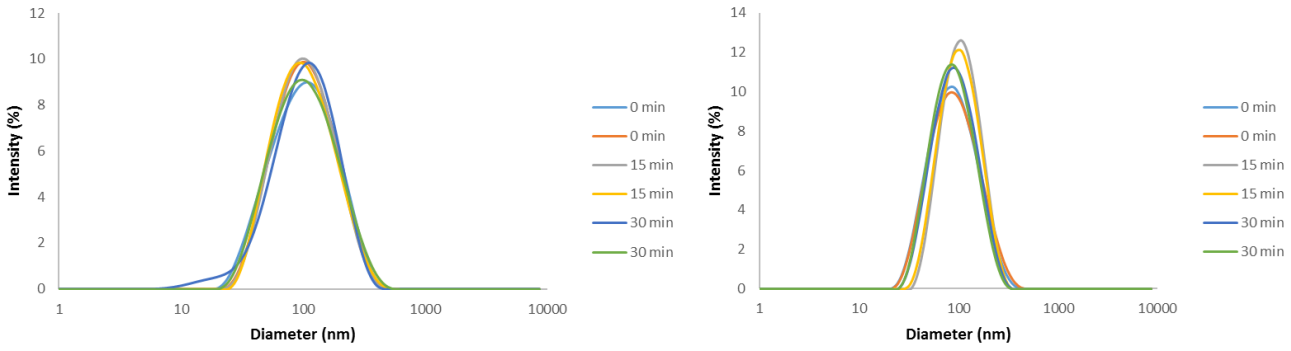

Figure 3. $Ho_3N@C_{80}$-DiPEG$_{2000}$ in PBS (left), and water (right) at time 0, 15 and 30 min.

Scanning Electron Microscope (SEM) images of $Ho_3N@C_{80}$-$DiPEG_{2000}$

With the SEM images of $Ho_3N@C_{80}$-$DiPEG_{2000}$ (**Figure 4**), the black spots represent the fullerene cages. In the resolution with 100 nm image, it clearly shows the aggregation of the functionalized fullerenes. These data indicate the water soluble metallofullerenes might share the similar property as amphiphilic compounds, the size of aggregation is concentration dependent. This work was done by Junghyun Kim at University of North Carolina at Chapel Hill.

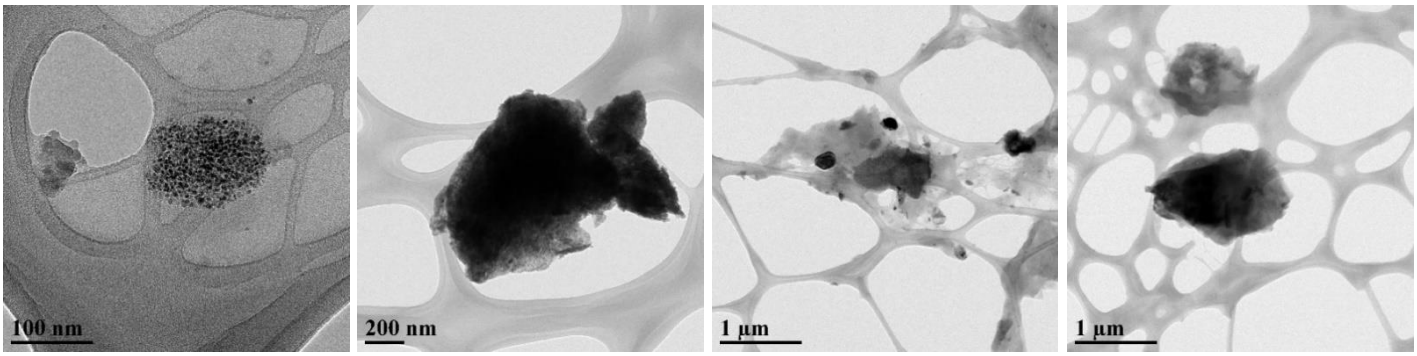

Figure 4. Scanning Electron Microscope (SEM) images of $Ho_3N@C_{80}$-$DiPEG_{2000}$.

The leaching study of $Ho_3N@C_{80}$ and $Ho_3N@C_{80}(OH)x$

The stable holmium isotopes can be encapsulated into the carbon cages, with neutron irradiation, the Ho-based fullerenes can be performed as the radiotherapeutic agents. The leaching study was

Table 2. The leaching study of $Ho_3N@C_{80}$ and $Ho_3N@C_{80}(OH)x$.

Fullerene	Radioactivity (CPM)	% Error	Corrected (Radioactivity - BG) (CPM)	Leaching (%)
$Ho_3N@C_{80}$	10750.7	0.6	10744.2	
H_2O (control)	6.4	38.7	0.0	
Wash 1	21.0	19.1	14.6	0.1
Wash 2	5.6	29.2	-0.9	0
Wash 3	2.8	35.4	-3.7	0

Fullerenol	Radioactivity (CPM)	% Error	Corrected (Radioactivity - BG) (CPM)	Leaching (%)
$Ho_3N@C_{80}(OH)x$	164296.65	0.6	164290.2	
H_2O (control)	16.62	38.7	0.0	
Wash 1	53.49	19.1	36.9	0.0
Wash 2	29.36	29.2	12.7	0.0
Wash 3	24.74	35.4	8.1	0.0

taken to test the stability of $Ho_3N@C_{80}$ and $Ho_3N@C_{80}(OH)x$ cage after one-hour irradiation. After irradiating, the holmium which might came out of the fullerene cages were separated with centrifugal filter (3 KDa and 50 KDa). Based on the preliminary result, both $Ho_3N@C_{80}$ and $Ho_3N@C_{80}(OH)x$ were very stable without holmium leaching. This work was done by Junghyun Kim at University of North Carolina at Chapel Hill.

Appendix C

Conjugation of cy5-FLFLFK-$C_{60}(OH)_5(CH_2CH_2COOH)_{15}$

The elaboration of the carboxyl group onto the cage surface of C_{60} was performed using an improved procedure from our earlier studies.[1-3] Briefly, 100 mg of the C_{60} and 160 mg succinic acid acyl peroxide (5 Equiv) were dissolved in 20 mL of 1,2-dichlorobenzene. The resultant solution was deoxygenated with flowing argon and heated at 84 °C for five days. Additional succinic acid acyl peroxide (5 equiv) was added every 12 hours. After the reaction, 15 mL of 0.2 M NaOH was added to extract the water-soluble product. The top layer was concentrated, and the residue was purified by a Sephadex G-25 size-exclusion gel column. The functionalized fullerene was characterized by FTIR and XPS to measure the elemental composition and empirical formula. In the FTIR spectrum (**Figure 1A**), the characteristic vibration bands of broad O-H, C=O, and C-O suggest the existence of both hydroxyl and carboxyl groups on the carbon cage. The XPS multiplex spectrum for functionalized fullerene are presented in **Figure 1B**. In the multiplex

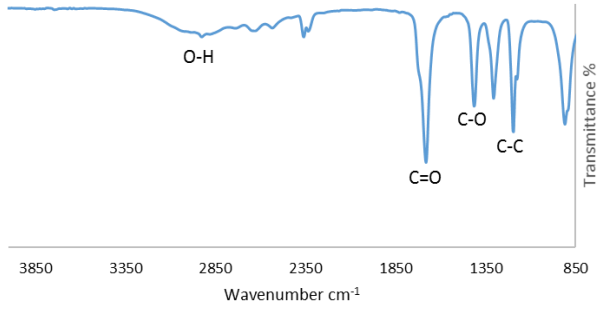

A

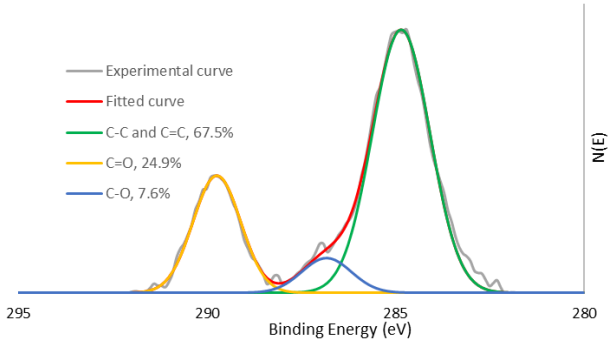

B

Bond (C1s)	Binding Energy (eV)	Area%	Intensity	FWHM(eV)
C-C, C=C	284.84	67.5%	911	1.80
C-O	286.82	7.6%	120	1.54
C=O	289.73	24.9%	406	1.49

Figure 1. Characterization of the functionalized C_{60}. A) FTIR spectrum. B) XPS multiplex spectrum and **Table 1** of the functionalized C_{60}.

spectrum, the C_{1s} peaks, centered at binding energy values of 284.8, 286.82, and 289.73 eV, were assigned to the C−C and C=C, C−O, and C=O, respectively (**Table 1**). Based on the peak deconvolution of the XPS profile, the average formula for functionalized fullerene can be described as $C_{60}(OH)_5(CH_2CH_2COOH)_{15}$.

A volume of 500 μL 15mg carboxylated C_{60} was dissolved in DMF, then the carboxyl groups were activated by 75 μmol of diisopropylcarbodiimide (DIC) and 1-hydroxybenzotriazole (HOBt) in DMF. After 4 hours, 200 μL of 0.2 μmol cy5-FLFLFK peptides (MW 1451.7) was added, vortexed and incubated at room temperature for 12 hours. The resulting solution was filtered through polyacrylamide desalting columns. The final product was further purified *via* LC-MS, using a gradient of H_2O 0.1% TFA: MeCN 0.1% TFA on a C_{18} reverse phase column.

References

(1) Xiao, L.; Li, T.; Ding, M.; Yang, J.; Rodriguez-Corrales, J.; LaConte, S. M.; Nacey, N.; Weiss, D. B.; Jin, L.; Dorn, H. C.; Li, X. *Bioconjug Chem* **2017**, *28*, 649.

(2) Shu, C.; Corwin, F. D.; Zhang, J.; Chen, Z.; Reid, J. E.; Sun, M.; Xu, W.; Sim, J. H.; Wang, C.; Fatouros, P. P.; Esker, A. R.; Gibson, H. W.; Dorn, H. C. *Bioconjug Chem* **2009**, *20*, 1186.

(3) Li, T.; Murphy, S.; Kiselev, B.; Bakshi, K. S.; Zhang, J.; Eltahir, A.; Zhang, Y.; Chen, Y.; Zhu, J.; Davis, R. M.; Madsen, L. A.; Morris, J. R.; Karolyi, D. R.; LaConte, S. M.; Sheng, Z.; Dorn, H. C. *J Am Chem Soc* **2015**, *137*, 7881.